JSCSEN 88(10)937–1064(2023)

ISSN 1820-7421(Online)

Journal of the Serbian Chemical Society

Version
electronic

VOLUME 88

No 10

BELGRADE 2023

Available on line at
СХД 1897
www.shd.org.rs/JCSC/

The **Journal of the Serbian Chemical Society** (formerly Glasnik Hemijskog društva Beograd), one volume (12 issues) per year, publishes articles from the fields of chemistry. The **Journal** is financially supported by the **Ministry of Education, Science and Technological Development of the Republic of Serbia.**

Articles published in the **Journal** are indexed in **Clarivate Analytics products: Science Citation Index-Expanded**$^{\text{TM}}$ – accessed *via* **Web of Science**$^{®}$ and **Journal Citation Reports**$^{®}$.

Impact Factor announced on 28 June, 2023: **1.000; 5-year Impact Factor**: **1.100**.

Articles appearing in the **Journal** are also abstracted by: **Scopus, Chemical Abstracts Plus (CAplus**$^{\text{SM}}$**), Directory of Open Access Journals, Referativnii Zhurnal (VINITI), RSC Analytical Abstracts, EuroPub, Pro Quest** and **Asian Digital Library.**

Publisher:	**Serbian Chemical Society**, Karnegijeva 4/III, P. O. Box 36, 1120 Belgrade 35, Serbia tel./fax: +381–11–3370–467, E-mails: **Society** – shd@shd.org.rs; **Journal** – jscs@shd.org.rs Home Pages: **Society** – http://www.shd.org.rs/, **Journal** – http://www.shd.org.rs/JSCS/
Internet Service:	Contents, Abstracts and full papers (from Vol 64, No. 1, 1999) are available in the electronic form at the Web Site of the **Journal** (http://www.shd.org.rs/JSCS/).

Former Editors:	**Nikola A. Pušin** (1930–1947), **Aleksandar M. Leko** (1948–1954), **Panta S. Tutundžić** (1955–1961), **Miloš K. Mladenović** (1962–1964), **Đorđe M. Dimitrijević** (1965–1969), **Aleksandar R. Despić** (1969–1975), **Slobodan V. Ribnikar** (1975–1985), **Dragutin M. Dražić** (1986–2006).
Editor-in-Chief:	BRANISLAV Ž. **NIKOLIĆ**, Serbian Chemical Society (E-mail: jscs-ed@shd.org.rs)
Deputy Editor:	DUŠAN **SLADIĆ**, Faculty of Chemistry, University of Belgrade
Sub editors:	
Organic Chemistry	DEJAN **OPSENICA**, Institute of Chemistry, Technology and Metallurgy, University of Belgrade JÁNOS **CSANÁDI**, Faculty of Science, University of Novi Sad
Biochemistry and Biotechnology	OLGICA **NEDIĆ**, INEP – Institute for the Application of Nuclear Energy, University of Belgrade
Inorganic Chemistry	MILOŠ **ĐURAN**, Serbian Chemical Society
Theoretical Chemistry	IVAN **JURANIĆ**, Serbian Chemical Society
Physical Chemistry	LJILJANA **DAMJANOVIĆ-VASILIĆ**, Faculty of Physical Chemistry, University of Belgrade
Electrochemistry	SNEŽANA **GOJKOVIĆ**, Faculty of Technology and Metallurgy, University of Belgrade
Analytical Chemistry	RADA **BAOŠIĆ**, Faculty of Chemistry, University of Belgrade
Polymers	BRANKO **DUNJIĆ**, Faculty of Technology and Metallurgy, University of Belgrade
Thermodynamics	MIRJANA **KIJEVČANIN**, Faculty of Technology and Metallurgy, University of Belgrade
Chemical Engineering	TATJANA **KALUĐEROVIĆ RADOIČIĆ**, Faculty of Technology and Metallurgy, University of Belgrade
Materials	RADA **PETROVIĆ**, Faculty of Technology and Metallurgy, University of Belgrade
Metallic Materials and Metallurgy	ANA **KOSTOV**, Mining and Metallurgy Institute Bor, University of Belgrade
Environmental and Geochemistry	VESNA **ANTIĆ**, Faculty of Agriculture, University of Belgrade
History of and Education in Chemistry	DRAGICA **TRIVIĆ**, Faculty of Chemistry, University of Belgrade
English Language Editors:	LYNNE **KATSIKAS**, Serbian Chemical Society VLATKA **VAJS**, Serbian Chemical Society JASMINA **NIKOLIĆ**, Faculty of Technology and Metallurgy, University of Belgrade
Technical Editors:	VLADIMIR **PANIĆ**, Institute of Chemistry, Technology and Metallurgy, University of Belgrade, MARIO **ZLATOVIĆ**, Faculty of Chemistry, University of Belgrade
Journal Manager & Web Master:	MARIO **ZLATOVIĆ**, Faculty of Chemistry, University of Belgrade
Office:	VERA **ĆUŠIĆ**, Serbian Chemical Society

Editorial Board

From abroad: **R. Adžić**, Brookhaven National Laboratory (USA); **A. Casini**, University of Groningen (The Netherlands); **G. Cobb**, Baylor University (USA); **D. Douglas**, University of British Columbia (Canada); **G. Inzelt**, Etvos Lorand University (Hungary); **J. Kenny**, University of Perugia (Italy); **Ya. I. Korenman**, Voronezh Academy of Technology (Russian Federation); **M. D. Lechner**, University of Osnabrueck (Germany); **S. Macura**, Mayo Clinic (USA); **M. Spiteller**, INFU, Technical University Dortmund (Germany); **M. Stratakis**, University of Crete (Grecce); **M. Swart**, University de Girona (Cataluna, Spain); **G. Vunjak-Novaković**, Columbia University (USA); **P. Worsfold**, University of Plymouth (UK); **J. Zagal**, Universidad de Santiago de Chile (Chile).

From Serbia: **B. Abramović, V. Antić, R. Baošić, V. Beškoski, J. Csanadi, Lj. Damjanović-Vasilić, A. Dekanski, V. Dondur, B. Dunjić, M. Đuran, S. Gojković, I. Gutman, B. Jovančićević, I. Juranić, T. Kaluđerović Radiočić, L. Katsikas, M. Kijevčanin, A. Kostov, V. Leovac, S. Milonjić, V.B. Mišković-Stanković, O. Nedić, B. Nikolić, J. Nikolić, D. Opsenica, V. Panić, M. Petkovska, R. Petrović, I. Popović, B. Radak, S. Ražić, D. Sladić, S. Sovilj, S. Šerbanović, B. Šolaja, Ž. Tešić, D. Trivić, V. Vajs, M. Zlatović**.

Subscription: The annual subscription rate is **150.00 €** including postage (surface mail) and handling. For Society members from abroad rate is **50.00 €**. For the proforma invoice with the instruction for bank payment contact the Society Office (E-mail: shd@shd.org.rs) or see JSCS Web Site: http://www.shd.org.rs/JSCS/, option Subscription.

Godišnja pretplata: Za članove SHD: **2.500,00 RSD**, za penzionere i studente: **1000,00 RSD**, a za ostale: **3.500,00 RSD**:za organizacije i ustanove: **16.000,00 RSD**. Uplate se vrše na tekući račun Društva: **205-13815-62**, poziv na broj **320**, sa naznakom "pretplata za JSCS".

Nota: Radovi čiji su svi autori članovi SHD prioritetno se publikuju.

Odlukom Odbora za hemiju Republičkog fonda za nauku Srbije, br. 66788/1 od 22.11.1990. godine, koja je kasnije potvrđena odlukom Saveta Fonda, časopis je uvršten u kategoriju međunarodnih časopisa (**M-23**). Takođe, aktom Ministarstva za nauku i tehnologiju Republike Srbije, 413-00-247/2000-01 od 15.06.2000. godine, ovaj časopis je proglašen za publikaciju od posebnog interesa za nauku. **Impact Factor** časopisa objavljen 28. juna 2023. godine je **1,000**, a petogodišnji **Impact Factor 1,100**.

Journal of the Serbian Chemical Society
eVersion electronic
JSCS-info@shd.org.rs • www.shd.org.rs/JSCS

J. Serb. Chem. Soc. Vol. 88, No. 10 (2023)

CONTENTS*

Organic Chemistry

Biochemistry and Biotechnology

Inorganic Chemistry

Theoretical Chemistry

Electrochemistry

Metallurgy and Metallic Materials

Environmental

Published by the Serbian Chemical Society
Karnegijeva 4/III, P.O. Box 36, 11120 Belgrade, Serbia
Printed by the Faculty of Technology and Metallurgy
Karnegijeva 4, P.O. Box 35-03, 11120 Belgrade, Serbia

---

* For colored figures in this issue please see electronic version at the Journal Home Page: http://www.shd.org.rs/JSCS/

Journal of the Serbian Chemical Society

JSCS-info@shd.org.rs • www.shd.org.rs/JSCS

J. Serb. Chem. Soc. *88* (10) 937–957 (2023)
JSCS–5672

Survey
Published 24 October 2023

SURVEY

Flavonoid derivatives as anticancer moiety and its effect on cancer cell lines: An updated review

CHANDRAMOULI MANOJMOULI*, THOPPALADA YUNUS PASHA, KOPPURAVURI NAGAPRASHANT, BEEVINAHALLI RAMESH, NOOR UL EAIN and KARDIGERE NAGARAJU PURUSHOTHAM

Department of Pharmaceutical Chemistry, Sri Adichunchanagiri College of Pharmacy, Adichunchanagiri University, B. G. Nagara, Karnataka, India

(Received 28 December 2022, revised 8 February, accepted 15 July 2023)

Abstract: Cancer is now considered the number one leading cause of premature death in industrialized countries. Chemotherapy drugs are quite expensive and cause multiple side effects. Natural products have been studied in depth for their potential as anticancer agents because of their remarkable chemical variability. Among the various natural metabolites, flavonoids are secondary metabolites that are extensively present in nature, have potent anti-cancer properties, have few adverse effects, and also show synergistic benefits. Numerous laboratories are diligently investigating the chemistry and biology of novel flavonoid derivatives due to the demand for and value of these drugs. In this survay, we have summarized clinical trials of various flavonoids, molecular pathways against various cancer cell lines and recent updates on the anticancer activity of flavonoid derivatives against various cancer cells synthesized by various methods, more studies are needed to develop the following mentioned flavonoid derivatives as an anticancer drug.

Keywords: flavonoids; cancer; chemotherapy; molecular targets.

CONTENTS

---

* Corresponding author. E-mail: manojmouli07@gmail.com
https://doi.org/10.2298/JSC221228041M

1. INTRODUCTION

A significant global issue in terms of human health is cancer. There are many different types of cancer, and each one is associated with an increase in the number of cells in the body. One element of the mechanisms that lead to cancer is cell proliferation and it is distinct from other tumors because of its ability to invade surrounding healthy tissues. The WHO reports that in 2020, there were 2.30 million new instances of breast cancer, 2.20 million cases of lung cancer, 1.90 million cases of colon and rectal cancer, 1.40 million cases of prostate cancer, 1.25 million cases of skin cancer, and 1.08 million cases of stomach cancer.[1–3] Anticancer therapies involve several methods such as surgery, chemotherapy and radiation, perhaps individually or in combination. However, side effects and multidrug resistance are two major obstacles to successful cancer treatment because this condition is a complicated issue, and it has been challenging to discover new medicines to combat it.[4] Cancer drug sales are forecast to reach $223.21 billion in 2022, up from $199.95 billion in 2021, at a compound annual growth rate (CAGR) of 11.6 %. Multiple laboratories are extensively investigating the chemistry and biology of novel anticancer agents due to the demand for and value of these drugs. Cytotoxic drugs, many of which are of natural origin, are currently the pillars of anticancer chemotherapy.

Natural products can be used as important sources for the development of new active molecules that might be used as leads or scaffolds to create novel, highly effective medicines with increased biological activity. Drugs that are obtained from natural sources show better anticancer activities with minimal side effects.[5] Among the various plant metabolites, flavonoids are plants' most significant low molecular weight secondary metabolites. These metabolites comprise a large number of polyphenolic compounds, including benzopyran with a substituted keto group on the pyran ring. The configuration, substitution of a hydroxy group and the number of the hydroxyl group on a parent moiety primarily affect the pharmacokinetics and pharmacological activity. There is a need to examine the relationship between structure and function since flavonoids are directly linked to human dietary components and health.[6,7] Today, flavonoids are considered a significant ingredient in a wide range of nutraceutical, pharmacological, therapeutic and cosmetic uses. This is explained by their ability to affect important cellular enzyme activity in addition to their antitumor, anti-inflammatory, antifungal, anti-aging, antiviral, antiallergic and antioxidant activities.[8] Flavonols, anthocyanidins, isoflavones, flavones, flavanones and flavanonols are the subclasses of flavonoids (Fig. 1).[9]

Anti-cancer drugs containing flavonoid moiety from the natural source showed minimal side effects and exhibited synergistic activity. Quercetin, wogonin, kaempferol, silibinin and apigenin are all recognized[10] as anticancer drugs without unwanted side effects. Luteolin showed synergistic activity with cisplatin against ovarian cancer. Quercetin with doxorubicin exhibited a synergistic effect against neuroblastoma and anaplastic osteosarcoma cell lines, quercetin with cisplatin against human mesothelioma cancer cell lines, and quercetin with temodar (temozolomide) against human astrocytoma cell line.[11]

For the last decade, researchers have mainly focused on synthesizing flavonoid derivatives. In the present review, we have summarized the clinical trials of flavonoids, mode of action, molecular targets for some important flavonoids against various cancer cells, and the results of the anticancer activity of different flavonoid derivatives synthesized by the various synthetic method in the past 4 years, *i.e.*, between the years 2019 and 2022, and described their potential against various cancer cell lines.

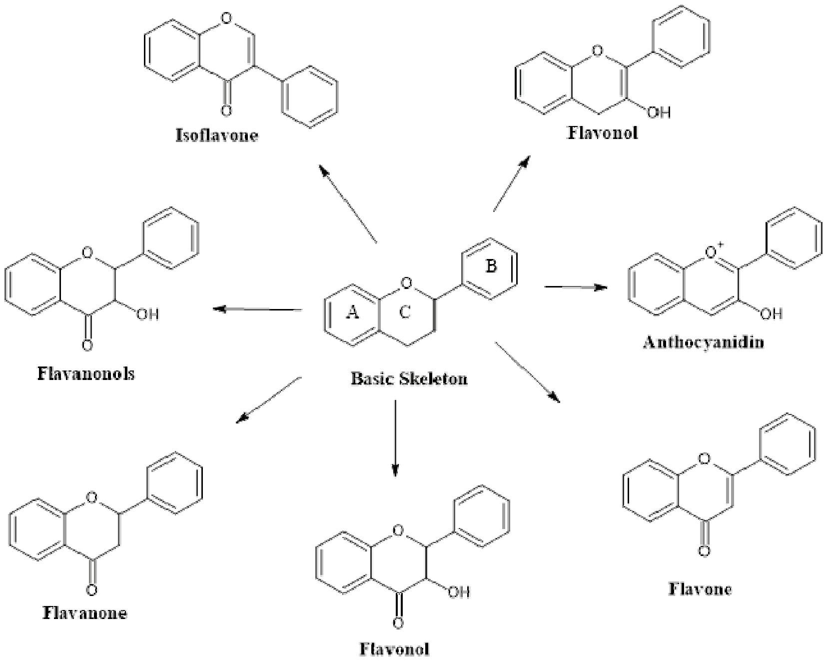

Fig. 1. The basic skeleton of flavonoids and their subclasses.

2. MODE OF ACTION OF FLAVONOIDS IN CHEMOTHERAPY

Flavonoids are believed to be bioactive, safe and widely available molecules, and they show a wide variety of anticancer activity through various mechanism of action like cell cycle arrest, mutagen inhibition and antiproliferation, inducing programmed cell death, inhibit the formation of new blood vessels (angiogenesis) and antioxidation, modulates ROS-scavenging enzyme activities, and reversal of multidrug resistance or a combination of these mechanisms (Table I). Followed by one of the significant drawbacks of anti-cancer agents is the cancer cells' susceptibility to or resistance to chemotherapeutics therapies. Flavonoids like kaempferol, quercetin or morin, exert potent activity to modulate cancer cell chemoresistance and increase the efficacy of chemotherapy by increased programmed cell death or apoptosis and induced cell cycle arrest in both chemo-resistant and sensitive cancer cells.[12–15]

TABLE I. List of various molecular targeted pathways for flavonoids against various cancer cell lines

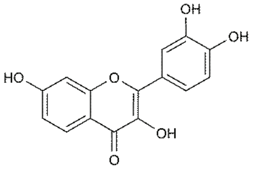 Quercetin	
Cancer cell lines	MCF-7, CNE2, HK1, HL-60, HPB-ALL and SCC-9 cancer cell lines
Targeted molecular pathway	Extracellular signal-regulated kinase (ERK), phosphoinositide 3 kinase target of rapamycin (PI3K/Akt/mTOR), mitochondrial and caspase cascade pathways.
IC_{50} values	MCF-7, 28 μM, HK1, 24 μM, HPB-ALL, 18 μM
References	16
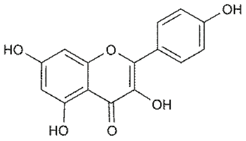 Kaempferol	
Cancer cell lines	PANC-1 and MIA PaCa-2 cancer cell lines
Targeted molecular pathway	Phosphoinositide 3 kinase target of rapamycin (PI3K/Akt/mTOR) signaling pathway
IC_{50} values	PANC-1, 78.75 μM and MIA PaCa-2, 79.07 μM
References	17
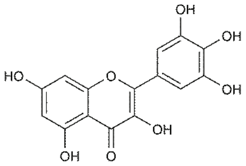 Myricetin	
Cancer cell lines	DU145, PC3, HCT-15, HT-29, A549, OVCAR-3, T24, PaCa-2, Panc1, SKOV3, MCF-7 and HepG2 cell lines
Targeted molecular pathway	Nuclear factor kappa B (NF-κB), nuclear factor erythroid 2-related factor 2 (Nrf2), phosphoinositide 3 kinase target of rapamycin (PI3K/ /Akt/mTOR), Janus kinase/signal transducers and activators of transcription (JAK/STAT), and canonical Wnt (Wnt/β-catenin) pathways
IC_{50} values	HT-29, 47.6μM and MCF-7, 50μM
References	18

TABLE I. Continued

	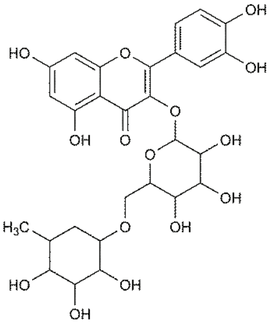 Rutin
Cancer cell lines	MCF-7, MDA-MB-231, A549, HT-29 and SW480 cancer cell lines
Targeted molecular pathway	Nuclear factor kappa B (NF-κB), nuclear factor erythroid 2-related factor 2 (Nrf2), extracellular signal-regulated kinase (ERK), c-Jun N-terminal kinases (JNK) and p38 mitogen-activated protein kinases (p38 MAPK) pathways
IC_{50} values	MDA-MB-231, 40 µM, HT-29, 46 µM and SW480, 54 µM
`References	19, 20
	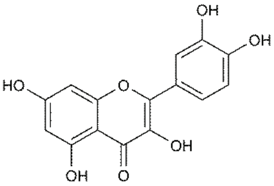 Luteolin
Cancer cell lines	HCT15, MV4-11, CO115 and MCF-7 cancer cell lines
Targeted molecular pathway	Nuclear factor kappa B (NF-κB), reactive oxygen species (ROS), canonical Wnt (Wnt/β-catenin), DNA topoisomerases and heat shock protein 90, E-cadherin, mammalian target of rapamycin (mTOR), integrin β1 and focal adhesion kinase, phosphoinositide-3-kinase (P13K) pathways
IC_{50} values	HCT15, 68 µM, MV4-11, 58 µM, CO115, 66 µM and MCF-7, 36 µM
`References	21
	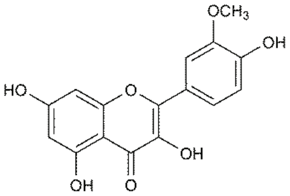 Isorhamnetin
Cancer cell lines	BT474, BT-549, MDA-MB-231, PANC-1, MCF7, T47D and MDA-MB-468 cancer cell lines

TABLE I. Continued

Targeted molecular pathway	Mitochondria-dependent intrinsic, phosphoinositide 3 kinase target of rapamycin (PI3K/Akt/mTOR), mitogen-activated protein kinase (MAPK) pathways
IC_{50} values	BT474, 10 μM, BT-549, 10 μM, MB-231, 16 μM, PANC-1, 26.5μM
References	22–24
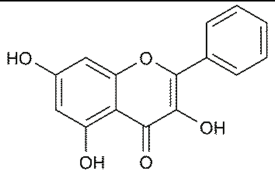 Galangin	
Cancer cell lines	MCF-7, T47D, Hs578T, AMN-3, CP70, OVAC-3, HeLa, TU212, HEP-2, hct-15, HT-29, A549, B16F10 and Eca9760 TE-1 cancer cell lines
Targeted molecular pathway	Activated protein kinase (AMPK), phosphoinositide 3 kinase target of rapamycin (PI3K/Akt/mTOR), poly (ADP-ribose) polymerase-1 pathways
IC_{50} values	MCF-7, 20 μM, T47D, 24 μM, Hs578T, 11 μM, OVAC-3, 34.5 μM, HeLa, 50 μM, TU212, 10 μM
References	25
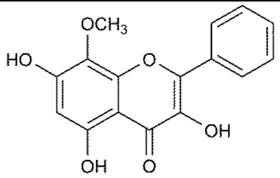 Wogonin	
Cancer cell lines	SW-480, A549, HCT-116, BT-549 and MCF-7 cancer cell lines
Targeted molecular pathway	Mitogen-activated protein kinase 1 (MEK1), nuclear factor kappa B (NF-*κ*B), peroxisome proliferator-activated receptor gamma (PPAR-*γ*) and tumor necrosis factor-*α* (TNF-*α*) pathways
IC_{50} values	SW480, 47.8 μM, HCT-116, 44.6 μM, BT-549, 36 μM
References	26
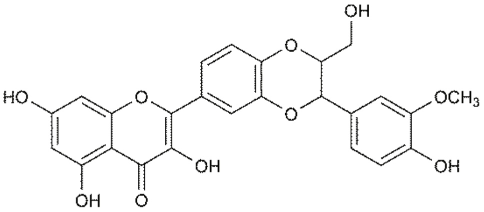 Silibinin	
Cancer cell lines	MCF-7, H460, HCC827, NCI-H1975, A549 and NCI-H1299 cancer cell lines
Targeted molecular pathway	Epidermal growth factor receptor (EGFR/LOX) pathway

TABLE I. Continued

IC_{50} values	NCI-H1975, 96.56 μM, MCF-7, 46μM, H460, 50.5 μM, H1975, 48 μM
References	27
	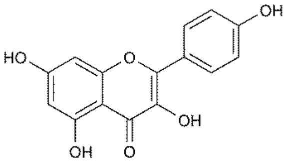 Apigenin
Cancer cell lines	SW480, A375, A549, BT-474, MDA-MB-231, DLD1, A2780, DU145 and C8161 cancer cell lines
Targeted molecular pathway	Janus kinase/signal transducers and activators of transcription (JAK/ /STAT), mitogen-activated protein kinase/extracellular-signal-regulated kinase (MAPK/ERK), canonical Wnt (Wnt/β-catenin), nuclear factor kappa B (NF-κB), phosphoinositide 3 kinase target of rapamycin (PI3K/Akt/mTOR) pathways
IC_{50} values	MDA-MB-231, 35.15 μM, A549, 79.8 μM
References	28

3. CLINICAL TRIALS OF FLAVONOID DERIVATIVES

Clinical trials were undertaken on 64 individuals (18–65 years) by Zwicker *et al.*[29] for 56 days to investigate the effectiveness of the drug isoquercetin (3-*O*-glucoside of quercetin) at two doses (500 mg for 28 patients and 1000 mg for 28 patients) in preventing venous thrombosis (blood clots) in individuals suffering from pancreatic and colorectal cancer by targeting protein disulfide isomerase (PDI). A thiol isomerase called protein disulfide isomerase (PDI), is released by vascular cells and is essential for thrombus development. At 500 mg, constipation affected one patient, diarrhea affected four patients, hyponatremia affected one patient, epistaxis affects one patient, and nausea affected two patients. At 1000 mg, only one patient was affected by gastrointestinal reflux.[29]

Clinical trials were performed by the University of Minnesota to determine the effectiveness of purple grape juice (rich in flavonoids) in improving vascular health in pediatric cancer survivors to determine the effect of purple color grape juice on endothelial function and biomarkers of vascular and systemic oxidative stress. Twenty-four individuals between the ages of 10 and 30 volunteered in the clinical studies.[30]

The University of Hohenheim, in collaboration with University Hospital Tuebingen and Quercegen Pharmaceuticals, conducted clinical trials to examine the efficiency of genistein (isoflavonoid) and quercetin (flavonoid), polyphenolic phytochemicals in comparison with placebo on the rate of increase in prostate-specific antigen (PSA). Analyzing malondialdehyde and protein carbonyl as markers of oxidative status as well as assessing the prevalence of prostate cancer are the secondary goals.[31]

The effectiveness of quercetin in preventing and treating chemotherapy-induced oral mucositis in blood cancer patients was investigated by Pegah Mosannen Mozafari of Mashhad University of Medical Sciences. They give 250 mg of quercetin capsules to 10 patients in the case group and give a placebo to 10 patients in the control group containing lactose. To determine the onset and severity of oral mucositis, patients underwent examinations every other day.[32]

Fenugreek seeds contain high concentrations of saponins and flavonoids, which are known to reduce blood lipid levels and improve insulin sensitivity. With the main goal of evaluating the decrease in ovarian volume and a decrease in the number of ovarian cysts, Dr. Amrita Sarkari Jaipuriar, MS, and Garg Hospital, Goalghar, conducted a clinical trial to examine the effectiveness of fenugreek seeds extract in patients with polycystic ovary syndrome.[33]

Clinical trials were conducted by Philip Diaz of Ohio State University to determine whether green tea (rich in flavonoids), may reduce the chance of developing certain cancers. The primary and secondary objective of this clinical trial is to determine the free radical scavenging and measuring NF-kappaB-inducing kinase by giving 4 cups of green tea for 6 weeks to patients.[34]

Brigham and Manson, and Women's Hospital, conducted clinical trials by giving 2 cocoa extract capsules (containing 500 mg of flavanols, 80 mg of epicatechin and 50 mg of theobromine) as a dietary supplement to evaluate whether cocoa extract decreases the risk of cardiovascular diseases and cancer by reviewing the various reports like pathology, surgical, operative and diagnostic review of both inpatients and outpatients.[35] The results of the above-mentioned clinical trials are summarized in Table II, in that some of them not disclosed their results of clinical trials.

TABLE II. Clinical trials data of flavonoids

Drugs/NCT No.	Target	Results
Isoquercetin/NCT02195232	Protein disulfide isomerase (PDI)	D-dimer plasma concentration (decrease, median value,–21.9 %, $p = 0.0002$). ↑ No venous thromboembolism events. Protein disulfide isomerase (PDI) inhibitory activity (37 % at 500 mg and 73.3 % at 1000 mg). ↓ Platelet-dependent thrombin generation (median value, –31.1 % at 500 mg and –57.2 % at 1000 mg). ↓Circulation of soluble platelet selectin at 1000 mg.

TABLE II. Continued

Drugs/NCT No.	Target	Results
Purple grape juice and apple juice/NCT01043939	Endothelial function and biomarkers of vascular and systemic oxidative stress (oxidized low-density lipoprotein, myeloperoxidase, high sensitivity C-reactive protein)	Enhances the antioxidant activity. Reduces the oxidation of low-density lipoprotein. Improves vasodilation.
Quercetin and genistein/NCT01538316	Prostate-specific antigen (PSA)	No results
Quercetin tablets/NCT01732393	Chemotherapy induced oral mucositis	No results
Furocyst (fenugreek seed extract)/NCT02789488	Reduction in ovary volume	No results
Green tea/NCT01162642	Scavenging of free radicals and NF-kappaB-inducing kinase	No results
Cocoa extract/NCT02422745	Cardiovascular events and invasive cancer	No results

4. FLAVONOID DERIVATIVES AS ANTICANCER MOIETY

Fikroh *et al.* synthesized the (2*E*)-3-(2-bromo-4,5-dimethoxyphenyl)-1-(2-methylphenyl)propanone by the Claisen–Schmidt condensation reaction of 2-bromo-4,5-dimethoxybenzaldehyde and 2-hydroxy-acetophenone with a good yield of 78 %. The chalcone derivative **1a** (Fig. 2) showed moderated action on breast cancer cell lines (MCF-7) at IC_{50} of 42.19 μg/ml.[36]

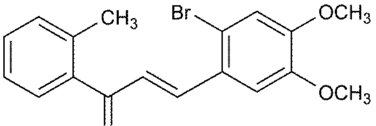

1a

Fig. 2. (2*E*)-3-(2-Bromo-4,5-dimethoxyphenyl)-1-(2-methylphenyl)propanone.

Ngameni *et al.* synthesized the novel series of *O*-substituted chalcone moieties containing various groups like allyl-, propargyl- or prenyl- substituent at different positions on both rings by the Claisen–Schmidt condensation of *O*-allyl, and *O*-propargyl vanillin and substituted aromatic ketones. Compound **2a** showed antitumor action against HCT116 p53 colon adenocarcinoma cells, **2b** against CCRF-CEM cells and MDA-MB-231-BCRP breast adenocarcinoma cells and **2c** against HCT116 p53 cells and HCT116 p53 human colon lung cancer cells (Fig. 3). All these compounds showed activity at IC_{50} values below 1 μM.[37]

Pangal *et al.* synthesized the chromen-2-one compounds by grinding of coumarin, trifluoro-substituted anilines and potassium carbonate under solvent-

-free conditions. Compounds **3a** and **c** showed good anticancer activity against HeLa cell lines at ≤10 μg/ml. Components **3a** and **b** (Fig. 4) showed moderate anticancer activity at a lower concentration against HeLa and MCF-7 cell lines.[38]

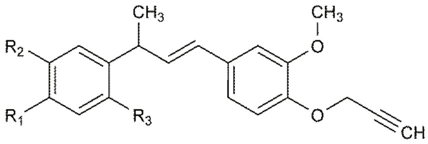

2a= R^1:OCH_3, R^2:OCH_3, R^3:H
2b= R^1:H, R^2:H, R^3:CH_3.

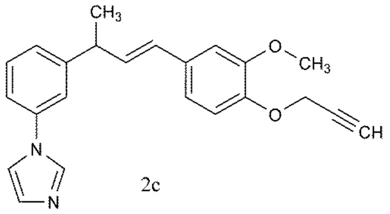

2c

Fig. 3. O-propargylchalcone derivatives (**2a** and **b**) and *O*-propargylated chalcone (**2c**).

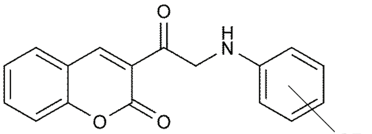

3a: 3-CF_3
3b: 3,5-CF_3
3c: 2-CF_3

Fig. 4. 3-(2-(Substituted-(trifluoromethyl) phenylamino)acetyl)-2*H*-chromen-2-one derivatives.

Mirzaei *et al.* synthesized the hybrids of quinoline and chalcones as tubulin inhibitors. Compound **4a** (Fig. 5) showed good antiproliferative activity at LD_{50} of 22.4 μM against four human cancer cell lines like A2780 (human ovarian cancer cell lines), A2780/RCIS (cisplatin resistant human ovarian cancer cell lines), MCF-7 (human breast cancer cell lines) and MCF-7/MX (mitoxantrone resistant human breast cancer cell lines) and normal Huvec cancer cell lines by causing cell cycle arrest at the G2/M phase.[39]

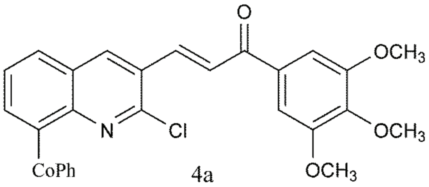

4a

Fig. 5. Benzoyl-2-chloroquinolin-3-yl (*E*)-3--(1,3,4,5-trimethoxyphenyl) propanone.

Wang *et al.* synthesized the chromone-2-aminothiazole scaffolds as novel CK2 inhibitors. Compound **5a** (Fig. 6) showed better activity against CK2 cells at IC_{50} value of 0.08 μM and exhibited more potent anticancer activity against HL-60 tumor cells at IC_{50} value of 0.25 μM by inhibiting the downstream of casein kinase II, including *α*-catenin/Akt pathway and PARP/survivin pathway.[40]

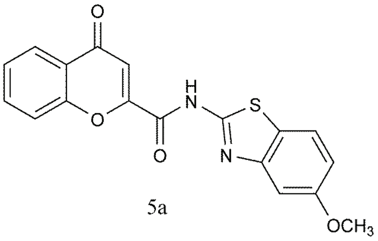

5a

Fig. 6. *N*-(5-methoxy-1,3-benzothiazol-2-yl)-4-oxo--4*H*-1-benzopyran-2-carboxamide.

Mayer *et al.* reported the synthesis of novel 7-aminochrysin derivatives by alkylated with *N*-phenylchloroacetamides at the 7th position. Compound **6a** (Fig. 7) exhibited anticancer activity against MCF7 (GI_{50} = 30nM) cell line of breast cancer and on the HCT-15 cell line of colon cancer cell line (GI_{50} = 60nM) at a nanomolar concentration.[41]

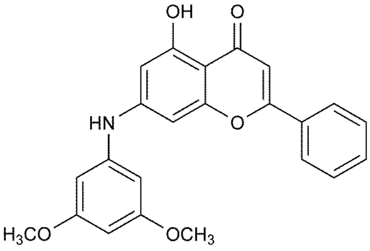

6a

Fig. 7. 7-(3,5-Dimethoxyanilino)-5-hydroxy-2-phenyl-4*H*-1-benzopyranone.

Parvinder Kaur *et al.* synthesized a new series of cinnamic acid derivatives by reacting 2-chloro-*N*-hydroxy acetamide and cinnamic acid amide. Compound **7a** (Fig. 8) showed potent activity against lung cancer cell lines (A-549) at an IC_{50} value of 10.36 μM among all synthesized derivatives.[42]

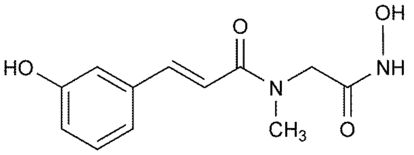

7a

Fig. 8. (2*E*)-*N*-Methyl-*N*-((hydroxycarbamoyl)-methyl)-3-(3-hydroxyphenyl)prop-2-enamide.

Rahimzadeh *et al.* synthesized the novel imidazole-chalcone moieties as inhibitors of tubulin polymerization and as an anticancer agent. In that series of derivatives, compound **8a** (Fig. 9) showed a better cytotoxicity effect against adenocarcinoma human alveolar basal epithelial cells (A549), human breast cancer cells (MCF-7), mitoxantrone resistant human breast cancer cells (MCF-7/MX) and human hepatocellular carcinoma cells (HEPG2) at IC_{50} value ranging from 7.05 to 63.43 μM.[43]

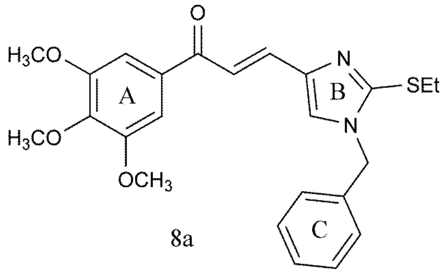

Fig. 9. (*E*)-3-(1-Benzyl-2-(ethylthio)-1*H*-imidazol-4-yl)-1-(3,4,5-trimethoxyphenyl)propenone.

Sarkate *et al.* reported the one pot synthesis of new series of flavonoid derivatives with different heterocyclic moieties. Compounds **9a** and **b** (Fig. 10) showed moderate anticancer activity by inhibiting the enzyme topoisomerase II with IC_{50} values of 10.28 and 12.38 µM against cancer cell lines.[44]

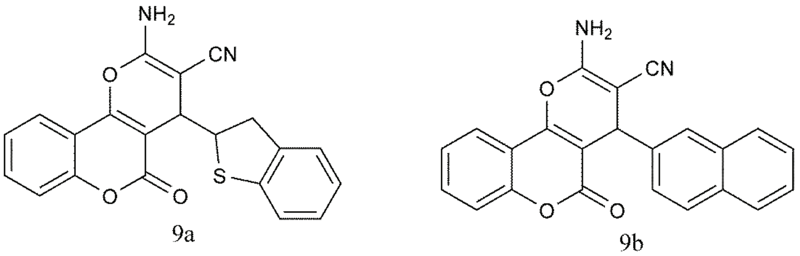

Fig. 10. Substituted 2-amino-4,5-dihydro-5-oxo-4-phenylpyrano[3,2-*c*]chromene-3-carbonitrile.

Yan *et al.* reported synthesizing new genistein and chrysin nitrogen mustard derivatives according to the principle of combination and hybridization. In this series, compound **10a** (Fig. 11) showed better cytotoxic activity against HeLa (IC_{50} = 1.43 µM), PC-3 (IC_{50} = 2.32µM), DU145 (IC_{50} = 2.91µM) and MCF-7 cancer cell lines (IC_{50} = 4.90µM), which were more than 4 times higher than melphalan.[45]

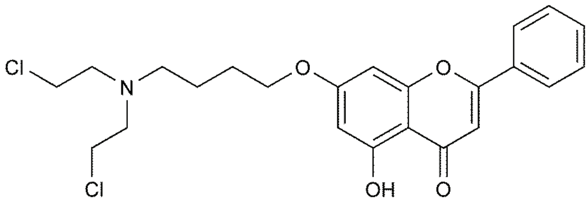

10a

Fig. 11. 7-[3-[Bis(2-chloroethyl)amino]propoxy]-5-hydroxy-2-phenyl-4*H*-chromenone.

Thorat *et al.* synthesized the *N*-benzyl derivatives of 6-aminofavone by using the multi-step synthetic procedure like methylation, Friedel–Craft acylation and in situ demethylation, Bekar–Venkataraman rearrangement and Buchwald coupling reaction; these reactions were employed in different steps for different starting materials as a potent novel anticancer moieties. In this series, compound **11a** (Fig. 12) showed high potent topoisomerase II enzyme inhibition activity at IC_{50} value of 12.10 μM.[46]

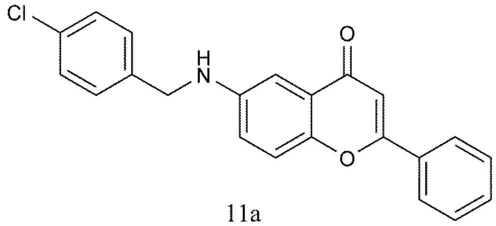

11a

Fig. 12. 6-{(4-Chlorophenyl)methyl]-amino}-2-phenyl-4*H*-1-benzopyranone.

Liu *et al.* designed and synthesized the novel 5,6,7-trimethoxy flavonoid salicylate moieties by combining 3 different moieties like trimethoxyphenyl, flavonoid and salicylic acid based on the principle of combination. In these derivatives, compound **12a** exhibits better anticancer activity against HGC-27 and MGC-803 cells with IC_{50} values of 10.20±6.90 μM and 17.20±3.04 μM, respectively.[47]

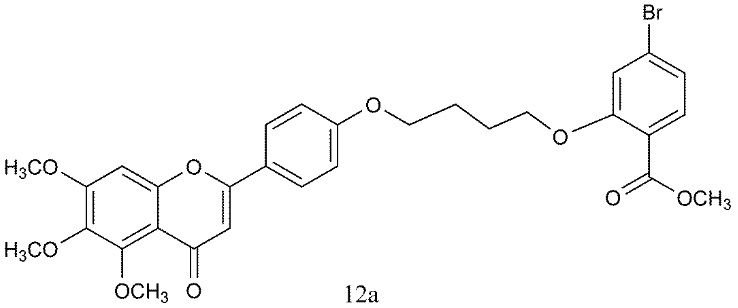

12a

Fig. 13. 5-Bromo-2-{3-[4-(5,6,7-trimethoxy-4-oxo-4*H*-chromen-2-yl)-phenoxy]-propoxy-benzoate of methyl acid.

Kozłowska *et al.* synthesized the novel derivatives of aminochalcones by using classical Claisen–Schmidt reaction of substituted aminoacetophenone with aromatic aldehydes. In this series of aminochalcones derivatives, compound **13a** (Fig 14) showed better anticancer activity against different human colon carcinoma cell lines at low IC_{50} values, *i.e.*, HT-29 (IC_{50} = 1.43μmL^{-1}), LS180 (IC_{50} = 2.06μmL^{-1}) LoVo (IC_{50} = 1.56μmL^{-1}), LoVo/DX (IC_{50} = 1.43μmL^{-1}), and COS7 (IC_{50} = 26.4μmL^{-1}).[48]

Assirey *et al.* synthesized the 4′,5,7-trihydroxy-flavanone through Knoevenagal condensation of an aldehyde, followed by an intramolecular Michael addition reaction. Compound **14a** (Fig. 15) exhibited potent anticancer activity against HCT-116, HepG-2, MCF-7 and A-549 tumor cell lines with IC_{50} values at 1.08, 2.42, 2.04 and 1.39 µg/mL, respectively.[49]

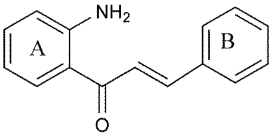

13a

Fig. 14. (2*E*)-1-(2-Aminophenyl)-3-phenylpropanone.

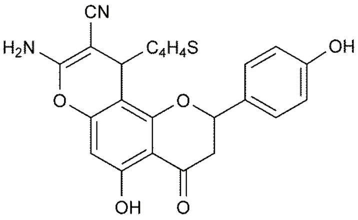

14a

Fig. 15. 8-Amino-10-(thiophene)-5-hydroxy-2-(4-hydroxy-phenyl)-4-oxo-3,4-dihydro-2*H*,10*H*-pyrano[2,3-*f*]chromene-9-carbonitrile.

Al-Oudat *et al.* designed and synthesized the derivatives of chrysin bearing the *N'*-alkylidene/arylideneacetohydrazide core by the reaction of hydrazide with different aldehydes. Compound **15a** (Fig. 16) with 4-benzyloxy substituent showed good antitumor activity against MDA-MB-231 and MCF-7 cell lines with IC_{50} values of 3.3 and 4.2 µM, respectively.[50]

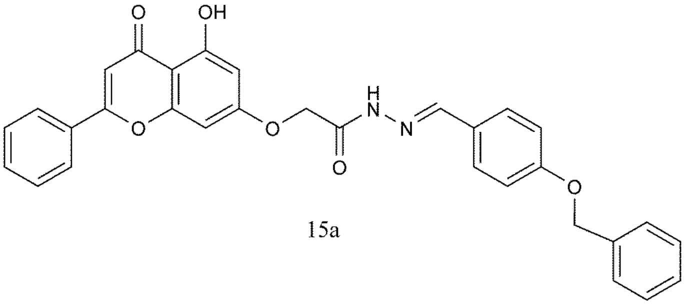

15a

Fig. 16. *N*-(4-(Benzyloxy)benzylidene)-2-((5-hydroxy-4-oxo-2-phenyl-4*H*-chromen-7-yl)-oxy)acetohydrazide.

Hou *et al.* designed and synthesized the novel derivatives of icaritin as inhibitors of putative DEPTOR by multi-step reaction. Compound **16a** (Fig. 17) exhibited a good antimultiple myeloma activity with an IC_{50} of 1.09 µM for human multiple myeloma cell lines (RPMI 8226) and induced RPMI 8226 apoptosis, and acts by blocking S phase of the cell cycle.[51]

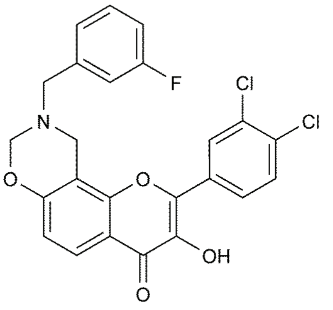

16a

Fig. 17. 2-(3,4-Dichlorophenyl)-9-(3-fluorobenzyl)-3--hydroxy-9,10-dihydro-4*H*,8*H*-chromeno[8,7-e]-[1,3]-oxazin-4-one.

Kumar *et al.* synthesized the chalcone derivatives incorporated benzothiazole-imidazopyridine by employing various reactions like the Suzuki-cross coupling reaction and Claisen–Schmidt condensation reaction. Compound **17a** (Fig. 18) showed potent cytotoxic activity against human prostate cancer cell line (PC3), human lung cancer cell line (A549), human breast cancer cell line (MCF--7) and human prostate cancer cell line (DU-145) at IC_{50} values of 0.03, 0.01, 0.12 and 0.17 μM, respectively.[52]

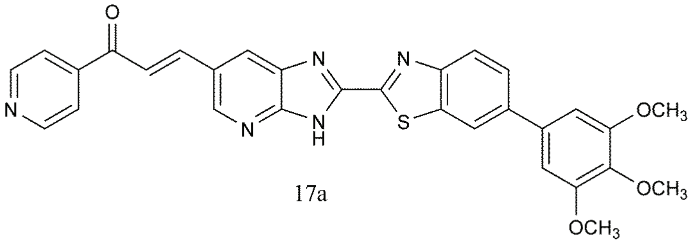

17a

Fig. 18. 3-(2-(6-(3,4,5-Trimethoxyphenyl)benzo[*d*]thiazol-2-yl)-3*H*-imidazo[4,5-*b*]pyridin-6--yl)-1-(pyridin-4-yl)propanone.

Silva *et al.* designed and synthesized the acetylated derivative of quercetin by acetylation of quercetin with acetic anhydride in the presence of pyridine. Compound **18a** (Fig. 19) exhibited a better cytotoxicity activity against hepatocellular cells (HepG2) and promyelocytic leukemia (HL-60) cell lines with IC_{50} values of 53.9 and 33.6 μM, respectively.[53]

Zhong *et al.* synthesized the novel hesperetin derivatives by the electrophilic substitution reaction in methanol at 40 °C at the C-6 position. Compound **19a** (Fig. 20) showed better antiproliferative effect on Breast cancer cell lines (MCF--7), human liver cancer cell lines (HepG2) and cervical carcinoma cell lines (HeLa) at IC_{50} value of 5.3, 8.8, and 8.6 μM, respectively.[54]

Insuasty *et al.* synthesized a novel symmetrical and unsymmetrical quinoline-based bis-chalcone series by Claisen–Schmidt condensation reaction. Among the synthesized derivatives, compound **20a** (Fig. 21) showed potent anticancer action against the different carcinoma cell lines like HCT-116 and HT29 with a GI_{50} value ranging from 0.16–5.45 μM.[55]

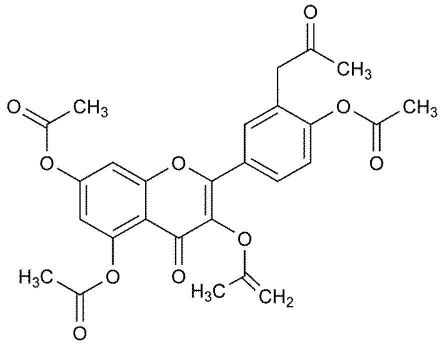

18a

Fig. 19. Quercetin pentaacetate.

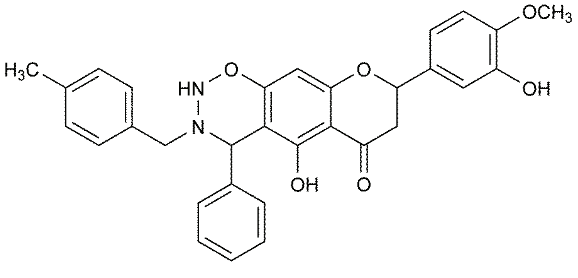

19a

Fig. 20. Hesperetin derivative.

Lu *et al.* prepared a novel amino chalcone derivatives as antiproliferative agents. Among the synthesized compounds, compound *21a* (Fig. 22) showed potent anticancer activity against MCF-7, HCT-116 and MGC-803 tumor cell lines with IC_{50} values of 2.54, 1.83 and 1.52 μM, respectively.[56]

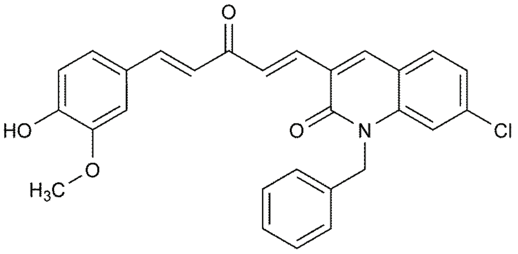

20a

Fig. 21. Benzyl-7-chloro-3-((1*E*,4*E*)-5--(4-hydroxy-3-methoxyphenyl)-3-oxopenta-1,4-dien-1-yl)quinolin-2(1*H*)-one.

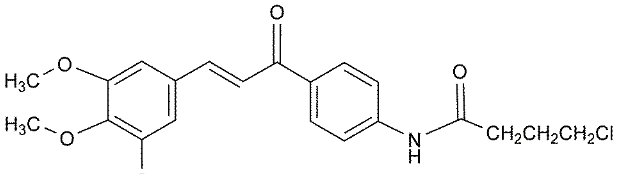

Fig. 22. 4-Chloro-*N*-(4-(3-oxo-3,4,5-trimethoxyphenyl)propenyl)phenyl butanamide.

5. CONCLUSION

World Health Organization (WHO) expressed worry about the rising cancer incidence and it has been expected to continue with the number of new cancer cases. Anticancer drugs cause numerous side effects and it also affects various healthy organs and tissues. Flavonoids are secondary metabolites that are unique lead compounds for drug design and development of potent anticancer drugs, particularly in chemotherapy. We have summarized the results of clinical trials of flavonoids and highlighted the synthesized flavonoid derivatives which showed better cytotoxic activity at lower concentrations against various cancer cells, for it could help the researchers to develop flavonoid derivatives as anticancer drugs by carrying out further clinical studies. Further, need to understand key enzymes related to neoplastic cells and metastasis in-vitro and in-vivo process also helps in providing novel potent flavonoid derivatives for fighting cancer.

ИЗВОД

ДЕРИВАТИ ФЛАВОНОИДА КАО АНТИКАНЦЕРСКЕ ГРУПА ЈЕДИЊЕЊА И ЊИХОВ ЕФЕКАТ НА ЋЕЛИЈСКЕ ЛИНИЈЕ КАНЦЕРА: АЖУРИРАНИ ПРЕГЛЕД

CHANDRAMOULI MANOJMOULI, THOPPALADA YUNUS PASHA, KOPPURAVURI NAGAPRASHANT,
BEEVINAHALLI RAMESH, NOOR UL EAIN и KARDIGERE NAGARAJU PURUSHOTHAM

Department of Pharmaceutical Chemistry, Sri Adichunchanagiri College of Pharmacy, Adichunchanagiri University, B. G. Nagara, Karnataka, India

Данас се канцер сматра примарним узроком преране смрти у индустријализованим земљама. Хемотерапије лековима су скупе и изазивају вишеструке споредне ефекте. Природни производи су детаљно испитивани због њиховог великог потенцијала као антиканцерских агенаса због њихове хемијске разноликости. Између многих природних метаболита, флавоноиди су секундарни метаболити широко распрострањени у природи, који имају значајна анти-канцерска својства, мало штетних ефеката, и показују синергистички користан утицај. Велики број истраживачких група марљиво истражује хемијска и биолошка својства нових деривата флавоноида због потреба за овим једињењима. У овом прегледу, сумирали смо резултате клиничких испитивања различитих флавоноида, синтетисаних различитим поступцима, њихов ефекат на различите ћелијске линије канцера и нове резултате активности флавоноида, према ћелијама канцера. Нова изучавања су неопходна за даљи развој нових деривата флавоноида као антиканцерских лекова.

(Примљено 22. децембра 2022, ревидирано 8. Фебруара, прихваћено 15. јула 2023)

REFERENCES

1. Y. Ouyang, J. Li, X. Chen, X. Fu, S. Sun, Q. Wu, *Biomolecules* **11** (2021) 894 (http://dx.doi.org/10.3390/biom11060894)
2. S. S. Qi, J. H. Sun, H. H. Yu, S. Q. Yu, *Drug Deliv* **24** (2017) 1909–1926 (http://dx.doi.org/10.1080/10717544.2017.1410256)
3. M. Lorscheider, A. Gaudin, J. Nakhle, K. L. Veiman, J. Richard, C. Chassaing, *Ther Deliv* **12** (2021) 55–76 (http://dx.doi.org/10.4155/tde-2020-0079)
4. S. Hussain, A. Singh, S. U. Nazir, S. Tulsyan, A. Khan, R. Kumar, N. Bashir, P. Tanwar, R. Mehrotra, *J Cell Biochem* **120** (2019) 14213–14225 (http://dx.doi.org/10.1002/jcb.28782)
5. Z. Zhang, J. Shi, E. C. Nice, C. Huang, Z. Shi, *Antioxidants* **10** (2021) 1138 (http://dx.doi.org/10.3390/antiox10071138)
6. A. N. Panche, A. D. Diwan, S. R. Chandra, *J Nutr Sci* **5** (2016) e47 (http://dx.doi.org/10.1017/jns.2016.41)
7. S. Kumar, A. K. Pandey, *The Scientific World Journal* **2013** (2013) 1–16 (http://dx.doi.org/10.1155/2013/162750)
8. Z. F. Fan, S. T. Ho, R. Wen, Y. Fu, L. Zhang, J. Wang, C. Hu, P. C. Shaw, Y. Liu, M. S. Cheng, *Molecules* **24** (2019) (http://dx.doi.org/10.3390/molecules24173180)
9. R. K. Singla, A. K. Dubey, A. Garg, R. K. Sharma, M. Fiorino, S. M. Ameen, M. A. Haddad, M. Al-Hiary, *JAOAC Int.* **102** (2019) 1397–1400 (http://dx.doi.org/10.5740/jaoacint.19-0133)
10. D. Veeramuthu, W. R. T. Raja, N. A. Al-Dhabi, I. Savarimuthu, *Flavonoids: Anticancer Properties*, in *Flavonoids - From Biosynthesis to Human Health*, InTech, 2017 (http://dx.doi.org/10.5772/68095)
11. A. Rauf, M. Imran, I. A. Khan, M. ur-Rehman, S. A. Gilani, Z. Mehmood, M. S. Mubarak, *Phytotherapy Research* **32** (2018) 2109–2130 (http://dx.doi.org/10.1002/ptr.6155)
12. A. U. Khan, H. S. Dagur, M. Khan, N. Malik, M. Alam, M. Mushtaque, *European Journal of Medicinal Chemistry Reports* **3** (2021) 100010 (http://dx.doi.org/10.1016/j.ejmcr.2021.100010)
13. D. M. Kopustinskiene, V. Jakstas, A. Savickas, J. Bernatoniene, *Nutrients* **12** (2020) 457 (http://dx.doi.org/10.3390/nu12020457)
14. A. Liskova, M. Samec, L. Koklesova, A. Brockmueller, K. Zhai, B. Abdellatif, M. Siddiqui, K. Biringer, E. Kudela, M. Pec, L. K. Gadanec, M. Šudomová, S. T. S. Hassan, A. Zulli, M. Shakibaei, F. A. Giordano, D. Büsselberg, O. Golubnitschaja & P. Kubatka, *EPMA Journal* **12** (2021) 155–176 (http://dx.doi.org/10.1007/s13167-021-00242-5)
15. M. K. Chahar, N. Sharma, M. P. Dobhal, Y. C. Joshi, *Pharmacog. Rev.* **5** (2011) 1–12 (http://dx.doi.org/10.4103/0973-7847.79093)
16. D. Kashyap, S. Mittal, K. Sak, P. Singhal, H. S. Tuli, *Tumor Biology* **37** (2016) 12927–12939 (http://dx.doi.org/10.1007/s13277-016-5184-x)
17. F. Wang, L. Wang, C. Qu, L. Chen, Y. Geng, C. Cheng, S. Yu, D. Wang, L. Yang, Z. Meng, Z. Chen, *BMC Cancer* **21** (2021) 396 (http://dx.doi.org/10.1186/s12885-021-08158-z)
18. Z. Javed, K. Khan, J. Herrera-Bravo, S. Naeem, M. J. Iqbal, Q. Raza, H. Sadia, S. Raza, M. Bhinder, D. Calina, J. Sharifi-Rad, W. C. Cho, *Cancer Cell Int.* **22** (2022) 239 (http://dx.doi.org/10.1186/s12935-022-02663-2)

19. Z. Nouri, S. Fakhri, K. Nouri, C. E. Wallace, M. H. Farzaei, A. Bishayee, *Cancers (Basel)* **12** (2020) 2276 (http://dx.doi.org/10.3390/cancers12082276)
20. P. Pandey, F. Khan, H. A. Qari, M. Oves, *Pharmaceuticals* **14** (2021) 1069(http://dx.doi.org/10.3390/ph14111069)
21. M. J. Tuorkey, *European Journal of Cancer Prevention* **25** (2016) 65–76 (http://dx.doi.org/10.1097/CEJ.0000000000000128)
22. S. Hu, L. Huang, L. Meng, H. Sun, W. Zhang, Y. Xu, *Mol. Med. Rep.* **12** (2015) 6745–6751 (http://dx.doi.org/10.3892/mmr.2015.4269)
23. J. L. Wang, Q. Quan, R. Ji, X. Y. Guo, J. M. Zhang, X. Li, Y. G. Liu, *Biomedicine and Pharmacotherapy* **108** (2018) 925–933 (http://dx.doi.org/10.1016/j.biopha.2018.09.105)
24. H. W. Zhang, J. J. Hu, R. Q. Fu, X. Liu, Y. H. Zhang, J. Li, L. Liu, Y. N. Li, Q. Deng, Q. S. Luo, Q. Ouyang, N. Gao, *Sci. Rep.* **8** (2018) 11255 (http://dx.doi.org/10.1038/s41598-018-29308-7)
25. S. Rampogu, R. G. Gajula, K. W. Lee, *Biomedicine and Pharmacotherapy* **141** (2021) 111808 (http://dx.doi.org/10.1016/j.biopha.2021.111808)
26. J. Sharifi-Rad, J. Herrera-Bravo, L. A. Salazar, S. Shaheen, S. Abdulmajid Ayatollahi, F. Kobarfard, M. Imran, A. Imran, L. Custódio, M. Dolores López, M. Schoebitz, M. Martorell, M. Kumar, H. Ansar Rasul Suleria, W. C. Cho, *Evidence-Based Complementary and Alternative Medicine* **2021** (2021) 9935451 (http://dx.doi.org/10.1155/2021/9935451)
27. X. Hou, H. Du, X. Quan, L. Shi, Q. Zhang, Y. Wu, Y. Liu, J. Xiao, Y. Li, L. Lu, X. Ai, M. Zhan, S. Yuan, L. Sun, *Front. Pharmacol.* **9** (2018) (http://dx.doi.org/10.3389/fphar.2018.00021)
28. X. Yan, M. Qi, P. Li, Y. Zhan, H. Shao, *Cell. Biosci.* **7** (2017) 50 (http://dx.doi.org/10.1186/s13578-017-0179-x)
29. R. A. Fikroh, S. Matsjeh, C. Anwar, *Molekul* **15** (2020) 34–39 (http://dx.doi.org/10.20884/1.jm.2020.15.1.558)
30. J. I. Zwicker, B. L. Schlechter, J. D. Stopa, H. A. Liebman, A. Aggarwal, M. Puligandla, T. Caughey, K. A. Bauer, N. Kuemmerle, E. Wong, T. Wun, M. McLaughlin, M. Hidalgo, D. Neuberg, B. Furie, R. Flaumenhaft, *JCI Insight* **4** (2019) (http://dx.doi.org/10.1172/jci.insight.125851)
31. US National Library of Medicine, ClinicalTrials.gov, *Purple Grape Juice in Improving Vascular Health in Childhood Cancer Survivors* (https://clinicaltrials.gov/study/NCT01043939) Accessed October 27, 2022. https://clinicaltrials.gov/ct2/show/NCT01043939
32. US National Library of Medicine, ClinicalTrials.gov, *Prostate Cancer Prevention Trial With Quercetin and Genistein (QUERGEN)* (https://clinicaltrials.gov/study/NCT01538316) Accessed October 27, 2022.
33. US National Library of Medicine, ClinicalTrials.gov, *Effect of Quercetin in Prevention and Treatment of Oral Mucositis* (https://clinicaltrials.gov/study/NCT01732393) Accessed October 27, 2022.
34. US National Library of Medicine, ClinicalTrials.gov, *Clinical Evaluation of Furocyst in Patients With Poly Cystic Ovary Syndrome* (https://clinicaltrials.gov/study/NCT02789488) Accessed October 27, 2022.
35. US National Library of Medicine, ClinicalTrials.gov, *Green Tea Anticancer Mechanisms in Smokers* (https://clinicaltrials.gov/study//NCT01162642) Accessed October 27, 2022.

36. H. D. Sesso, J. E. Manson, A. K. Aragaki, P. M. Rist, L. G. Johnson, G. Friedenberg, T. Copeland, A. Clar, S. Mora, M. V. Moorthy, A. Sarkissian, W. R. Carrick, G. L. Anderson, J. E. Manson, *et al.*, *American Journal of Clinical Nutrition* **115** (2022) 1490–1500 (http://dx.doi.org/10.1093/AJCN/NQAC055)
37. B. Ngameni, K. Cedric, A. T. Mbaveng, M. Erdoğan, I. Simo, V. Kuete, A. Daştan, *Bioorg. Med. Chem. Lett.* **35** (2021) 127827 (http://dx.doi.org/10.1016/j.bmcl.2021.127827)
38. A. Pangal, Y. Mujahid, B. Desai, J. A. Shaikh, K. Ahmed, *Current Chemistry Letters* **11** (2022) 105–112 (http://dx.doi.org/10.5267/j.ccl.2021.8.004)
39. S. Mirzaei, F. Hadizadeh, F. Eisvand, F. Mosaffa, R. Ghodsi, *J. Mol. Struct.* **1202** (2020) 127310 (http://dx.doi.org/10.1016/j.molstruc.2019.127310)
40. Q. Wang, X. Hu, W. Shi, H. Long, H. Wang, *Bioorg. Med. Chem. Lett.* **69** (2022) 128799 (http://dx.doi.org/10.1016/j.bmcl.2022.128799)
41. S. Mayer, P. Keglevich, P. Ábrányi-Balogh, Á. Szigetvári, M. Dékány, C. Szántay, L. Hazai, *Molecules* **25** (2020) 888 (http://dx.doi.org/10.3390/molecules25040888)
42. Parvinder Kaur, Ajmer Singh Grewal, Deepti Pandita, Deepti Pandita, *Biointerface Res. Appl. Chem.* **13** (2022) 150 (http://dx.doi.org/10.33263/BRIAC132.150)
43. S. Rahimzadeh Oskuei, S. Mirzaei, M. Reza Jafari-Nik, F. Hadizadeh, F. Eisvand, F. Mosaffa, R. Ghodsi, *Bioorg. Chem.* **112** (2021) 104904 (http://dx.doi.org/10.1016/j.bioorg.2021.104904)
44. A. P. Sarkate, V. S. Dofe, S. v. Tiwari, D. K. Lokwani, K. S. Karnik, D. D. Kamble, M. H. S. H. Ansari, S. Dodamani, S. S. Jalalpure, J. N. Sangshetti, R. Azad, P. V. L. S. Burra, S. v. Bhandari, *Bioorg. Med. Chem. Lett.* **40** (2021) 127916 (http://dx.doi.org/10.1016/j.bmcl.2021.127916)
45. X. Yan, J. Song, M. Yu, H. L. Sun, H. Hao, *Bioorg. Chem.* **96** (2020) 103613(http://dx.doi.org/10.1016/j.bioorg.2020.103613)
46. N. M. Thorat, A. P. Sarkate, D. K. Lokwani, S. v. Tiwari, R. Azad, S. R. Thopate, *Mol. Divers.* **25** (2021) 937–948 (http://dx.doi.org/10.1007/s11030-020-10079-1)
47. R. Liu, X. Deng, Y. Peng, W. Feng, R. Xiong, Y. Zou, X. Lei, X. Zheng, Z. Xie, G. Tang, *Bioorg. Chem.* **96** (2020) 103652 (http://dx.doi.org/10.1016/j.bioorg.2020.103652)
48. J. Kozłowska, B. Potaniec, D. Baczyńska, B. Zarowska, M. Anioł, *Molecules* **24** (2019) 4129 (http://dx.doi.org/10.3390/molecules24224129)
49. E. Assirey, A. Alsaggaf, A. Naqvi, Z. Moussa, R. M. Okasha, T. H. Afifi, A. S. Abd-El-Aziz, *Molecules* **25** (2020) 544 (http://dx.doi.org/10.3390/molecules25030544)
50. B. A. Al-Oudat, M. A. Alqudah, S. A. Audat, Q. A. Al-Balas, T. El-Elimat, M. A. Hassan, I. N. Frhat, M. M. Azaizeh, *Drug Des. Devel. Ther.* **13** (2019) 423–433 (http://dx.doi.org/10.2147/DDDT.S189476)
51. Y. Hou, W. Kuang, W. Min, Z. Liu, F. Zhang, K. Yuan, X. Wang, C. Sun, H. Cheng, L. Wang, Y. Xiao, S. Pu, G. Z. Xin, P. Yang, *J. Med. Chem.* **64** (2021) 14942–14954 (http://dx.doi.org/10.1021/acs.jmedchem.1c00087)
52. V. K. Kumar, V. swamy Puli, K. R. S. Prasad, G. Sridhar, *Chemical Data Collections* **33** (2021) 100696 (http://dx.doi.org/10.1016/j.cdc.2021.100696)
53. S. V. S. da Silva, O. M. Barboza, J. T. Souza, É. N. Soares, C. C. dos Santos, L. V. Pacheco, I. P. Santos, T. B. D. S. Magalhães, M. B. P. Soares, E. T. Guimarães, C. S. Meira, S. L. Costa, V. D. A. da Silva, L. L. B. de Santana, A. de F. Santos Júnior, *Molecules* **26** (2021) 6923 (http://dx.doi.org/10.3390/molecules26226923)

54. G. Zhong, J. Shen, Z. Chen, Z. Lin, L. Long, J. Wu, C. Long, S. Huang, P. Lian, G. Luo, *Molecules* **27** (2022) 879 (http://dx.doi.org/10.3390/molecules27030879)
55. D. Insuasty, S. García, R. Abonia, B. Insuasty, J. Quiroga, M. Nogueras, J. Cobo, G. L. Borosky, K. K. Laali, *Arch. Pharm. (Weinheim)* **354** (2021) 2100094 (http://dx.doi.org/10.1002/ardp.202100094)
56. C. F. Lu, S. H. Wang, X. J. Pang, T. Zhu, H. L. Li, Q. R. Li, Q. Y. Li, Y. F. Gu, Z. Y. Mu, M. J. Jin, Y. R. Li, Y. Y. Hu, Y. B. Zhang, J. Song, S. Y. Zhang, *Molecules* **25** (2020) 5530 (http://dx.doi.org/10.3390/molecules25235530).

Journal of the Serbian Chemical Society
JSCS@tmf.bg.ac.rs • www.shd.org.rs/JSCS

J. Serb. Chem. Soc. 88 (10) 959–974 (2023)
JSCS–5673

Original scientific paper
Published 24 October 2023

DBUHI3 complex an efficient catalyst for the synthesis of 2-phenylbenzimidazole and benzothiazole derivatives

RAMESH GAWADE[1,2] and PRAMOD S. KULKARNI[1,3]*

[1]Department of Chemistry Baburaoji Gholap College, Sangvi, Pune 411027, India, [2]S. M. Joshi College Hadapsar, Tal-Haveli, Pune 411028, India and [3]Department of Chemistry and Post Graduate Center in Organic Chemistry, Hutatma Rajguru Mahavidyalaya, Rajgurunagar, Pune 410505, India

(Received 26 May, revised 30 December 2022, accepted 11 February 2023)

Abstract: Herein, we have reported the facile synthesis of various benzimidazole/benzothiazole by using DBU–iodine–iodide as a green and simple catalyst. The R3NHI3 complexes have been formed by reacting an aqueous mixture of ammonium iodide and molecular iodine with the aqueous solution of amine. The structure of R3NHI3 complexes has been confirmed by spectroscopic techniques. The prepared amine–iodine complexes were screened as a catalysts in the synthesis of benzimidazole/benzothiazoles. Among the screened catalysts DBUHI3 complex has been found as most efficient catalyst. The synthesis of benzimidazoles and benzothiazoles has been achieved with the reaction of *o*-phenylene diamine/*o*-aminothiophenol and various substituted aryl aldehyde using DBUHI3 as a catalyst. The present protocol has offered some advantages over other reported protocols such as the mild reaction condition, commercially available precursors, inexpensive catalyst, short reaction time, the broad scope of the substrate, high yield, simple isolation of the product and environmentally benign method.

Keywords: amine–iodine complexes; benzimidazole; benzothiazole; oxidative cyclization; organocatalysis.

INTRODUCTION

Benzimidazoles and benzothiazoles are valuable heterocyclic scaffolds due to their many applications in diverse fields such as agrochemicals, veterinary, and pharmaceuticals.[1–3] They are potent privileged bicyclic aromatic nuclei in organic and medicinal chemistry. They showed diverse biological activity.[4–7] Benzimidazole and benzothiazole are the core structural skeleton in a variety of drug molecules specifically pantoprazole, riluzole, clemizole, bendamustine, thiabendazole, telmisartan, benzitramide, omeprazole, Hoechst 33342, pimoben-

---

* Corresponding author. E-mail: pramodskulkarni3@gmail.com

https://doi.org/10.2298/JSC220526007G

dan, mibefradil, dovitinib EGFR-3, sulfathiazole, ritonavir, abafungin, tiazofurin and benazolin. This class of heterocyclic compounds display valuable properties like photochromic, biochemical luminescence, and solvatochromic properties.[8,9] These heterocyclic molecules have significant biological activity and great pharmaceutical potential to attract more attention from synthetic chemists (Fig. 1).

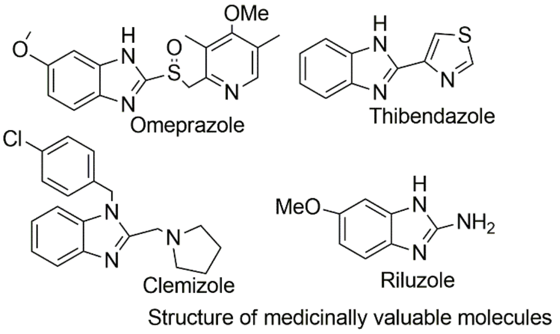

Fig. 1. Benzimidazoles ring containg drug molecules.

The robust method for synthesis of these molecules involves the treatment of *o*-phenylenediamine[10] and 2-aminothiophenol[11] with carbonyl compounds, such as aldehyde using Bronsted or Lewis acid catalyst[12] and carboxylic acids[13] or their derivative (nitrile, amide, ester, acid chloride)[14] at elevated temperature. Another approach involves metal-catalyzed direct alkylation of these molecules *via* C–H activation followed by carbon–carbon bond formation.[15] Synthesis of these molecules was achieved by microwave,[16] ultrasonic wave,[17] ionic liquid,[18] ionic liquid gel,[19] nanomaterial,[20] DMF[21] and under oxidative condition using various oxidative and catalytic reagents cited in the reference.[22,23] The certain green synthesis of benzimidazole was accomplished by homogeneous catalysis such as use of triflate erbium catalyst,[24] use of active deep eutectic solvent[25] and montmorillonite K 10 heterogenous green catalyst.[26] Generally, nearly all methods of benzimidazole synthesis have worked for benzothiazole.[27] The reported methods have limitations such as harsh reaction conditions, poor yield, high temperature, hazardous and carcinogenic solvent, expensive catalyst, side reaction, slow reaction rate, toxic reagents or tedious workup procedure and difficulty to isolate the product from the reaction mixture. Consequently, a search for better catalyst and environmentally benign methodology has continued for the economy and operational simplicity. Our catalytic procedure for amine–iodine complex is overcoming these problems.

Iodine catalysis has been known for more than 100 years. It has remarkably catalyzed various types of reactions.[28,29] The drawback of molecular iodine catalyzed synthesis of 2-substituted benzimidazole and benzothiazole is the sublimation of molecular iodine and moisture sensitivity, we have overcome these problems with amine-iodine-iodide complex organocatalyst.

We have synthesized the new R3NHI3 complexes using amine, ammonium iodide and molecular iodine.[30] The R3NHI3 complexes were characterized by spectroscopic technique and confirmed.[31] These catalysts were air-stable, and iodine never sublimates or deliquescent. Amine–iodine complex catalyzes the synthesis of 2-aryl benzimidazole and benzothiazole, also offers several adventages namely short reaction time, easy workup procedure and environmentally benign protocol. Amine–iodine complexes are organocatalysts that have an indispensable part in synthetic green chemistry because they are stable, less expensive, less toxic and easily applicable to a wide range of substrates. Herein, we have reported amine–iodine complexes catalyzed condensation and cyclization of a wide variety of aryl aldehyde with *o*-phenylenediamine and *o*-aminothiophenol, respectively. Moreover, we described the synthesis of new amine–iodine complexes (**1a**–**e**) and their synthetic application.

EXPERIMENTAL

The commercially available chemical reagents and solvents were used and their purity was ensured before use. Solvents that were entirely dry and free of impurities were used. Reaction of the progress was checked on Merck TLC silica gel 60 F254 plates using UV lamp (365 and 254 nm) and iodine chamber. The melting point was determined using open capillary method. The recorded melting points were uncorrected. PerkinElmer FTIR spectrometer was used to record IR spectra. Bruker Avance III HD NMR 500 MHz spectrometer was used to obtained ^{1}H-NMR and ^{13}C-NMR spectra in DMSO-d_6 and CDCl$_3$. HRMS analysis was obtained on a Bruker Impact II UHR-TOF mass spectrometer system.

Preparation of DBU–Iodine complexes

2.665 g of Ammonium iodide (18.352 mmol, 2.8 eq.) was added to 5.2 mL water (2 volumes) to get a clear solution in a 250 mL beaker, followed by the addition of 1.667 g of iodine (6.568 mmol, 1 eq). This solution was added dropwise to a stirred solution of 1 g DBU (6.568 mmol, 1 eq) in 8 mL water (8 volumes) in a 250 mL round bottom flask. The solid product has formed during addition, the mixture stirred for 15 min, and the solid product filtered off. The product has been washed with cold water and dried under a vacuum to provide the desired complexes. After drying the complex, the yield has been reported.

Typical process for the synthesis of benzimidazole/benzothiazole from o-*phenylenediamine/thiophenol and aldehyde*

A mixture of *o*-phenylenediamine/*o*-aminothiophenol (1 mmol) and aryl aldehydes (1 mmol) was dissolved in 2 mL ethanol in a 25 mL round bottom flask. The catalyst DBUH+I$_3$ complex **1a** (15 mol %) added to the reaction mixture, and the reaction mixture was stirred for 30 min. The progress of the reaction was monitored by (hexane:ethyl acetate) TLC. After completion of the reaction, the solvent evaporated under a vacuum. The crude reaction mixture was quenched with 20 % sodium thiosulfate solution. The product was isolated by extracting with ethyl acetate. The organic layer was dried over sodium sulfate and purified by column chromatography. The structure of the compound was confirmed by the spectroscopic techniques and matched with the reported.

RESULTS AND DISCUSSION

We have prepared a series of R3NHI3 complexes (**1a**–**e**), with minor modification in the reported procedure,[27,28] by replacing potassium iodide with ammonium iodide. This change has led to a drastic change in the structure and composition of catalysts. In the previous reported procedure by Livia *et al.*[72] a precipitate of the complex with composition $R_2NH:I_2:KI$ has formed. In the present work, we have got a composition as R3NHI3 (Scheme 1). Amine must contain two heteroatoms in the cyclic system for precipitation and stability of the complex. The amines like pyrrolidine, piperidine and amino acid proline did not form solid complexes by the same procedure as a result of a single nitrogen atom in the cyclic structure.

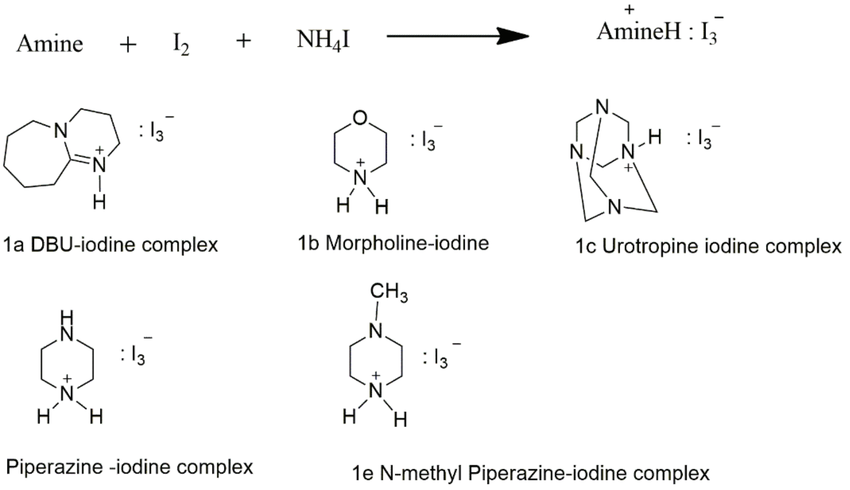

Scheme 1. Synthesis of amine-H–I_3 complex and structure of respective complex.

The various amine–iodine–iodide complexes have been prepared using easily available amine, ammonium iodide and molecular iodine. The molecular iodine was dissolved in the aqueous solution of ammonium iodide then added to an aqueous solution of amine dropwise, amine–iodine–iodide complex precipitated out and respective amine was obtained (Table I). The product was washed with excess water till filtrate was free from ammonia, confirmed by moist turmeric paper.

The structure of synthesized amine-iodine complexes (**1a-1e**) was confirmed by spectroscopic techniques such as UV, IR, HRMS, EDS, ^{1}H- and ^{13}C-NMR. These new homogenous catalysts were screened for the synthesis of 2-aryl benzimidazole. We have chosen ethanol as a solvent for screening catalytic activity of the amine-iodine complex catalyst because they are freely soluble in ethanol and partly soluble in various other organic solvents.

TABLE I. Synthesis of R3NHI3 complexes; amine (6.568, 1 eq.), iodine (6.568 mmol, 1 eq.) and ammonium iodide (18.352 mmol, 2.5 eq.) in 2 mL water

No.	Complex	Color	Yield[a], %
1	DBU-H+I$_3$ complex	Greenish yellow	92
2	Morpholine-H+I$_3$ complex	Orange yellow	62
3	Urotropine-H+I$_3$ complex	Brown yellow	58
4	Piperazine-H+I$_3$ complexes	Dark brown yellow	73
5	*N*-methyl piperazine-H+I$_3$ complexes	Pinkish yellow	66s

[a] Isolated yield after purification

Initially, our studies were with the screening of prepared amine iodine complexes (**1a**–**e**) for synthesis of benzimidazole *via* condensation and cyclization reaction of commercially available *o*-phenylenediamines with *p*-chorobenzaldehyde (Scheme 2). The DBUHI3 complex has given high yield of 2-(4-chlorophenyl)-*1H*-benzimidazole and the results are in Table II.

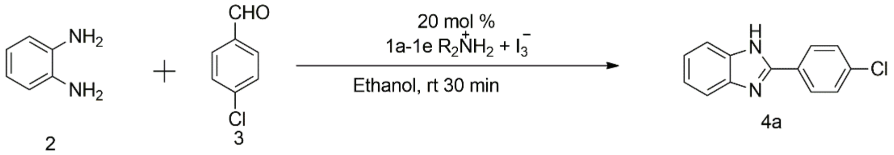

Scheme 2. Model reaction for screening of R$_2$NH$_2$+I$_3$ complex for synthesis of benzimidazole.

TABLE II. Screening of R3NHI3 complex catalyst in the synthesis of 2-(4-chlorophenyl)-1*H*--benzimidazole (**4a**); reaction conditions: *o*-phenylenediamine (1 mmol), *p*-chlorobenzaldehyde (1 mmol), R3NHI3 complexes **1a**–**e** (20 mol %) in ethanol (2 mL) at room temperature for 30 min

Sr. No.	Complex	Yield[a], %
1	DBUH+I$_3$ complex	91
2	Morpholine-H+I$_3$complex	74
3	Urotropine-H+I$_3$ complex	85
4	Piperazine-H+I$_3$ complexes	80
5	*N*-Methylpiperazine-H+I$_3$ complexes	78
6	Iodine	70
7	Without catalyst	Trace

[a] Isolated yield after purification

Next, we have decided to optimize the amount of DBUHI3 complex with the same reaction condition. The amount of DBUHI3 was optimized by increasing the amount from 5 to 20 mol % for 1 mmol scale reaction. When the reaction was performed in the absence of the catalyst, the product has formed in a trace amount (Table III, entry 1). The yield has increased with the mol % of amine––iodine complex (Table III, entries 2–5). Nevertheless, there was no increase in the yield when the amount of R3NHI3 catalyst loading has increased from 15 to

20 % mol. From Table III was observed that the 15 mol % of DBUHI3 complex was sufficient to achieve excellent yield.

TABLE III. Optimizing the amount of DBUH+I_3 complex in synthesis of 2-(4-chlorophenyl)--1*H*-benzimidazole (**4a**); reaction conditions: *o*-phenylenediamine (1 mmol), *p*-chlorobenzaldehyde (1 mmol), DBUHI3 complex **1a** in ethanol (2 mL) at room temperature for 30 min

Entry	Catalyst quantity, mol %	Yield[a], %
1	Without catalyst	Trace
2	5	65
3	10	80
4	15	91
5	20	91

[a] Isolated yield after purification

We have studied the effect of various solvents on product yield (Table IV, entries 1–9). Among the screened solvents ethanol, toluene, and chloroform have given excellent yield, and ethanol was found the best solvent for the reaction as a high amount of product was obtained. Second, fortunately the choice of ethanol also falls on the fact that it is less toxic and more eco-sustainable solvent than chloroform and toluene. Hence, we have selected the solvent for the synthesis of benzimidazole. The solvents DMF, DMSO and acetonitrile offered a moderate product yield.

TABLE IV. Effect of solvent in synthesis of 2-(4-chlorophenyl)-1*H*-benzimidazole (**4a**) using DBUH–I_3 complex catalyst; reaction conditions: *o*-phenylenediamine (1 mmol), *p*-chlorobenzaldehyde (1 mmol), DBUHI3 complex **1a** (15 mol %) in ethanol (2 mL) at room temperature for 30 min

Entry	Name of solvent	Yield[a], %
1	Ethanol	91
2	Toluene	86
3	Dimethyl formamide	58
4	Dimethyl sulphoxide	66
5	Chloroform	80
6	Acetic acid	50
7	Acetonitrile	61
8	Tetrahydrofuran	31
9	Water	25

[a] Isolated yield after purification

With the investigated optimum reaction condition, we have synthesized various substituted benzimidazole (Scheme 3). The 2-aryl substituted benzimidazole have been synthesized from *o*-phenylenediamine (1mmol) with several substituted aryl aldehyde (1 mmol) *via* condensation and cyclization reaction in the presence of DBUHI3 complex (15 mol %) at room temperature in ethanol (Table V). It was found that various substituted aryl aldehyde containing electron-donating groups (*p*-halogen and methoxy (Table V, entries 1, 4, 5 and 16) and electron-withdrawing group (nitro, Table V, entries 2, 6 and 14) were formed the product with good yield, under optimized condition. The heterocyclic aromatic aldehyde (Table V, entries 10a and 13a) gave a comparatively lower yield under the same condition. Hydroxy benzaldehyde (Table V, entries 11 and 12) has afforded an unexpectedly low yield, which may be due to solubility in water. The aryl aldehyde bearing electron-withdrawing at ortho/para nitro group (Table V, entries 13 and 15) has afforded product in poor yield. The *o*-substituted aryl aldehyde (Table V, entries 3, 12 and 15) has afforded a low yield due to steric hindrance in cyclization.

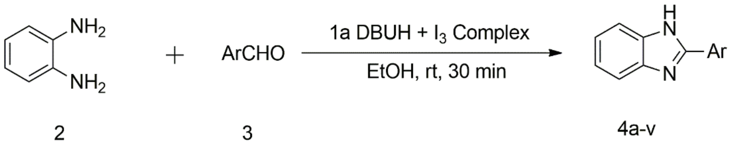

Scheme 3. DBU–iodine–iodide catalyzed synthesis of substituted benzimidazole.

TABLE V. Synthesis of 2-aryl substituted benzimidazole; reaction conditions: *o*-phenylenediamine (1 mmol), substituted arylaldehyde (1 mmol), DBUHI3 complex **1a** (15 mol %), EtOH 2 ml, 30 min at rt

Entry	Product (**4**)	Yield^{a}, %	M. P., °C	Literature M. P., °C
1	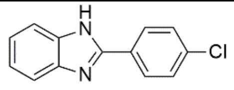 **4a**	91^{c}	290–293	290–292[29]
2	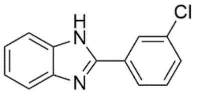 **4b**	86^{c}	228–230	227–229[20]
3	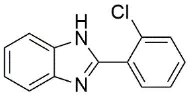 **4c**	73^{e}	232–234	231–233[29]
4	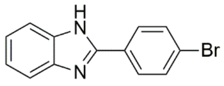 **4d**	78^{d}	286–290	292–293[29]
5	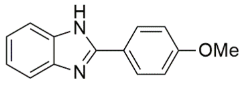 **4e**	76^{d}	223–225	222–223[30]

TABLE V. Continued

Entry	Product (**4**)	Yield[a], %	M. P., °C	Literature M. P., °C
6	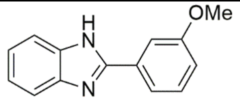 **4f**	81[c]	202–205	200–202[29]
7	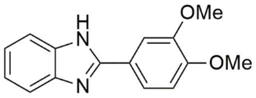 **4g**	64[d]	225–227	223–226[31]
8	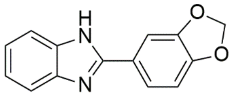 **4h**	72[d]	238–240	239–241[30]
9	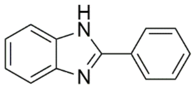 **4i**	80[c]	243–245	242–244[20]
10	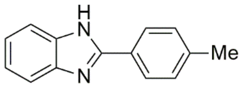 **4j**	65[d]	216–219	214–216[20]
11	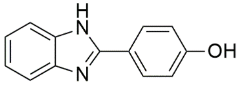 **4k**	80[c]	252–254	254–255[29]
12	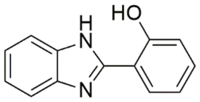 **4l**	44[c]	204–206	205–206[31]
13	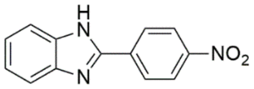 **4m**	41[d]	301–303	300[18]
14	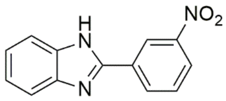 **4n**	72[c]	196–198	199[18]
15	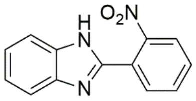 **4o**	38[c]	229–231	230[18]
16	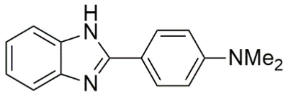 **4p**	72[d]	280–283	277–279[29]

TABLE V. Continued

Entry	Product (**4**)	Yield[a], %	M. P., °C	Literature M. P., °C
17	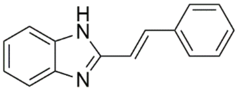 **4q**	51[f]	270–273	164–166[20]
18	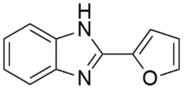 **4r**	68[d]	226–228	221–223[20]
19	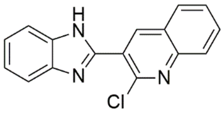 **4s**	63[d]	219–222	202[32]
20	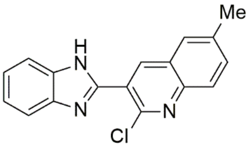 **4t**	73[d]	221–224	220[33]
21	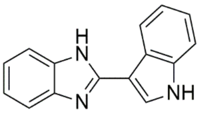 **4u**	72[f]	220–223	226–227[23]
22	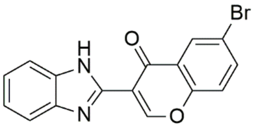 **4v**	76[e]	269–271	–

[a] Isolated yield after purification; [b] product was purified by recrystallization in ethanol; [c] product was purified by column chromatography mobile phase hexane: ethyl acetate; [d] product was purified by recrystallization in chloroform; [e] product was purified by column chromatography mobile phase chloroform

Thus, the R3NHI3 complex was catalyzing the synthesis of 2-aryl substituted benzimidazole using a diverse range of aryl aldehydes and *o*-phenylenediamine. All synthesized benzimidazole derivatives were characterized by ^{1}H-, ^{13}C-NMR and physical constants compared with standard data. The ^{1}H-NMR displays a characteristic nitrogen-bearing proton chemical shift δ value 12.5–13.5 ppm that reflected in each derivative, whereas the ^{13}C-NMR show a typical chemical shift δ value 150 ppm for carbon located between two nitrogens (Supplementary material to this paper).

The synthesis of 2-substituted aryl benzothiazole derivative (Scheme 4) was achieved from 2-aminothiophenol and diversity of aryl aldehydes in the presence of DBUHI3 complex **1a**. The aromatic aldehyde bearing electron-donating group (*p*-halogen, methoxy, hydroxyl, amino (Table VI, entries 1, 4, 5, 8, 11, 12, 13, and 17)) and electron-withdrawing group (*m*-halogen, methoxy, nitro group, Table VI, entries 2, 6 and 14–16) provided a good yield of the product under same optimized process. Also, this reaction works well with the heterocyclic aromatic aldehyde to form a product **7** in moderate yield (Table VI, entries 19––22). The *o*-substituted benzaldehyde has afforded a poor yield of the product because of a steric hindrance (Table VI, entry 3). The unexpectedly *o*-nitro benzaldehyde has afforded a product in the higher yield owing to the high polarity of aldehyde (Table VI, entry 16). Overall, the amine–iodine complex has remarkably catalyzed the synthesis of 2-substituted aryl benzothiazole derivatives. The structure of all synthesized compounds were confirmed by NMR spectroscopic data and physical constants compared with standard data. The ^{13}C NMR spectra of benzothiazole have shown a characteristic value of chemical shift *δ* 168 ppm for carbon between two heteroatoms sulfur and nitrogen (Supplementary material).

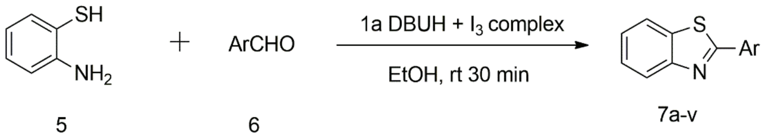

Scheme 4. DBUHI3 catalysed synthesis of benzothiazole derivatives.

TABLE VI. Synthesis of 2-aryl substituted benzothiazole; reaction conditions: *o*-aminothiophenol (1 mmol), substituted arylaldehyde (1 mmol), DBUHI3 complex **1a** (15 mol %), ethanol 2 mL, 30 min at rt

Entry	Product (**7**)	Yield[a], %	M. P., °C	Literature M. P., °C
1	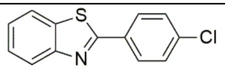 **7a**	84[d]	115–117	111–112[31]
2	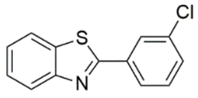 **7b**	72[c]	94–95	93–94[31]
3	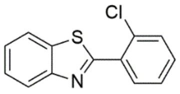 **7c**	58[d]	80–82	83–84[31]
4	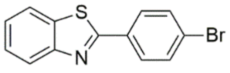 **7d**	80[c]	127–129	129–131[33]

TABLE VI. Continued

Entry	Product (**7**)	Yield[a], %	M. P., °C	Literature M. P., °C
5	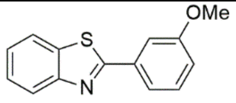 **7e**	74[c]	120–121	120–122[34]
6	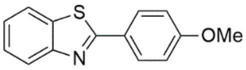 7f	64[d]	99–102	98–100[35]
7	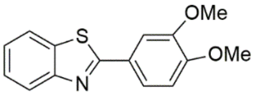 **7g**	61[f]	229–231	230–232[36]
8	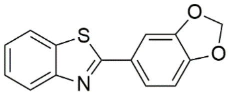 **7h**	83[d]	130–132	128–130[37]
9	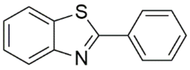 **7i**	91[d]	112–113	109–110[33]
10	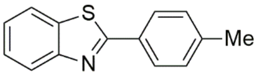 **7j**	62[e]	85–86	87–88[38]
11	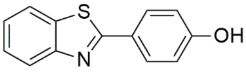 **7k**	79[c]	227–229	225–227[39]
12	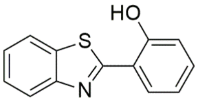 **7l**	86[c]	131–132	124–126[39]
13	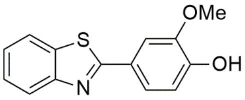 **7m**	83[c]	160–162	161–163[39]
14	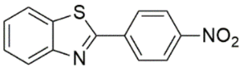 **7n**	82[e]	320–322	228–230[39]
15	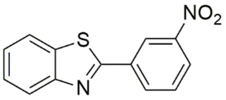 **7o**	78[e]	190–193	185–187[36]

TABLE VI. Continued

Entry	Product (**7**)	Yield[a], %	M. P., °C	Literature M. P., °C
16	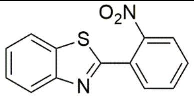 **7p**	80[e]	195–197	191–193[40]
17	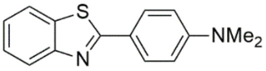 **7q**	92[c]	161–163	160–162[39]
18	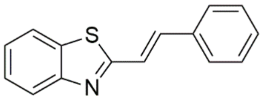 **7r**	65[d]	107–110	110–112[39]
19	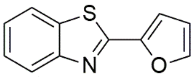 **7s**	67[d]	103–104	101–102[35]
20	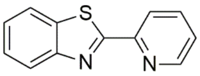 **7t**	73[c]	132–134	130–132[40]
21	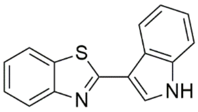 **7u**	72[e]	146–148	144–147[40]
22	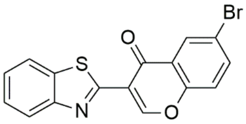 **7v**	78[c]	254–256	New compound

[a]Isolated yield after purification; [b]product was purified by recrystallization in ethanol; [c]product was purified by column chromatography mobile phase hexane: ethyl acetate; [d]product was purified by recrystallization in chloroform; [e]product was purified by column chromatography mobile phase chloroform

Further, the scope of the reaction has extended with the aliphatic aldehydes like crotonaldehyde, propionaldehyde, acetaldehyde and formaldehyde with *o*-phenylenediamine and *o*-aminothiophenol. The reaction has not proceeded with aliphatic aldehydes and has not afforded the desired product.

Although the exact mechanism is not clear, a proposed mechanism for the formation of benzimidazole and benzothiazole is shown in Scheme 5. In first step the aldehyde (**A**) oxygen was protonated by abstraction of proton from DBUHI3 complex to form compound (**C**) and liberate DBUI3 complex. Simultaneously liberated DBUI3 complex, I$^-$ abstract the hydrogen from amines (**B**) to form compound (**D**) and liberates DBUI2 complex. In next step, **C** and **D** reacted to form intermediate (**E**). The intermediate **E** on reaction DBUI2 complex, DBU abstract the proton of XH to form X^- and iodine coordinate with I_2 undergo cyclization to form intermediate **G** which undergo oxidative elimination to form C=N double bond to formed final product (**H**).

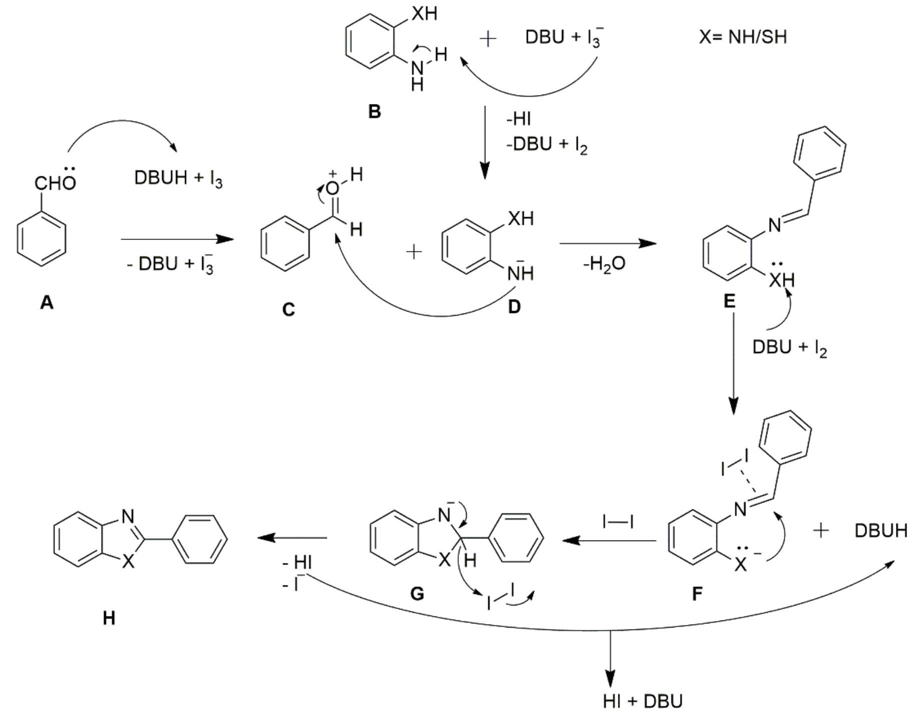

Scheme 5. Tentative mechanism of DBU-H–I_3 catalyzed synthesis of benzimidazole and benzothiazole.

CONCLUSION

In the present work, we have prepared the new R3NHI3 complexes and studied their catalytic activity in the preparation of 2-aryl substituted benzimidazole and benzothiazole derivatives. Among the screened amine–iodine catalysis, DBUHI3 was found an efficient catalyst for the preparation of 2-aryl substituted benzimidazole and benzothiazole. We believe that the present method is more convenient, efficient, greener, simpler and environmentally benign compared to most reported methods in the literature. The present method has not afforded the benzimidazole and benzothiazole derivatives with aliphatic aldehydes.

SUPPLEMENTARY MATERIAL

Additional data and information are available electronically at the pages of journal website: https://www.shd-pub.org.rs/index.php/JSCS/article/view/11893, or from the corresponding author on request.

Acknowledgements. The authors wish to sincerely thanks the central instrumentation facility of Savitribai Phule Pune University Pune and B. G. college Sangvi Pune for analytical support.

ИЗВОД

КОМПЛЕКС DBUHI3 КАО ЕФИКАСАН КАТАЛИЗАТОР ЗА СИНТЕЗУ ДЕРИВАТА 2-ФЕНИЛБЕНЗИМИДАЗОЛА И БЕНЗОТИАЗОЛА

RAMESH GAWADE[1,2] и PRAMOD S. KULKARNI[1,3]

[1]*Department of Chemistry Baburaoji Gholap College, Sangvi, Pune 411027, India* [2]*S. M. Joshi College Hadapsar, Tal- Haveli, Pune 411028, India и* [3]*Department of Chemistry and Post Graduate Center in Organic Chemistry, Hutatma Rajguru Mahavidyalaya, Rajgurunagar, Pune 410505, India*

У овом раду је описана једноставна синтеза различитих бензимидазола/бензотиазола, употребом DBU–јод–јодида као једноставног и еколошки прихватљивог катализатора. Настаје комплекс R3NHI3 у реакцији смеше амонијум-јодида, молекулског јода и амонијака у води. Структура комплекса R3NHI3 потврђена је спектроскопским техникама. Каталитичка својства добијеног амин–јодидног комплекса су испитане у реакцији синтезе бензимидазола/бензотиазола. Од испитаних катализатора DBUHI3 комплекс се показао као ефикасан. Синтеза бензимидазола и бензотиазола је постигнута у реакцијама *o*-фенилендиамина/*o*-аминотиофенола са различитим супституисаним арил-алдехидима користећи DBUHI3 комплекс као катализатор. У односу на друге, приказани протокол има неколико предности, као што су благи реакциони услови, комерцијално доступни прекурсори, катализатор који није скуп, кратко реакционо време, ширк опсег супстрата, висок принос, једноставан поступак изоловања производа, и поступак који није штетан за животну средину.

(Примљено 26. маја, ревидирано 30. децембра 2022, прихваћено 11. фебруара 2023)

REFERENCES

1. J. Velk, V. Baliharov, J. Fink-Gremmels, S. Bull, J. Lamka, L. Sklov, *Res. Vet. Sci.* **76** (2004) 95 (https://doi.org/10.1016/j.rvsc.2003.08.005)
2. C. D. Hadole, J. D. Rajput, R. S. Bendre, *Org. Chem. Curr. Res.* **7** (2018) 195 (https://doi.org/10.4172/2161-0401.1000195)
3. P. C. Sharmal, A. Sinhmar, A. Sharma, H. Rajak , D.P. Pathak, *J. Enzym. Inhib. Med. Chem.* **28** (2013) 240 (https://doi.org/10.3109/14756366.2012.720572)
4. V. S. Padalkar, B. N. Borse, V. D. Gupta, K. R. Phatangare, V. S. Patil, P. G. Umape, N. Sekar, *Arabian J. Chem.* **9** (2016) 1125 (https://doi.org/10.1016/j.arabjc.2011.12.006)
5. M. A. Abdelgawad, R. B. Bakr, H. A. Omar, *Bioorg. Chem.* **74** (2017) 82 (https://doi.org/10.1016/j.bioorg.2017.07.007)
6. I. Roberta, C. Antonio, M. Silvia, C. Paola, S. Gabriele, P. Sandra, S. Simona, L. Roberta, S. Giuseppina, *Viruses* **13** (2021) 58 (https://doi.org/10.3390/v13010058)
7. S. Noel, S. Cadet, E. Gras, C. Hureau, *Chem. Soc. Rev.* **42** (2013) 7747 (https://doi.org/10.1039/C3CS60086F)
8. Y. Gao, W. Xu, H. Ma, A. Obolda, W. Yan, S. Dong, M. Zhang, F. Li, *Chem. Mater.* **29** (2017) 6733 (https://doi.org/10.1021/acs.chemmater.7b01521)
9. G. Singh, H. K. Sahota, *Plant Physiol. Biochem.* **132** (2018) 166 (https://doi.org/10.1016/j.plaphy.2018.09.001)

10. M. Faheem, Anjali Rathaur, A. Pandey, V. K. Singh, A. K. Tiwari, *Chem. Select.* **5** (2020) 3981 (https://doi.org/10.1002/slct.201904832)
11. X. Gao, J. Liu, X. Zuo, X. Feng, Y. Gao, *Molecules* **25** (2020) 1675 (https://doi.org/10.3390/molecules25071675)
12. Zhan- Zhan-Hui Zhang, Liang Yin, Yong-Mei Wang, *Catal. Commun.* **8** (2007) 1126 (http://dx.doi.org/10.1016/j.catcom.2006.10.022)
13. Rui Wang, Xiao-xia Lu, Xiao-qi Yu, Lin Shi, Yong Sun, *J. Mol. Catal., A* **266** (2007) 198 (https://doi.org/10.1016/j.molcata.2006.04.071)
14. S. Rostamizadeh, M. Nojavan, F. Heshmatpoor, *Heterocycl. Commun*. **13** (2007) 305 (https://doi.org/10.1515/HC.2007.13.5.305)
15. F. Abdellaoui, C. Youssef, H. Ben Ammar, T. Roisnel, J. F. Soule, H. Doucet, *ACS Catal.* **6** (2016) 4248 (https://doi.org/10.1021/acscatal.6b00678)
16. P.R. Fernandes, P. Patil R. Shete, *J. Chem. Rev*. **4** (2022) 25 (https://dx.doi.org/10.22034/jcr.2022.316076.1132)
17. M. Bharathi, S. Indira, G. Vinoth, T. Mahalakshmi, E. Induja, K. Shamuga Bharathi, *J. Coord. Chem.* **73** (2020) 1 (http://dx.doi.org/10.1080/00958972.2020.1730335)
18. S. Majumdar, M. Chakraborty, N. Pramanikb, D. K. Maiti, *RSC Adv.* **5** (2015) 51012 (https://doi.org/10.1039/C5RA08183A)
19. T. T. Nguyen, X.-T. T. Nguyen, T.-L. H. Nguyen, P. H. Tran, *ACS Omega* **4** (2019) 368 (https://doi.org/10.1021/acsomega.8b02932)
20. M. A. Tzani, C. Gabriel, I. N. Lykakis, *Nanomaterials* **10** (2020) 2405 (https://doi.org/10.3390/nano10122405)
21. K. B. Rasal, Ganapati D. Yadav, *Catal. Today* (2017) 309 (http://dx.doi.org/10.1016/j.cattod.2017.10.014)
22. S. Singhal, P.j Khanna, S. S. Panda, and L. Khanna, *J. Heterocycl. Chem.* **56** (2016) 2702 (https://doi.org/10.1002/jhet.3649)
23. J. Kovvuri, B. Nagaraju, A. Kamal, A. K. Srivastava, *ACS Comb. Sci.* **18** (2016) 644 (https://doi.org/10.1021/acscombsci.6b00107)
24. N. H. Cano, J. G. Uranga, M. Nardi, A. Procopio, D. A. Wunderlin, and A. N. Santiago, *Beilstein J. Org. Chem*. **12** (2016) 2410 (https://doi.org/10.3762/bjoc.12.235)
25. S. Bonacci, G. Iriti, S. Mancuso, P. Novelli, R. Paonessa, S. Tallarico, and M. Nardi *Catalysts* **10** (2020) 845 (https://doi.org/10.3390/catal10080845)
26. M. L. Di Gioia, R. Cassano, P. Costanzo, N. H. Cano, L. Maiuolo, M. Nardi, F. P. Nicoletta, M. Oliverio, A. Procopio, *Molecules* **24** (2019) 2885 (https://doi.org/10.3390/molecules24162885)
27. N. P. Prajapati, R. H. Vekariya, M. A. Borad, H. D. Patel, *RSC Adv*. **4** (2014) 60176 (https://doi.org/10.1039/C4RA07437H)
28. J. J. Koenig, M. Breugst, in *Catalysis by Molecular Iodine*, H. Stefan, Ed., Wiley-VCH Publication, Weinheim, 2021, p. 233 (https://doi.org/10.1002/9783527825738.ch7)
29. S. Samanta, S. Mondal, *Asian J. Org. Chem.* **10** (2021) 2503 (https://doi.org/10.1002/ajoc.202100424)
30. L. C. R. M. da Frota, R. C. P. Canavez, S. L. da S. Gomes, P. R. R. Costa, A. J. M. da Silva, *J. Braz. Chem.* **20** (2009) 1916 (https://doi.org/10.1590/S0103-50532009001000021)
31. M. S. Refat, H. Al. Didamony, K. M. A. El-Nour, L. El-Zayat, *J. Saudi Chem. Soc.* **14** (2010) 323 (https://doi.org/10.1016/j.jscs.2010.04.004)

32. H. Naeimi, N. Alishahi, *Org. Chem. Int.* **2012** (2012) Article ID 498521 (https://doi.org/10.1155/2012/498521)
33. K. Gopalaiah, S. N. Chandrudu, *RSC Adv.* **5** (2015) 5015 (https://doi.org/10.1039/C4RA12490A)
34. S. V. Goswami, P. B. Thorat, V. N. Kadam, S. R. Bhusare, *J. Chem. Biol. Phys. Sci.* **1** (2011) 164 (https://www.researchgate.net/publication/269934184)
35. M. Malathi, P. S. Mohan, R. J. Butcher, C. K. Venil, *Can. J. Chem*. **87** (2009 1692 (https://doi.org/10.1139/V09-139)
36. C. Lia, H. Deng, T. Jin, Z. Liu, R. Jiang, C. Li, X. Jia, J. Li, *Synthesis* **49** (2017) 4350 (https://doi.org/10.1055/s-0036-1588487)
37. B. Maleki, H. Salehabadi, *Eur. J. Chem.* **1** (2010) 377 (https://doi.org/10.5155/eurjchem.1.4.377-380.165)
38. R. Bhata, S. Karhale, S. Ardeb, V. Helavia, *Iranian J. Catal.* **9** (2019) 173 (http://ijc.iaush.ac.ir/article_664816_76d3680235636f284a8f914d9421b93e.pdf)
39. M. Maphupha, W. P. Juma, C. B. de Koning, D. Brady, *RSC Adv.* **8** (2018) 39496 (https://doi.org/10.1039/C8RA07377E)
40. C. Praveen, A. Nandkumar, P. Dheenkuma, D. Muralidharan, P. T. Perumal, *J. Chem. Sci.* **124** (2012) 609 (https://doi.org/10.1007/s12039-012-0251-3)
41. Y. Han, X. Wang, X, Wang, L. Lv, G. Diao, Y. Yuan, *Synthesis* **44** (2012) 3027 (https://www.thieme-connect.com/products/ejournals/abstract/10.1055/s-0032-1317035)
42. S. Ray, P. Das, B. Banerjee, A. Bhaumik, C. Mukhopadhyay, *RSC Adv.* **5** (2015) 72745 (http://dx.doi.org/10.1039/c5ra14894d)
43. W. Senapak, R. Saeeng, J. Jaratjaroonphong, U. Sirion, *Mol. Catal.* **458** (2018) 97 (https://doi.org/10.1016/j.mcat.2018.06.017).

Journal of the Serbian Chemical Society
JSCS@tmf.bg.ac.rs • www.shd.org.rs/JSCS
J. Serb. Chem. Soc. 88 (10) S276–S298 (2023)
Supplementary material

SUPPLEMENTARY MATERIAL TO

DBUHI3 complex an efficient catalyst for the synthesis of 2-phenylbenzimidazole and benzothiazole derivatives

RAMESH GAWADE[1,2] and PRAMOD S. KULKARNI[1,3]*

[1]Department of Chemistry Baburaoji Gholap College, Sangvi, Pune 411027, India, [2]S. M. Joshi College Hadapsar, Tal- Haveli, Pune 411028, India and [3]Department of Chemistry and Post Graduate Center in Organic Chemistry, Hutatma Rajguru Mahavidyalaya, Rajgurunagar, Pune 410505, India

J. Serb. Chem. Soc. 88 (10) (2023) 959–974

EXPERIMENTAL AND ANALYTICAL DATA

General:

All local brand chemicals were purchase checked their purity by TLC and purified. The melting point were determined in open capillary and are uncorrected. For analysis technique following instruments were used.Solvents that were entirely dry and free of impurities were used. Reaction of the progress was checked on Merck TLC Silica gel 60 F254 plates using UV lamp (365 nm and 254 nm) and iodine chamber.

Sr. No.	Analysis Type	Instrument
1	HRMS	Brucker Impact HD
2	UV-visible Spectrum	shimadzuCorp, Model UV-2600
3	IR Spectrum	shimadzu Corp, FTIR-shimay, Model IR affinity

---

* Corresponding author. E-mail: pramodskulkarni3@gmail.com

4	FESM	FEI Nova NanoSEM 450
5	EDS	Brucker XFlash 6130
6	TGA-DTA	shimadzu Corp
7	NMR (^{1}H &^{13}C)	500MHz &125MHZ Brucker

Synthesis of amine-iodine complexes

Ammonium iodide (2.8 eq.) was added to water (2 volume) has obtained clear solution in 250 mL beaker and then added iodine (1 eq). This mixture of the solution was added dropwise to a stirred solution of amine (1 eq) in water (8 Volume) in 250 mL round bottom flask. The solid product has formed during addition, stirred mixture for 15 minutes and filter off the solid product. The product was washed with cold water and dried under vacuum to provide the desired complexes and the yield of the complex was reported.

Typical Process for the synthesis of benzimidazole / benzothiazole from o-phenylenediamine/thiophenol and aldehyde.

A mixture of *o*-phenylenediamine/*o*-amino thiophenol (1 mmol) and arylaldehyde (1 mmol) was dissolved in 2 mL ethanol in 25 mL round bottom flask. The catalyst (**1a**) (15mol%) was added and the reaction mixture was stirred for 30 min. The progress of the reaction was monitored by (hexane: ethyl acetate) TLC. The TLC clearly have showed the disappearance of thestarting material. After completion of the reaction, the solvent was evaporated under vacuum. The crude solid product was extracted in ethyl acetate after the addition of 20 % sodium thiosulphate solution. The organic layer was dried over sodium sulfate and purified by column chromatography. The structure of the compound was confirmed by the spectroscopic techniques and match with the reported.

1a. DBU-Iodine complex (Table 1, Entry 1, 1a): Greenish Yellow solid M. P. 87^{0}C.

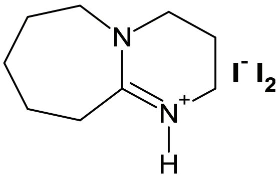

M. F. = $C_9H_{17}N_2\, I^- I_2$ Mol. Wt. = 533.79

HRMS: Positive ion polarity: 153.138 (cal. 153.242).

Negative ion polarity: 126.904 (cal. 126.904), 380.712 (cal. 380.713).

UV-visible Spectrum(nm): 210, 307,364 (λ_{max} =**364nm**).

IR Spectrum(cm^{-1}): 530, 601, 633, 1203, 1319, 1440, 1574, 1638, 3133, 3267.

SEM: Clumpy and agrummerated morphology.

Field Emission Scanning Electron Microscopy Energy Dispersive X-ray Spectroscopy (FESEM - EDS):

Element	At. Number	Wt. %	At. %
Iodine	53	78.97	26.69
Carbon	6	17.57	62.74
Nitrogen	7	3.45	10.57
		100	100

TGA: DBU-iodine complex was stable up to 200°C after that gradual weight loss start up to 380°C then fast weight loss observed and stop 410°C. After 410°Cslow weight loss starts and end by complete vanishing of complex at 500°C.

DTA: Endotherm was observed at 110°Cand exotherm at 410°C. Both peaks are very sharp.

Strong exotherm and sharp weight loss was located in graph at 410°C.

^{1}HNMR:(500 MHz,DMSO-d$_6$):δ9.47 (s, 1H), 3.55 (t, 2H *J*=3.55 Hz), 3.48 (t, 2H *J*=3.48 Hz), 3.24-3.26 (m, 2H), 2.63 (t, 2H *J*=2.64 Hz), 1.92(q, *J*=1.94Hz) 1.54-1.72 (m, 6H);**^{13}CNMR:(125 MHz,DMSO-d$_6$) δ**:165.88, 53.89, 48.38, 38.10, 32.22, 28.70, 26.38, 23.78, 19.34.

1b. Morpholine-Iodine complex (Table 1, Entry 2, 1b): Orange Yellow solid M. P. 78^{0}C.

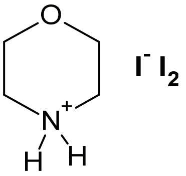

M. F. = C_4H_9NO I^- I_2 Mol. Wt. = 467.73

HRMS: Positive ion polarity: 88.075 (cal. 88.126).

Negative ion polarity: 126.905 (cal. 126.904), 380.713 (cal. 380.713).

UV-visible Spectrum(nm): 210, 360, 365, 366. (λ_{max} = **360nm**).

IR Spectrum (cm^{-1}): 585, 626, 817, 859, 1006, 1033, 1083, 1159, 1243, 1295, 1357, 1438, 2858, 3183.

SEM: Clumpy and agrummerated morphology.

Field Emission Scanning Electron Microscopy Energy Dispersive X-ray Spectroscopy (FESEM - EDS):

Element	**At. Number**	**Wt. %**	**At. %**
Iodine	53	66.21	16.45
Carbon	6	23.94	62.86
Oxygen	8	5.36	10.57
Nitrogen	7	4.49	10.11
		100	100

TGA: The morpholine-iodine complex was stable up to 150°C then underwent fast weight loss till 300°Cthen gradual weight loss observed end at 500°Cby complete disappearing complex.

DTA: It displaysharp endotherm at 150°C and very broad exotherm peak at 480°C.

^{1}HNMR: (500 MHz, DMSO-d_6):δ 3.66-3.77 (m, 4H), 3.35-3.41(m, 4H);**^{13}CNMR:(125 MHz, DMSO-d_6)δ**:44.09, 45.24, 64.46, 65.55.

1c. Urotropine-Iodine complex (Table 1, Entry 3, 1c): Brown Yellow solid M. P. 130^{0}C.

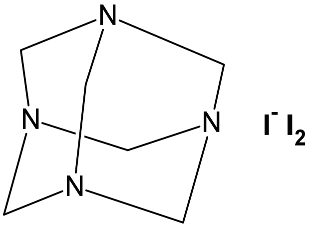

M. F. = $C_6H_{13}N_4$ I^- I_2 Mol. Wt. = 521.76

HRMS: Positive ion polarity: 141.113 (cal. 141.192).

Negative ion polarity: 126.905 (cal. 126.904).

UV-visible Spectrum(nm): 308, 113, 324, 369 (λ_{max} = **369nm**).

IR Spectrum (cm^{-1}): 523, 656, 705, 734, 819, 901, 991, 1028, 1230, 1250, 1381, 1455.

SEM: Clumpy and agrummerated morphology.

Field Emission Scanning Electron Microscopy Energy Dispersive X-ray Spectroscopy (FESEM - EDS):

Element	At. Number	Wt. %	At. %
Iodine	53	74.50	22.60
Carbon	6	16.03	51.37
Nitrogen	7	09.47	26.03
		100	100

TGA: The complex was very stable up to 255°C after that sharp decrease in weight continue till temperature 340°C.

DTA: It show sharp three band at temperature 145°C, 255°Cand 450°C.

^{1}HNMR:(500 MHz, DMSO-d_6):δ4.73(s, 12H);**^{13}CNMR:(125 MHz, DMSO-d_6)δ**:73.85.

1d. Piperazine-Iodine complex (Table 1, Entry 4, 1d): Dark Brown Yellow Solid M. P. 346^{0}C.

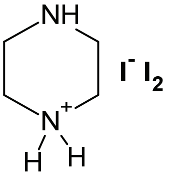

M. F. = $C_4H_{11}N_2$ I^- I_2 Mol. Wt. = 467.74

HRMS: Positive ion polarity: 87.091(cal. 87.142).

Negative ion polarity: 126.905 (cal. 126.904).

UV-visible Spectrum(nm): 210, 306, 319, 361, 368 (λ_{max} = **368nm**).

IR Spectrum (cm^{-1}): 636, 860, 988, 1084, 1242, 1358, 1400, 1436, 3180.

SEM: Clumpy and agrummerated morphology.

Field Emission Scanning Electron Microscopy Energy Dispersive X-ray Spectroscopy (FESEM - EDS):

Element	At. Number	Wt. %	At. %
Iodine	53	89.50	45.67
Carbon	6	07.55	40.73
Nitrogen	7	02.94	13.60
		100	100

TGA: The complex show stability till temperature 115°Cafter sharp and slow weight loss continue up to 325°C.

DTA: This graph indicates one sharp exothermic band at 325°C.

^{1}HNMR: (500 MHz, DMSO-d_6): δ8.48(s, 2H), 3.81 (s, 1H), 3.22(t, 1H, *J*=3.22 Hz), 3.07 (t, 4H, *J*= 3.08Hz), 2.99 (s, 1H), 2.61-2.64 δ(q, 1H);**^{13}CNMR: (125 MHz, DMSO-d_6) δ**:47.85, 46.74, 44.28, 43.54.

1e. N-Methyl-Piperazine-Iodine complex (Table 1, Entry 5, 1e):
Pinkish Yellow solid M. P. 178^{0}C.

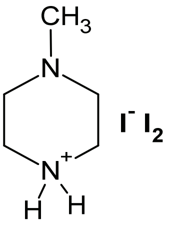

M. F. = $C_5H_{13}N_2$ I^- I_2 Mol. Wt. = 481.75

HRMS: Positive ion polarity: 101.107 (cal. 101.168).

Negative ion polarity: 126.905 (cal. 126.904).

UV-visible Spectrum(nm): 210, 306, 317, 365 (λ_{max} = **364nm**).

IR Spectrum (cm^{-1}): 573, 847, 893, 960, 990, 1100, 1365, 1438, 1553, 1651, 2436, 2707.

SEM: Clumpy and agrummerated morphology.

Field Emission Scanning Electron Microscopy Energy Dispersive X-ray Spectroscopy (FESEM - EDS):

Element	At. Number	Wt. %	At. %
Iodine	53	76.30	23.96
Carbon	6	18.18	60.32
Nitrogen	7	05.52	15.71
		100	100

TGA: The complex was stable till 200°C above this temperature gradual weight loss till 320°C.

DTA: One sharp exothermic band observed at 320°C.

^{1}HNMR:(500 MHz, DMSO-d$_6$): δ8.46 (s, 2H), 2.96-3.05(m, 4H), 2.61-2.63(m, 4H), 2.35(s, 3H);**^{13}CNMR:(125 MHz, DMSO-d$_6$) δ**:51.47, 45.40, 43.02.

CHARACTERISATION DATA OF 2-SUBSTITUTED PHENYL BENZIMIDAZOLE.

1. 2-(4-chlorophenyl)-*1H*-benzimidazole (Table 5, Entry 1, 4a): Yellow solid M. P. 290-293°C (290-292°C)[1]

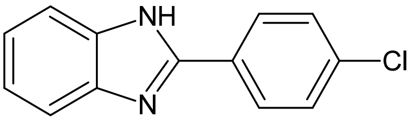

^{1}HNMR: (500 MHz, DMSO-d_6): **δ** 12.98 (s, 1H), 8.17-8.20 (m, 2H), 7.73 (d, 1H, *J*=7.73 Hz), 7.64-7.68 (m, 1H), 7.63 (t, 1H, *J*= 7.62 Hz), 7.61 δ (d, 1H *J*= 7.60 Hz), 7.20-7.36 (m, 2H); **^{13}CNMR: (125 MHz, DMSO-d_6)δ**: 150.61, 144.20, 135.48, 134.95, 129.54, 129.27, 128.60, 123.24, 122.31, 119.43, 111.88.

2. 2-(3-chlorophenyl)-1*H*-benzimidazole (Table 5, Entry 2, 4b): Brown solid M. P. 228-230°C (227-229°C)[2]

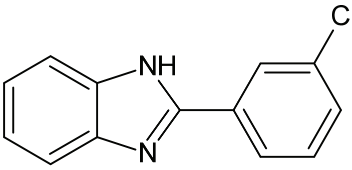

^{1}HNMR: (500 MHz, DMSO-d_6): **δ** 13.04 (s, 1H), 8.23 (t, 1H *J*= 8.22 Hz), 8.17 (t, 1H *J*= 8.17 Hz), 8.15 (t, 1H, *J*= 8.13 Hz) 7.57-7.66 (m, 1H), 7.55 (t, 1H, *J*= 7.54 Hz), 7.30 (q, 1H), 7.20 – 7.27 δ (m, 2H); **^{13}CNMR: (125 MHz, DMSO-d_6)δ**: 150.19, 144.11, 135.45, 134.23, 132.67, 131.42, 130.01, 126.48, 125.48, 123.43, 122.41, 119.56, 111.98.

3. 2-(2-chlorophenyl)-*1H*-benzimidazole (Table 5, Entry 3, 4c):Yellow solid M. P. 232-234°C (231-233^{0}C)[1]

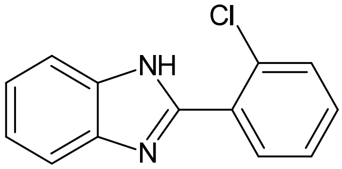

^{1}HNMR: (500 MHz, DMSO-d_6): δ 12.73 δ (s, 1H), 7.90-7.91 (m, 1H), 7.66 (d, 1H, *J*= 7.65 Hz), 7.65 (d, 2H, *J*=7.65 Hz), 7.50-7.56 (m, 2H), 7.22-7.26 (m, 2H); ^{13}**CNMR: (125 MHz, DMSO-*d_6*)δ** :149.55, 132.56, 132,09, 131.68, 130.82, 130.43, 127.91, 122.72, 120.07.

4. 2-(4-bromophenyl)-*1H*-benzimidazole (Table 5, Entry 4, 4d):Yellow solid M. P. 286-290°C (292-293°C)[1]

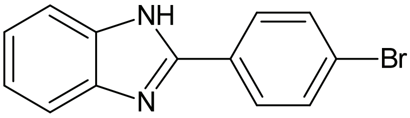

5. 2-(4-Methoxyphenyl)-*1H*-benzimidazole (Table 5, Entry 5, 4e):White solid M. P. 223-225°C (222-223°C)[3]

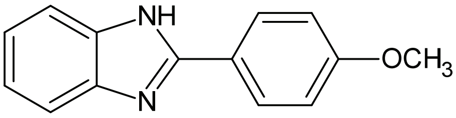

^{1}**HNMR: (500 MHz, DMSO-*d_6*): δ** 12.73 (s, 1H), 8.10 - 8.12 (m, 2H), 7.61 (d, 1H, *J*= 7.60 Hz), 7.48 (d, 1H, *J*=7.48 Hz), 7.17 (t, 2H, *J*= 7.16 Hz) 7.13 (d 1H *J*=7.13 Hz) 7.11 (d, 1H *J*=7.10 Hz) 3.84 (s, 3H); ^{13}**CNMR: (125 MHz, DMSO-*d_6*)δ**: 161.05, 151.79, 144.34, 135.43, 128.45, 123.15, 122.53, 121.90, 118.95, 114.83, 111.49.

6. 2-(3-methoxyphenyl)-1*H*-benzimidazole (Table 5, Entry 6, 4f):Yellow solid M. P. 202-205°C (200-202°C)[1]

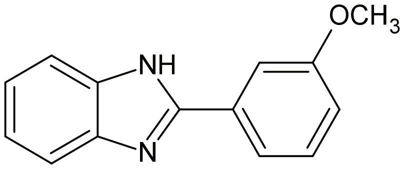

7. 2-(3,4-dimethoxyphenyl)-*1H*-benzimidazole (Table 5, Entry 7, 4g): White solid M. P. 225-227°C (223-226°C)[4]

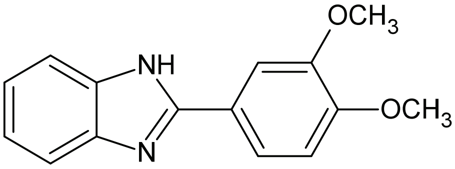

8. 2-(2H-1,3-benzodioxol-5-yl)-*1H*-benzimidazole (Table 5, Entry 8, 4h):Yellow solid 238-240°C (239-241°C)[3]

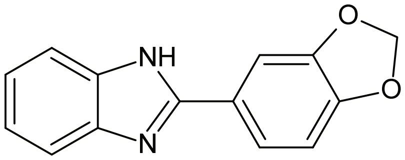

^{1}HNMR: (500 MHz, DMSO-*d*$_6$): δ 12.80 (s, 1H), 7.67 (q, 1H, *J*= 7.66 Hz), 7.45-7.47 (m, 1H), 7.27 (d, 1H, *J*= 7.26 Hz), 7.21-7.23 (m, 3H), 6.59(d, 1H, *J*= 6.58 Hz), 5.96 (s, 2H); **^{13}CNMR: (125 MHz, DMSO-*d*$_6$)δ**: 153.50, 148.07, 147.04, 143.02, 136.25, 124.22, 123.00, 122.60, 119.85, 119.55, 111.53, 108.91, 107.22, 101.58.

9. 2-phenyl-*1H*-benzimidazole (Table 5, Entry 9, 4i): Brown solid M. P. 243-245°C (242-244°C)[2]

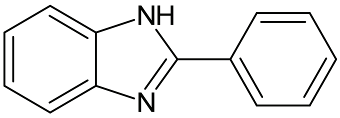

^{1}HNMR: (500 MHz, DMSO-*d*$_6$): δ 12.91 (s, 1H), 8.19 (t, 2H *J*=8.18 Hz), 7.67 (d, 1H, *J*=7.67 Hz), 7.53-7.57 (m, 3H), 7.50 (t, 1 H *J*=7.48 Hz) 7.18-7.24 (m, 2H); **^{13}CNMR: (125 MHz, DMSO-*d*$_6$)δ**: 151.68, 144.28, 135.47, 130.64, 130.30, 129.41, 129.25, 127.09, 126.90, 122.99, 122.13, 119.34, 111.78.

10. 2-(4-methylphenyl)-*1H*-benzimidazole (Table 5, Entry 10, 4j):Brown Solid M. P. 216-219°C (214-216°C)[2]

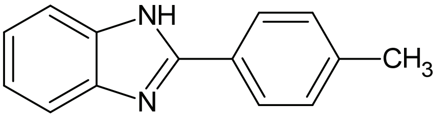

11. 4-(*1H*-benzimidazole-2-yl) phenol (Table 5, Entry 11, 4k): White solid M. P. 252-254°C (254-255°C)[1]

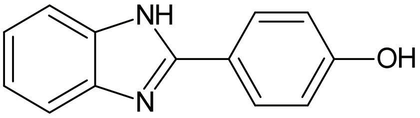

^{1}HNMR: (500 MHz, DMSO-d_6): δ 15.33 (s, 1H), 10.87 (s, 1H), 8.25 (d, 2H *J*= 8.24 Hz) 7.77-7.81 (m, 2H), 7.51-7.54 (m, 2H), 7.09-7.11 (d, 2H, *J*=7.09 Hz); **^{13}CNMR: (125 MHz, DMSO-d_6)δ**: 162.86, 149.60, 132.12, 130.74, 125.97, 116.98, 114.04, 113.78.

12. 2-(*1H*-benzimidazole-2yl) phenol (Table 5, Entry 12, 4l):Brown solid 204-206°C (205-206°C)[5]

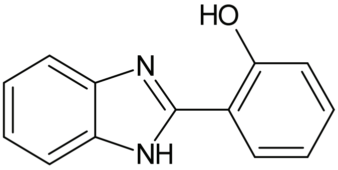

^{1}HNMR: (500 MHz, DMSO-d_6): δ 13.29 (s, 1H), 13.09 (s, 1H), 8.06 (d, 1H, *J*=8.05 Hz), 7.94-7.97 (m, 2H), 7.90 (d, 1H, *J*=7.89Hz), 6.61-7.64 (m, 2H), 7.48-7.51(m, 1H), 7.38-7.41(m, 1H); **^{13}CNMR: (125 MHz, DMSO-d_6)δ**: 156.85, 152.58, 142.33, 131.85, 128.83, 127.16, 123.10, 122.99, 119.50, 116.88, 115.50, 111.29.

13. 2-(4-nitrophenyl)-*1H*-benzimidazole (Table 5, Entry 13 4m):Yellow solid M. P. 301-303°C (300°C)[6]

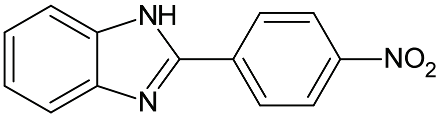

14. 2-(3-nitrophenyl)-*1H*-benzimidazole (Table 5, Entry 14, 4n):Yellow solid M. P. 196-198°C (199°C)[6]

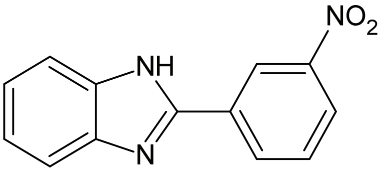

15. 2-(2-nitrophenyl)-*1H*-benzimidazole (Table 5, Entry 15, 4o):Yellow solid M. P. 229-231°C (230°C)[6]

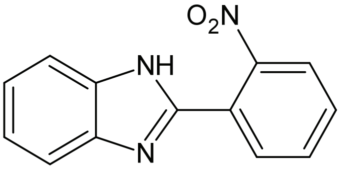

^{1}HNMR: (500 MHz, DMSO-*d$_6$*): δ 13.06 (s, 1H), 8.03 (dd, 1H, *J*=8.02 Hz), 7.98 δ (dd, 1H, *J*=7.97 Hz) 7.85-7.88 (m, 1H), 7.74-7.77 (m, 1H) 7.69 (d, 1H, *J*=7.65 Hz), 7.57 (d, 1H *J*=7.56 Hz) 7.20-7.29 (m, 2H); 13**CNMR: (125 MHz, DMSO-*d$_6$*)δ**:149.42, 147.76, 144.05, 135.07, 133.12, 131.38, 124.77, 124.67, 123.56, 122.36, 119.71, 112.14.

16. 4-(*1H*-benzimidazole-2-yl)-N, N-dimethylaniline (Table 5, Entry 16,4p):Yellow solid M. P. 280-283°C (277-279°C)[1]

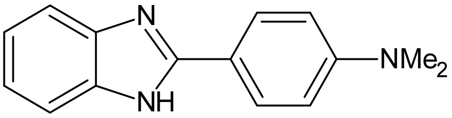

^{1}HNMR: (500 MHz, CDCl$_3$): 12.51 (s, 1H), 7.61-7.64 (m, 1H), 7.23-7.26 (m, 1H), 7.15-7.20 (m, 1H), 7.01 (d, 1H, *J*=7.01 Hz), 6.67-6.74 (m, 2H), 3.00 (m, 3H), 2.92 (m, 3H); **^{13}CNMR: (125 MHz, CDCl$_3$)δ**: 155.04, 149.98, 143.30, 136.38, 130.31, 126.94, 124.34, 122.16, 119.26, 117.39, 112.81, 111.81, 110.40, 40.57, 40.23.

17. 2-[(*E*)-2-phenylethenyl]-*1H*-benzimidazole (Table 5, Entry 17 4q):Yellow solid M. P. 270-273°C (164-166°C)[2]

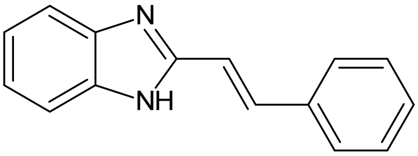

18. 2-(furan-2-yl)-*1H*-benzimidazole (Table 5, Entry 18, 4r):Brown solid M. P. 226-228°C(221-223°C)[2]

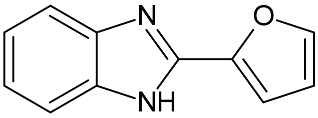

^{1}HNMR: (500 MHz, DMSO-d_6): δ 12.95(m, 1H), 7.96(dd, *J*=1.71&0.90Hz, 1H), 7.57(d, *J*=7.11Hz, 1H), 7.51 (d, *J*=7.15Hz, 1H) 7.17-7.22 (m, 3H), 6.72(dd, *J*=3.4 Hz &0.95 Hz, 1H); **^{13}CNMR: (125 MHz, DMSO-d_6) δ**:147.12, 143.37, 135.00, 134.44, 129.02, 128.68, 127.15, 123.01, 121.90, 117.81, 112.59.

19. 3-(*1H*-benzimidazole-2-yl)2-chloroquinoline (Table 5, Entry 19, 4s):Yellow solid M. P. 219-222°C (202°C)[7]

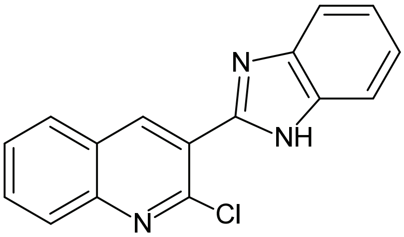

^{1}HNMR: (500 MHz, DMSO-d_6): δ 10.41 (s, 1H), 9.34 (s, 1H), 8.08 (d, 1H, *J*=8.06 Hz), 8.06 (d, 1H, *J*=8.05Hz), 7.98-8.00 (m, 1H), 7.81-7.85 (m, 1H), 7.35-7.60 (m, 2H); **^{13}CNMR: (125 MHz, DMSO-d_6) δ**: 147.57, 147.02, 145.58, 143.07, 141.48, 133.96, 131.98, 128.41, 128.30, 128.09, 127.05, 124,12, 123.22, 122,74, 119.86, 111.29.

20. 3-(*1H*-benzimidazol-2-yl)-2-chloro-6-methylquinoline (Table 5, Entry 20, 4t):White solid M. P. 221-224°C (220°C)[7]

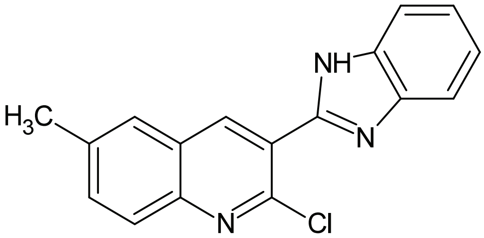

^{1}HNMR: (500 MHz, DMSO-*d_6*): δ 12.94 (s, 1H), 8.87 (s, 1H), 8.59 (s, 1H), 7.75-7.78 (m, 2H), 7.61-7.74 (m, 2H), 7.28-7.59 (m, 2H), 2.63 (s, 3H); **^{13}CNMR: (125 MHz, DMSO-*d_6*) δ**: 148.31, 146.73, 145.95, 141.20, 138.32, 134.71, 127.93, 127.60, 126.83, 124.87, 123.53, 122.41, 119.66, 112.32, 21.64.

21. 2-(1*H*-indol-2-yl)-*1H*-benzimidazole (Table 5, Entry 21, 4u):Black solid 220-223°C (226-227°C)[17]

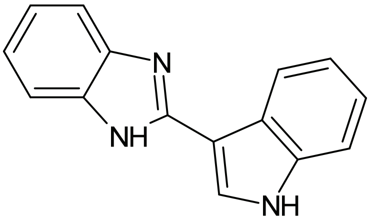

^{1}HNMR:(500 MHz DMSO-*d_6*): **δ** 12.59 (s, 1H), 11.66 (s, 1H), 8.49 (t, 1H, *J*= 8.48 Hz), 8.14 (d, 1H, *J*=8.13 Hz), 7.49-7.55 (m, 2H), 7.54-7.55 (m, 2H), 7.49-7.50 (q, 1H), 7.19-7.21 (m, 1H), 7.13-7.16 (m, 1H); **^{13}CNMR:**(125 MHz DMSO-*d_6*) δ: 149.84, 136.96, 126.77, 125.54, 122.73, 121.78, 120.78, 112.41, 106.74.

22. 3-(*1H*-benzimidazol-2-yl)-6-bromo-4*H*-1-benzopyran-4-one (Table 5, Entry 22, 4v): Yellow solid M. P. 269-271°C.

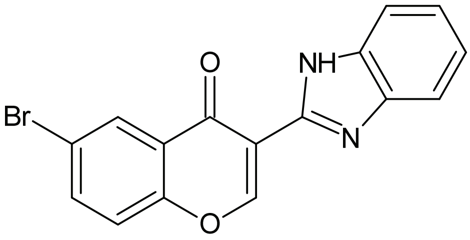

^{1}HNMR: (500 MHz, DMSO-d_6):δ 12.65 (s, 1H), 8.32 (s, 1H), 9.41 (s, 1H), 8.32 (d, 1H, *J*= 8.31 Hz), 8.06-8.09 (m, 1H), 7.67-7.70 (m, 1H), 7.62-7.66 (m, 1H), 7.18-7.22 (m, 2H); **^{13}CNMR: (125 MHz, DMSO-d_6) δ**: 174.11, 158.91, 155.05, 145.27, 142.70, 137.89, 134.93, 127.82, 125.57, 122.70, 122.40, 121.96, 119.22, 118.73, 115.03, 112.97.

HRMS: [MF: $C_{16}H_{10}O_2N_2Br$(M+H)]: 342.99 (Calculated: 342.16)

CHARACTERISATION DATA OF 2-SUBSTITUTED PHENYL BENZOTHIAZOLE.

1. 2-(4-chlorophenyl)-1,3-benzothiazole (Table 6, Entry 1, 7a): White solid M. P. 115-117°C (111-112°C)[8]

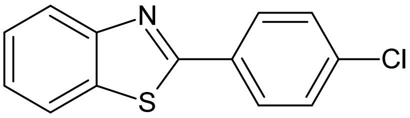

2. 2-(3-chlorophenyl)-1,3-benzothiazole (Table 6, Entry 2. 7b): White solid M. P. 94-95°C (93-94°C)[8]

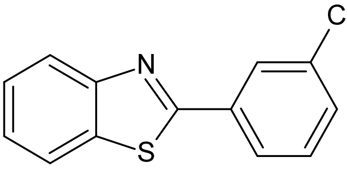

3. 2-(2-chlorophenyl)-1,3-benzothiazole (Table 6, Entry 3, 7c): White solid M. P. 80-82°C (83-84°C)[8]

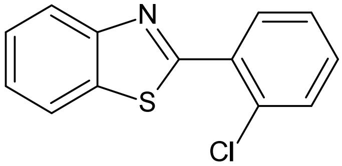

4. 2-(4-bromophenyl)-1,3-benzothiazole (Table 6, Entry 4, 7d): White Solid M. P. 127-129°C (129-131°C)[9]

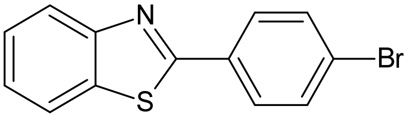

^{1}HNMR: (500 MHz, $CDCl_3$): **δ** 8.06 (d, 1H, *J*=8.05 Hz), 7.94-7.91 (m, 2H), 7.90(d, 1H, *J*= 7.89 Hz), 7.61-7.64(m, 2H), 7.48-7.51 (m, 1H), 7.38-7.41 (m, 1H); **^{13}CNMR: (125 MHz, $CDCl_3$)δ**: 166.70, 154.06, 135.03, 132.54, 132.23, 128.90, 126.51, 125.45, 125.42, 123.31, 121.67.

5. 2-(4-methoxyphenyl)-1,3-benzothiazole (Table 6, Entry 5, 7e): White Solid M. P. 120-121°C (120-122°C)[9]

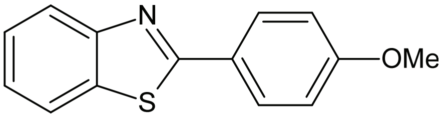

^{1}HNMR: (500 MHz, $CDCl_3$): δ 8.02-8.04 (m, 3H), 7.86 (d, 1H, *J*=7.86 Hz), 7.44-7.48 (m, 1H), 7.33-7.36 (m, 1H), 6.98-7.01 (m, 2H), 3.87 (s, 3H); **^{13}CNMR: (125 MHz, $CDCl_3$) δ**: 167.86, 161.91, 154.22, 134.85, 129.10, 126.43, 126.19, 124.78, 122.81, 121.50, 114.36, 55.46.

6. 2-(3-methoxyphenyl)-1,3-benzothiazole (Table 6, Entry 6, 7f): Yellow solid M. P. 99-102°C (98-100°C)[10]

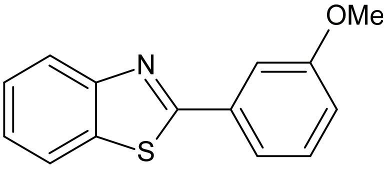

7. 2-(3,4-dimethoxyphenyl)-1,3-benzothiazole (Table 6, Entry 7, 7g): Brown solid M. P. 229-231°C (230-232°C)[11]

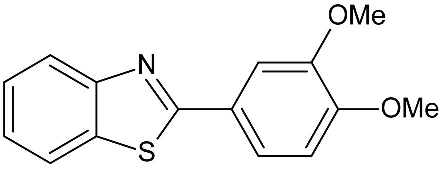

8. 2-(2*H*-1,3-benzodioxol-5-yl)-1,3-benzothiazole (Table 6, Entry 8, 7h):Yellow solid M. P. 130-132°C (128-130°C)[12]

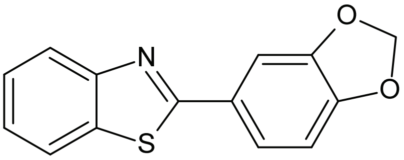

^{1}HNMR: (500 MHz, $CDCl_3$): δ 8.00 (d, 1H, *J*=7.99 Hz), 7.81 (d, 1H, *J*=7.81 Hz), 7.57 (d, 1H, *J*=7.56 Hz), 7.42-7.45 (m, 1H), 7.30-7.35 (m, 1H), 6.85 (d, 1H, *J*=6.84 Hz), 5.99 (s, 2H); **^{13}CNMR: (125 MHz, $CDCl_3$) δ**: 167.49, 154.01, 150.01, 148.29, 134.80, 127.94, 126.20, 124.89, 122.86, 122.66, 122.43, 108.56, 107.43, 101.67.

9. 2-phenyl-1,3 benzothiazole (Table 6, Entry 9, 7i): White solid M. P. 112-113°C (109-110°C)[8]

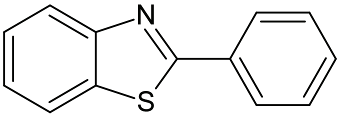

10. 2-(4-methylphenyl)-1, 3-benzothiazole (Table 6, Entry, 10, 7j): Yellow solid M. P. 85-86°C (87-88°C)[13]

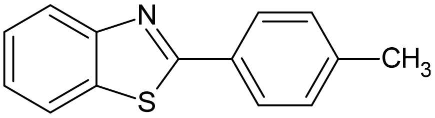

11. 4-(1,3-benzothiazol-2-yl) phenol (Table 6, Entry 11, 7k): White solid M. P. 227-229°C (225-227°C)[14]

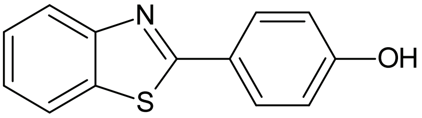

^{1}HNMR: (500 MHz DMSO-d_6): δ 10.24 (s, 1H), 8.09 (d, 1H, *J*=8.07), 8.07 (d, 1H, *J*=8.06), 7.93-7.00 (m, 2H), 7.49-7.52 (m, 1H), 7.39-7.42 (m, 1H), 6.96 (t, 2H, *J*=6.95); **^{13}CNMR: (125 MHz DMSO-d_6) δ**: 167.92, 160.99, 154.19, 134.57, 129.74, 129.51, 129.27, 126.89, 125.36, 124.50, 122.76, 122.58, 116.55.

12. 2-(1,3-benzothiazol-2-yl) phenol (Table 6, Entry 12, 7l): White solid M. P. 131-132°C (124-126°C)[14]

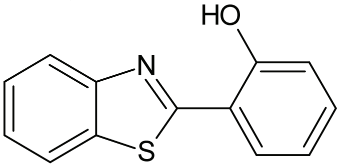

^{1}HNMR: (500 MHz, CDCl$_3$): δ 12.50 (s, 1H), 7.97 (d, 1H, *J*=7.96 Hz), 7.87 (d, 1H, *J*=7.87 Hz), 7.66-7.68 (m, 1H), 7.47-7.50 (m, 1H), 7.35-7.70 (m, 2H), 7.09-7.10 (m, 1H), 6.92-6.96 (m, 1H); **^{13}CNMR: (125 MHz, CDCl$_3$) δ**: 169.35, 157.92, 151.81, 132.73, 132.56, 128.39, 128.14, 126.66, 125.52, 122.16, 121.49, 119.53, 117.85.

13. 4-(1,3-benzothiazol-2-yl)-2-methoxyphenol (Table 6, Entry 13, 7m): White solid M. P. 160-162°C (161-163°C)[14]

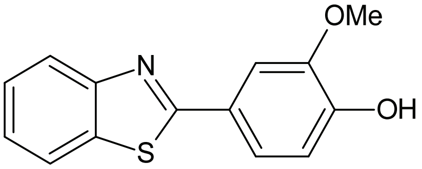

^{1}HNMR: (500 MHz, CDCl$_3$): δ 8.03 (d, 1H, *J*= 8.01 Hz), 7.86 (q, 1H), 7.71 (d, 1H, *J*= 7.70 Hz), 7.54 (q, 1H), 7.45-7.48 (m, 1H), 7.33-7.37 (m, 1H), 7.00 (q, 1H), 6.10 (s, 1H) 4.00(s, 3H); **^{13}CNMR: (125 MHz, CDCl$_3$) δ**: 168.15, 154.04, 148.52, 146.95, 134.81, 126.22, 126.17, 124.84, 122.72, 121.94, 121.51, 114.71, 109.24, 56.17.

14. 2-(4-nitrophenyl)-1,3-benzothiazole (Table 6, Entry14, 7n): Brown solid M. P. 320-322°C (228-230°C)[14]

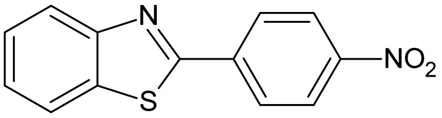

^{1}HNMR: (500 MHz, CDCl$_3$): δ 8.92 (s, 1H), 8.40 (d, 1H, *J*=8.40 Hz), 8.31 (d, 1H, *J*=8.30 Hz), 8.11 (d, 1H, *J*=8.10 Hz), 7.94 (d, 1H, *J*=7.93 Hz), 7.67 (t, 1H, *J*= 7.68 Hz), 7.56 (t, 1H, *J*=7.56 Hz), 7.45 (t, 1H, *J*=7.45 Hz); **^{13}CNMR: (125 MHz, CDCl$_3$) δ**: 164.89, 153.93, 148.74, 135.17, 133.01, 130.12, 126.85, 126.05, 125.19, 123.75, 122.69, 122.32, 121.85.

15. 2-(3-nitrophenyl)-1,3-benzothiazole (Table 6, Entry 15, 7o): Yellow solid M. P. 190-193°C (185-187°C)[15]

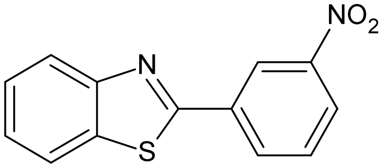

16. 2-(2-nitrophenyl)-1,3-benzothiazole (Table 6, Entry 16, 7p): Orange brown solid M. P. 195-197°C (191-193°C)[15]

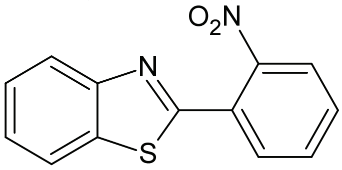

^{1}HNMR: (500 MHz, $CDCl_3$): δ 8.08 (d, 1H *J*=8.07 Hz), 7.88-7.94 (m, 2H) 7.79 (q, 1H), 7.67-7.70 (m, 1H), 7.61-7.64 (m, 1H), 7.51-7.54 (m, 1H), 7.43-7.46 (m, 1H); **^{13}CNMR: (125 MHz, $CDCl_3$) δ**: 162.40, 153.51, 148.91, 135.79, 132.39, 131.81, 130.93, 128.10, 126.59, 125.87, 124.61, 123.94, 121.58.

17. 4-(1,3-benzothiazol-2-yl)-*N*, *N*-dimethylaniline (Table 6, Entry 17, 7q):White solid 161-163°C (160-162°C)[14]

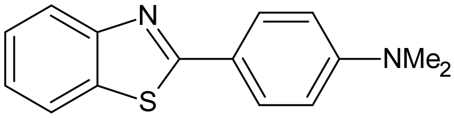

18. 2-[(*E*)-2-phenylethenyl]-1,3-benzothiazole (Table 6, Entry 18, 7r):White solid M. P. 107-110°C (110-112°C)[14]

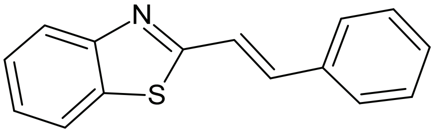

19. 2-(furan-2-yl)-1,3-benzothiazole (Table 6, Entry 19, 7s): White solid M. P. 103-104°C (101-102°C)[10]

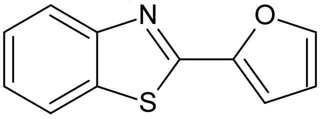

^{1}HNMR: (500 MHz, $CDCl_3$): δ 8.04 (d, 1H, *J*=8.04 Hz), 7.88 (d, 1H, *J*=7.88 Hz), 7.60 (d, 1H, *J*=7.59 Hz), 7.47-7.50 (m, 1H), 7.36-7.39 (m, 1H), 7.18 (d, 1H, *J*=7.18 Hz), 6.59-6.60 (m, 1H); **^{13}CNMR: (125 MHz, $CDCl_3$)δ**:157.56, 153.74, 148.73, 144.70, 134.26, 126.48, 125.19, 123.11, 121.57, 112.53, 111.43.

20. 2-(pyridin-2-yl)-1,3-benzothiazole (Table 6, Entry 20, 7t): Brown solid 132-134°C (130-132°C)[16]

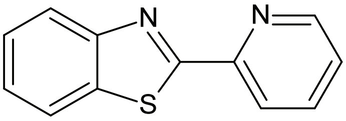

^{1}HNMR: (500 MHz, CDCl$_3$): δ 8.67-8.68 (m, 1H), 8.36 (d, 1H, *J*=8.35 Hz), 8.08 (d, 1H, *J*=8.08 Hz), 7.94 (d, 1H, *J*=7.94 Hz), 7.80-7.84 (m, 1H), 7.47-7.51 (m, 1H), 7.34-7.42 (m, 2H); **^{13}CNMR: (125 MHz, CDCl$_3$) δ**: 169.35, 154.25, 151.36, 149.63, 136.99, 136.09, 126.26, 125.63, 125.25, 123.55, 122.00, 120.73.

21. 2-(1*H*-indol-2-yl)-1,3-benzothiazole (Table 6, Entry 21, 7u):Brown solid M. P. 146-148°C (144-147°C)[16]

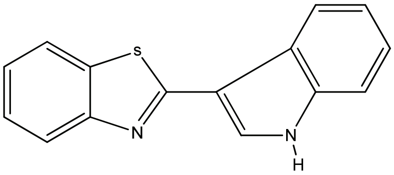

^{1}HNMR:(500 MHz, CDCl$_3$):δ 8.82 (s, 1H), 8.44 (d, 1H, *J*=8.43 Hz), 8.03 (d, 1H, *J*=8.03 Hz), 7.93 (d, 1H, *J*=7.92 Hz), 7.88 (d, 1H, *J*=7.87 Hz), 7.46 δ (t, 1H, *J*=7.46 Hz), 7.43 (t, 1H, *J*=7.41 Hz) 7.35-7.28 (m, 3H); **^{13}CNMR: (125 MHz, CDCl$_3$) δ**: 163.00, 153.730, 136.46, 133.84, 126.34, 126.07, 124.92, 124.23, 123.44, 122.11, 121.83, 121.30, 121.05, 112.46, 111.67.

22: 3-(1,3-benzothiazol-2-yl)-6-bromo-4*H*-1-benzopyran-4-one. (Table 6, Entry 22, 7v): Yellow solid M. P. 254-256 °C.

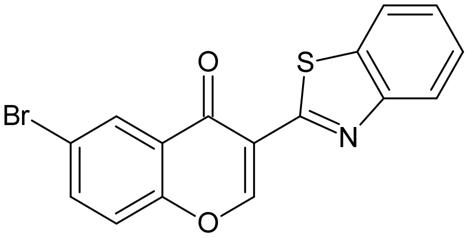

^{1}**HNMR:**(500 MHz, $CDCl_3$): **δ** 9.28 (s, 1H), 8.50 (d, 1H, *J*=8.49 Hz), 7.98-8.04 (m, 2H), 7.83 (q, 1H), 7.46-7.53 (m, 2H), 7.41 (t, 1H, *J*=7.40 Hz); ^{13}**CNMR:(125 MHz, $CDCl_3$) δ:** 173.58, 158.03, 156.55, 154.69, 151.63, 137.33, 136.08, 128.98, 126.32, 125.17, 124.97, 122.57, 121.68, 120.34, 119.75, 118.52.

HRMS: [MF: $C_{16}H_9O_2NSBr$(M+H)]: 359.95 (Calculated: 359.21).

REFERENCES

1. Hossein Naeimi and Nasrin AlishahiHindawi Publishing Corporation *Organic Chemistry International* Volume **2012**, Article ID 498521
2. Marina A. Tzani, Catherine Gabriel and Ioannis N. Lykakis*Nanomaterials***2020**, 10, 2405.
3. KovuruGopalaiah and Sankala Naga Chandrudu*RSC Adv.*, **2015**,5, 5015-5023
4. A. Viswanath, B. Keerthana, G. HimaBindu, B. Sudha Rani and P. Srinivasa Babu *IJPCBS* **2016**, 6(2), 215-221.
5. Santosh V. Goswami, Prashant B. Thorat, Vijay N. Kadam and Sudhakar R. *Bhusare J. Chem. Bio. Phy. Sci.***2011**, Vol.1, N0.2, Sec.A, 164-168.
6. Swapan Majumdar, Mithun Chakraborty, NabyenduPramanikb and Dilip K. Maiti*RSC Adv.*, **2015**, 5, 51012–51018.
7. Mahalingam Malathi, Palathurai Subramaniam Mohan, Raymond J. Butcher and Chidambaram KulandaisamyVenil*Can. J. Chem.* **2009**, 87, 1692-1703.
8. Chengliang Lia, Hongmei Deng, Tao Jin, Zhiqiang Liu, Ruolan Jiang, Chunju Li, Xueshun Jia, Jian Li *Synthesis***2017**, 49, (18), 4350-4356
9. Behrooz Maleki and Hafezeh Salehabadi*European Journal of Chemistry* **2010,**1 (4) 377 -380.
10. Rahul Bhata, ShrikrishnaKarhalea, Satyanarayan Ardeb, Vasant Helavia*Iranian Journal of Catalysis***2019**, 9(2), 173-179.
11. MudzuliMaphupha, Wanyama P. Juma, Charles B. de Koning and Dean Brady *RSC Adv.*, **2018**, 8, 39496.
12. C Praveen, A Nandkumar, P Dheenkuma, D Muralidharan and P T Perumal *J. Chem. Sci.* Vol. 124, No. 3, May **2012**, pp. 609–624.
13. Ying Han, Xiaohu Wang, Xiaowei Wang, LiangzhongLv, GuowangDiao, Yu Yuan *Synthesis* **2012**, 44, 3027–3032.
14. Suman Ray, Paramita Das, Biplab Banerjee, Asim Bhaumik and Chhanda Mukhopadhyay *RSC Adv.*,**2015**,5, 72745-72754.
15. MudzuliMaphupha, Wanyama P. Juma, Charles B. de Koning and Dean Brady *RSC Adv.*, **2018**, 8, 39496.
16. WarapongSenapak, RungnaphaSaeeng, Jaray Jaratjaroonphong, UthaiwanSirion*Molecular Catalysis***2018**, 458, 97-105.
17. JeshmaKovvuri, BurriNagaraju, Ahmed Kamal and Ajay K. Srivastava *ACS Comb. Sci.* **2016,** 18, 10, 644–650.

Journal of the Serbian Chemical Society
JSCS@tmf.bg.ac.rs • www.shd.org.rs/JSCS

J. Serb. Chem. Soc. *88* (10) 975–983 (2023)
JSCS–5674
Original scientific paper
Published 24 October 2023

Synthetic study on the angular triquinanes

MIHAILO N. STJEPANOVIĆ[1], ALEKSANDAR V. JANKOVIĆ[2], BOJAN Z. VULOVIĆ[1#], RADOMIR V. MATOVIĆ[2] and RADOMIR N. SAIČIĆ[1,3*]

[1]University of Belgrade – Faculty of Chemistry, Studentski trg 16, 11158 Belgrade, Serbia, [2]ICTM – Center for Chemistry, Njegoseva 12, 11158 Belgrade, Serbia and [3]Serbian Academy of Sciences and Arts, Kneza Mihaila 35, 11000 Belgrade, Serbia

(Received 28 June, revised 1 July, accepted 24 July 2023)

Abstract: The synthesis of an angular triquinane, which could serve as a suitable platform for the synthesis of several natural products (panaginsene, silphinene, senoxydene) is described. The synthesis is based on two consecutive cyclopentene annulations, where alkenes were used as latent carbonyl functionalities (*via* Wacker reaction), and cyclopentenone annulation was effected by aldol condensation.

Keywords: cyclopentane; natural products; organic synthesis; Wacker oxidation; aldol condensation.

INTRODUCTION

Among the thousands of structurally diverse, naturally occurring sesquiterpene compounds, the subgroup of triquinanes, although not numerous, occupies a prominent place, due to peculiar structures and a range of biological activities. These polycyclic compounds are assembled from condensed cyclopentane rings and, depending on the fusion pattern, can be classified as linear, angular or propellane (Fig. 1). Triquinane structural subunits are also embedded into tetraquinane skeletons. Not surprisingly, they have attracted considerable interest from the synthetic community.[1]

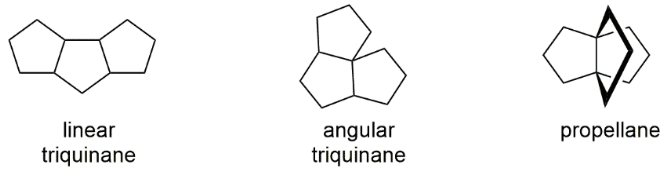

Fig. 1. Three types of triquinane fusion.

---

* Corresponding author. E-mail: rsaicic@chem.bg.ac.rs

[#] Serbian Chemical Society member.

https://doi.org/10.2298/JSC230627046S

The naturally occurring angular triquinanes comprise four skeletal types, namely isocomanes, silphinanes, pentalenanes and silphiperfolanes (Fig. 2). Some of them exhibit interesting biological activities, such as subergorgic acid (**1**, member of the isocomane family), which is cardiotoxic,[2] but also shows antiholinesterase activity,[3] and hence the ability to act as antidote against Soman in mice.[4] Oxygenated congeners of pentalenene **2**, such as pentalenolactone, show antibiotic activity.[5] Silphinene **3** is a biosynthetic precursor of oxygenated products such as aspergilanes,[6] or penifulvins; penifulvin A possesses significant insecticidal activity.[7]

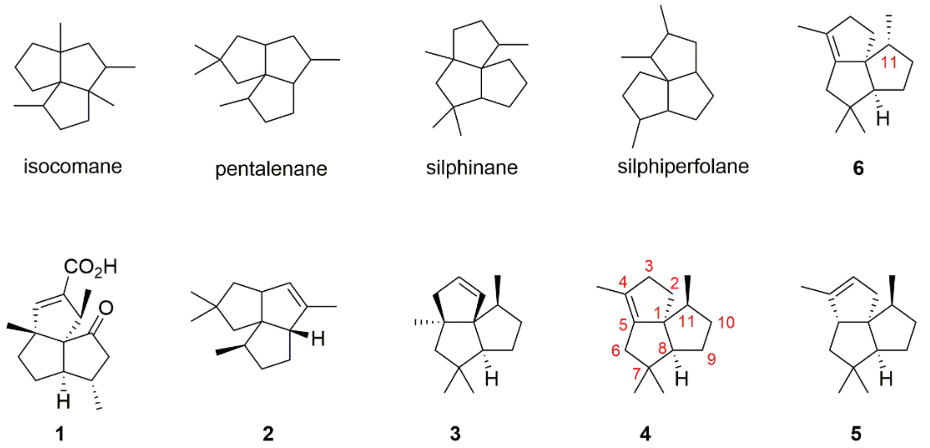

Fig. 2. Examples of naturally occurring angular triquinanes.

We became interested in silphinene **3** and its congeners – panaginsene **4**[8] and senoxydene **5**. These compounds share the common angular triquinane skeleton, with some differences in the position of the alkene bond and one methyl substituent. One stereochemical difference is also of note: the methyl group at C-11 may be of either *trans*-configuration (in panaginsene and senoxydene), or *cis*-oriented (in silphinene), with respect to the cyclopentene ring. Interestingly, panaginsene was initially assigned as *cis*-configured isomer **6**, which was later revised (corrected structure: **4**).[9] Nine total syntheses of silphinene have been reported, the first one by Ito and coworkers, who used bicyclopentadiene as the starting material.[10] Paquette and Leone-Bay constructed the triquinane skeleton by iterative application of 3-oxo-organocuprate 1,4-addition/aldol condensation reaction tandem.[11] Sternbach and coworkers relied on the intramolecular Diels–Alder reaction, followed by oxidative fragmentation of the transient tricycle to the diquinane intermediate.[12] The synthesis by Wender and Ternansky hinges on arene-olefin meta-photocycloaddition, followed by reductive cleavage of cyclopropane ring in the tetracyclic intermediate.[13] Crimmins and Mascarella used a tactical combination of reactions: [2+2] alkene photocycloaddition/cyclobutane fragmentation to access racemic **3**.[14] Synthetic approach by Nagarajan and Rao is based on two cyclopentane annulations, the first by intramolecular Horner-Wadsworth- Emmons reaction and the second by a radical 5-*exo*-cyclization.[15] Yamamura and coworkers created a tricyclic intermediate by an intramolecular cycloaddition of electrochemically generated phenoxy cation; this intermediate was then elaborated into a triquinane framework.[16] Franck-Neumannm, Miesch and Gross developed "the cyclobutenic way" to silphinene, which comprises the cyclopropanation of bicyclo[3.2.0.]hept-6-ene cycloadduct, followed by solvolysis of a highly strained tricyclic intermediate.[17] Fraser-Reid and Dickson used the chiron approach and synthesized (–)-**3** from mannose.[18] Two syntheses of panaginsene have been reported: Lee and Geum used as a key step an intramolecular cycloaddition *via* biradical intermediate,[9] whereas Chakraborty and Singh relied on McMurry coupling for the cyclopentene ring closure.[19] As for senoxydene, two syntheses have been reported: Paquette and coworkers used intramolecular ene cyclization for the stereoselective formation of the key bicyclic intermediate,[20] whereas Ito and coworkers exploited the common intermediate from their previous synthesis of silphinene.[21]

RESULTS AND DISCUSSION

We set out to develop a method that would allow for the efficient construction of the angular triquinane **7**, which contains the skeleton of these three congeners, and where the configuration of the C-11 methyl group could be established subsequently (*i.e.*, in late stages of synthesis), possibly giving rise to both diastereoisomers.

Our retrosynthetic analysis is blueprinted in Scheme 1. Cyclopentenone disconnection in **7** by aldol condensation transformation simplifies the target to bicyclic ketone **8**, which could be obtained from **9** by tactical combination of reactions: allylation/Wacker oxidation. Bicyclic ketone **9** should be accessible by aldolization/isomerization tandem reaction; we were aware that this step would need a study on the reaction conditions/product distribution relationship. The dicarbonyl precursor **10** of enone **9** could be prepared by Wacker oxidation of

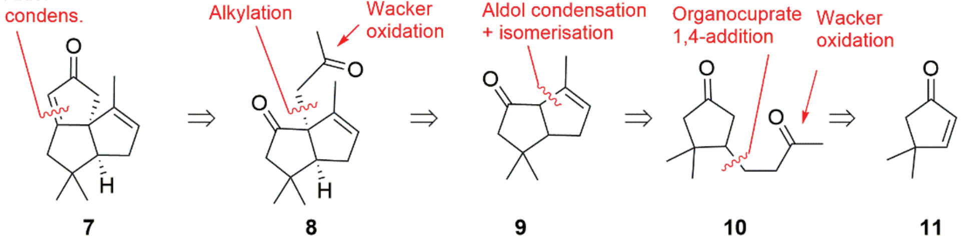

Scheme 1. Retrosynthetic analysis of angular triquinane **7**.

3-butenylcyclopentanone derivative (not shown), on its turn obtainable from known 4,4-dimethyl-2-cyclopentene-1-one (**11**).[22]

The synthesis commenced with 1,4-addition of a butenyl cuprate reagent to the known 4,4-dimethylcyclopent-2-ene-1-one (**11**), which afforded the adduct **12** (Scheme 2). This transformation was reported earlier;[20b] however, modifying the reaction conditions – activation by trimethylsilyl chloride and lithium chloride – improved the yield considerably (82 *vs*. 65 % in the previous publication).[23] Wacker oxidation of **12** under an oxygen atmosphere required 72 h at 50 °C, but provided dione **10** in 84 % yield. Various reaction conditions were tried to accomplish the cyclization step (*i.e.*, **10** → **9**), including potassium hydroxide in aqueous ether, potassium *tert*-butoxide in *tert*-butanol, or in THF, pyrrolidine (alone, or in the presence of acetic acid, or *p*-TsOH), but in all cases the mixtures of conjugated (**13**) and deconjugated (**9**) product were obtained. Finally, we found that the cyclization could be performed in boiling toluene, in the presence of catalytic amounts of *p*-TsOH, to provide the desired bicyclic enone **9** in 83 % yield (accompanied with 9 % of the conjugated isomer **13**). The next step was the installation of acetonyl moiety, to obtain dione **8**. From several synthons available as synthetic equivalents of "acetonyl cation" we chose the structurally simplest one – allyl bromide – for two reasons: a) minimization of steric hindrance and b) the allylation product **14** should be amenable also to aldehyde **15** – an intermediate whose role is explained below (in Scheme 3). The regioselective allylation of **9** was promoted by sodium hydride in boiling THF, where single regio- and diastereoisomer **14** was obtained (85 %). It is of note that the regioselectivity in the reactions of this type is highly dependent on a substrate structure; thus, in the allylation of the structurally related bicyclic system, the less substituted α-position of the ketone required protection, in order to secure allylation at the more substituted α'-position.[20] The Wacker oxidation of **14** pro-

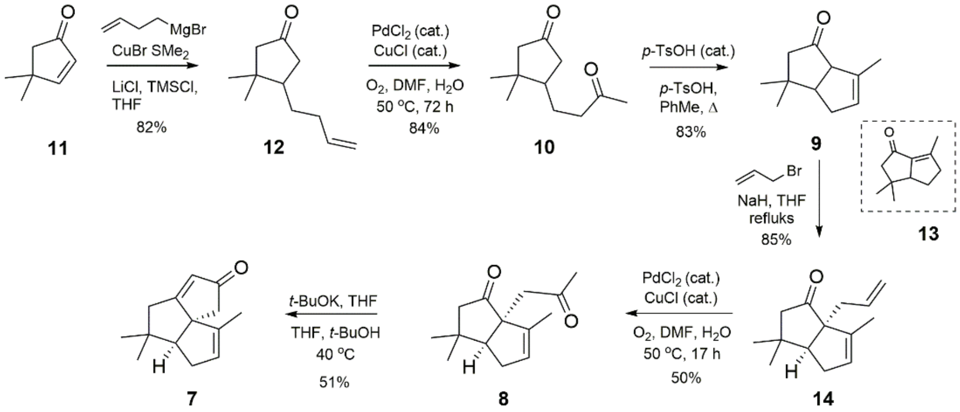

Scheme 2. Synthesis of triquinane **7**.

ceeded much faster than the previous one (*i.e.*, **12** → **10**), and provided bicyclic dione **8** in 50 % yield (accompanied with 10 % of aldehyde **15**). Upon the treatment with potassium *tert*-butoxide in *tert*-butanol, **8** cyclized into triquinane **7** (51 %), thus providing the target molecule in six steps (12 % overall yield) from the starting 4,4-dimethylcyclopent-2-ene-1-one (**11**).

The scope of sesquiterpene natural products targeted by this methodology is not limited to angular triquinanes, but extends to bridged diquinanes, *i.e.*, cedrenes. Thus, regioisomeric oxidation of intermediate **14** should provide aldehyde **15**, from which the assembly of cedrene skeleton would be accomplished by an intramolecular aldol reaction (Scheme 3). In this way, a single synthetic intermediate (*i.e.*, **14**) would provide access to several members of two distinct classes of quinane natural products.

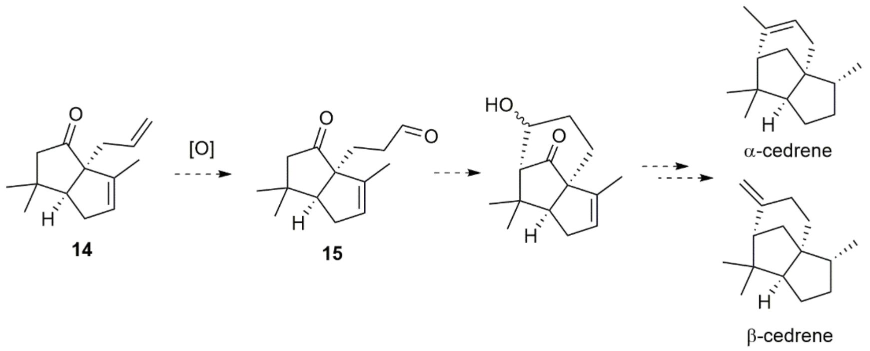

Scheme 3. Towards *α*- and *β*-cedrene.

CONCLUSION

To summarize, the efficient synthesis of the advanced intermediate **7** for the synthesis of triquinane sesquiterpenes (panaginsene, senoxydene and silphinene) is described, which relies on iterative application of the Wacker oxidation/aldol condensation tactical combination of reactions (*i.e.*, **12** → **9**; **14** → **7**). The research aiming to the conversion of this intermediate into the target natural products, as well as extension of this methodology to the synthesis of cedrenes (according to Scheme 3), is underway in our laboratories.

EXPERIMENTAL

General experimental details

All chromatographic separations were performed on silica gel 60 (0.063–0.2 mm), Merck. Standard techniques were used for the purification of reagents and solvents. NMR spectra were recorded on Varian/Agilent 400 (^{1}H-NMR at 400 MHz, ^{13}C-NMR at 100 MHz in deuterated chloroform, if not otherwise stated. Chemical shifts are expressed in ppm (*δ*) using tetramethylsilane as internal standard, coupling constants (*J*) are in Hz. IR spectra were recorded on Thermo Scientific Nicolet Summit FT-IR instrument, and are expressed in cm^{-1}. Mass spectra were obtained on Orbitrap Exploris 240 spectrometer.

The physical data and NMR spectra of the synthesized compounds are given in Supplementary material to this paper.

*4-(But-3-en-1-yl)-3,3-dimethylcyclopentan-1-one (**12**)*

To the solution of $CuBr \cdot SMe_2$ (9.7 g, 47 mmol, 2.16 eq) and LiCl (2 g, 47 mmol, 2.16 eq) in THF (50 mL) a solution of Grignard reagent prepared from magnesium turnings (1.42 g, 58.44 mmol) and 4-bromo-1-butene (6 g, 44.44 mmol) was added dropwise at –78 °C, and the reaction mixture was stirred for additional 30 min. A solution of ketone **11** (2.4 g, 21.8 mmol, 1 eq.) and TMSCl (7 mL, 5.98 g, 55 mmol, 2.52 eq.) in THF (51 mL) was added dropwise over 30 min. The reaction mixture was allowed to warm to room temperature overnight, quenched with acetic acid (22 mL) and stirred for 1.5 h. The mixture was transferred into a beaker and saturated solution of $NaHCO_3$ (160 mL) was added in portions. The mixture was filtered through Celite and extracted three times with methylene chloride. The combined organic layer was washed with brine, and dried over anh. $MgSO_4$, filtered, concentrated at rotovap and purified by dry-flash chromatography (petroleum ether/ethyl acetate = 7/1) to afford 2.96 g (82 %) of product **12** as a pale yellow oil.

*3,3-Dimethyl-4-(3-oxobutyl)cyclopentan-1-one (**10**)*

Ketone **12** (610 mg, 3.67 mmol, 1 eq) was added to the solution of $PdCl_2$ (40 mg, 0.225 mmol, 0.06 eq) and CuCl (150 mg, 1.51 mmol, 0.41 eq.) in DMF (2.8 mL) and H_2O (0.5 mL, 27.76 mmol, 7.56 eq.) under an O_2 atmosphere. The reaction mixture was stirred at 50 °C for 72 h, then diluted with water and extracted with Et_2O. Organic layer was washed with water and brine, dried over anh. $MgSO_4$, filtered, concentrated at rotovap and purified by dry-flash chromatography (petroleum ether/ethyl acetate = 7/1) to afford 561 mg (84 %) of product **10** as pale yellow oil.

*3,3,6-Trimethyl-3,3a,4,6a-tetrahydropentalen-1(2*H*)-one (**9**)*

$TsOH \cdot 2H_2O$ (55 mg, 0.29 mmol, 0.22 eq) was added to the solution of diketone **10** (240 mg, 1.32 mmol) in toluene (20 mL). The flask was equipped with Deak-Stark apparatus and the reaction mixture was refluxed for 5 h. The mixture was transferred into a separatory funnel, diluted with DCM, washed with saturated solution of $NaHCO_3$, dried over anh. $MgSO_4$, concentrated at rotovap and purified by dry-flash chromatography (petroleum ether/ethyl acetate = 95/5) to afford 182 mg (83 %) of product **9** (R_f = 0.32 (petroleum ether/ethyl acetate = = 95/5)) followed by 15 mg (9 %) of conjugated ketone **13** (R_f = 0.17 (petroleum ether/ethyl acetate = 95/5)).

*6*a*-Allyl-3,3,6-trimethyl-3,3*a*,4,6*a*-tetrahydropentalen-1(2*H*)-one (**14**)*

A solution of ketone **9** (200 mg, 1.22 mmol, 1 eq.) in THF (3 mL) was added to the suspension of NaH (73 mg (60 %), 1.83 mmol, 1.5 eq.) in THF (1 mL), the mixture was heated to reflux and stirred for 30 min when allyl bromide (0.21 mL, 2.43 mmol, 2 eq.) was added. After 4 h, more allyl bromide was added (0.21 mL, 2.43 mmol, 2 eq.) and refluxing was continued overnight. Reaction was quenched with water, acidified with few drops of 1.5 M HCl, extracted with DCM, washed with brine, dried over anh. $MgSO_4$, filtered, concentrated at rotovap and purified by dry-flash chromatography (petroleum ether/ethyl acetate = = 95/5) to afford 213 mg (85 %) of product **14** as colourless oil.

*3,3,6-Trimethyl-6a-(2-oxopropyl)-3,3a,4,6a-tetrahydropentalen-1(2H)-one (**8**)*

Ketone **14** (64 mg, 0.31 mmol, 1 eq.) was added to the solution of $PdCl_2$ (16.6 mg, 0.09 mmol, 0.3 eq.) and CuCl (40.3 mg, 0.41 mmol, 1.3 eq.) in DMF (0.7 mL) and H_2O (0.128 mL) under an O_2 atmosphere. The reaction mixture was stirred at 50 °C for 17 h, then diluted with water and extracted with Et_2O. Organic extract was washed with water and brine, dried over anh. $MgSO_4$, filtered, concentrated at rotovap and purified by column chromatography (hexane/ethyl cetate = 9/1) to afford 35 mg (51 %) of product **8** as colourless oil.

5,5,8-Trimethyl-4,5,5a,6-tetrahydrocyclopenta[c]pentalen-2(1H)-one (7)

The solution of diketone **8** (18 mg, 0.082 mmol, 1 eq.), *t*-BuOK (20 mg, 0.175 mmol, 2.14 eq.) and *t*-BuOH (0.1 mL) in THF (3.5 mL) was heated to 40 °C for 1 h. After cooling to room temperature, the reaction mixture was diluted with water and few drops of 1.5 M HCl, extracted with Et_2O, washed with saturated solution of $NaHCO_3$ and brine, dried over anh. $MgSO_4$, filtered, concentrated at rotovap and purified by column chromatography (petroleum ether/ethyl acetate = 5/1) to afford 8.5 mg (51 %) of product **7** as colourless oil.

SUPPLEMENTARY MATERIAL

Additional data and information are available electronically at the pages of journal website: https://www.shd-pub.org.rs/index.php/JSCS/article/view/12460, or from the corresponding author on request.

Acknowledgement. This research was supported by the Ministry of Science, Technological Development and Innovation of Republic of Serbia, Contract number: 451-03-47/ /2023-01/200168.

ИЗВОД

СИНТЕТИЧКА СТУДИЈА АНГУЛАРНИХ ТРИКИНАНА

МИХАИЛО Н. СТЈЕПАНОВИЋ[1], АЛЕКСАНДАР В. ЈАНКОВИЋ[2], БОЈАН З. ВУЛОВИЋ[1], РАДОМИР В. МАТОВИЋ[2] и РАДОМИР Н. САИЧИЋ[1,3]

[1]Универзитет у Београду – Хемијски Факултет, Студентски трг 16, 11158 Београд, [2]ИХТМ – Центар за Хемију, Његошева 12, 11158 Београд и [3]Српска академија наука и уметности, Кнеза Михаила 35, 11000 Београд

Представљена је синтеза ангуларног трикинана, који може послужити као кључни интермедијер за синтезу неколико природних производа (панагинсена, силфинена, сеноксидена). Ситеза се заснива на две узастопне анулације циклопентеновог прстена, код којих су алкени искоришћени као латентне карбонилне функционалне групе (преко Wacker реакције), а анулације циклопентенона су остварене алдолним кондензацијама.

(Примљено 28. јуна, ревидирано 1. јула, прихваћено 24. јула 2023)

REFERENCES

1. For review articles on triquinane synthesis, see: a) G. Mehta, A. Srikrishna, *Chem. Rev.* **97** (1997) 671 (https://doi.org/10.1021/cr9403650); b) L. A. Paquette, A. M. Doherty, *Polyquinane Chemistry*, 1st ed., Springer, Heidelberg, 1987 (https://doi.org/10.1007/978-3-642-72598-2); c) L. A. Paquette, De Gruyter, *Top. Curr. Chem.* **119** (1984) 1 (https://doi.org/doi:10.1515/9783112539286); d) L. A. Paquette, *Top. Curr. Chem.* **79** (1979) 41 (https://doi.org/10.1007/BFb0048476); e) M. B. Chanon R; Baralotto, C; Julliard, M; Hendrickson, J B, *Synthesis (Stuttg).* **11** (1998) 1559 (https://doi.org/10.1055/s-1998-2191); For a recent review article on the synthesis of

tetraquinanes, see: f) S. Kotha, A. Fatma, *Asian J. Org. Chem.* **11** (2022)e202100595 (https://doi.org/10.1002/ajoc.202100595)

2. a) A. Groweiss, W. Fenical, H. Cun-heng, J. Clardy, W. Zhongde, Y. Zhongnian, L. Kanghou, *Tetrahedron Lett*. **26** (1985) 2379–2382 (https://doi.org/10.1016/S0040-4039(00)94832-9); b) See also: V. Dragojlovic, *Molecules* **5** (2000) 674 (https://doi.org/10.3390/50400674)
3. B.-H. Chen, K.-F. Jiao, Q.-E. Ji, H.-Q. Song, *J. Mol. Struct. THEOCHEM* **188** (1989) 167 (https://doi.org/10.1016/0166-1280(89)85035-3)
4. X. Tan, H. Ye, L. Zeng, Z. Cui, S. He, *Zhongguo Haiyang Yaowu* **9** (1990) 11 (*Chemical Abstracts* 1991, 115: 35564g) [C.A 115/1991 35564g]
5. D. E. Cane, *Sesquiterpene Biosynthesis: Cyclization Mechanisms* in *Compr. Nat. Prod. Chem*., Sir D. Barton, K. Nakanishi, O. Meth-Cohn, Eds., Pergamon Press, Oxford, 1999, pp. 155–200 (https://doi.org/10.1016/B978-0-08-091283-7.00039-4)
6. a) I. R. George, M. López-Tena, A. P. Sundin, D. Strand, *Org. Lett.* **23** (2021) 3536 (https://doi.org/10.1021/acs.orglett.1c00955); b) T. Kobayashi, Y. Teshigahara, M. Sakakibara, K. Murakami, Y. Kawamoto, H. Ito, *Org. Lett*. **25** (2023) 4510 (https://doi.org/10.1021/acs.orglett.3c01530)
7. S. H. Shim, J. B. Gloer, D. T. Wicklow, *J. Nat. Prod.* **69** (2006) 1601 (https://doi.org/10.1021/np060327z)
8. R. Richter, S. Basar, A. Koch, W. A. König, *Phytochemistry* **66** (2005) 2708 (https://doi.org/10.1016/j.phytochem.2005.09.012)
9. S. Geum, H.-Y. Lee, *Org. Lett.* **16** (2014) 2466 (https://doi.org/10.1021/ol500849m)
10. T. Tsunoda, M. Kodama, S. Itô, *Tetrahedron Lett*. **24** (1983) 83 (https://doi.org/10.1016/S0040-4039(00)81333-7)
11. L. A. Paquette, A. Leone-Bay, *J. Am. Chem. Soc.* **105** (1983) 7352 (https://doi.org/10.1021/ja00363a024)
12. D. D. Sternbach, J. W. Hughes, D. F. Burdi, B. A. Banks, *J. Am. Chem. Soc*. **107** (1985) 2149 (https://doi.org/10.1021/ja00293a053)
13. P. A. Wender, R. J. Ternansky, *Tetrahedron Lett*. **26** (1985), 2625 (https://doi.org/10.1016/S0040-4039(00)98120-6)
14. a) M. T. Crimmins, S. W. Mascarella, *J. Am. Chem. Soc.* **108** (1986) 3435 (https://doi.org/10.1021/ja00272a044); b) M. T. Crimmins, S. W. Mascarella, *Tetrahedron Lett*. **28** (1987) 5063 (https://doi.org/10.1016/S0040-4039(00)95590-4)
15. Y. K. Rao, M. Nagarajan, *Tetrahedron Lett*. **29** (1988) 107 (https://doi.org/10.1016/0040-4039(88)80029-7)
16. Y. Shizuri, M. Ohkubo, S. Yamamura, *Tetrahedron Lett*. **30** (1989) 3797 (https://doi.org/10.1016/S0040-4039(01)80658-4)
17. M. Franck-Neumann, M. Miesch, L. Gross, *Tetrahedron Lett*. **32** (1991) 2135 (https://doi.org/10.1016/S0040-4039(00)71256-1)
18. J. K. Dickson, Jr., B. Fraser-Ried, *J. Chem. Soc. Chem. Commun*. (1990) 1440 (https://doi.org/10.1039/C39900001440)
19. V. K. Singh, T. K. Chakraborty, *Chem. Asian J.* **16** (2021) 753 (https://doi.org/10.1002/asia.202100144)
20. a) L. A. Paquette, R. A. J. Galemmo, J. P. Springer, *J. Am. Chem. Soc.* **105** (1983) 6975 (https://doi.org/10.1021/ja00361a046); b) L. A. Paquette, R. A. Galemmo Jr, J. C. Caille, R. S. Valpey, *J. Org. Chem.* **51** (1986) 686 (https://doi.org/10.1021/jo00355a019)
21. T. Tsunoda, Y. Kabasawa, S. Itô, M. Kodama, *Tetrahedron Lett.* **25** (1984) 773 (https://doi.org/10.1016/S0040-4039(01)80023-X)

22. a) P. D. Magnus, M. S. Nobbs, *Synth. Commun.* **10** (1980) 273 (https://doi.org/10.1080/00397918008062750) ; b) D. Pauley, F. Anderson, T. Hudlicky, *Org. Synth.* **67** (1989) 121 (https://doi.org/10.15227/orgsyn.067.0121) ; c) J. Yang, Y. O. Long, L. A. Paquette, *J. Am. Chem. Soc.* **125** (2003) 1567 (https://doi.org/10.1021/ja021177r)
23. J. Richers, A. Pöthig, E. Herdtweck, C. Sippel, F. Hausch, K. Tiefenbacher, *Chem. Eur. J.* **23** (2017) 3178 (https://doi.org/10.1002/chem.201605362).

Journal of the Serbian Chemical Society
JSCS@tmf.bg.ac.rs • www.shd.org.rs/JSCS
J. Serb. Chem. Soc. 88 (10) S299–S306 (2023)
Supplementary material

SUPPLEMENTARY MATERIAL TO

Synthetic study on the angular triquinanes

MIHAILO N. STJEPANOVIĆ[1], ALEKSANDAR V. JANKOVIĆ[2], BOJAN Z. VULOVIĆ[1], RADOMIR V. MATOVIĆ[2] and RADOMIR N. SAIČIĆ[1,3]*

[1]*University of Belgrade – Faculty of Chemistry, Studentski trg 16, 11158 Belgrade, Serbia,* [2]*ICTM – Center for Chemistry, Njegoseva 12, 11158 Belgrade, Serbia and* [3]*Serbian Academy of Sciences and Arts, Kneza Mihaila 35, 11000 Belgrade, Serbia*

J. Serb. Chem. Soc. 88 (10) (2023) 975–983

TABLE OF CONTENTS

1. PHYSICAL DATA

*1.1. 5,5,8-Trimethyl-4,5,5a,6-tetrahydrocyclopenta[c]pentalen-2(1H)-one (**7**):*

^{1}H NMR (400 MHz, $CDCl_3$) δ 5.96 (s, 1H), 5.42 (s, 1H), 2.53 - 2.43 (m, 1H), 2.42 (s, 3H), 2.42 (s, 2H), 2.01 (dd, J_1 = 7.8 Hz, J_2 = 1.6 Hz, 1H), 1.43 – 1.41 (m, 3H), 1.11 (s, 3H), 0.91 (s, 3H). **^{13}C NMR** (100 MHz, $CDCl_3$) δ 210.5, 188.8, 140.9, 126.8, 125.3, 70.0, 56.0, 48.2, 43.2, 33.5, 32.5, 26.6, 11.4. **IR** (ATR) ν_{max}: 3404, 3038, 2956, 2924, 2860, 1710, 1636, 1441, 1410, 1382, 1365, 1167, 1018, 826, 802. **HRMS** (m/z) $[M+H]^+$ calcd. for $C_{14}H_{18}O$: 203.14304, found: 203.14204.

---

* Corresponding author. E-mail: rsaicic@chem.bg.ac.rs

*1.2. 3,3,6-Trimethyl-6a-(2-oxopropyl)-3,3a,4,6a-tetrahydropentalen-1(2H)-one (**8**):*

^{1}H NMR (400 MHz, $CDCl_3$) δ 5.40 (s, 1H), 2.90 (d, J = 17.6 Hz, 1H), 2.67 (d, J = 17.6 Hz, 1H), 2.58 (dd, J_1 = 7.30 Hz, J_2 = 2.25 Hz, 1H), 2.47 (d, J = 17 Hz, 1H), 2.41 – 2.31 (m, 2H), 2.19 (d, J = 17 Hz), 2.08 (s, 3H), 1.61 (s, 3H), 1.12 (s, 3H), 0.93 (s, 3H). **^{13}C NMR** (100 MHz, $CDCl_3$) δ 218.8, 207.1, 140.0, 128.3, 66.4, 53.9, 53.0, 47.7, 36.1, 32.0, 30.7, 30.7, 25.1, 12.5. **IR** (ATR) ν_{max}: 3037, 2957, 2867, 1732, 1444, 1387, 1360, 1274, 1274, 1214, 1160, 795, 569. **HRMS** (m/z) $[M+H]^+$ calcd. for $C_{14}H_{20}O_2$: 221.15361, found: 221.15257.

*1.3. 3,3,6-Trimethyl-3,3a,4,6a-tetrahydropentalen-1(2H)-one (**9**):*

^{1}H NMR (400 MHz, $CDCl_3$) δ 5.37 – 5.33 (m, 1H), 3.11 (d, J = 8.30 Hz, 1H), 2.76 – 2.69 (m, 1H), 2.49 – 2.33 (m, 2H), 2.23 (d, J = 16.65 Hz, 1H), 1.98 (dt, J_1 = 16.65 Hz, J_2 = 1.25 Hz, 1H), 1.76 (s, 3H), 1.08 (s, 3H), 1.04 (s, 3H). **^{13}C NMR** (100 MHz, $CDCl_3$) δ 217.2, 136.9, 127.0, 62.7, 51.9, 51.0, 37.0, 34.0, 30.4, 24.4, 15.3. **IR** (ATR) ν_{max}: 3039, 2956, 2928, 2867, 1736, 1453, 1410, 1370, 1287, 1261, 1219, 1180, 1154, 1124, 1018, 964, 802. **HRMS** (m/z) $[M+H]^+$ calcd. for $C_{11}H_{16}O$: 165.12739, found: 165.12660.

*1.4. 3,3-Dimethyl-4-(3-oxobutyl)cyclopentan-1-one (**10**):*

^{1}H NMR (400 MHz, $CDCl_3$) δ 2.52 – 2.34 (m, 3H), 2.15 (s, 3H), 2.12 (s, 2H), 1.96 – 1.80 (m, 3H), 1.45 – 1.35 (m, 1H), 1.17 (s, 3H), 0.91 (s, 3H). **^{13}C NMR** (100 MHz, $CDCl_3$) δ 217.8, 208.4, 55.5, 46.0, 42.8, 42.6, 38.8, 30.1, 27.5, 23.5, 21.7. **IR** (ATR) ν_{max}: 3467, 2956, 2871, 1741, 1716, 1464, 1406, 1368, 1273, 1219, 1183, 1164, 1164, 530. **HRMS** (m/z) $[M+H]^+$ calcd. for $C_{11}H_{18}O_2$: 183.13796, found: 183.13705.

*1.5. 4-(But-3-en-1-yl)-3,3-dimethylcyclopentan-1-one (**12**):*

^{1}H NMR (400 MHz, $CDCl_3$) δ 5.85 – 5.75 (ddt, J_1 = 17.05 Hz, J_2 = 10.22 Hz, J_3 = 6.50 Hz, 1H), 5.05 – 5.00 (dd, J_1 = 17.16 Hz, J_2 = 1.50 Hz, 1H), 4.99 – 4.96 (dd, J_1 = 10.18 Hz, J_2 = 0.7 Hz, 1H), 2.49 – 2.38 (m, 1H), 2.18 – 2.09 (m, 1H), 2.11 (s, 2H), 2.04 – 1.88 (m, 3H), 1.70 – 1.63 (m, 1H), 1.31 – 1.22 (m, 1H), 1.15 (s, 3H), 0.89 (s, 3H). **^{13}C NMR** (100 MHz, $CDCl_3$) δ 218.6, 138.5, 115.0, 55.6, 45.9, 42.8, 38.7, 33.0, 28.9, 27.5, 21.8.

*1.6. 6a-Allyl-3,3,6-trimethyl-3,3a,4,6a-tetrahydropentalen-1(2H)-one (**14**):*

^{1}H NMR (400 MHz, $CDCl_3$) δ 5.65 – 5.55 (m, 1H), 5.39 (s, 1H), 5.10 – 5.02 (m, 2H), 2.61 (dd, J_1 = 14.25 Hz, J_2 = 6.50 Hz, 1H), 2.45- 2.42 (m, 1H), 2.39 – 2.35 (m, 1H), 2.28 (d, J = 16.10, 1H), 2.13 (dd, J_1 = 14.20 Hz, J_2 = 7.90 Hz, 1H), 2.01 (d, J = 16.10 Hz, 1H), 1.64 – 1.62 (m, 3H), 1.06 (s, 3H), 1.00 (s, 3H). **^{13}C NMR** (100 MHz, $CDCl_3$) δ 218.3, 139.5, 134.4, 128.1, 117.8, 68.9, 53.6, 52.4, 38.5, 36.2, 32.8, 30.5, 24.7, 12.5. **IR** (ATR) ν_{max}: 3076, 3037, 2959, 2926, 2858, 1731, 1640, 1440, 1413, 1380, 1369, 1161, 993, 914, 805. **HRMS** (m/z) $[M+H]^+$ calcd. for $C_{14}H_{20}O$: 205.15869, found: 205.15773.

2. COPIES OF ^{1}H AND ^{13}C NMR SPECTRA FOR SYNTHESIZED COMPOUNDS

*2.1. 5,5,8-Trimethyl-4,5,5a,6-tetrahydrocyclopenta[c]pentalen-2(1H)-one (**7**):*

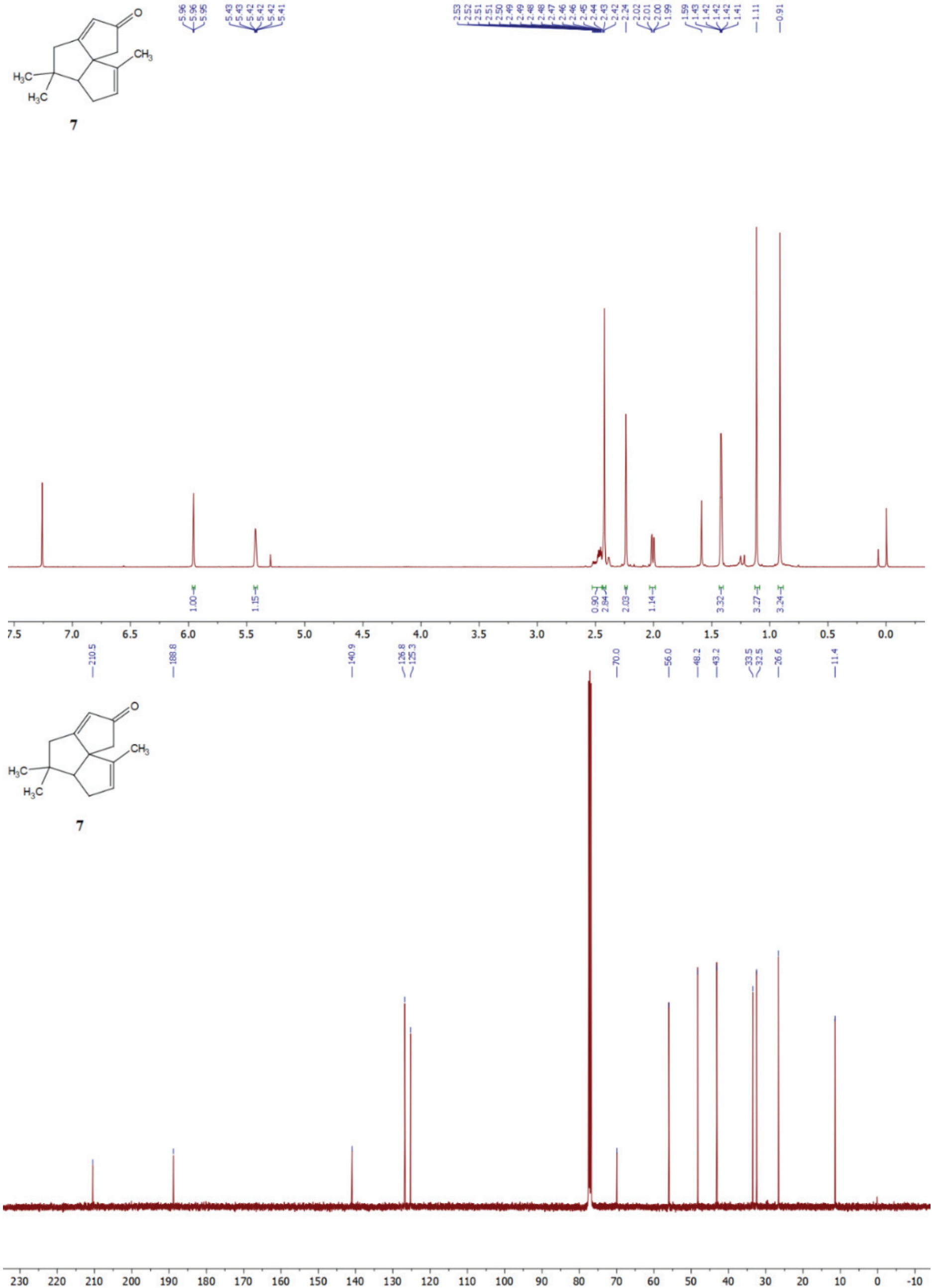

Fig. S1 – ^{1}H and ^{13}C NMR spectra of 5,5,8-trimethyl-4,5,5a,6-tetrahydrocyclopenta[c]pentalen-2(1*H*)-one (**7**)

*2.2. 3,3,6-Trimethyl-6a-(2-oxopropyl)-3,3a,4,6a-tetrahydropentalen-1(2H)-one (**8**):*

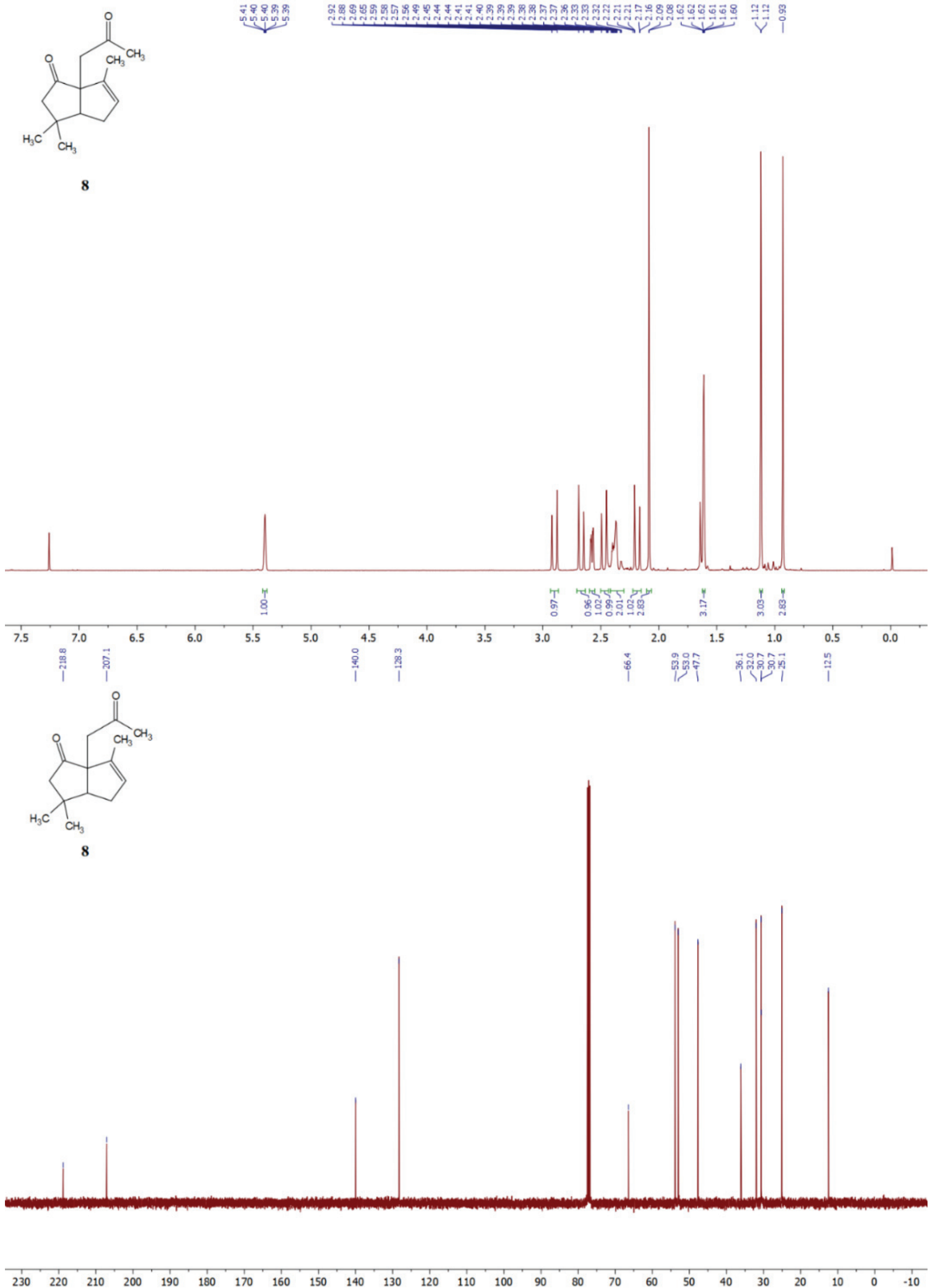

Fig. S2 – ^{1}H and ^{13}C NMR spectra of 3,3,6-trimethyl-6a-(2-oxopropyl)-3,3a,4,6a-tetrahydropentalen-1(2*H*)-one (**8**)

*2.3. 3,3,6-Trimethyl-3,3a,4,6a-tetrahydropentalen-1(2H)-one (**9**):*

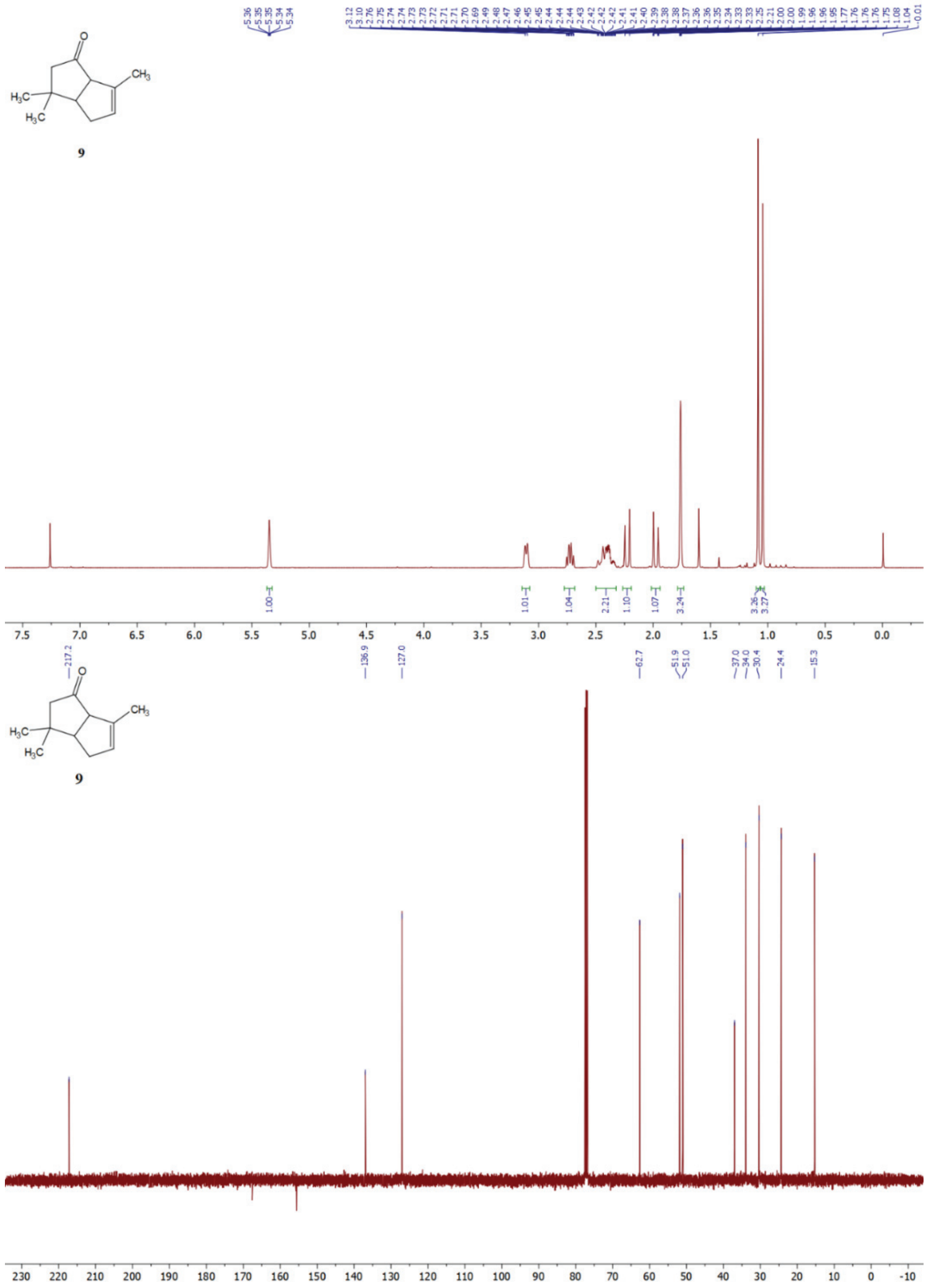

Fig. S3 – ^{1}H and ^{13}C NMR spectra of 3,3,6-trimethyl-3,3a,4,6a-tetrahydropentalen-1(2*H*)-one (**9**)

*2.4. 3,3-Dimethyl-4-(3-oxobutyl)cyclopentan-1-one (**10**):*

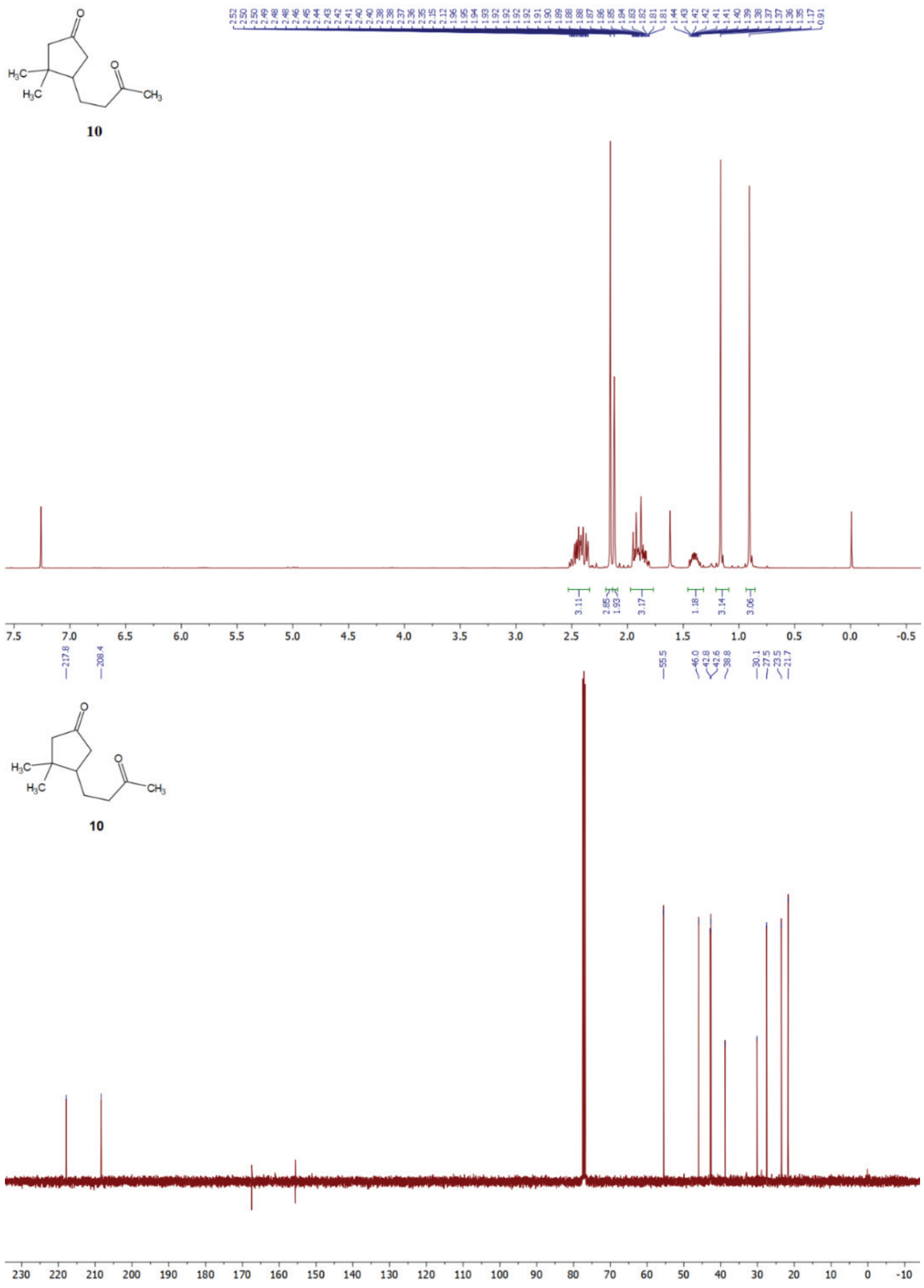

Fig. S4 – ^{1}H and ^{13}C NMR spectra of 3,3-dimethyl-4-(3-oxobutyl)cyclopentan-1-one (**10**)

*2.5. 4-(But-3-en-1-yl)-3,3-dimethylcyclopentan-1-one (**12**):*

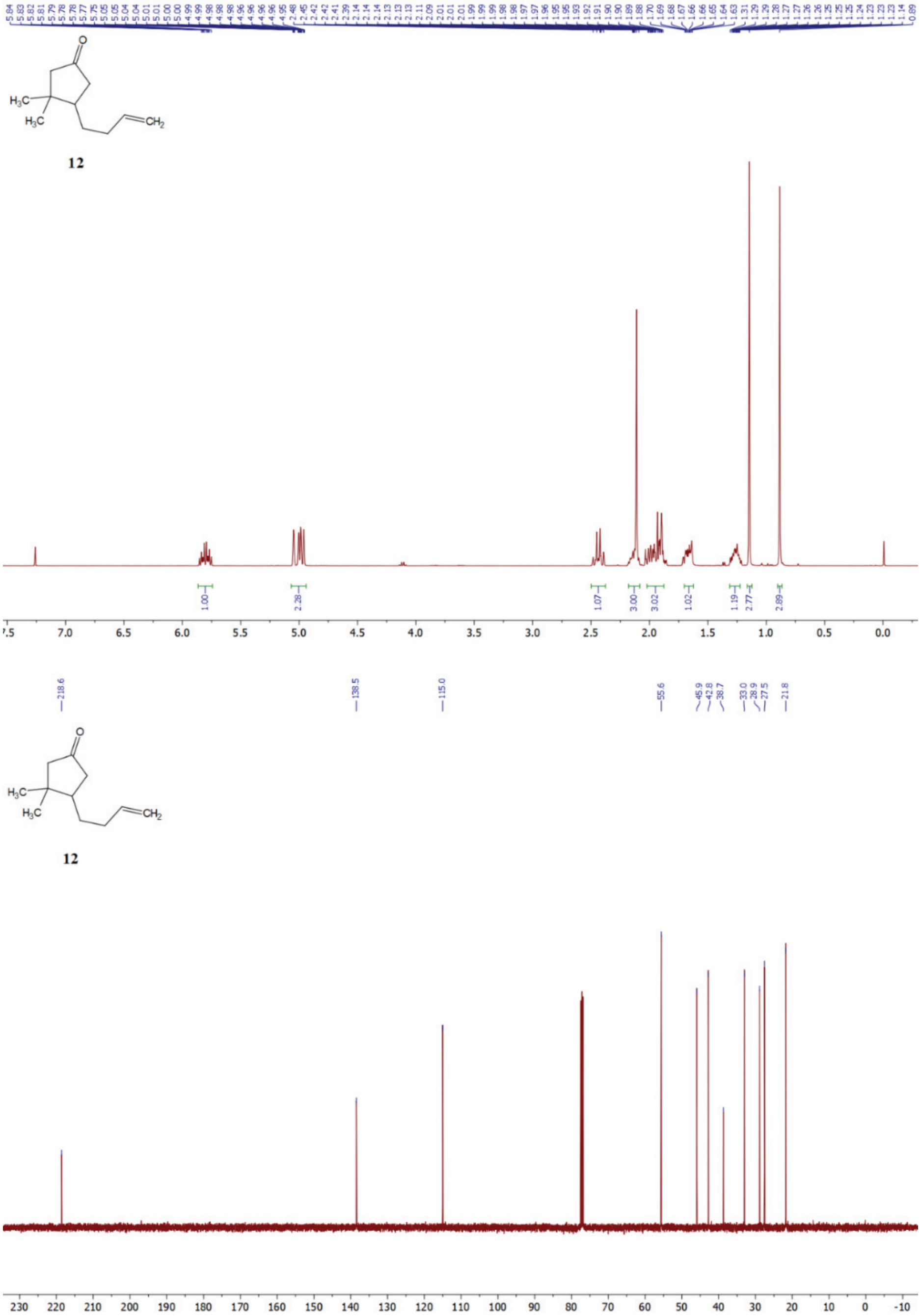

Fig. S5 – ^{1}H and ^{13}C NMR spectra of 4-(but-3-en-1-yl)-3,3-dimethylcyclopentan-1-one (**12**)

*2.6. 6a-Allyl-3,3,6-trimethyl-3,3a,4,6a-tetrahydropentalen-1(2H)-one (**14**):0*

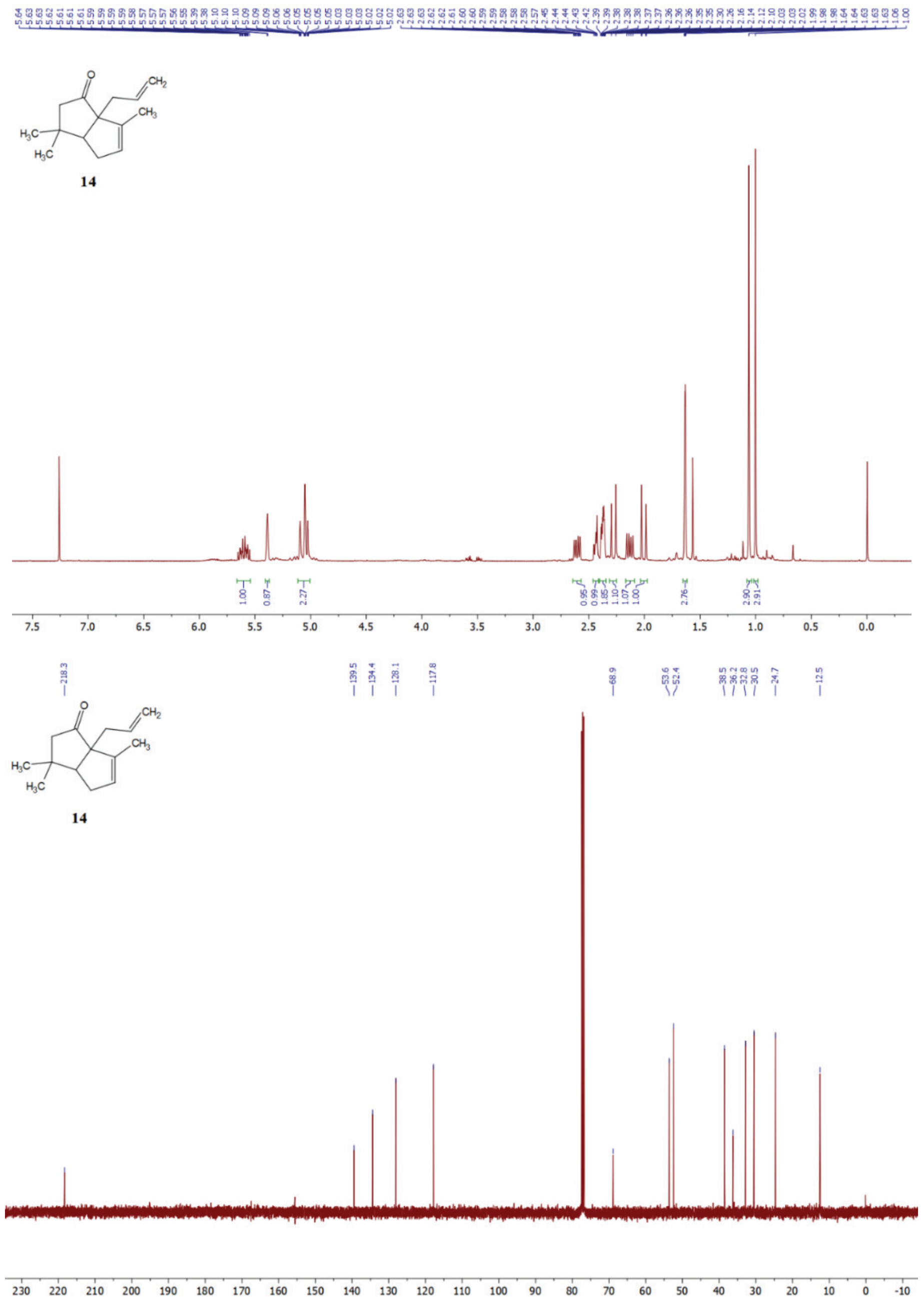

Fig. S6 – ^{1}H and ^{13}C NMR spectra of 6a-allyl-3,3,6-trimethyl-3,3a,4,6a-tetrahydropentalen-1(2*H*)-one (**14**).

Journal of the Serbian Chemical Society

JSCS@tmf.bg.ac.rs • www.shd.org.rs/JSCS

J. Serb. Chem. Soc. *88* (10) 985–997 (2023)
JSCS–5675

Original scientific paper
Published 25 October 2023

A novel PGA/TiO_2 nanocomposite prepared with poly(γ-glutamic acid) from the newly isolated *Bacillus subtilis* 17B strain

MARINELA ŠOKARDA SLAVIĆ[1]*§, VANJA RALIĆ[2]§, BRANISLAV NASTASIJEVIĆ[3], MILICA MATIJEVIĆ[2], ZORAN VUJČIĆ[4] and ALEKSANDRA MARGETIĆ[1]#

[1]University of Belgrade – Institute of Chemistry, Technology and Metallurgy – National Institute of the Republic of Serbia, Department of Chemistry, Belgrade, Serbia, [2]Center for light-based research and technologies, COHERENCE, Department of Atomic Physics, Vinča Institute of Nuclear Sciences, National Institute of the Republic of Serbia, University of Belgrade, Belgrade, Serbia, [3]Vinča Institute of Nuclear Sciences, National Institute of the Republic of Serbia, University of Belgrade, Belgrade, Serbia and [4]University of Belgrade – Faculty of Chemistry, Department of Biochemistry, Belgrade, Serbia

(Received 16 November 2022, revised 23 January, accepted 3 March 2023)

Abstract: Poly(γ-glutamic acid) (PGA), naturally produced by *Bacillus* species, is a biodegradable, non-toxic, biocompatible and non-immunogenic negatively charged polymer. Due to its properties, it has found various applications in the food, cosmetic and pharmaceutical industries. In this work, *Bacillus subtilis* 17B was selected as the best PGA producer among fifty wild-types *Bacillus* strains tested and characterized as a glutamate-independent producer. The production of PGA by the newly identified strain was optimized and increased tenfold using the Box–Behnken experimental design. The purity of PGA after recovery and purification from the fermentation broth was confirmed by SDS-PAGE followed by methylene blue staining. PGA was characterized by ESI MS and used for the preparation of a new nanocomposite with TiO_2. The synthesis of PGA/TiO_2 nanocomposite, its structural analysis, and cytotoxic effect on the cervical cancer cell line (HeLa cell) was investigated to determine the potential anti-cancer usage of this newly prepared material. It is encouraging that PGA/TiO_2 nanocomposite showed an increased cytotoxic effect compared to TiO_2 alone.

Keywords: PGA production; wild-type *Bacillus* strain; PGA characterization; cytotoxicity.

---

* Corresponding author. E-mail: marinela.sokarda@ihtm.bg.ac.rs

\# Serbian Chemical Society member.

§ Authors contributed equally to this work.

https://doi.org/10.2298/JSC221116011S

INTRODUCTION

Polyglutamic acid (PGA) is a biodegradable naturally occurring biopolymer that consists of L- and D-glutamic acid. PGA is a negatively charged water-soluble polymer. Unlike amino acids in polypeptides, glutamic acid monomers in PGA create amide bonds between α-amino and γ-carboxyl groups.[1] PGA was first discovered in 1937. as a major component of the *B. anthracis* capsule.[2] Owing to its biodegradability, PGA has various current and potential applications such as: drug carrier, anti-cancer drug delivery treatment of rheumatoid arthritis, genes, protein and peptide delivery, water treatment polluted by heavy metal and basic dye adsorber, thickener and bitterness relieving agent, cryoprotectant, *etc*.[3] PGA proved to be an efficient drug delivery matrix as a nontoxic, biodegradable, biocompatible and non-immunogenic polymeric material for water-soluble and insoluble drugs and other molecules as nanoparticles.[3] Negatively charged serum proteins and erythrocytes were reported to not aggregate with anionic polymeric carriers (*e.g*., PGA), which overcame serum inhibitory effects.[4] It is also known that polymeric nanoparticles can collect specifically in cancer tissues,[5] making them effective anticancer drug carriers. Studies of titanium dioxide nanoparticles and their various organic compound hybrid materials are becoming increasingly important due to their potential use in novel medical therapies. Furthermore, to improve efficient anticancer and antimicrobial therapies, many other approaches utilizing TiO_2 have been tested.[6] The importance of the development of new formulations is also indicated by the fact that increasing the therapeutic efficiency of TiO_2 can be achieved by using nanocomposites.

Currently, the majority of commercial γ-PGA is made by cost-effective microbial fermentation from biomass instead of chemical synthesis, peptide synthesis or biotransformation. Polyglutamic acid is mainly produced by bacteria of the genus *Bacillus*. Most common species include *B. licheniformis*, *B. subtilis*, *B. megaterium*, *B. pumilis*, *B. mojavensis* and *B. amyloliquefaciens*.[1] A few unusual PGA producers include the halophilic archaebacterium *Natrialba aegyptiaca*[7] and the Gram-negative bacterium *Fusobacterium nucleatum.*[8] These microorganisms produce PGA as an extracellular viscous material during fermentation that can then be isolated and purified.[9]

Bacillus species are widely used industrial organisms due to their high growth rates, short fermentation cycle times and relatively inexpensive nutritional requirements.[10] The types and characteristics of a PGA-producing bacterial strain dictate the medium composition. Firstly, all PGA-producing bacteria can be divided into glutamic acid-dependent and independent.[11] Glutamic acid-dependent strains require the presence of L-glutamic acid in the fermentation broth, usually, in the range of 20–30 g L^{-1}.[12] For successful PGA production, it is necessary to take into account the individual but also synergistic impact of the above factors for the design of bacterial growth and production medium. According to the literature, the DoE approach has successfully been used for carbon and nitrogen source selection for PGA production.[13] To find optimal production conditions, it is necessary to use a statistical method that takes into account the analysis of the synergistic effect of at least three important factors, such as Box–Behnken design (BBD). There are examples in the literature where a high level of production of a significant product was obtained by using BBD to optimize the microbiological process.[14]

As the possibility of preparation of PGA/TiO$_2$ nanocomposite and the potential of its anticancer activity has not been investigated so far, this was set as the goal of this work.

In this study, the best PGA producer, among 50 different natural *Bacillus* isolates originating from the soil and different locations in Serbia, was selected and identified. In order to achieve the highest level of PGA production influence of carbon source was analyzed using the DoE approach (BBD) where concentrations of glucose, glycerol and glutamate were varied. Purified PGA was used for the preparation of nanocomposite with TiO$_2$. Both, PGA and PGA/TiO$_2$ were structurally characterized by ESI MS, whereas PGA/TiO$_2$ cytotoxicity was examined using cervical cancer (HeLa) cells.

EXPERIMENTAL

Chemicals

Unless otherwise stated, all reagents and solvents were purchased from Merck and Sigma–Aldrich. All chemicals were of the best available purity and used without further purification.

Screening of γ-PGA producers

PGA production was investigated in 50 isolated wild-type strains of *Bacillus* sp. An overnight culture of each strain was prepared by incubation of a single colony in 5 mL of sterilized Luria–Bertani (LB) medium and grown for 18 h at 37 °C and 150 rpm. The screening medium was prepared according to the medium most commonly used for PGA production and contains per liter:[15] glucose, 100 g; sodium glutamate, 0.5 g; citric acid, 0.5 g; NH_4Cl, 10 g, KH_2PO_4, 0.34 g; $Na_2HPO_4 \cdot 12H_2O$, 0.895 g; $MgSO_4 \cdot 7H_2O$, 0.5 g; $FeCl_3 \cdot 6H_2O$, 0.04 g; $CaCl_2 \cdot 2H_2O$, 0.15 g; $MnCl_2 \cdot 4H_2O$, 0.26 g. The fermentation broth was prepared by mixing 2 mL of an overnight culture of each strain with 48 mL of the screening medium. Fermentation was carried out for 5 days at 37 °C and 150 rpm. The best producer strain was selected and used in further experiments.

Identification of selected strain

The selected *Bacillus* 17B strain was identified by 16S rRNA gene sequence analysis. Total DNA from *Bacillus* 17B strain was isolated using the phenol-chloroform extraction method previously described by Hopwood and co-authors with minor modifications.[16] Logarithmic phase cells were treated with lysozyme (4 mg mL^{-1}, for 15 min at 37 °C) prior to treatment with 2 % SDS. The 16S rRNA gene was amplified using 27F (5'-AGA GTT TGA TCC TGG CTC AG-3') and 1492R (5'-GGT TAC CTT GTT ACG ACT T-3') universal primers.[17] The amplified PCR fragment was sequenced by a Macrogen sequencing service

(Macrogen Europe, Amsterdam, Netherlands). Sequence annotation and a database search for sequence similarities were completed using the BLAST program of the National Center for Biotechnology Information – NCBI.[18]

Optimization of PGA production media

Box–Behnken design (BBD) was used to identify optimal concentrations of three different carbon sources using Design-Expert software (version 11, Stat-Ease, Inc., Minneapolis, MN, USA). Three analyzed factors were glucose (A), glycerol (B) and glutamate (C). The evaluated response Y was the level of γ-PGA production (g L^{-1}). All three factors (A, B and C) were studied at three different levels (concentrations, Table S-I of the Supplementary material to this paper) through sets of 14 experiments (Table S-II of the Supplementary material). The other components of the medium were constant (citric acid, 0.5 g; NH_4Cl, 10 g, KH_2PO_4, 0.34 g; $Na_2HPO_4 \cdot 12H_2O$, 0.895 g; $MgSO_4 \cdot 7H_2O$, 0.5 g; $FeCl_3 \cdot 6H_2O$, 0.04 g; $CaCl_2 \cdot 2H_2O$, 0.15 g; $MnCl_2 \cdot 4H_2O$, 0.26 g). The fermentation broth was prepared by mixing 2 mL of an overnight culture with 48 mL of medium. Production fermentations were carried out for 5 days at 37 °C and 150 rpm in a thermostat shaker (KS 4000i, IKA).

The experimental data of the BBD was represented in the general form of the two-factor interaction (2FI) model as shown in Eq. (1), to develop an empirical model which will be used to analyze the effect of factor interactions.

$$y = \beta_0 + \sum_{i=1}^{q} \beta_i x_i + \sum_{1 \le i \le j}^{q} \beta_{ij} x_i x_j + \varepsilon \tag{1}$$

where y is the predicted response (PGA yield), β_0 is a constant coefficient, q is the number of variables, β_i is the linear coefficient, β_{ij} represents the interaction coefficient and x_i and x_j are the process variables and ε is the residual. Analysis of variance (ANOVA) was used to assess the significance of the model and the impact of coefficients in regression analysis.

Isolation of γ-PGA from the culture broth

The culture broth was centrifuged at 10000*g* for 20 min at 25 °C. The supernatant was adjusted to pH 3 using 1 M H_2SO_4 and stored at 4 °C for 12 h. The precipitate was removed by centrifugation at 10000*g* for 20 min at 25 °C. The resulting supernatant was mixed with ice-cold ethanol in a volume ratio of 1:3. The PGA precipitate formed was separated after centrifugation at 5000*g* for 20 min at 4 °C. The obtained PGA precipitate was dissolved in distilled water and purified using a Sephadex G-25 column. The remaining proteins in the PGA solution were hydrolyzed with 50 µg mL^{-1} Proteinase K,[19] and the resulting mixture was ultrafiltered through a Microcon membrane with a 30 kDa cut-off to protein hydrolysis products. The retentate (PGA) was air-dried and used for further analysis.

To confirm the purity of the isolated PGA, SDS PAGE was performed using a Hoefer™ Mighty Small™ II Mini Vertical Electrophoresis System with a 10 % polyacrylamide gel.[20] The gel was stained by the modified method of Yamaguchi *et al.*[21] To verify the presence of proteins, the gel was first stained with Coomassie brilliant blue (G-250) and rinsed with 7 % acetic acid/5 % ethanol. After a short rinse with distilled water, PGA in the gel was stained with 0.5 % methylene blue dissolved in 3 % acetic acid. The gel was rinsed with distilled water.

Fourier-transform infrared spectroscopy

Fourier-transform infrared spectroscopy (FTIR) of PGA and TiO_2 was done using Thermo Electron Corporation Nicolet 380 spectrometer in attenuated total reflection (ATR) mode. Spectra resolution was 4 cm^{-1} in the range of 4000–400 cm^{-1}.

Electrospray ionization mass spectrometry

An isolated polymer of glutamic acid and acidic hydrolyzed PGA was analyzed by electrospray ionization mass spectrometry (ESI MS) on a Waters Quattro micro API mass spectrometer. All samples were previously diluted with 0.1 % water solution of formic acid to the concentration of 0.1 mg mL^{-1}, whereas the hydrolysate was diluted 1000 times, to avoid the influence of the high concentration of HCl used for its hydrolysis.

PGA was hydrolyzed by using a microwave digestor (Milestone START D, SK-10T) in the presence of 6 M HCl. The process was performed according to the manufacturer´s instructions and it was finished within 20 min.

The spectra acquisition was done in the positive ion mode in the mass range from 50 to 4000 Da. The temperature of the ionization source was 125 °C, of a gas carrier 380 °C, the capillary voltage was 3 kV, whereas the conus voltage was in the range from 20 to 90 V, depending on the sample.

PGA/TiO$_2$ nanocomposite

Formation and characterization of nanocomposite. Colloidal spherical TiO$_2$ nanoparticles (average diameter, *d* of 5 nm) were synthesized by the modified method of Rajh *et al.*[22] Nanoparticle concentration was determined after dissolving the particles in concentrated H$_2$SO$_4$ by the concentration of the peroxide complex, as previously described.[23]

PGA and TiO$_2$ were mixed in different ratios (present in Table S-III of the Supplementary material) and incubated for 2 h at 25 °C with agitation at 150 rpm.[24] A formed white PGA/TiO$_2$ nanocomposite (NC) precipitate was recovered by centrifugation at 10000*g* for 30 min and air-drying.

Cytotoxic effect of nanocomposite. HeLa cells were cultured in Dulbecco's modified eagle's medium supplemented with glucose, L-glutamine, fetal bovine serum, penicillin and streptomycin solution, according to the supplier's instructions. Cells were seeded in flat-bottomed 96-well microtiter plates (2000 per well) and incubated overnight with varying concentrations of PGA, TiO$_2$ nanoparticles and an NC. Samples were prepared in distilled water and incubation terminated after 48 h. Cell viability was determined using the sulphorhodamine B (SRB) assay.[25] The absorbance was measured at 550 nm with a reference wavelength of 690 nm in a microplate reader (Wallac, VICTOR2 1420 Multilabel counter, PerkinElmer, Turku, Finland). The results were presented as a percent of cell viability determined according to the following equation:

$$\text{Cell viability}\left(\%\right)=100\frac{\text{Absorbance of sample}}{\text{Absorbance of control}} \tag{2}$$

The measurements were made in quintuplicate and the results were presented as the mean ± standard deviation.

RESULTS AND DISCUSSION

PGA producer screening

PGA is an extracellular polymer produced by certain *Bacillus* species including *Bacillus paralicheniformis* ATCC 9945a,[26] which was used as a standard PGA producer strain for comparisons with wild-type isolates. The PGA-producing ability of 50 different *Bacillus* sp. strains originating from Serbia, deposited in a laboratory bank UB483, was investigated. Screened *Bacillus* isolates produced PGA in the range of 0.40 to 4.07 mg mL^{-1}. The strain indicated as 17B exhibited the highest yield of PGA (4.07 mg mL^{-1}), higher even than *B. paralicheniformis* ATCC 9945a (2.27 mg mL^{-1}) under the conditions used for fast selection of strains. Selected isolate (17B) was identified as *B. subtilis* according to the highest identity (99 %) with the 16S rRNA gene of the species *Bacillus subtilis* from the NCBI database. Strain *B. subtilis* 17B was selected for medium optimization, as it showed the highest PGA-producing capabilities.

Optimization of culturing conditions for PGA production

The Box–Behnken experimental design was set using the concentrations of carbon sources (glucose, glutamate and glycerol) as variables and PGA yield was measured as a response (Table I). Response surface methodology (RSM) was used to determine the synergistic effect of glucose, glycerol and glutamate concentrations on PGA yield, and the results are given in Table I.

TABLE I. Box–Behnken experimental design PGA yield

Run	c_{glucose} /g L^{-1} (A)	c_{glycerol} /g L^{-1} (B)	$c_{\text{glutamate}}$ /g L^{-1} (C)	Yield$_{\text{PGA}}$, mgmL^{-1} (y)	
				Actual value[a]	Predicted value
1	10	0	2.75	13.9	13.7
2	80	0	2.75	28.0	28.3
3	10	50	2.75	38.6	37.0
4	80	50	2.75	34.0	32.9
5	10	25	0.5	18.8	23.6
6	80	25	0.5	28.4	32.6
7	10	25	5	28.0	27.1
8	80	25	5	30.0	28.6
9	45	0	0.5	20.6	17.7
10	45	50	0.5	40.0	38.5
11	45	0	5	21.6	24.3
12	45	50	5	27.3	31.4
13	45	25	2.75	37.4	27.9
14	45	25	2.75	25.2	27.9

[a]All data are significantly different from each other according to Tukey's test ($p < 0.05$)

The regression analysis has produced a two-factor interaction (2FI) model that describes PGA yield as a function of independent variables and their interactions in terms of coded factors:

$$\begin{aligned}\text{PGA yield}\left(\text{mg mL}^{-1}\right) &= 27.99 + 2.64A + 6.98B - 0.113C \\ &\quad -4.68AB - 1.90AC - 3.42B\end{aligned} \tag{3}$$

The coefficients are obtained based on the least-squares method in such a way that the sum of the squares of the errors, ε, is minimized. A positive coefficient value indicates that this variable has a positive effect on PGA yield, while a minus indicates a negative impact. Statistical analysis was performed to assess the significance of the model used and the coefficients in the 2FI regression equation. ANOVA parameters are shown in Table S-IV of the Supplementary material. Models F and p values, 3.88 and 0.049, respectively, indicate that the model is significant. Both glucose and glycerol have a positive impact on PGA production, while glutamate has a negative impact. Based on ANOVA, only glycerol shows the significant impact on the increase of PGA yield. The two-factor interactions of these components have insignificant negative impacts. Response surface 3D graphs show the two-interactive effects of independent variables on PGA yield (Fig. S-1 of the Supplementary material). Fig. S-1a represents the combined effects of glucose and glycerol concentrations, while Fig. S-1b shows the effects of glycerol and glutamate concentrations on PGA production. Glycerol has a higher linear coefficient and steeper rise than glucose (Fig. S-1a), thus positively impacting PGA production. Even though glutamate has a negative effect on PGA yield with its linear coefficient being –0.113, its impact is barely detectable. Neither graph reveals a finite plateau, implicating a possibility of further medium and yield improvement. According to the results, a minimal concentration of glutamate (0.5 g L^{-1}) is optimal. Also, it is necessary to provide a high concentration of glucose and glycerol (80 and 50 g L^{-1}, respectively) for the production of 38 g L^{-1} of PGA.

The obtained result indicates that *B. subtilis* 17B used in this study is a glutamate-independent strain, which in the literature implies a potentially lower production cost. [27] In recent years, studies on the synthesis of PGA have mostly concentrated on glutamate-dependent strains.[28,29] However, the main limitation for large-scale production of PGA is the high production costs due to the addition of significant amounts of expensive exogenous L-glutamate.[30] Since glutamate-independent strains could significantly lower the cost of PGA synthesis and simplify the fermentation process, more attention is given to them nowadays.[31] Glutamate-independent strains were considered ineligible for industrial γ-PGA production, limited by their low γ-PGA productivity,[31] but based on the results shown in this study this state could be modified. In a screening study, *B. subtilis* 17B strain showed two times higher productivity of PGA than *B. paralicheniformis* ATCC 9945a and after optimization of the cultivation, productivity was improved tenfold.

Isolation and purification of PGA

PGA was purified from the fermentation broth from accompanying small molecules including yellow pigment and proteins (using Proteinase K) and analyzed by SDS-PAGE after standard CBB staining and methylene blue staining.[32] SDS PAGE electropherogram is given in Fig. 1. Samples before Proteinase K treatment are rich in proteins (line 1). After the treatment with Proteinase K, most proteins were removed from samples (line 2). Detection of PGA in SDS PAGE was not possible by staining with CBB, therefore the basic dye methylene blue was used for PGA's visualization (Fig. 1, MB). This is most likely because polyglutamic acid is a negatively charged polymer with no hydrophobic regions that could be stained using CBB.[33] The polymer (1–2 MB) showed multiple wide blue bands. Methylene blue staining of PGA was better after proteinase treatment, presumably because of the stronger interaction of PGA and methylene blue in absence of proteins. This phenomenon could be due to the formation of electrostatic interactions between PGA and proteins from the sample, thus reducing the number of free functional groups available for interaction with methylene blue. Furthermore, successful basic dye staining proved the presence of a negatively charged polymer.

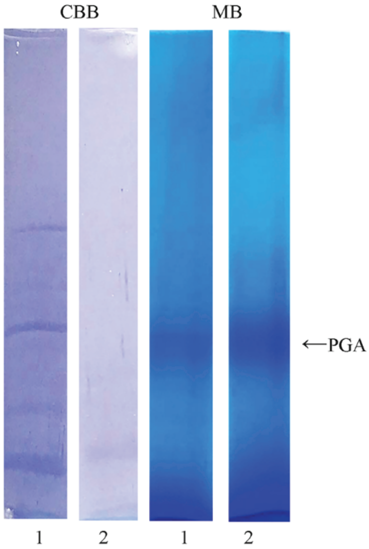

Fig. 1. SDS PAGE electropherograms of PGA produced by *B. subtilis* 17B stained with CBB and methylene blue (MB). 1 – before; 2 – after Proteinase K treatment.

Mass spectrometry of isolated PGA

Detection of the number of Glu units in the PGA was determined by ESI MS, and the identity of individual signals was confirmed by comparison with hydrolyzed polymer and standard (Glu). The sample ionization has been assisted by the addition of formic acid, in order to increase the ion yield, and the positive ion ESI mass spectra are given in Fig. S-2 of the Supplementary material, whereas the signal identity is listed in Table S-V of the Supplementary material. ESI MS is, a so-called, "soft" ionization technique,[34] thus the extent of fragmentation are low. Mostly, the loss of H_2O, CO or CO_2 from the –COOH group was detectable.

In summary, all detected ions imply that isolated polymer contains Glu and that the highest number of Glu units is 15 which is in agreement with the literature.[35]

Characterization of PGA–TiO_2 nanocomposite systems and potential application

The potential application of PGA produced by *B. subtilis* 17B was tested by the formation of PGA/TiO_2 NC for the possibility to increase the cytotoxic effect of TiO_2 nanoparticles against HeLa cells. To examine nanocomposite formation, we recorded the spectra of purified PGA, PGA/TiO_2 nanocomposite and TiO_2 nanoparticles (Fig. S-3 of the Supplementary material).

The band at 1650–1660 cm^{-1} in the PGA FTIR spectrum can be identified as the amide I band. The signal at 1079–1116 cm^{-1} is the result of a C–N bond. The low-intensity signal at 1450–1457 cm^{-1} originates from weak carbonyl absorption and is consistent with the literature.[36] The over 3000 cm^{-1} region is of lower intensity, presumably because the sample was isolated from the basic medium making it mostly deprotonated. This reduces the number of hydrogen bonds that otherwise amplify the O–H and N–H bond signals. To this broad region signals of aliphatic N–H stretching, that have no clear bands, belong. However, region 3409–3442 cm^{-1} can be distinguished and may correspond to OH group absorption.[37] All the assigned signals indicate a glutamic acid polymer, while the absence of a C–O bond confirms the absence of polysaccharide and that PGA was successfully purified.

Although the PGA/TiO_2 nanocomposite FTIR spectrum shows a significant difference compared to the PGA spectrum, the problem might arise from the concentration ratios, as the TiO_2 signals dominate. It seems that all of the main signals from the PGA spectrum disappear in the NC spectrum, implying the existence of PGA–TiO_2 interaction. The high-intensity signals at 2321–2365 cm^{-1} for the PGA spectrum and 2312–2355 cm^{-1} for the nanocomposite spectrum originate from the asymmetric stretching of CO_2 that was present in both samples and it is stemming from the air.[38] However, the interaction between these two components is demonstrated by slower sedimentation of TiO_2 nanoparticles in the presence of PGA in the solution. The experiment that was performed by centrifugation of suspensions containing varying PGA: TiO_2 mass ratio at 12000*g* was done. Whereas only a short impulse was required to sediment TiO_2 nanoparticles from a physiological solution without PGA (pH 7), at the PGA: TiO_2 ratios at 1:25 to 1:2, more than 30 min of centrifugation was necessary, which indicates stabilization of TiO_2 in the physiological solution. Since the electrostatic interactions between an organic polymer (alginate) and TiO_2 nanoparticles resulting in their stabilization have already been demonstrated,[39] we assume that in a similar manner, a –COO– group interacts with the surface of TiO_2 nanoparticles.

In the next step, we preliminarily tested the cytotoxicity of all components and the NC system against HeLa cells. Namely, colloidal TiO_2 nanoparticles form a stable colloidal solution at pH 2, which is not in a physiological range and limit their application in biological systems.[40] Therefore, our hypothesis was that the addition of PGA will stabilize the system and enable its application in the physiological range.

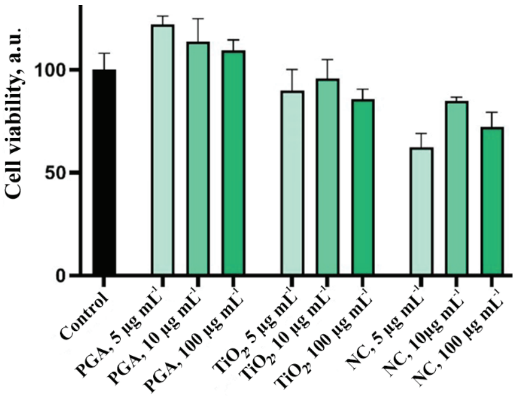

Fig. 2. HeLa cells viability after treatment with three different concentrations of PGA isolated from *B. subtilis* 17B, TiO_2 nanoparticles, and PGA/TiO_2 NCs.

As presented in Fig. 2, the addition of PGA produced by *Bacillus* sp. 17B increased the cytotoxic effect of TiO_2, whereas PGA alone showed no cytotoxicity, as compared to control/untreated cells. Although the TiO_2 nanoparticles demonstrated a light-induced cytotoxic effect, there are also data that show that these nanoparticles can also be cytotoxic in the dark,[41] and our results are in line with these findings.

These preliminary results demonstrated the potential application of PGA as stabilizers for TiO_2 nanoparticles that have various biological applications,[42] but the mechanism of its action and other physicochemical properties of the system need to be further investigated in more detail.

CONCLUSION

The newly isolated strain of *B. subtilis* 17B, a natural isolate from the soil, a promising PGA producer (initially showing twice the PGA production compared to the commercially used strain *B. paralicheniformis* ATCC 9945a) produced a high level of PGA after applying statistical optimization methods (PGA production increased tenfold). *B. subtilis* 17B was characterized as glutamate-independent which candidate it as a promising strain for PGA production due to the cost-effectiveness process. The PGA–TiO_2 nanocomposite showed better cytotoxicity toward HeLa cells than TiO_2, which opened up the possibility of application in biological systems considering that TiO_2 nanoparticles are not stable in a physiological pH range.

SUPPLEMENTARY MATERIAL

Additional data and information are available electronically at the pages of journal website: https://www.shd-pub.org.rs/index.php/JSCS/article/view/12132, or from the corresponding author on request.

Acknowledgments. This work was financially supported by the Ministry of Education, Science and Technological Development of the Republic of Serbia (Grant No. 451-03-68/ /2022-14/200026; 451-03-68/2022-14/200168; 450-03-68/2022-14/200017). The authors are thankful to Dr Marijana Petković, COHERENCE Center, for their critical reading of the manuscript, and Dr Jelena Zakula, for the cell cytotoxicity assay.

ИЗВОД

НОВИ НАНОКОМПОЗИТ PGA/TIO$_2$ ДОБИЈЕН ОД ПОЛИ(γ-ГЛУТАМИНСКЕ КИСЕЛИНЕ) ИЗ НОВОИЗОЛОВАНОГ СОЈА *Bacillus subtilis* 17Б

МАРИНЕЛА ШОКАРДА СЛАВИЋ[1], ВАЊА РАЛИЋ[2], БРАНИСЛАВ НАСТАСИЈЕВИЋ[3], МИЛИЦА МАТИЈЕВИЋ[2], ЗОРАН ВУЈЧИЋ[4] и АЛЕКСАНДРА МАРГЕТИЋ[1]

[1]*Универзитет у Београду – Институт за хемију, технологију и металургију – Институт од националног значаја за Републику Србију, Београд*, [2]*Центар за конверзију светлосне енергије COHERENCE, Лабораторија за атомску физику, Институт за нуклеарне науке „Винча" – Институт од националног значаја за Републику Србију, Универзитет у Београду, Београд*, [3]*Институт за нуклеарне науке „Винча" – Институт од националног значаја за Републику Србију, Универзитет у Београду, Београд* и [4]*Универзитет у Београду – Хемијски факултет, Београд*

Поли(γ-глутаминска киселина) (PGA), коју производе бактерије рода *Bacillus*, је биоразградив, нетоксичан, биокомпатибилан и неимуноген негативно наелектрисани полимер. Због својих својстава нашао је разноврсну примену у прехрамбеној, козметичкој и фармацеутској индустрији. У овом раду, *Bacillus subtilis* 17Б је изабран као најбољи ПГК продуцер међу педесетак тестираних природних изолата бактерија из овог рода и окарактерисан као глутамат независтан продуцер. Производња ПГК овим новоидентификованим сојем је оптимизована и десетоструко увећана коришћењем Box– –Behnken експерименталног дизајна. Чистоћа PGA након изоловања и пречишћавања из ферметационе течности је потврђена електрофорезом (SDS-PAGE) након бојења метиленским плавим. PGA је окарактерисана масеном спекроскопијом (ESI-MS) и коришћена за добијање новог нанокомпозита са TiO$_2$. Синтеза PGA/TiO$_2$ нанокомпозита, његова структурна анализа и цитотоксични ефекат на ћелијску линију рака грлића материце (HeLa ћелије) је испитан да би се утврдила потенцијална употреба овог новодобијеног материјала у борби против ћелија рака. Нанокомпозит PGA/TiO$_2$ показао је повећан цитотоксични ефекат на поменуте ћелије рака у поређењу са самим TiO$_2$.

(Примљено 16. новембара 2022, ревидирано 23. јануара, прихваћено 3. марта 2023)

REFERENCES

1. I. Bajaj, R. Singhal, *Bioresour. Technol.* **102** (2011) 5551 (https://doi.org/10.1016/j.biortech.2011.02.047)
2. W. E. Hanby, H. N. Rydon, *Biochem. J.* **40** (1946) 297 (https://doi.org/10.1042/bj0400297)
3. S. bin Park, M. H. Sung, H. Uyama, D. K. Han, *Prog. Polym. Sci.* **113** (2021) 101341 (https://doi.org/10.1016/j.progpolymsci.2020.101341)
4. C. Wang, M. Feng, J. Deng, Y. Zhao, X. Zeng, L. Han, S. Pan, C. Wu, *Int. J. Pharm.* **398** (2010) 237 (https://doi.org/10.1016/j.ijpharm.2010.07.048)
5. M. Moriyama, H. Uyama, A. J. van der Vlies, U. Hasegawa, *Colloid Polym. Sci.* **293** (2015) 1245 (https://doi.org/10.1007/s00396-015-3516-9)

6. D. Ziental, B. Czarczynska-Goslinska, D. T. Mlynarczyk, A. Glowacka-Sobotta, B. Stanisz, T. Goslinski, L. Sobotta, *Nanomaterials* **10** (2020) 387 (https://doi.org/10.3390/nano10020387)
7. F. F. Hezayen, B. H. A. Rehm, B. J. Tindall, A. Steinbüchel, *Int. J. Syst. Evol. Microbiol.* **51** (2001) 1133 (https://doi.org/10.1099/00207713-51-3-1133)
8. T. Candela, M. Moya, M. Haustant, A. Fouet, *Can. J. Microbiol.* **55** (2009) 627 (https://doi.org/10.1139/w09-003)
9. J. H. Do, H. N. Chang, S. Y. Lee, *Biotechnol. Bioeng.* **76** (2001) 219 (https://doi.org/10.1002/bit.1186)
10. M. Schallmey, A. Singh, O. P. Ward, *Can. J. Microbiol.* **17** (2004) 1 (https://doi.org/10.1139/W03-076)
11. A. Goto, M. Kunioka, *Biosci. Biotechnol. Biochem.* **56** (1992) 37 (https://doi.org/10.1271/bbb.56.1031)
12. G. Du, G. Yang, Y. Qu, J. Chen, S. Lun, *Process Biochem.* **40** (2005) 2143 (https://doi.org/10.1016/j.procbio.2004.08.005)
13. F. Shi, Z. Xu, P. Cen, *Biotechnol. Bioprocess Eng.* **11** (2006) 251 (https://doi.org/10.1007/BF02932039)
14. C. Zhang, D. Wu, X. Qiu, *Sci. Rep.* **8** (2018) 17934 (https://doi.org/10.1038/s41598-018-36439-4)
15. Y. H. Ko, R. A. Gross, *Biotechnol. Bioeng.* **57** (1998) 430 (https://doi.org/10.1002/(SICI)1097-0290(19980220)57:4<430::AID-BIT6>3.0.CO;2-N)
16. D. A. Hopwood, M. J. Bibb, K. F. Chater, T. Kieser, C. J. Bruton, H. M. Kieser, D. J. Lydiate, C. P. Smith, M. Ward, H. Schrempf, *Genetic Manipulation of Streptomyces: A Laboratory Manual*, John Innes Foundation, Foulsham, 1985
17. D. J. Lane, 16S/23S rRNA Sequencing. in *Nucleic acid techniques in bacterial systematics*, E. Stackebrandt and M. Goodfellow, Eds., Wiley, New York, 1991
18. S. F. Altschul, T. L. Madden, A. A. Schäffer, J. Zhang, Z. Zhang, W. Miller, D. J. Lipman, *Nucleic Acids Res.* **25** (1997) 3389 (https://doi.org/10.1093/nar/25.17.3389)
19. C. Park, J.-C. Choi, Y.-H. Choi, H. Nakamura, K. Shimanouchi, T. Horiuchi, H. Misono, T. Sewaki, K. Soda, M. Ashiuchi, M.-H. Sung, *J. Mol. Catal., B* **35** (2005) 128 (https://doi.org/10.1016/j.molcatb.2005.06.007)
20. U. K. Laemmli, *Nature* **227** (1970) 680 (https://doi.org/10.1038/227680a0)
21. F. Yamaguchi, Y. Ogawa, M. Kikuchi, K. Yuasa, H. Motai, *Biosci. Biotechnol. Biochem.* **60** (1996) 255 (https://doi.org/10.1271/bbb.60.255)
22. T. Rajh, A. E. Ostafin, O. I. Micic, D. M. Tiede, M. C. Thurnauer, *J. Phys. Chem.* **100** (1996) 4538 (https://doi.org/10.1021/jp952002p)
23. R. C. Thompson, *Inorg. Chem.* **23** (1984) 1794 (https://doi.org/10.1021/ic00181a003)
24. D. Lin, S. D. Story, S. L. Walker, Q. Huang, W. Liang, P. Cai, *Environ. Pollut.* **228** (2017) 35 (https://doi.org/10.1016/j.envpol.2017.05.025)
25. P. Skehan, R. Storeng, D. Scudiero, A. Monks, J. McMahon, D. Vistica, J. T. Warren, H. Bokesch, S. Kenney, M. R. Boyd, *J. Natl. Cancer Inst.* **82** (1990) 1107 (https://doi.org/10.1093/jnci/82.13.1107)
26. G. A. Birrer, A.-M. Cromwick, R. A. Gross, *Int. J. Biol. Macromol.* **16** (1994) 265 (https://doi.org/10.1016/0141-8130(94)90032-9)
27. J. M. Buescher, A. Margaritis, *Crit. Rev. Biotechnol.* **27** (2007) 1 (https://doi.org/10.1080/07388550601166458)
28. H. Xu, M. Jiang, H. Li, D. Lu, P. Ouyang, *Process Biochem.* **40** (2005) 519 (https://doi.org/10.1016/j.procbio.2003.09.025)

29. D. Wang, J.-S. Hwang, D.-H. Kim, S. Lee, D.-H. Kim, M.-H. Joe, *Process Biochem.* **92** (2020) 164 (https://doi.org/10.1016/j.procbio.2019.11.034)
30. W. Zeng, G. Chen, Y. Guo, B. Zhang, M. Dong, Y. Wu, J. Wang, Z. Che, Z. Liang, *AMB Express* **7** (2017) 213 (https://doi.org/10.1186/s13568-017-0512-0)
31. M. Cao, W. Geng, L. Liu, C. Song, H. Xie, W. Guo, Y. Jin, S. Wang, *Bioresour. Technol.* **102** (2011) 4251 (https://doi.org/10.1016/j.biortech.2010.12.065)
32. M. Ashiuchi, K. Soda, H. Misono, *Biochem. Biophys. Res. Commun.* **263** (1999) 6 (https://doi.org/10.1006/bbrc.1999.1298)
33. F. Yamaguchi, Y. Ogawa, M. Kikuchi, K. Yuasa, H. Motai, *Biosci. Biotechnol. Biochem.* **60** (1996) 255 (https://doi.org/10.1271/bbb.60.255)
34. C. Ho, C. Lam, M. Chan, R. Cheung, L. Law, L. Lit, K. Ng, M. Suen, H. Tai, *Clin. Biochem. Rev.* **24** (2003) (https://pubmed.ncbi.nlm.nih.gov/18568044)
35. I. Kwiecień, I. Radecka, M. Kowalczuk, K. Jelonek, A. Orchel, G. Adamus, *J. Am. Soc. Mass Spectrom.* **28** (2017) 2223 (https://doi.org/10.1007/s13361-017-1731-y)
36. G. Kedia, D. Hill, R. Hill, I. Radecka, *J. Nanosci. Nanotechnol.* **10** (2010) 5926 (https://doi.org/10.1166/jnn.2010.2614)
37. A. R. Bhat, V. U. Irorere, T. Bartlett, D. Hill, G. Kedia, M. R. Morris, D. Charalampopoulos, I. Radecka, *AMB Express* **3** (2013) 1 (https://doi.org/10.1186/2191-0855-3-36)
38. S. W. Bruun, A. Kohler, I. Adt, G. D. Sockalingum, M. Manfait, H. Martens, *Appl. Spectrosc.* **60** (2006) 1029 (https://doi.org/10.1366/000370206778397371)
39. A. S. Adeleye, A. A. Keller, *Environ. Sci. Technol.* **50** (2016) 12258 (https://doi.org/10.1021/acs.est.6b03684)
40. G. R. Wiese, T. W. Healy, *J. Colloid Interface Sci.* **52** (1975) 452 (https://doi.org/10.1016/0021-9797(75)90270-2)
41. M. Hamzeh, G. I. Sunahara, *Toxicology* in Vitro **27** (2013) 864 (https://doi.org/10.1016/j.tiv.2012.12.018)
42. S. Jafari, B. Mahyad, H. Hashemzadeh, S. Janfaza, T. Gholikhani, L. Tayebi, *Int. J. Nanomedicine* **15** (2020) 3447 (https://doi.org/10.2147/IJN.S249441).

JSCS@tmf.bg.ac.rs • www.shd.org.rs/JSCS

J. Serb. Chem. Soc. 88 (10) S307–S311 (2023)

Supplementary material

SUPPLEMENTARY MATERIAL TO

A novel PGA/TiO_2 nanocomposite prepared with poly(*γ*-glutamic acid) from the newly isolated *Bacillus subtilis* 17B strain

MARINELA ŠOKARDA SLAVIĆ[1]*, VANJA RALIĆ[2], BRANISLAV NASTASIJEVIĆ[3], MILICA MATIJEVIĆ[2], ZORAN VUJČIĆ[4] and ALEKSANDRA MARGETIĆ[1]

[1]*University of Belgrade – Institute of Chemistry, Technology and Metallurgy – National Institute of the Republic of Serbia, Department of Chemistry, Belgrade, Serbia,* [2]*Center for light-based research and technologies, COHERENCE, Department of Atomic Physics, Vinča Institute of Nuclear Sciences, National Institute of the Republic of Serbia, University of Belgrade, Belgrade, Serbia,* [3]*Vinča Institute of Nuclear Sciences, National Institute of the Republic of Serbia, University of Belgrade, Belgrade, Serbia and* [4]*University of Belgrade – Faculty of Chemistry, Department of Biochemistry, Belgrade, Serbia*

J. Serb. Chem. Soc. 88 (10) (2023) 985–997

MASS SPECTROMETRY OF ISOLATED PGA

The spectra of glutamic acid (Fig. S-2) contain only the signals corresponding to the ions generated by the proton or sodium addition (*m/z* 148.09 or 170.09, respectively). In addition, the ions formed by the proton/sodium replacement or the loss of water molecules were observed, which is in agreement with previously analyzed spectra of amino acids.[1] In the spectrum of a hydrolyzed polymer (Fig. S-2B), the ions detected at low m/z positions arise from inorganic ions present in the carrier fluid, whereas ions in the mass range m/z 140-180 arise from glutamic acid. Because of the high concentration of HCl in the solution, required for hydrolysis, no Na-adducts are detectable in the spectra. These results strongly imply that Glu does not polymerize during the acquisition of mass spectra and that the signals detected in the polymer spectra arise exclusively from the ions present in the isolate (Fig. S-2C). Although ESI mass spectra can contain multiply charged ions, in the spectra acquired under our conditions, we have detected only singly charged ions, and the highest number of units detected is 15. Ions are generated by the loss of CO, and the spectra are in agreement with the literature data.[2]

---

* Corresponding author. E-mail: marinela.sokarda@ihtm.bg.ac.rs

Table S-I. Limits of the Studied Parameters

Factor	Factor levels			
	Symbol	Low (-1)	Central (0)	High (+1)
c_{glucose} /g L^{-1}	A	10	45	80
c_{glycerol} /g L^{-1}	B	0	25	50
$c_{\mathrm{glutamate}}$ /g L^{-1}	C	0.5	2.75	5

Table S-II. Three-Factor Box-Behnken Experimental Design

Run	A	B	C
1	-1	-1	0
2	1	-1	0
3	-1	1	0
4	1	1	0
5	-1	0	-1
6	1	0	-1
7	-1	0	1
8	1	0	1
9	0	-1	-1
10	0	1	-1
11	0	-1	1
12	0	1	1
13	0	0	0
14	0	0	0

Table S-III. TiO_2 and PGA concentrations (c / μg mL^{-1}) used for nanocomposite formation and cell cytotoxicity assay.

Sample	TiO_2	PGA
NC1	1000	200
NC2	1000	400
NC3	1000	500

Table S-IV. ANOVA

Source	Sum of Squares	df	Mean Square	F-value	p-value	
Model	593.74	6	98.96	3.88	0.0496	Significant
A-Glucose	55.65	1	55.65	2.18	0.1833	
B-Glycerol	389.21	1	389.21	15.25	0.0059	
C-Glutamate	0.1013	1	0.1013	0.0040	0.9515	
AB	87.42	1	87.42	3.43	0.1066	
AC	14.44	1	14.44	0.5658	0.4764	
BC	46.92	1	46.92	1.84	0.2172	
Residual	178.63	7	25.52			
Lack of Fit	104.21	6	17.37	0.2334	0.9161	Not significant
Pure Error	74.42	1	74.42			
Cor Total	772.38	13				

Table S-V. Position and signal identity of peaks detected in the positive ion ESI mass spectra given in Fig. 5: (A) glutamic acid, (B) hydrolyzed polymer, and (C) isolated PGA is given.

Position, m/z	Signal identity	Position, m/z	Signal identity
130,04	Glu-H2O+H+	306,94	Glu2+H2O+Na+-H+
142,09	Glu-CO+Na+	448,96	Glu3+2Na+-2CO-H++H2O
164,93	Glu+H2O-H+	590,86	Glu4+3Na+-3CO+H2O+H+
148,09	Glu+H+	1150,07	n.i.
170,09	Glu+Na+	1662,81	Glu13-CO+H+
192,09	Glu+2Na+-H+	1793,11	Glu14-CO+H+
214,08	Glu+3Na+-2H+	1957,2	Glu15+H+
226,08	n.i.		

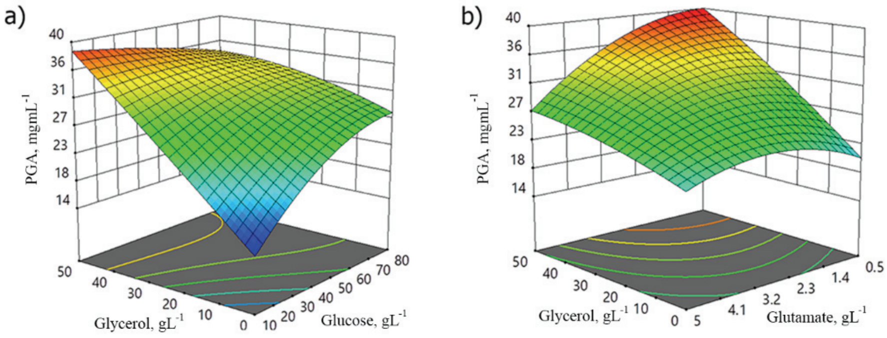

Fig. S-1. 3D response surface graph for the effects of a) concentrations of glycerol and glucose and b) concentrations of glycerol and glutamate on PGA yield. The third variable was held constant at the center point.

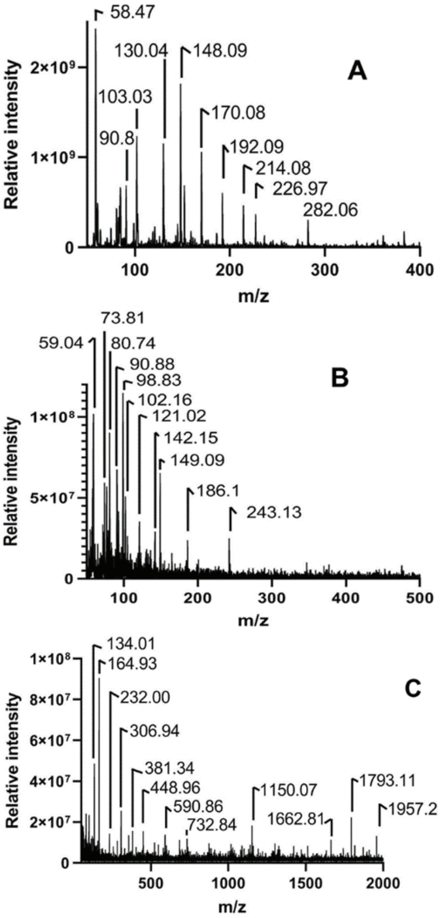

Fig. S-2. Positive ion ESI mass spectra of glutamic acid (A), hydrolyzed isolated PGA (B) and isolated PGA (C).

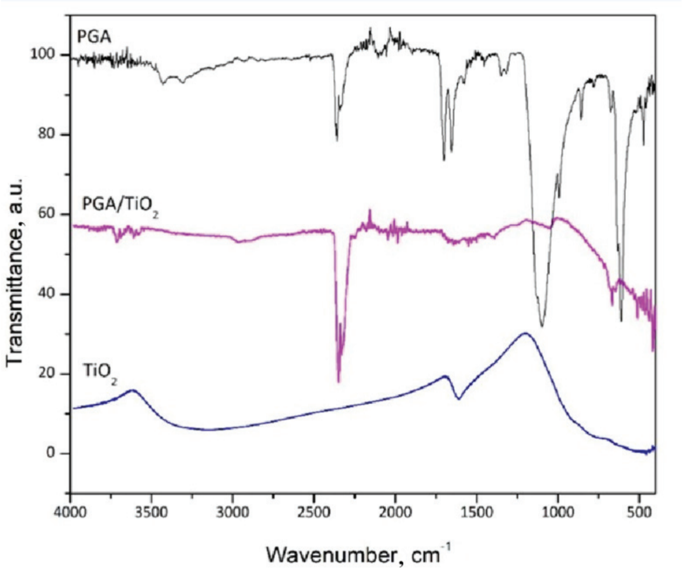

Fig. S-3. FTIR spectra of purified PGA, PGA/TiO$_2$ nanocomposite, and TiO$_2$.

REFERENCES

1. P. Zhang, W. Chan, I. L. Ang, R. Wei, M. M. T. Lam, K. M. K. Lei, & T. C. W. Poon, *Sci. Rep.* **9** (2019) 1 (https://doi.org/10.1038/s41598-019-42777-8)
2. I. Kwiecień, I. Radecka, M. Kowalczuk, K. Jelonek, A. Orchel, & G. Adamus, *J. Am. Soc. Mass Spectrom.* **28** (2017) 2223 (https://doi.org/10.1007/s13361-017-1731-y).

Journal of the Serbian Chemical Society
JSCS-info@shd.org.rs • www.shd.org.rs/JSCS
J. Serb. Chem. Soc. *88* (10) 999–1012 (2023)
JSCS–5676
Original scientific paper
Published 24 October 2023

Synthesis of sodium silicate crystals from rice husk ash

STELLA ADEDUNNI EMMANUEL[1], ALHASSAN ADEKU SALLAU[1]*, OLUWASEYE ADEDIRIN[1], HUSSAIN DOKO IBRAHIM[2], MOHAMMED LAWAL BUGA[2], ANTHONY OKEREKE[2], GERTRUDE NGOZI OZONYIA[2] and FORTUNE MIEBAKA ALABI[2]

[1]*Chemistry Advanced Research Center, SHESTCO, Abuja, Nigeria and* [2]*Raw Materials Research and Development Council, RMRDC, Maitama, Abuja, Nigeria*

(Received 26 November 2022, revised 3 April, accepted 10 July 2023)

Abstract: The rich husk is an agricultural waste of rice cultivation worldwide, which is highly rich in amorphous silica. Rice husk obtained from Dagiri was pyrolyzed at 750 °C to give white ash (RHA) which was further treated with acid (ARHA). The ash was reacted with sodium hydroxide at 90 °C for 2.5 h to produce sodium silicate crystals. Sodium silicate synthesized in the study was characterized for some physicochemical parameters. Their structural and morphological properties were assessed using a Fourier transform infra-red spectrophotometer (FTIR), X-ray diffractometer (XRD) and scanning electron microscope (SEM). The mineralogical composition of the ash and sodium silicate was investigated with energy-dispersive X-ray fluorescence (EDXRF) spectrometer. The sodium silicate produced has a melting point of 61 °C, pH of 12.03 and appeared as brownish–white to clear-white in colour. The RHA and ARHA from XRD investigation showed patterns which match the mineral phase cristobalite, while that of the sodium silicate XRD patterns match the mineral heptahydrate disodium trioxosilicate as the most dominant phase. Rietveld refinement of the XRD pattern for the sodium silicate gave $R_{wp} = 12.81$, $R_{exp} = 5.55$, $\chi^2 = 5.3274$ and $GoF = 2.3081$ against a dual phase analysis. The crystals synthesized are suitable for use in cosmetic formulations.

Keywords: acid treated ash; cosmetic; crystal structure; paddy; silica; water glass.

INTRODUCTION

Rice husk is an agricultural waste material produced *via* the cultivation of rice[1]. Rice production worldwide was pegged at over 952 million tons in 2016 according to a 2018 data report by the Food and Agriculture Organization (FAO). The rice husk, which is the outer cover of the rice, accounts for 20 % of the paddy produced annually (about 190 million tons).[2]

---

* Corresponding author. E-mail: creamysal@yahoo.co.uk
https://doi.org/10.2298/JSC221126040E

The world has seen a tremendous increase in annual rice production in recent years when compared with the previous report of an estimated 40 million tons in 2003. It is regarded as the second most-produced cereal in the world and geographically concentrated in Asia with over 90 % of the world output. While, Nigeria is putting efforts to develop this sector of agricultural produce, the bulk of rice husks generated is mostly sent to landfills, burnt as fuel to generate energy and leading to residual ashes (RHA) containing over 60 % silica content.[3,4]

Rice husk contains high ash content,[5,6] varying from 13 to 29 wt. % depending on the variety, climate, and geographic location. The ash is largely composed of silica (87–97 %) with small amounts of inorganic salts.[6,7] The high ash content can be recovered as amorphous silica.[8] The amorphous nature of silica in rice husk makes it extractable at a lower temperature range of 90–110 °C.[3]

Sodium silicate solutions are complex mixtures of silicate anions and polymer silicate particles with a mole ratio of SiO_2 to $Na_2O > 2$ and are commercially referred to as water glass.[4] The solutions are generated in different grades as characterized by their SiO_2:Na_2O ratios, varying water contents and low viscosity.[9] Sodium silicate is among the alkali silicates that gave rise to extensive studies due to their importance in mineralogy, solid-state chemistry and chemical technology. About 12 natural sodium silicates minerals are known to exist and nine of them have been studied structurally.[10] Anhydrous sodium silicate are considered important raw materials in production of finished products in both inorganic chemistry and technical mineralogy.[11] Some of industrial applications include production of water glass solutions or manufacture of acid-resistant enamel frits, components of refractory cements, steel and alloy castings, electrodes, dyeing, printing, textile auxiliaries as inorganic binders or builders in washing powders (soap and detergent cake).[11–13] Crystalline sodium silicates such as $Na_2Si_2O_5$ have been shown to exhibit high ion-exchange capacity, selectivity and multifunctionality; such as buffering capacity, water softening ability and ability to degrade fats by hydrolysis and as such suggested as alternative replacement of sodium tripolyphosphate builder in detergents.[14,15] It has been suggested that soluble sodium silicates play other vital role of corrosion inhibition in many of its applications such as engine antifreeze and detergents.[16] Sodium silicate in surfactants have been applied in detergent technology for pre-flush technology, with the main role of sodium silicate targeted at removal of hardness (Ca^{2+}, Mg^{2+}) which can complex with anionic surfactants making them less reactive or unstable. The silicates minimize these unwanted charges by sequestering the metals *via* a precipitation reaction. The silica anion also competes for active, positively-charged sites on the casing and wellbore thereby reversing their surface charge and repelling surfactants.[12] Sodium silicate is also used as a binder in cosmetic products, such as face powders, eyeliners and lipsticks, to give them a smooth and creamy texture. It helps to bind the different ingredients together and prevent them from separating.[17] Sodium silicate can be used as a thickener in shampoos and conditioners, to improve viscosity and consistency. Sodium silicate can also be used as a pH stabilizer in lotions and creams, to help maintain their pH levels. This is important because certain cosmetic ingredients can become less effective or even unstable at certain pH levels. Sodium silicate can be used as a preservative in liquid soaps and facial cleansers, to help prevent the growth of bacteria and other microorganisms. It works by altering the pH level of the product, which makes it less hospitable to microorganisms. Sodium silicate can also be used as a skin protectant in sunscreens and lotions, to help shield the skin from harmful UV rays and other environmental pollutants. It forms a protective film on the skin, which helps to prevent moisture loss and maintain the skin's natural barrier function.[18,19]

The work aims to synthesize a sodium silicate crystal from rice husk ash for possible use in the cosmetic industries.

EXPERIMENTAL

Rice husk was obtained from rice mill at Dagiri, Gwagwalada local government of Federal Capital Territory, Abuja, Nigeria, analar grade sodium hydroxide and hydrochloric acid from Sigma Aldrich were used. All solutions were prepared with distilled de-ionized water.

Sample pre-treatment

Rice husk was washed with water to remove sand and dust particles. The washed rice husk was then spread on tray and air dried for 24 h. Dried rice husk was placed in stainless steel cylinder and turned to ashes at 750 °C for 3 h in a Carbolite muffle furnace available at Sheda Science and Technology Complex (SHESTCO), Abuja. The pyrolyzed sample tagged RHA were weighed (200 g) separately and treated with 1600 mL of HCl (10 and 20 %) in a Pyrex beaker and heated for 2 h at 90 °C. The reaction mixtures were filtered and washed repeatedly with distilled deionized water until the filtrate becomes neutral to litmus. The residues designated 10 % ARHA and 20 % ARHA (acid treated RHA) were dried at 105 °C for 12 h in a carbolite hot air oven and kept in a desiccator for subsequent steps.

Preparation of sodium silicate

Modified method[20] was adopted: 150 g of ARHA was reacted with 1200 mL NaOH (10 %) in a Pyrex beaker and heated at 90 °C for 2.5 h. The reaction mixture was filtered and the filtrate concentrated by heating to 2/3 of its original volume. The concentrate was seeded with a pinch of pure sodium silicate crystals to induce rapid crystallization. The sodium silicate crystals formed were separated by decanting the supernatant liquid. The crystals were rinsed with iced cold distilled deionized water and allowed to drain on a filter. The drained crystals were stored in polyethylene container.

Physicochemical characterization of crystal

Determination of sodium oxide content (IS 6773 (2008)). The sodium oxide content of crystal obtained was determined by titrating dissolved crystal sample with standard hydrochloric acid to pH 4.3 using methyl orange indicator. 5 g of sodium silicate crystals were dissolved in 50 mL deionized water and transferred to 100 mL volumetric flask then diluted to mark with deionized water. A 25 mL portion of the solution was titrated against 0.2 M HCl to orange end-point colour.

Calculations.

$$c_{Na_2O}=\frac{3.1VM}{w} \tag{1}$$

where V is volume of hydrochloric acid used, M is the molarity of the hydrochloric acid and w is the mass of crystal sample.

Viscosity measurement. The viscosity of liquid sodium silicate solutions was determined using the Brookfield rotational viscometer according to the ASTM D2983 by insertion of number 2 spindle, rotating at 60 rpm at 25 °C in the sodium silicate liquor. The viscosity was read from the display reading. The determination of viscosity of sodium silicate liquor was essential to determine the optimum thickness for effective crystallization of the sodium silicate crystals from its water glass liquor.

Determination of total solid (IS 6773 (2008)). The total solids of liquid silicates were determined by weighing 5 mL (5 g) into a known weight of pre-fired porcelain crucible and placed in a muffle furnace at 1050 °C for 30 min. A few drops of 30 % hydrogen peroxide were added to prevent spattering. After cooling in a desiccator and the crucible was reweighted. The weight of the residue was taken and the relative content of solids were reported to the nearest 0.01 %.

Determination of silicon dioxide content (IS 6773 (2008)). The SiO_2 content was calculated by subtracting the % of sodium oxide from the % of total solids.

Sodium silicates are often described by the weight ratio of the silicon dioxide to the sodium oxide, with the sodium oxide as unity. It may be calculated directly by dividing the % of SiO_2 content by the % of Na_2O content that has been chemically determined.

Determination of pH (ASTM D4972). A 0.1 % solution of sodium silicate was prepared by dissolving 0.1 g of sodium silicate crystals in 100 mL deionized water. The pH of the sodium silicate liquor and 0.1 % sodium silicate solution was measured using the pH electrode and Orion Versa Star Pro meter advanced electrochemistry meter.

Melting point determination (DIN 53736). The microscopic hot stage method melting point apparatus by Bristoline was used. A single crystal sample of the sodium silicate was placed on a hot stage and the heater turned on. The temperature at the point the crystal melts was read from the inserted thermometer.

Characterization of crystals

Empyrean pan-analytical XRD (with CuKα at $\lambda = 1.54060$ Å, $U = 40$ V, $I = 40$ mA and 5 to 74°, 2θ angle), EDXRF (vacuum and air atmosphere geological sample analysis) and Phenom ProX scanning electron microscope available at the central laboratory of Umar Musa Yar'adua University, Katsina, were used to study the crystal structure, mineral composition and morphology of the crystal respectively. Thermo-Scientific Nicolet iS5 FT-IR spectrometer equipped with iD7 ATR sampler was used to asses any functional group available in the RHA, ARHA and sodium silicate crystals over the range 500–4000 cm^{-1} and resolution of 0.5 cm^{-1}. The thermal behaviour was investigated by the Perkin-Elmer MSE-TGA 4000 TGA (30–950 °C at 10 °C/min) available at Ahmadu Bello University, Zaria.

RESULTS AND DISCUSSION

Physicochemical properties of sodium silicate crystals

The physical properties of sodium silicate crystals are shown in Fig. 1 and some other chemical properties are given in Table I. From the images in Fig. 1, the appearance of the crystal was originally brownish–white but on further washing, it became brightly white and soapy to the touch. The pH of sodium silicate solution was found to fall within the commonly reported range of 11–12.5, as a solid with alkaline properties in solution it is readily neutralized to silica solid in the presence of acid. This forms the basis for most reported work on the synthesis of silica from rice husk ash.[21–24]

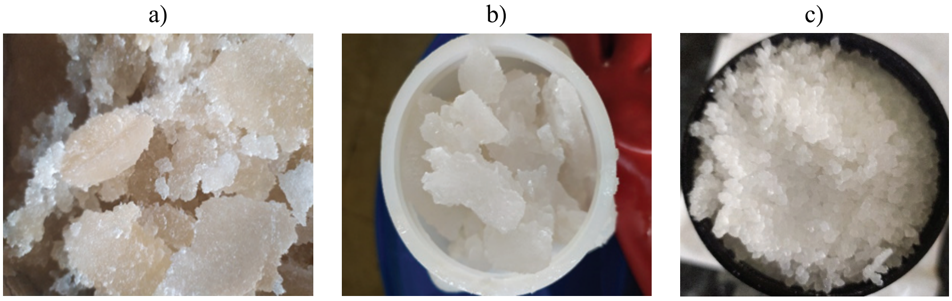

Fig. 1. Images of samples obtained: a) brownish silicate, b) washed silicate and c) crystalline appearance of washed silicate.

TABLE I. Some physical and chemical properties of sodium silicate crystals and silica

Property	Sodium silicate crystals	Sodium silicate liquor (Water glass)	750 °C RHA	10 % ARHA	20 % ARHA
Colour	Brownish to white	Brownish	White	White	White
pH	12.03	12.03	Neutral	Neutral	Neutral
Solubility, g dm^{-3}	High	High	Insoluble	Insoluble	Insoluble
Density, g cm^{-3}	–	1.415	–	–	–
Viscosity, mPa s	–	25	–	–	–
Stability in air	Slow efflorescence	Stable	Stable	Stable	Stable
Melting point, °C	61	–	–	–	–
Na_2O content, %	12.40	11.54	–	–	–
SiO_2 content, %	25.99	25.30	–	–	–
Sio_2/Na_2O	2.00	2.19	–	–	–
Total solid	38.39	36.84	–	–	–

RHA – sodium silicate crystals composition analysis

The elemental composition of the RHA, ARHA and sodium silicate crystals obtained from X-ray fluorescence analysis (by the air and vacuum atmosphere) are shown in Table II. It can be noticed that the percentage composition of SiO_2 increases progressively as the acid treatment concentration increase from 10 to 20 %, while other metal oxides concentration decreases.

TABLE II. EDXRF oxides composition (%) of RHA, ARHA and crystals

Oxide	750 °C RHA	10 % ARHA	20 % ARHA	Sodium silicate
Fe_2O_3	0.4698	0.15836	0.18990	0.1576
Na_2O	–	–	–	14.739
MgO	3.30	1.46	0.35	1.379
Al_2O_3	1.443	1.147	1.063	1.3516
SiO_2	72.148	90.344	91.567	18.665
P_2O_5	4.761	0.7510	0.8647	0.8505
SO_3	0.1647	0.0780	0.0777	0.3631
Cl	0.0256	0.01778	0.02052	0.0824
K_2O	3.3802	0.5772	0.5897	0.2346
CaO	0.7572	0.1326	0.1220	0.03335
MnO	0.4367	0.08555	0.08706	0.00799
SnO_2	1.00	1.00	1.00	–
Others	0.17478	0.07515	0.08312	0.05111

This decrease indicates the effectiveness of acid treatment in purifying the rice husk ash samples, as a means of preventing unnecessary side reactions. The SiO_2 and Na_2O content of the sodium silicate crystals were 18.665 and 14.739 % respectively. This will indicate that the ratio of SiO_2 to Na_2O is 1, which is not in agreement with the classical method result. This deviation may be attributed to the consequential presence of traces of CaO, MgO, Al_2O_3, K_2O and Fe_2O_3, which might equally react with the acid during the titrimetric determination of Na_2O, thus giving a higher false value of Na_2O. According to the study by Owoeye *et al.*, the synthesis of a sodium disilicate from RHA at different concentration of 3, 4 and 5 M of NaOH was found to contain 28.64, 42.25 and 36.97 % SiO_2 while the Na_2O content was 12.32, 17.23 and 18.24 %, respectively,[25] which were all higher than the 18.665 % of SiO_2 and 14.739 % of Na_2O content obtained in the present study at lower concentration of NaOH (10 % ≡ 2.5 M). Similarly, Siregar *et al.* reported the synthesis of sodium silicate from both corn cob and rice husk with content of Na of 43.29 and 22.63 %, that of O of 36.48 and 71.98 % while the Si content was 20.23 and 5.39 %, respectively.[26]

XRD of the solid obtained

The diffractogram of RHA obtained is shown in Fig. 2. The RHA, 10 % ARHA and 20 % ARHA diffractogram patterns correspond to the mineral cristobalite (96-900-8111). The diffractogram obtained for RHA treated at 750 °C, confirms that heat treatment of rice husk at a higher temperature such as 750 °C results in the formation of crystalline silica. A similar report showed that treatment of rice husk between 450–700 °C generally results in silica predominated with amorphous phase,[27] while the higher temperature of 1000–1350 °C results in silica predominant by crystalline phase. Similarly, Shihab and Twej reported obtaining amorphous and crystalline phases when rice husk was treated at 650 and 1000 °C, respectively.[24]

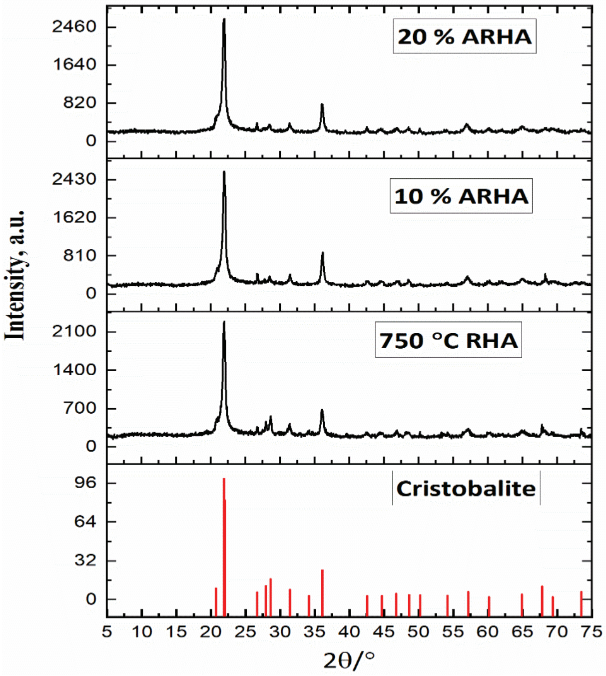

Fig. 2. XRD patterns of RHA, ARHA and reference pattern.

It was also observed that there was no specific change in the crystalline phase nature of the RHA when it was acid treated at different concentrations of 10 and 20 % HCl.

The diffractogram of the sodium silicate crystals obtained (Fig. 3) match the reference phase 2106900 of the crystallography open diffractogram with a chemical name of sodium hydrogen tetraoxosilicate heptahydrate ($Na_2H_2SiO_4 \cdot 7H_2O$).[10]

The suggested properties associated with this crystal show that it is monoclinic, and the Rietveld refinement of the XRD pattern for the sodium silicate performed by the profex software, v. 5.0, gave $R_{wp} = 12.81$, $R_{exp} = 5.55$, $\chi^2 = 5.3274$, $GoF = 2.3081$ for $Na_2H_2SiO_4 \cdot 7H_2O$ and $Na_3HSiO_4 \cdot 2H_2O$ phase analysis.[28] The inability of the χ^2 value found to meet up to the threshold value of 1.5 may be due to the presence of some impurities (majorly Al and Mg and traces of Ca, Fe, Zn, *etc.*) associated with the synthesis.

FT-IR spectra of rice husk ash and sodium silicate

The infrared spectra of the rice husk ash treated under high temperature and acid treatment are shown in Fig. 4. There were very week absorption peaks at posit-

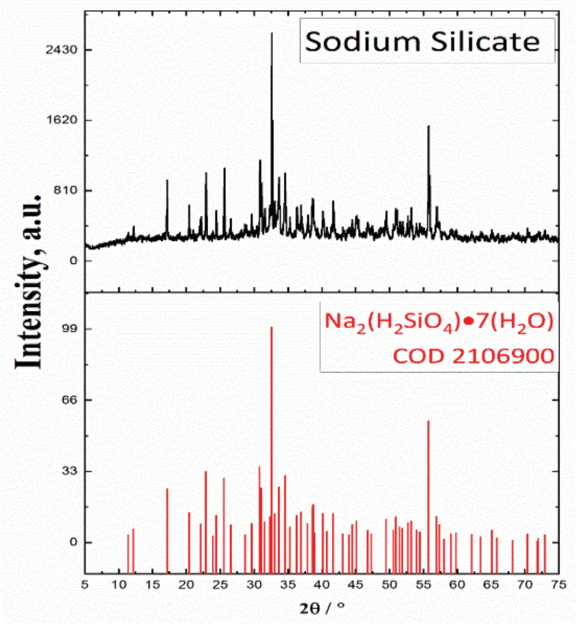

Fig. 3. Diffractogram pattern of synthesized sodium silicate.

ion of 3000 and 3500 cm^{-1} which are usually attributed to O–H group for moisture in the 750 °C RHA sample. For 20 % ARHA and 10 % ARHA there was no visible absorption in the same region of 3000 to 3500 cm^{-1}, which is a representation of −O−H group from water or Si−O−H.[22],[29] The peaks at 1021, 1098 and 1090 cm^{-1} at 750 °C for 10 % ARHA and 20 % ARHA samples, respectively, are often attributed to Si−O−Si asymmetric bond stretching vibration.[30] The peaks at 797, 794 and 795 cm^{-1} are attributed to the Si−O bending vibration band.[31] Most of the absorption peaks detected in the 750 °C RHA sample were also noticed to have disappeared in the 10 % ARHA and 20 % ARHA samples. This may be linked to effective removal of remnants lignin, cellulose and hemicellulose by the acid treatments. The spectra of sodium silicate show a strong broad peak at 3048.42 cm^{-1} which was attributed to presence of −OH group, associated to moisture. The peak at 1667.16 cm^{-1} is similarly a complementary −OH group caused by bending vibration of water.[17] While the strong stretching peak at 987.89 cm^{-1} is due the Si−O bond stretching of the silicon tetrahedron.[32,33] The peak at 1443.94 cm^{-1} may be attributed to C−O symmetric stretching of C−O−Si, due to some C sneaked or CO_2 absorbed into the separated solid.[34] Also the peak at 2355.14 cm^{-1} position may be attributed to O=C=O stretching, since sodium silicate crystals may have been exposed to atmospheric carbon(IV) oxide during the draining process of the crystal.

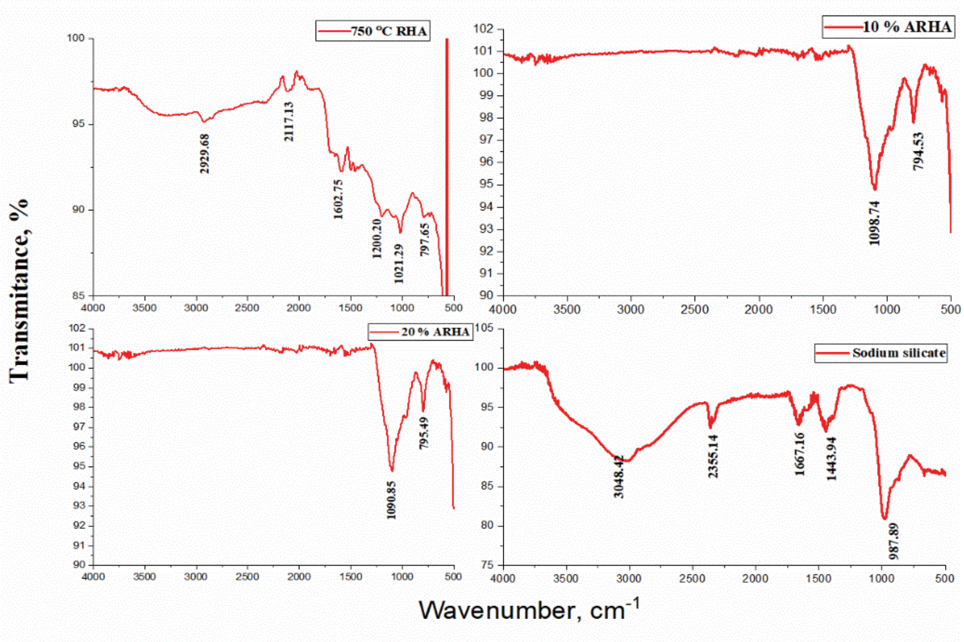

Fig. 4. FT-IR spectra of sodium silicate crystals.

Thermogravimetric analysis of sodium silicate crystals

The results of TGA for 750 °C RHA, 10 % ARHA, 20 % ARHA and sodium silicate crystals are shown in Fig. 5. It can be observed that a two-step weight loss occurs during the temperature treatments of RHA and 10 % ARHA. The first weight losses of 0.242 and 0.122 %, which occurs before 200 °C, can be attributed to physically adsorbed water.[35] The second step weight loss occurs between 200 and 400 °C, which may be attributed to loss of other volatile, probably trapped in the sample's matrix during initial preparation. The 20 % ARHA sample TGA curve depicts only one-step weight loss of 1.05 % between 28 and 450 °C. This weight loss may be attributed to release of trapped moisture as well as other volatiles. Overall, the TGA of 750 °C RHA, 10 % ARHA and 20 % ARHA samples appeared to be stable to heat treatment as about 98 % of the materials remain after 850–900 °C.

The TGA for the crystal sample shows that there was also two-step weight loss between 30 and 400 °C and between 400 and 500 °C. The first weight loss is considered a dehydration step, which is attributed to the loss of moisture in the crystal near and above its melting point as evidenced by the low weight loss of 1.777 %. The second weight loss may be attributed to the removal of mole equivalents of crystal water molecules from the crystals sample as signified by the large weight loss of 34.475 %. The residue obtained after the attainment of

550 °C is attributed to the formation of anhydrous sodium silicate. Beyond the 550 °C, the anhydrous silicate was relatively stable with about 55 % of sample remaining.

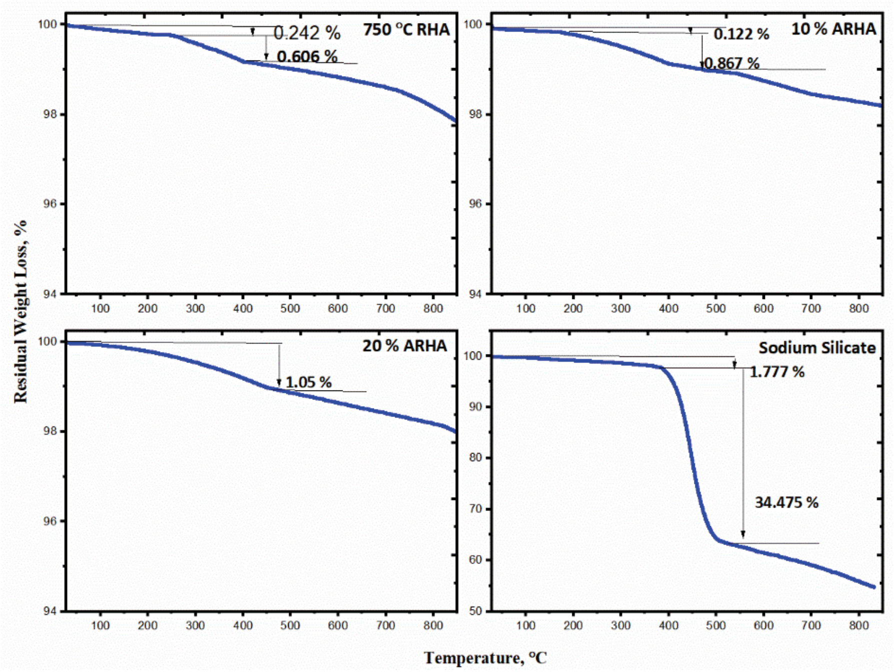

Fig. 5. Loss in weight measurements.

SEM morphological observation

The surface morphological appearance of the RHA obtained at 750 °C shows a micro-flaky and irregular shape with agglomeration (Fig. 6). For the 10 % ARHA the micro-flaky agglomeration possesses a wavy opening fitted with lateral pores much like an oval hexagon and the 20 % ARHA showed no wavy pattern opening while also showing rod-like microstructure and some micropores. The isolated rod-like structure seen in the 20 % ARHA bears evidence of induced crystallinity as a result of increased acid concentration. The sodium silicate morphology at 12000× magnification, Fig. 6d, shows an uneven surface and the appearance of tiny pores on the surface of agglomerated morphology. The surface of the crystal also appears to have slight indentation while the irregular pores appears to run deep.

Significant agglomeration of particles on the surface of the amorphous silica, used in the synthesis of sodium silicate from corncob and rice husk, as well as existence of pores within the agglomerates was also reported.[26]

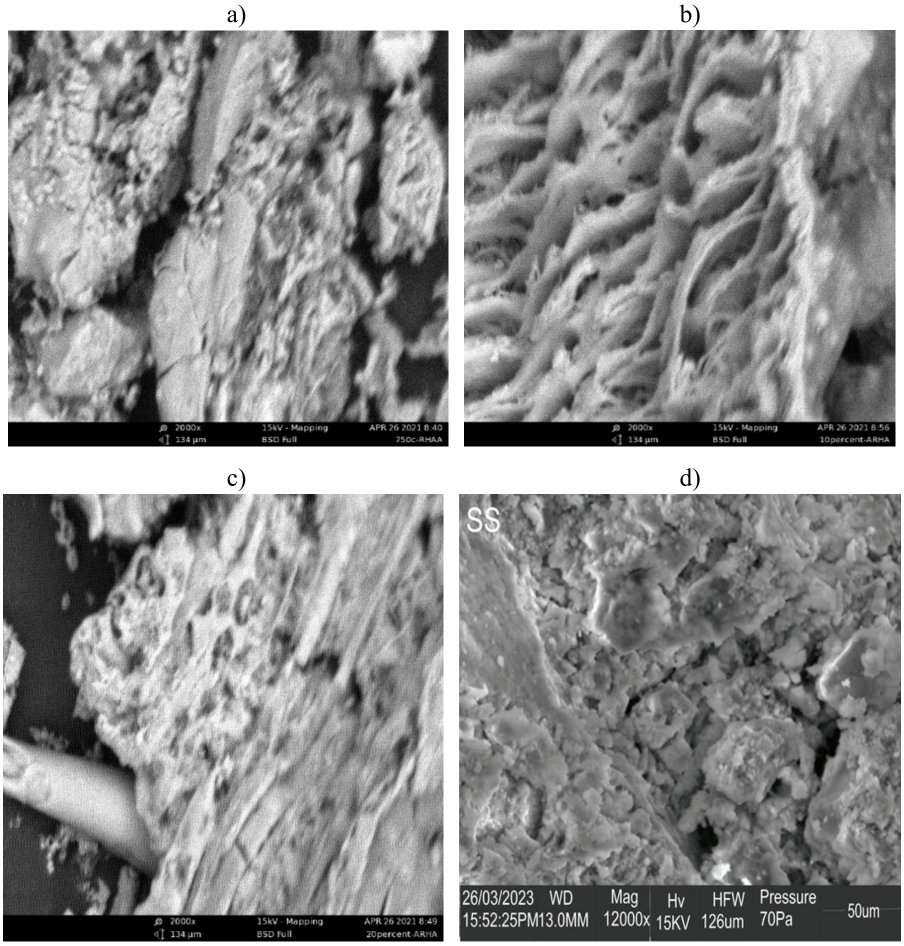
a) b) c) d)

Fig. 6. Scanning electron microscopic images of: a) 750 °C RHA, b) 10 % ARHA, c) 20 % ARHA and d) sodium silicate (SS) crystal surface.

CONCLUSION

Rice husk ash was used to synthesize crystalline sodium silicates. The acid treatment of RHA showed improvement on the purification of silica obtained as well as improved crystal structure. The similarity of all the RHA (750 °C, 10 % ARHA and 20 % ARHA) to the cristobalite phase also shows that treatment type affects the crystallinity of the silica obtained. The sodium silicate sample synthesized was found to contain two phases namely disodium orthosilicate (91.91 % $Na_2H_2SiO_4·7H_2O$) and trisodium orthosilicate (8.10 % $Na_3HSiO_4·2H_2O$), as revealed by the rietveld refinement analysis. Since disodium orthosilicate are often used in cosmetic formulations as an exfoliating agent or abrasive. The synthesized orthosilicate will be useful in improving skin texture when added to cosmetics.

LIST OF SYMBOLS AND ABBREVIATIONS

ARHA – Acid treated rice Husk Ash
ATR – Attenuated total reflectance
BSCA – Brownish Silicate Crystal Abuja
COD – Crystallography Open Database
DTA – Differential thermal analysis
EDXRF – Energy–dispersive X–ray fluorescence spectrometer
FAO – Food and Agriculture Organization
FTIR – Fourier transform infra-red spectrophotometer
RMRDC – Raw Materials Research and Development Council
RHA – Rice Husk Ash
SEM – Scanning electron microscope
SHESTCO – Sheda Science and Technology Complex
TGA – Thermogravimetry analysis
XRD – X-Ray diffraction/diffractometer
$R_{\rm wp}$ – Weight profile R-factor
$R_{\rm exp}$ – Expected R-factor
GoF – Goodness of fit

Acknowledgement. This work was supported by the Raw Material Research and Development Council of Nigeria.

ИЗВОД

СИНТЕЗА КРИСТАЛА НАТРИЈУМ-СИЛИКАТА ИЗ ПЕПЕЛА ПИРИНЧАНЕ ЉУСКЕ

STELLA ADEDUNNI EMMANUEL[1], ALHASSAN ADEKU SALLAU[1], OLUWASEYE ADEDIRIN[1], HUSSAIN DOKO IBRAHIM[2], MOHAMMED LAWAL BUGA[2], ANTHONY OKEREKE[2], GERTRUDE NGOZI OZONYIA[2] и FORTUNE MIEBAKA ALABI[2]

[1]*Chemistry Advanced Research Center, SHESTCO, Abuja, Nigeria и* [2]*Raw Materials Research and Development Council, RMRDC, Maitama, Abuja, Nigeria*

Због узгоја пиринча широм света, пиринчана љуска представља веома распрострањени пољопривредни отпад богат аморфним силицијумом. У овом раду, пиролизом на 750 °C пиринчана љуска је претворена у бели пепео (RHA), који је затим третиран киселином (ARHA). Након тога, добијена суспензија је третирана натријум-хидроксидом на 90 °C током 2,5 h, при чему долази до издвајања кристала натријум-силиката. Кристали натријум-силиката су окарактерисани на бази различитих физичко–хемијских параметара. За одређивање структуре силиката употребљени су инфрацрвени спектрофотометар са Фуријеовом трансформацијом (FT-IR), рендгенски дифрактометар (XRD) и скенирајући електронски микроскоп (SEM). За испитивање минералошког састава пепела и натријум-силиката коришћен је енергетски дисперзивни рендгенски флуоресцентни спектрометар (EDXRF). Тачка топљења добијених кристала натријум-силиката је 61 °C, pH 12,03, док је њихова боја била између светлосмеђе и светлосиве. Испитивања белог пепела помоћу XRD, након његове реакције са киселином (ARHA), показала су да испитивани узорци имају структуру минерала кристобалита, док структура натријум-силиката одговара структури минерала натријум-триоксосиликат-хептахидрат. Методом раздвајања по Ритвелду (*Rietveld refinement method*) примењеном на дифрактограме кристала натријум-силиката добијене су следеће вредности: $R_{\rm wp} = 12,81$, $R_{\rm exp} = 5,55$, $\chi^2 =$

= 5,3274 и GoF = 2,3081. Нађено је да су кристали натријум-силиката погодни за припрему козметичких формулација.

(Примљено 26. новембра 2022, ревидирано 3. априла, прихваћено 10. јула 2023)

REFERENCES

1. S. A. Ajeel, K. A. Sukkar, N. K. Zedin, *IOP Conf. Ser.: Mater. Sci. Eng.* **881** (2020) 012096 (https://doi.org/10.1088/1757-899X/881/1/012096)
2. K. T. Tong, R. Vinai, M. N. Soutsos, *J. Clean. Prod.* **201** (2018) 272 (https://doi.org/10.1016/j.jclepro.2018.08.025)
3. H. Gandhi, A. N. Tamaskar, H. Parab, & S. Purohit, *J. Basic Appl. Eng. Res.* **2** (2015) 330 (https://www.krishisanskriti.org/vol_image/07Jul2015100713xxHeta%20Gandhi%20%20%20%20%20%20%20%20%20%20%20%20%20%20330-333.pdf)
4. S. S. Owoeye, O. E. Isinkaye, *Sci. J. Chem.* **5** (2017) 8 (https://doi.org/10.11648/j.sjc.20170501.12)
5. G. T. Adylov, S. A. Faiziev, M. S. Paizullakhanov, S. Mukhsimov, É. Nodirmatov, *Tech. Phys. Lett.* **29** (2003) 221 (http://dx.doi.org/10.1134/1.1565639)
6. M. K. Omatola, D. A. Onojah*, Int. J. Phy. Sci.* **4** (2009)189 (http://www.academicjournals.org/ijps/PDF/pdf2009/April/Omotola%20and%20Onojah.pdf)
7. R. V Krishnarao, J. Subrahmanyam, & T. J. Kumar, *J. Eur. Ceram. Soc.* **21** (2001) 99 (https://doi.org/10.1016/S0955-2219(00)00170-9)
8. A. Mehta, R. P. Ugwekar, *IJERA* **5** (2015) 43 (https://www.ijera.com/papers/Vol5_issue8/)
9. H. Engelhardt, L. E. Von Borstel, *Z. Dtsch. Ges. Grundwasser* **165** (2020) 115 (https://doi.org/10.1127/1860-1804/2014/0057)
10. N. V. Zubkova, I. V. Pekov, D. Yu. Pushcharovsky, *Min. Mag*. **78** (2014). 253 (https://doi.org/10.1180/minmag.2014.078.2.03)
11. V. Kahlenberg, *Min. Chim.* **64** (2010) 716 (https://doi.org/10.2533/chimia.2010.716)
12. M. Macdonald, X. Li, *AADE Fluids Tech. Conf. Exh.(2014)*, 2014, pp. 1–6 (https://www.aade.org/download_file/2069/420)
13. M. Adamu, J. O. Okafor, G. T. David*, J. Sci. Technol. Math. Educ.* **11** (2015) 163 (https://jostmed.futminna.edu.ng/image/JOSTMED/Jostmed_11_2_August_2015)
14. J. X. Dong, L. P. Li, H. Xu, F. Deng, G. Y. Zhang, J. P. Li, X. J. Ai, *Tenside Surf. Det.* **44** (2007) 34 (https://doi.org/10.3139/113.100326)
15. S. Yunusa, I. A. Mohammed-Dabo, A. S. Ahmed, *Int. J. Sci. Eng. Res.* **6** (2015) 1183 (http://www.ijser.org)
16. J. L. Thompson, B. E. Scheetz, M. R. Schock, D. A. Lytle, *Pro. AWWA Wat. Qual. Tech. Conf.* **9** (1997) (https://aniq.org.mx/pdf)
17. G. K. Sharma, J. Gadiya and M. Dhanawat, *Textbook of Cosmetic Formulations* (https://www.researchgate.net/publication/325023106)
18. E. L. Foletto, E. Gratieri, L. H. Oliveira, S. L. Jahn, *Mater. Res.* **9** (2006) 335 (https://doi.org/10.1590/S1516-14392006000300014)
19. Y. Shen, P. Zhao, Q. Shao, *Micropor. Mesopor. Mater.* **188** (2014) 46 (https://doi.org/10.1016/j.micromeso.2014.01.005)
20. X. Liu, Z. Li, H. Chen, L. Yang, Y. Tian, Z. Wang, *Res. Chem. Intermed.* **42** (2015) 3887 (https://doi.org/10.1007/s11164-015-2251-7)

21. J. Monzo, M. V Borrachero, A. Mellado, L. M. Ordon, J. Paya, *Cem. Concr. Res.* **31** (2001) 227 (https://doi.org/10.1016/S0008-8846(00)00466-X)
22. R. Patil, R. Dongre, J. Meshram, *IOSR J. Appl. Chem.* **2014** (2014) 26 (https://www.iosrjournals.org/iosr-jac/papers/ICAET-2014/volume-1/6.pdf)
23. *G. V. V. Gowthami, A. Sahoo*, *MSc Thesis*, National Institute of Technology, Rourkela, 2015 (http://ethesis.nitrkl.ac.in/6867/1/Preparation_Gowthami_2015.pdf)
24. B. F. Shihab, *Iraqi J. Phys.* **16** (2018) 117 (https://doi.org/10.30723/ijp.v16i39.109)
25. S. S. Owoeye, S. M. Abegunde, B. Oji, *Global J. Eng. Tech. Adv.* **06**(01) (2021) 066 (https://doi.org/10.30574/gjeta.2021.6.1.0001)
26. A. G. A. Siregar, R. Manurung, T. Taslim, *Indones. J. Chem.* **21** (2021) 88 (https://doi.org/10.22146/ijc.53057)
27. E. L. Foletto, E. Gratieri, L. H. de Oliveira, S. L. Jahn, *Mater. Res*. **9** (2006) 335 (https://doi.org/10.1590/S1516-14392006000300014)
28. N. Döbelin, R. Kleeberg, *J. Appl. Crystallogr.* **48** (2015) 1 (https://doi.org/10.1107/S1600576715014685)
29. I. U. Haq, K. Akhtar, A. Malik, *J. Chem. Soc. Pak.* **36** (2014) 382 (https://www.researchgate.net/publication/286071234)
30. P. Taylor, J. P. Nayak, J. Bera, *Trans. Indian Ceram. Soc.* **68** (2015) 37 (https://doi.org/10.1080/0371750X.2009.11082163)
31. I. M. Joni, L. Nulhakim, M. Vanitha, C. Panatarani, *J. Phys. Conf. Ser.* **1080** (2018) 012006 (https://doi.org/10.1088/1742-6596/1080/1/012006)
32. L. Fernández-Carrasco, D. Torrens-Martín, L.M. Morales, Sagrario Martínez-Ramírez, in *Infrared Spectroscopy – Materials Science, Engineering and Technology*, T. Theophanides, Ed.,. InTech, Rijeka, 2012 (https://doi.org/10.5772/36186)
33. C. Kongmanklang, K. Rangsriwatananon, *J. Spectrosc., Spectrosc. Mater. Chem.* **2015** (2015) 696513 (https://doi.org/10.1155/2015/696513)
34. J. Coates, in *Encyclopedia of Analytical Chemistry,* R.A. Meyers, Ed., John Wiley & Sons Ltd, Chichester, 2000, pp. 10815–10837 (https://analyticalscience.wiley.com/do/10.1002/sepspec.10120education/full/i97dca9608c7bfa88fcf79f9b29f68226.pdf)
35. P. E. Imoisili, K. O. Ukoba, T. Jen, *Bol. Soc. Esp. Cerám. Vidrio* **59** (2020) 159 (https://doi.org/10.1016/j.bsecv.2019.09.006).

Journal of the Serbian Chemical Society
JSCS@tmf.bg.ac.rs • www.shd.org.rs/JSCS

J. Serb. Chem. Soc. *88* (10) 1013–1023 (2023)
JSCS–5677

Original scientific paper
Published 24 October 2023

Identification of organic compounds using artificial neural networks and refractive index

INNOCENT ABEL KIRIGITI[1], NANIK SITI AMINAH[1]* and SAMSON THOMAS[2]

[1]Department of Chemistry, Faculty of Science and Technology, Universitas Airlangga, Surabaya 60115, Indonesia and [2]Department of Chemistry, Faculty of Mathematics and Natural Sciences, Universitas Indonesia, Depok 16424, Indonesia

(Received 1 February, revised 15 February, accepted 4 August 2023)

Abstract: Identification of chemical compounds has many applications in science and technology. However, this process still relies significantly on the knowledge and experience of chemists. Thus, the development of techniques for faster and more accurate chemical compound identification is essential. In this work, we demonstrate the feasibility of using artificial neural networks to accurately identify organic compounds through the measurement of refractive index. The models were developed based on the refractive index measurements in different wavelengths of light, from UV to the far-infrared region. The models were trained with about 250,000 records of experimental optical constants for 60 organic compounds and polymers from published literature. The models performed with accuracies of up to 98 %, with better performance observed for the refractive index measurements across the visible and IR regions. The proposed models could be coupled with other devices for autonomous identification of chemical compounds using a single-wavelength dispersive measurement.

Keywords: machine learning; ANNs; classification, deep learning, materials identification.

INTRODUCTION

Organic material identification is a vital process across various industries such as pharmaceuticals, food, agriculture and environmental science. The ability to identify organic compounds quickly and accurately is imperative for the development of new products, monitoring environmental pollutants and detecting contaminants in food and drugs.[1–3] However, the traditional methods of material identification, such as gas chromatography and mass spectrometry, can be tedious and costly.[4,5] Therefore, it is crucial to explore new ways to facilitate organic

---

* Corresponding author. E-mail: nanik-s-a@fst.unair.ac.id

https://doi.org/10.2298/ JSC230201049K

materials identification. One such approach that has gained attention recently is the use of machine learning techniques.

Machine learning (ML) is a branch of computer science that focuses on developing algorithms that can learn from and make decisions based on complex data.[6] One recent development in ML is deep learning, a cutting-edge field that uses artificial neural networks (ANNs) to improve the performance of traditional ML models.[7] ANNs are artificial systems that are modelled after biological neural networks and are able to learn and perform tasks without pre-programmed rules by being exposed to various datasets and examples.[8] Deep learning is among the most effective, efficient, and cost-effective approaches to ML.[9] Additionally, ANNs have the advantage of being able to increase their accuracy in production. Unlike traditional ML models like random forests, ANNs do not need to be fully re-trained as more data becomes available; this can lead to significant cost savings in terms of computational resources. Therefore, ANNs are a suitable approach to ML.

ANNs have found applications in various fields such as environmental science, where they are used to predict the percentage of water pollutant removal based on experimental variables such as temperature and treatment time.[10–12] Moreover, Raman spectroscopy imaging has been widely used in combination with machine learning (ML) techniques to identify the properties and structures of organic compounds. Raman spectroscopy is a non-destructive imaging method that provides information about the vibrational modes of a compound, which can be used to determine its chemical structure and composition.

One of the key benefits of using Raman spectroscopy imaging in conjunction with ML algorithms is its ability to accurately identify the chemical structure and composition of various organic compounds.[13,14] Studies have reported ML models based on Raman spectra that were able to classify materials like biomolecules, organics and inorganics.[15–18]

Despite the higher performance of ML models using spectra images as input, the setup and equipment for obtaining associated spectra data is more complex and expensive. Therefore, a simple measurement like the refractive index (n) can offer alternatives. Refractive index of a sample is defined as the ratio of the speed of light in a vacuum to its speed in the sample medium.

The chemical composition of a sample can also affect its refractive index through the presence of certain functional groups or atoms that can interact with light in specific ways.[19] For example, refractive index has been used for detection of components with low chromophoric activities such as sugars, triglycerides, organic acids, pharmaceutical excipients, and polymers.[20] So, the refractive index is an optical property that carries enough information related to chemical composition.

Machine learning models for predicting refractive indices of polymers have been previously reported.[21,22] In another work, refractive index was used as the input to ML models to differentiate between normal and malignant tissues in biomedical.[23]

This work was inspired by a study attempting to apply random forests (RF), a traditional ML algorithm and refractive index to identify organic compounds.[24] In order to train the machine learning models, we use data from a public database of refractive indices for organic compounds and polymers. The database contains data from literature gathered over a long period of time.[25]

To the best of our knowledge, this is the first work to report the use of refractive index for classification of organic compounds with artificial neural networks (ANNs).

EXPERIMENTAL

Database

Version 1.0.0 of a web scrapper built using Python was run on the refractive index website, which is a database for experimental optical constants from published literature since 1940.[25] The scrapper targeted 60 organic compounds and polymers. The scrapped data was stored as comma-separated values (CSV). The file contains four columns: organic compound (book), wavelength (λ), refractive index (n) and extinction coefficient (k). The scrapped database has a total of 248,756 entries and 9645 missing values of k.

The database was split into five categories as follows (Fig. 1): ultraviolet (0–0.4 μm), visible (0.4–0.75μm), near IR (0.75–1.5 μm), IR (1.5–4μm) and far IR (>4 μm).

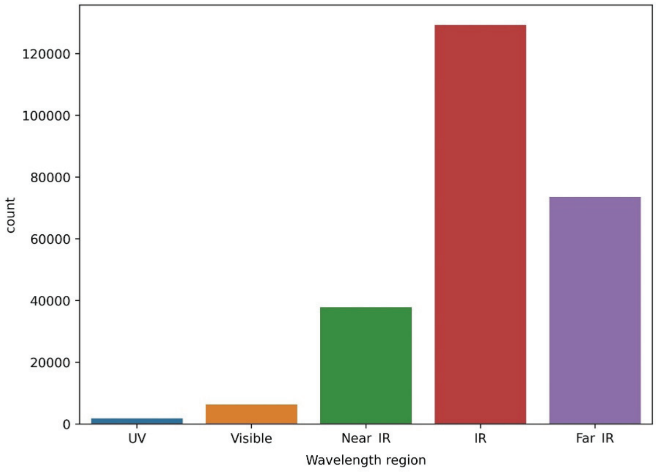

Fig. 1. Raw scrapped data from the refractive index website.

Data pre-processing

All the missing values for extinction coefficients in the raw database were replaced by zero. Since the UV and visible data was not enough for training the models, the data augmentation was performed on these regions using the Sellmeier equation.[26] This is a mathematical formula that can be used to predict the refractive index of a material as a function of wavelength. The data augmentation was required to artificially synthesize more data using domain knowledge,[27] which is a technique used previously with Raman spectra-based organic classifiers.[16–18]

The Sellmeier equation is given by the following equation:

$$n^2(\lambda) = 1 + \frac{B_1\lambda_2}{\lambda_2 - C_1} + \frac{B_2\lambda_2}{\lambda_2 - C_2} + ... \tag{1}$$

Where $n(\lambda)$ is the refractive index at wavelength λ. B_1, B_2,... and C_1, C_2,... are Sellmeier coefficients that are specific to the material. A custom Python script was used to estimate the missing Sellmeier coefficients by curve fitting (see the supporting information).

Artificial neural network classifiers (ANNs) for organic compounds

Scikit-Learn, TensorFlow and Keras Python libraries were used for training and evaluating the accuracy of the ANN classifiers. This was done in a Google Collaboratory environment.[28,29] Seven different models were developed according to available categories (see Fig. 4 later on). Each model contains three main layers: an input layer, hidden layers, and an output layer. The input layer takes in three independent variables: λ, n and the extinction coefficient (k). Hidden layers contain neurons; they extract and represent features from the input data, allowing the network to learn. The output layer performs the final compound classification, which is based on voting among 60 possible compounds. The compound with a high probability is considered the output of the model.[7,28] An overview of the model design is shown in Fig. 2.

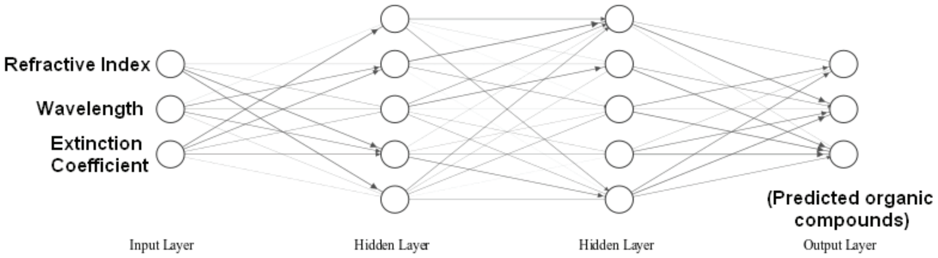

Fig. 2. ANN organic classifier model architecture.

To evaluate the model's performance, monitoring was performed during the training and testing stages. In the training stage, the loss and accuracy of all models were monitored by a validation data set. If the model's prediction is perfect, the loss is zero. This tells how poorly or well a model behaves after each iteration of the optimization.[29,30] On the other hand, the testing stage was performed using a test data set; the test data serves as an estimate of its performance on new, unseen, data.

Accuracy, precision, recall and the $F1$ score were used as evaluation metrics for the classifier. Precision tells us how many of the positive predictions were correct; recall tells us how many of the actual positives were identified while the $F1$ score gives a single metric to evaluate the overall performance of the model by balancing precision and recall.[28,31] These evaluation metrics are mathematically defined as follows:

$$\text{Precision} = \frac{TP}{TP + FP} \tag{2}$$

$$\text{Recall} = \frac{TP}{TP + FN} \tag{3}$$

$$F1\text{score} = \frac{2\times\text{Precision}\times\text{Recall}}{\text{Precision}+\text{Recall}} \tag{4}$$

where the term true positives (*TP*) refer to the number of samples correctly predicted as positive, while false positives (*FP*) indicate the number of samples incorrectly predicted as positive. Similarly, true negatives (*TN*) refer the number of samples correctly predicted as negative and false negatives (*FN*) represents the number of samples incorrectly predicted as negative.

RESULTS AND DISCUSSION

Data pre-processing

Analysis of the raw data revealed the percent of missing extinction coefficient values in each region as follows (Fig. 3): UV (58.99 %), visible (82.67 %), near IR (7.28 %), IR (0.32 %) and far IR (0.25 %). The final database with data augmentation contains seven categories (Fig. 4). The UV region data was increased from 1807 to 132314, and the visible region data was increased from 6268 to 120455. The amount of data in other regions was left unaltered.

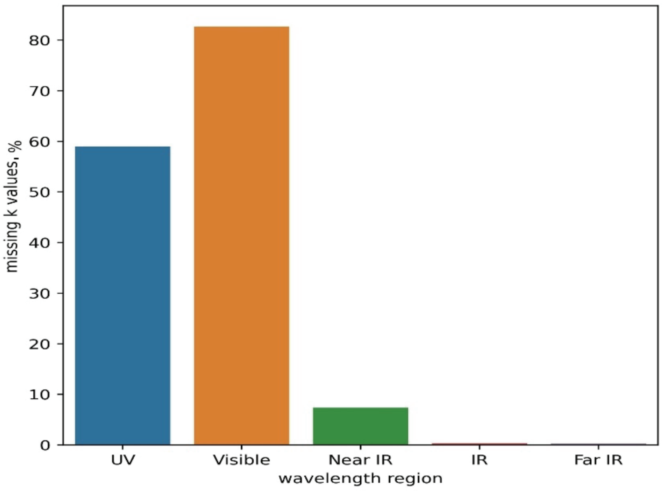

Fig. 3. Missing extinction coefficient values in raw data.

Performance of artificial neural network classifiers

The accuracies of the ANN models are listed in the following order: Near IR (98.44 %) > IR (97.72 %) > visible-augmented (86.60 %) > far IR (84.09 %) > UV-augmented (81.49 %) > visible (69.22 %) > UV (59.00 %). It is observed that models in the near IR and IR regions outperform other regions (Fig. 5). Moreover, from Figs. 6 and 7, the losses of the near IR and IR regions converge to low and stable values, while the accuracy reaches high and stable values. This indicates that the models in the near IR and IR regions are generalizing well and not overfitting.[28,32] The precision, recall and *F*1 scores of the near IR and IR models shows high performance of above 98 % (Table I).

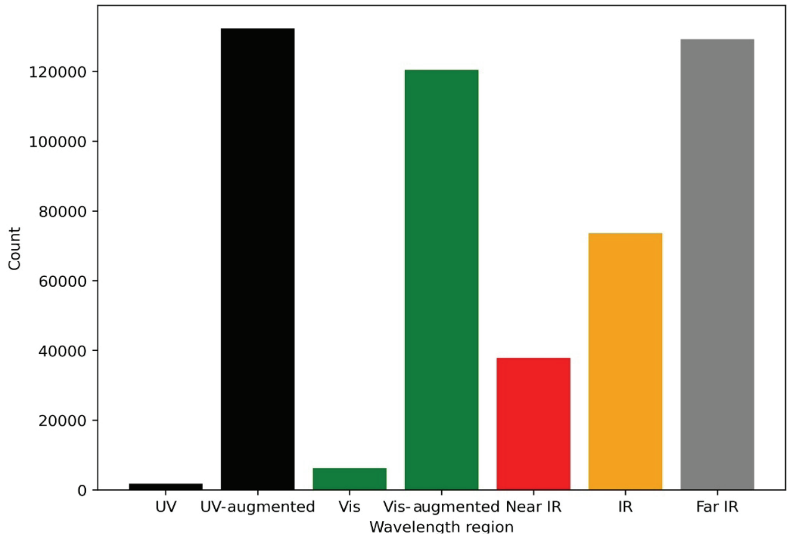

Fig. 4. Augmented refractive index data.

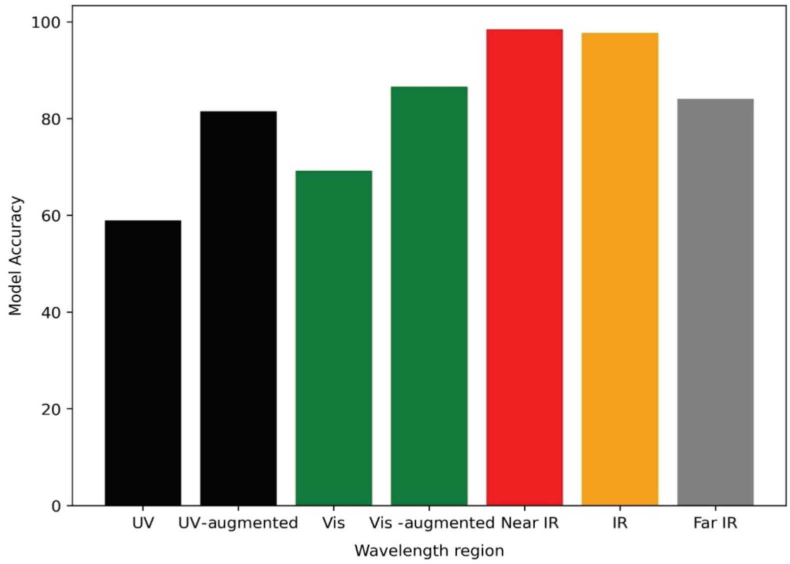

Fig. 5. Testing accuracies for the ANN classifiers.

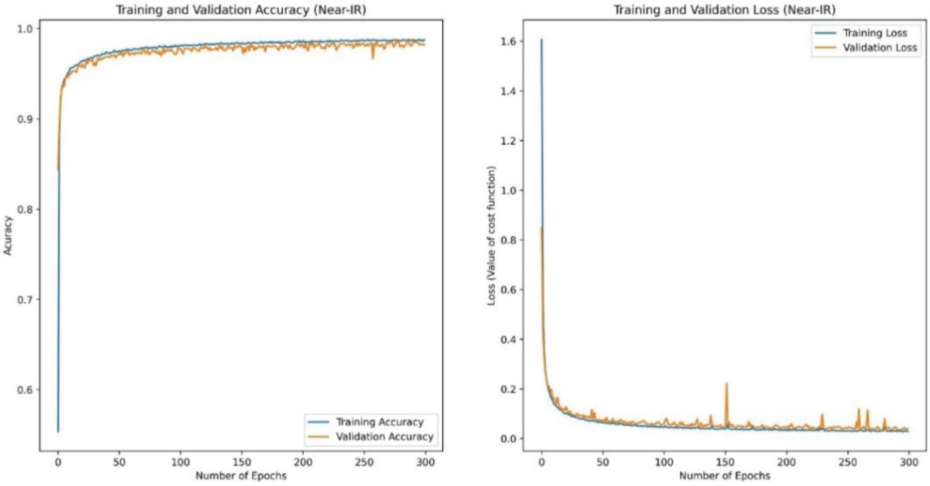

Fig. 6. Training and validation for ANN model in near IR region.

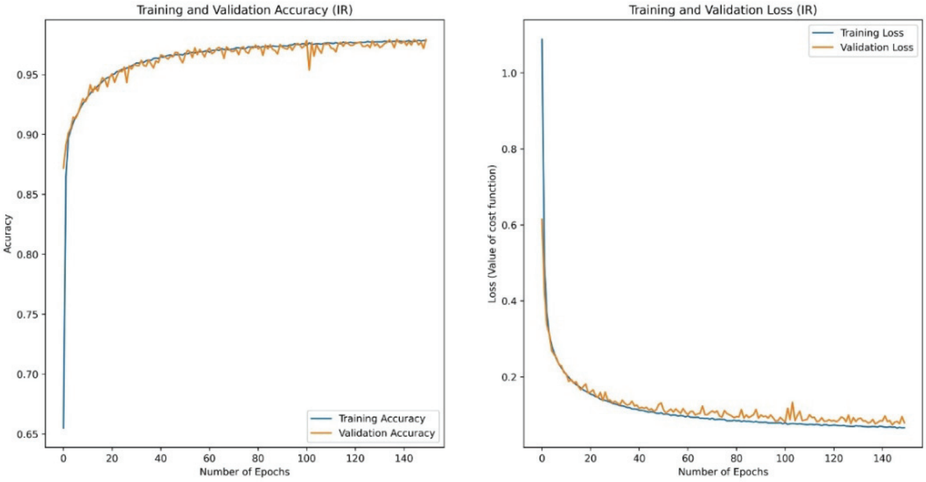

Fig. 7. Training and validation for ANN model in IR region.

TABLE I. Performance evaluation for ANN classifiers

ANN Model	Precision, %	Recall, %	*F*1 score, %	Accuracy, %
UV	79.00	81.00	79.00	59.00
UV – augmented data	82.00	82.00	81.00	81.49
Visible	73.00	69.00	67.00	69.22
Visible – augmented data	86.00	87.00	85.00	86.60
Near IR	99.00	98.00	98.00	98.44
IR	98.00	98.00	98.00	97.72
Far IR	85.00	84.00	84.00	84.09

Meanwhile, the performance of models in the far IR, UV and visible regions is unsatisfactory. The recall, precision and $F1$ scores in these regions are low (Table I). Their loss-accuracy plots show unstable values, and bumpy non-converging lines, indicating their unreliability (Figs. S1–S5 of the Supplementary material tp this paper). For UV and visible regions, more than 58 % of k values were missing in their datasets (Fig. 3), which may provide the model with less information to accurately learn the relationships between input and output variables. As a result, overfitting or poor generalization performance may be observed.[33]

Nevertheless, the accuracies for UV and visible models were observed to increase by more than 17 % with data augmentation (Fig. 5); this suggests the possibility of improving the performance by increasing the amount of training data in these regions.

The accuracy and loss plots obtained from the near IR (Fig. 6) and IR (Fig. 7) models are smoother, and the lines converge well, while plots for models containing augmented data show convergence but with bumpy lines (Fig. S1––S5). This implies that the validation dataset is not a good representation of the training data set; this may be due to artificially synthesized data from the data augmentation process, which introduced noise.[28,32]

Comparison with other machine learning organic classifiers

The developed models are comparable with models from previous studies (Table II), indicating the potential of using the refractive index measurement to facilitate the identification of organic compounds using machine learning.

TABLE II. Comparison of this work with some previous studies using Raman spectra data with machine learning. ResNet = residual neural network, DRCNN = deeply-recursive convolutional neural network, ANN = artificial neural network, CNN = convolutional neural network, *K*NN = *K*-nearest neighbor, ML = machine learning

Method	Dataset	Accuracy, %	Reference
ResNet	Organic biomolecules	100.00	15
CNN	Organic and inorganic compounds	100.00	16
DRCNN	Organic compounds and minerals	98.10	17
KNN	Organic biomolecules	93.90	15
KNN	Edible oils (fatty acids)	88.90	18
ANN classifier	Organic compounds and polymers	81.49 (UV) 86.60 (Vis) 98.44 (Near IR) 97.72 (IR) 84.09 (Far IR)	This work

CONCLUSION

In this study, the artificial neural network classifiers (ANNs) for identifying organic compounds were developed and tested successfully. The models rely on refractive index measurements across the UV and far IR spectral regions. Information related to the refractive index of an organic compound and the wavelength of light used facilitate its accurate identification by artificial neural networks.

ANNs in the near IR and IR regions showed better performance, with the accuracy levels above 97 %, suggesting the potential of refractive index measurements in these regions. The observed performance is comparable to models using Raman spectra as inputs. Although the accuracies for the UV, visible and far IR regions are slightly lower, ranging from 81 to 86 %, the additional data and hyperparameter optimizations showed the possibility of improving performance in the future.

This study demonstrates the feasibility of using artificial neural networks to identify organic compounds using a single wavelength dispersive measurement.

SUPPLEMENTARY MATERIAL

Additional data and information are available electronically at the pages of journal website: https://www.shd-pub.org.rs/index.php/JSCS/article/view/12261, or from the corresponding author on request.

ИЗВОД

ИДЕНТИФИКАЦИЈА ОРГАНСКИХ ЈЕДИЊЕЊА КОРИШЋЕЊЕМ ВЕШТАЧКИХ НЕУРОНСКИХ МРЕЖА И ИНДЕКСА ПРЕЛАМАЊА

INNOCENT ABEL KIRIGITI[1], NANIK SITI AMINAH[1] и SAMSON THOMAS[2]

[1]*Department of Chemistry, Faculty of Science and Technology, Universitas Airlangga, Surabaya 60115, Indonesia and* [2]*Department of Chemistry, Faculty of Mathematics u Natural Sciences, Universitas Indonesia, Depok 16424, Indonesia*

Идентификација хемијских једињења има много примена у науци и технологији. Међутим, овај се процес још увек много ослања на знање и искуство хемичара. Тако је од суштинске важности развој техника за брже и поузданије идентификовање хемијских једињења. У овом раду, представићемо изводљивост коришћења неуронских мрежа за поуздано идентификовање органских једињења мерењем индекса преламања. Развијени су модели засновани на мерењима индекса преламања на различитим таласним дужинама светлости, од UV до далеке инфрацрвене области. Модели су тренирани са око 250,000 записа експерименталних оптичких константи за 60 органских једињења и полимера из публиковане литературе. Модели су извођени са поузданошћу до 98 %, са бољим резултатом опаженим за мерења индекса преламања у видљивој и ИЦ области. Предложени модели се могу спрегнути са другим уређајима за аутономну идентификацију хемијских једињења дисперзивним мерењем на једној таласној дужини.

(Примљено 1. фебруара, ревидирано 15. фебруара, прихваћено 4. августа 2023)

REFERENCES

1. W. Shi, W.-E. Zhuang, J. Hur, L. Yang, *Water Res.* **188** (2021) 116406 (https://doi.org/10.1016/j.watres.2020.116406)
2. J. Borrull, A. Colom, J. Fabregas, F. Borrull, E. Pocurull, *J. Chromatogr., A* **1621** (2020) 461090 (https://doi.org/10.1016/j.chroma.2020.461090)
3. L. Díaz de León-Martínez, R. Flores-Ramírez, C. M. López-Mendoza, M. Rodríguez-Aguilar, G. Metha, L. Zúñiga-Martínez, O. Ornelas-Rebolledo, L. E. Alcántara-Quintana, *Clin. Chim. Acta* **522** (2021) 132 (https://doi.org/10.1016/j.cca.2021.08.014)
4. C. Zarfl, *Anal. Bioanal. Chem.* **411** (2019) 3743 (https://doi.org/10.1007/s00216-019-01763-9)
5. B. Nozière, M. Kalberer, M. Claeys, J. Allan, B. D'Anna, S. Decesari, E. Finessi, M. Glasius, I. Grgić, J. F. Hamilton, T. Hoffmann, Y. Iinuma, M. Jaoui, A. Kahnt, C. J. Kampf, I. Kourtchev, W. Maenhaut, N. Marsden, S. Saarikoski, J. Schnelle-Kreis, J. D. Surratt, S. Szidat, R. Szmigielski, A. Wisthaler, *Chem. Rev.* **115** (2015) 3919 (https://doi.org/10.1021/cr5003485)
6. T. F. G. G. Cova, A. A. C. C. Pais, *Front. Chem.* **7** (2019) 809 (https://doi.org/10.3389/fchem.2019.00809)
7. C. Janiesch, P. Zschech, K. Heinrich, *Electron. Mark.* **31** (2021) 685 (https://doi.org/10.1007/s12525-021-00475-2)
8. P. P. Shinde, S. Shah, in *Proceedings of 2018 Fourth Int. Conf. Comput. Commun. Control Autom.,* 2018, pp. 1–6 (https://doi.org/10.1109/ICCUBEA.2018.8697857)
9. S. Dargan, M. Kumar, M. R. Ayyagari, G. Kumar, *Arch. Comput. Methods Eng.* **27** (2020) 1071 (https://doi.org/10.1007/s11831-019-09344-w)
10. E. Yabalak, *J. Environ. Sci. Heal., A* **53** (2018) 975 (https://doi.org/10.1080/10934529.2018.1471023)
11. E. Yabalak, Ö. Yilmaz, *J. Iran. Chem. Soc.* **16** (2019) 117 (https://doi.org/10.1007/s13738-018-1487-8)
12. E. Yabalak, B. Külekçi, A. M. Gizir, *J. Environ. Sci. Heal., A* **54** (2019) 1412 (https://doi.org/10.1080/10934529.2019.1647749)
13. M. H. W. N. Jinadasa, A. C. Kahawalage, M. Halstensen, N.-O. Skeie, K.-J. Jens, in *Recent developments in atomic force microscopy and Raman spectroscopy for materials characterization*. C. S. Pathak, S. Kumar, Eds., InTech Open, Rijeka, 2021 (https://doi.org/10.5772/INTECHOPEN.99770)
14. L. Pan, P. Zhang, C. Daengngam, S. Peng, M. Chongcheawchamnan, *J. Raman Spectrosc.* **53** (2022) 6 (https://doi.org/10.1002/jrs.6225)
15. X. Chen, L. Xie, Y. He, T. Guan, X. Zhou, B. Wang, G. Feng, H. Yu, Y. Ji, *Analyst* **144** (2019) 4312 (https://doi.org/10.1039/C9AN00913B)
16. T. Cooman, T. Trejos, A. H. Romero, L. E. Arroyo, *Chem. Phys. Lett.* **787** (2022) 139283 (https://doi.org/10.1016/J.CPLETT.2021.139283)
17. W. Zhou, Y. Tang, Z. Qian, J. Wang, H. Guo, *RSC Adv.* **12** (2022) 5053 (https://doi.org/10.1039/D1RA08804A)
18. C. Berghian-Grosan, D. A. Magdas, *Talanta* **218** (2020) 121176 (https://doi.org/10.1016/J.TALANTA.2020.121176)
19. J. M. Hollas, *Modern spectroscopy*, 4th ed., Wiley & Sons, Chichester, 2004, ISBN: 978--1-118-68160-2
20. M. W. Dong, *Sep. Sci. Technol.* **6** (2005) 47 (https://doi.org/10.1016/S0149-6395(05)80047-9)

21. J. P. Lightstone, L. Chen, C. Kim, R. Batra, R. Ramprasad, *J. Appl. Phys.* **127** (2020) 215105 (https://doi.org/10.1063/5.0008026)
22. S. A. Schustik, F. Cravero, I. Ponzoni, M. F. Díaz, *Commun. Comput. Inf. Sci.* **1408** (2021) 279 (https://doi.org/10.1007/978-3-030-76310-7)
23. N. Qi, Z. Zhang, Y. Xiang, Y. Yang, X. Liang, P. D. B. Harrington, *Anal. Methods* **7** (2015) 2333 (https://doi.org/10.1039/C4AY02665A)
24. T. Bikku, R. A. Fritz, Y. J. Colón, F. Herrera, *Machine learning identification of organic compounds using visible light,* 2022 (https://doi.org/10.48550/arxiv.2204.11832)
25. M. N. Polyanskiy, *Refractive index database*, https://refractiveindex.info/ (accessed: August 20, 2022)
26. J. W. Gooch, *Encycl. Dict. Polym.* (2011) 653 (https://doi.org/10.1007/978-1-4419-6247-8_10447)
27. J. K. Kim, J. Shao, *Statistical Methods for Handling Incomplete Data*, Chapman and Hall/CRC, Boca Raton, FL, 2021 (https://doi.org/10.1201/9780429321740)
28. A. Géron, *Hands-on machine learning with Scikit-Learn and TensorFlow : concepts, tools, and techniques to build intelligent systems*, 2nd ed., O'Reilly Media, Inc., Sebastopol, CA, 2019, ISBN: 9781492032649
29. E. Bisong, *Building Machine Learning and Deep Learning Models on Google Cloud Platform*, Apress, Berkeley, CA, 2019 (https://doi.org/10.1007/978-1-4842-4470-8)
30. *Machine Learning in Chemistry*, H. M. Cartwright, Ed., Royal Society of Chemistry, 2020 (https://doi.org/10.1039/9781839160233)
31. J. Han, J. Pei, H. Tong, *Data mining: concepts and techniques*, Morgan Kaufmann, Burlington, MA, 2011, ISBN 978-0-12-381479-1
32. F. Chollet, *Deep Learning with Python*, Manning Publications Co, Shelter Island, NY, 2017, ISBN 9781617294433
33. M. Fernández-Delgado, E. Cernadas, S. Barro, D. Amorim, A. Fernández-Delgado, *J. Mach. Learn. Res.* **15** (2014) 3133 (http://jmlr.org/papers/v15/delgado14a.html).

Journal of the Serbian Chemical Society
JSCS@tmf.bg.ac.rs • www.shd.org.rs/JSCS
J. Serb. Chem. Soc. 88 (10) S312–S315 (2023)
Supplementary material

SUPPLEMENTARY MATERIAL TO

Identification of organic compounds using artificial neural networks and refractive index

INNOCENT ABEL KIRIGITI[1], NANIK SITI AMINAH[1]* and SAMSON THOMAS[2]

[1]Department of Chemistry, Faculty of Science and Technology, Universitas Airlangga, Surabaya 60115, Indonesia and [2]Department of Chemistry, Faculty of Mathematics and Natural Sciences, Universitas Indonesia, Depok 16424, Indonesia

J. Serb. Chem. Soc. 88 (10) (2023) 1013–1023

Table S-I. Accuracy scores for the developed ANNs

ANN Model (Per wavelength region)	Training Accuracy (%)	Validation Accuracy (%)	Testing Accuracy (%)
UV	60.00	59.00	59.00
UV - augmented data	82.59	76.73	81.49
Visible	73.33	70.76	69.22
Visible – augmented data	86.17	86.65	86.60
Near IR	98.62	98.58	98.44
IR	97.89	97.76	97.72
Far IR	86.81	83.79	84.09

---

* Corresponding author. E-mail: nanik-s-a@fst.unair.ac.id

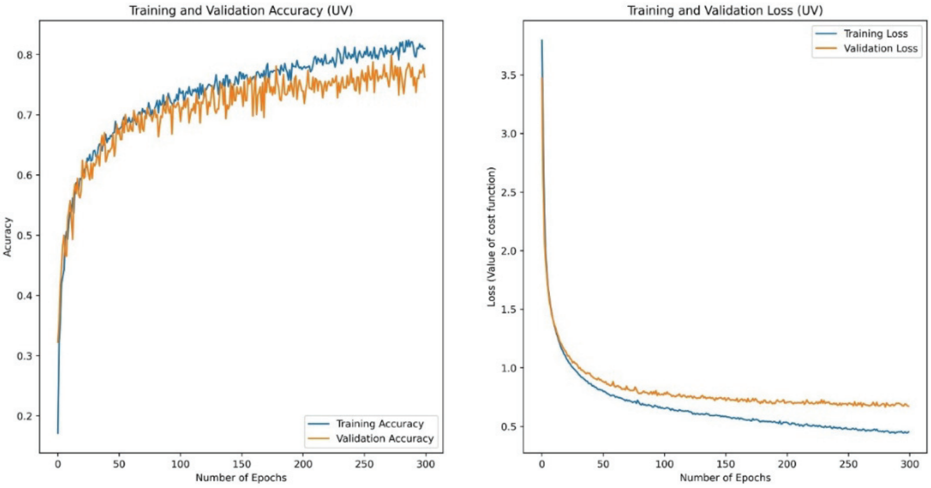

Fig. S-1. Training and validation for ANN model in UV region

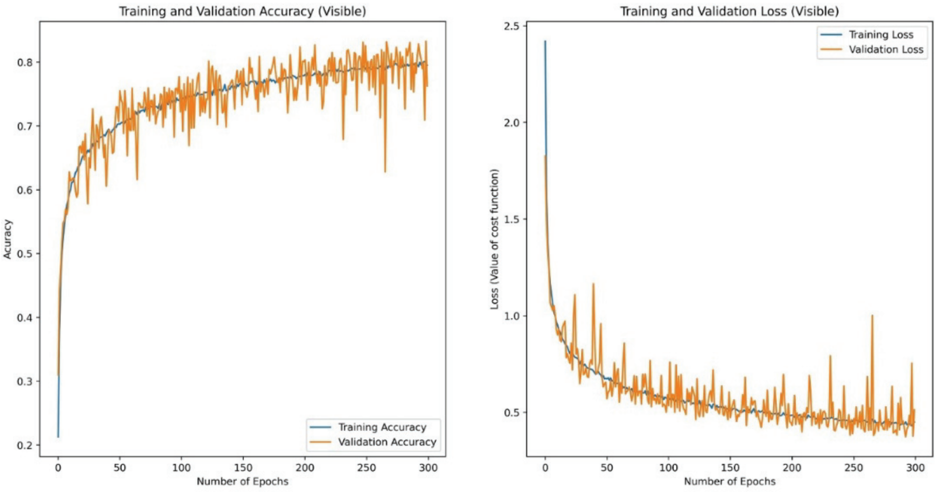

Fig. S-2. Training and validation for ANN model in UV (augmented)

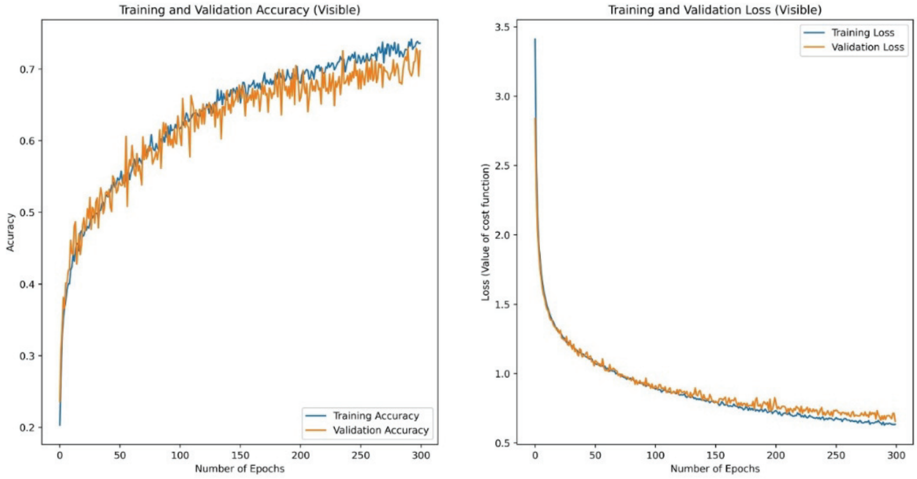

Fig. S-3. Training and validation for ANN model in visible region

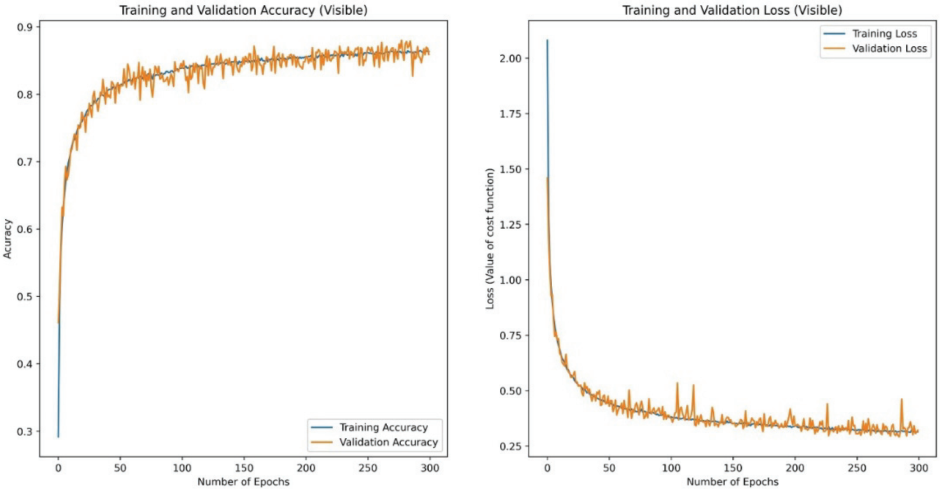

Fig. S-4. Training and validation for ANN model in visible (augmented)

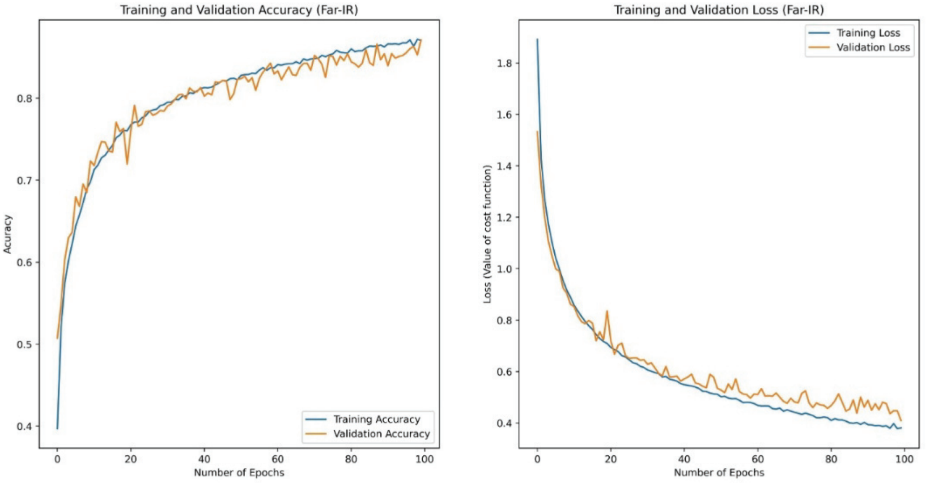

Fig. S-5. Training and validation for ANN model in far IR region.

Journal of the Serbian Chemical Society
JSCS-info@shd.org.rs • www.shd.org.rs/JSCS

J. Serb. Chem. Soc. 88 (10) 1025–1037 (2023)
JSCS–5678

Original scientific paper
Published 24 October 2023

Impedance response of aluminum alloys with varying Mg content in Al–Mg systems during exposure to chloride corrosion environment

JELENA ŠĆEPANOVIĆ[1], MARIJANA R. PANTOVIĆ PAVLOVIĆ[2,3#], DARKO VUKSANOVIĆ[1], GAVRILO M. ŠEKULARAC[2] and MIROSLAV M. PAVLOVIĆ[2,3#*]

[1]*Faculty of Metallurgy and Technology, University of Montenegro, Podgorica, Montenegro.* [2]*Institute of Chemistry, Technology and Metallurgy, National Institute of the Republic of Serbia, Department of Electrochemistry, University of Belgrade, Belgrade, Serbia and* [3]*Center of Excellence in Environmental Chemistry and Engineering, Institute of Chemistry, Technology and Metallurgy, Belgrade, Serbia*

(Received 5 May, revised 23 June, accepted 1 July 2023)

Abstract: This research discusses the corrosion behavior of as-cast Al alloys with different Mg content by potentiostatic electrochemical impedance spectroscopy (PEIS). The complex plane spectra of all samples feature a high-frequency loop, followed by semi-infinite diffusion impedance characteristics at low frequencies, with the corrosion-induced formation of a defined porous structure of a layer making finite diffusion through the pores dominant upon prolonged exposure. The most compact layer causes the most pronounced and well-resolved finite diffusion features in the impedance spectra of the sample with the highest Mg content, while the sample with the lowest Mg content has a highly porous layer unable to slow down the corrosion rate at the layer/ /sample interface. The highest layer capacitance and diffusion admittance are found in the sample with the highest Mg content, with a more adherent protective film expected to form. However, the growth rate of the layer was not adequate for the remarkable closing of the pits, indicating the weakness of this sample towards pit activity. The results show that increasing Mg content improves corrosion resistance and clearly separates bulky corrosion from localized pitting corrosion, but it also increases the thickness of a more compact, poorly adhesive layer.

Keywords: electrochemical impedance spectroscopy; aluminum alloys; corrosion behavior; chemical composition; mechanical properties.

---

* Corresponding author. E-mail: miroslav.pavlovic@ihtm.bg.ac.rs
\# Serbian Chemical Society member.

https://doi.org/10.2298/JSC230505031S

INTRODUCTION

Aluminum and its alloys have a wide range of applications in industry as well as consumption due to their unique properties, such as light weight, high strength and good corrosion resistance.[1–3] Due to the broad application and economic importance of aluminum and its alloys, increasing attention is being paid to researching the corrosion characteristics of these materials in cast, aged, and technically processed states.[1,4,5] Aluminum–magnesium alloys have been the subject of numerous studies on corrosion rates in various solutions.[5–9] The formation of a protective oxide layer is the main reason behind its excellent corrosion resistance. However, under saline conditions, such as those encountered in marine environments, aluminum alloys are vulnerable to localized degradation in the form of pitting and crevice corrosion. This type of corrosion occurs due to the adsorption of anions, particularly chlorides, at the oxide–solution interface.[5] From the standpoint of corrosion rate, in a chloride environment, Al–Mg alloys are susceptible to localized degradation in the form of pitting corrosion. The highest corrosion rate is observed in alloys containing around 0.8 mass % of magnesium.[4] A higher magnesium content in Al alloys generally indicates a higher degree of surface oxidation, where magnesium content varies from 6 to 8 %.[9,10] The passive stable surface film serves as a barrier for the transfer of cations from the metal to the environment and for the counter diffusion of oxygen and other anions.[11] Chemically homogeneous, single-phase amorphous alloys free from crystalline defects such as precipitates, segregates, grain boundaries and dislocations often create a conducive environment for the formation of a uniform passive film without any weak points.[6] Dragos *et al.*[12] shows results of elongation and structural analysis of Al–Mg alloy before and after heat treatment and artificial aging. On the other hand, alloys with magnesium are structural metals that are lightweight. The lightweight nature of such materials is the main reason for the interest in Al–Mg alloys in various industrial applications.[13]

Aluminum forms a protective oxide film in the pH range 4.0–8.5, but this depends on temperature, form of oxide present and the presence of substances that form soluble complexes or insoluble salts with aluminum. This implies that the oxide film is soluble at pH values below 4.0 and above 8.5. Several investigations reported that the pitting potential of aluminum in chloride solutions is independent of pH in the range 4–9.[14–16] However, pitting corrosion rate was found increased at slightly acidic and alkaline solutions with respect to neutral solutions.

The corrosion behavior of aluminum alloys is significantly affected by the presence of particles in the matrix.[3] Literature data[2,8,14,16,19] showed that Mg_2Si particles tend to be anodic in relation to the matrix and can act as initiation sites for corrosion. Most often, the Mg_2Si phase dissolves, leaving behind a cavity that acts as a nucleation site for pitting.[14–16,20,21] These observations were made during investigations carried out on commercial aluminum alloys with low Si/Mg mole ratios.[7,22]

Crevice corrosion is a highly localized form of corrosion that occurs by infiltration of water into closely fitted surfaces. The presence of aggressive ions, such as chloride, often creates extensive localized attack.[14] Metals like aluminum that depend on oxide films or passive layers for corrosion resistance are particularly susceptible to crevice corrosion. Attack from this phenomenon can be aggravated when combined with the presence of crystalline defects such as Mg_2Si precipitates. The possibility exists for reducing drastically the alloy susceptibility to corrosion if its microstructure is modified by appropriate heat treatment prior to usage. The research conducted in this study aimed to determine the corrosion rate of an Al alloy in its cast and aged states, as well as to compare the corrosion rate for both states. Aluminum and its alloys have been used in a wide range of industries due to their favorable characteristics such as high strength-to-weight ratio, excellent formability and resistance to corrosion. Aluminum alloys are increasingly utilized in a diverse array of products, including airplane parts, components for the aerospace industry and the shipbuilding sector.[17,18] These industries require materials with high strength-to-weight ratios and superplasticity. Compared to other metals, aluminum alloys offer superior strength while being lightweight. The development of materials with superplasticity aims to enhance their mechanical and forming properties.[18] Various manufacturing techniques have been employed to fabricate and improve these superplastic materials, such as extrusion, rolling, forging, stir casting, as well as more recent methods like friction stir processing.[17] However, the corrosion resistance of these materials is influenced by factors such as alloy composition, processing history, and environmental exposure. Therefore, understanding the corrosion behavior of these materials is crucial for their effective and sustainable use in various applications. The aim of the presented investigation was to analyze the influence of Mg content on the corrosion behavior of Al alloys in order to contribute to reliable prediction of their behavior and to the development of improved corrosion-resistant Al alloy for specific applications.

EXPERIMENTAL

The investigated alloys were obtained by casting and air-cooling in the Foundry Laboratory at the Faculty of Metallurgy and Technology in Podgorica. A 5.5 kW resistance furnace with a working temperature of 1100 °C was used to obtain the alloys. The melting of the alloys was carried out in a graphite crucible placed in the furnace.

High-purity magnesium was used as an alloying element in the alloys, with the Mg content of 2.42, 3.14 and 7.90 mass % in alloys 1,2 and 3, respectively. Copper, zinc, chromium, and manganese were also used as alloying elements in the alloys. The chemical composition of the obtained alloys was analyzed at the Aluminum Combine Podgorica (KAP) using a non-destructive X-ray quantometer method. The selection of the alloying elements was based on previous research, with a focus on the effect of magnesium content on the corrosion characteristics while keeping the content of other alloying elements approximately constant. After casting, all three alloys were subjected to heat treatment, including heating at 515±5 °C for 6 h and quenching in warm water.

Corrosion and electrochemical potentiodynamic investigations were carried out using accelerated testing equipment – the PAR system consisting of a potentiostat/galvanostat model 273, a differential electrometer, a corrosion cell K0047, a saturated calomel electrode (SCE), auxiliary electrodes – cylindrical electrographite, a computer with corrosion software SOFTCORR 352 II, and a printer. All potentials are expressed on SCE scale.

Corrosion testing was performed using the following methods:

– monitoring the change in corrosion potential over time, $E_{\text{corr}} = f(\tau)$;

– polarization resistance method, R_{p};

– potentiodynamic method.

A NaCl solution with a concentration of 0.51 M was used as the corrosion medium.

The electrochemical behavior was also assessed using potentiostatic electrochemical impedance spectroscopy (PEIS). The measurements were carried out using a three-electrode cell system in a 0.51 M NaCl solution, with platinum wire and SCE serving as the counter and reference electrodes, respectively. Prior to PEIS measurements, the electrolyte was purged with N_2 for 30 min. A potentiostat/galvanostat SP-240 (BioLogic SAS, Grenoble, France) was used for PEIS measurements at open circuit potential.

Optical images were taken with Leica 20 MP Ultra Wide Angle Lens, f/2.2 aperture camera.

RESULTS AND DISCUSSION

The results of the chemical composition of the obtained alloys are presented in Table I. The table shows the percentage of each alloying element used in the production of the alloys, which is an important factor that can affect their properties, including their resistance to corrosion.

TABLE 1. Results of the chemical composition of Al alloys in mass %

Alloy	Fe	Si	Ti	Cu	Zn	V	Cr	Mn	Mg	Sn	Ni	Pb
L1	0.29	0.12	0.14	0.34	0.59	0.012	0.21	0.33	2.42	0.001	0.002	0.007
L2	0.30	0.12	0.13	0.35	0.62	0.012	0.25	0.25	3.14	0.001	0.002	0.008
L3	0.24	0.14	0.13	0.52	0.83	0.013	0.26	0.29	7.90	0.001	0.002	0.001

Table I shows that these are multi-component alloys with different contents of alloying elements. The table lists the mass percentage of each element in the alloys. It can be observed that the alloys have varying amounts of Mg, Cu, Zn, Cr, Mn and Fe. The presence and the amount of each element in the alloys can significantly affect their properties, such as strength, hardness and corrosion resistance. Therefore, understanding the chemical composition of the alloys is crucial for predicting and controlling their behavior in different applications.

Fig. 1 shows the corrosion potential over time of as-cast Al alloys in 0.51 M NaCl solution. Before starting the polarization measurements, the system needs to be stabilized, which is judged by acceptable stability in time of the corrosion potential. Corrosion potential is monitored upon sample immersion into the electrolyte. From the results shown in Fig. 1, a shift in potential of the tested samples towards more positive values can be observed. The shift in potential of the alloys towards more positive values is interpreted as passivation, or the formation of an oxide film on the surface of the tested samples. The protective layer becomes thicker and more compact over time. This film prevents the passage of aggressive chloride ions from the solution, thus protecting the material from further corrosion.

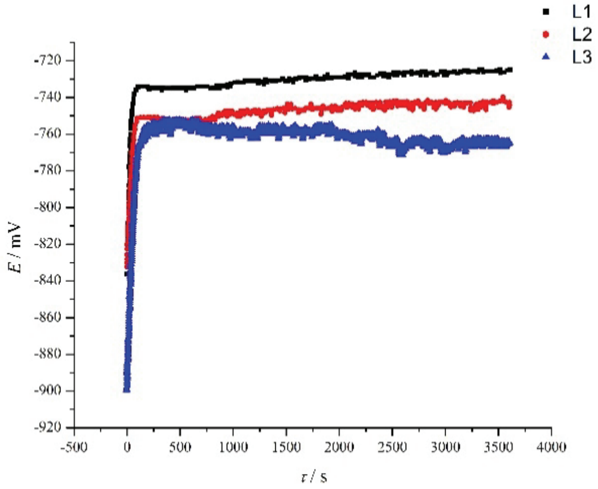

Fig 1. Corrosion potential of as-cast Al alloys over time in 0.51 M NaCl solution.

It can also be seen that corrosion potential takes more positive values as the Mg content increases. This indicates that greater protective ability of the passive films are reached with lower Mg content.

Linear polarization is an electrochemical technique used for monitoring corrosion. It is based on the determination of the polarization resistance, R_p from the slope of the polarization line near the corrosion potential. Based on the results shown in Fig. 2a, and numerical values of the experimental measurements which are shown in Table II, it can be concluded that the samples are stable in the tested solution. Comparing the results, based on the value of the polarization resistance R_p (Table II), it can be observed that there is highest corrosion resistance for the L2 sample, followed by L1 and L3.

Fig. 2b shows the potentiodynamic cathodic and anodic polarization curves of the tested samples in a 0.51 M NaCl solution. In the cathodic region, a small change in current density with potential is observed, indicating a low corrosion rate of the tested samples in the NaCl solution, while in the anodic region, a larger change in current density with potential is observed. The results of the measurements are presented in Table III. Based on the values of j_corr and $E_{j=0}$ given in Table III, it can be concluded that L1 is the lowest rate of corrosion in the tested environment, followed by L3 and L2. The potentiodynamic polarization curves provide valuable information about the corrosion behavior of the materials, as well as the values of the corrosion potential and the current density at which corrosion rate is negligible.

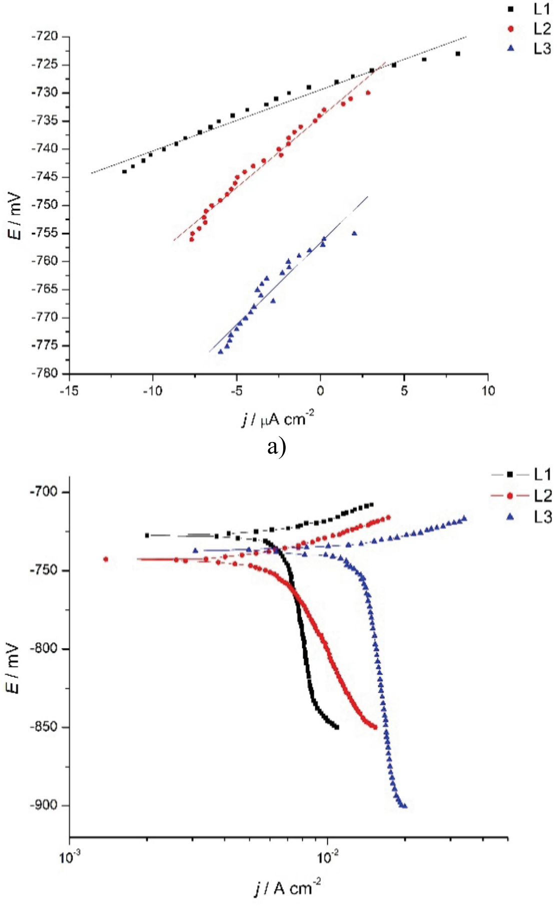

a)

b)

Fig. 2. a) Linear polarization and b) potentiodynamic cathodic and anodic polarization curves of Al alloys in the as-cast state in a 0.51 M NaCl solution.

TABLE II. Change of corrosion potential over time of as-cast Al alloys in a 0.51 M NaCl solution

Sample	E_{start} / mV	E_{fin} / mV
L1	–836	–725
L2	–834	–743
L3	–879	–740

Tables II and III present the complete results of corrosion studies in 0.51 M NaCl on alloys L1, L2 and L3 in as-cast state. The tables provide information on corrosion potential, corrosion current density, polarization resistance, corrosion rate and other related parameters. By analyzing these data, one can gain insight into the effectiveness of different alloy composition in preventing corrosion and choose the optimal material for specific applications.

TABLE III. Corrosion potential change over time of as-cast Al alloys in a 0.51 M NaCl solution

Sample	$E_{j=0}$ / mV	R_p / kΩ cm^{-2}	β_a / mV	j_{corr} / μA cm^{-2}
L1	–727.5	1.106	19.63	19.64
L2	–743.3	2.554	25.57	8.503
L3	–736.7	0.4605	16.93	47.15

Fig. 3 shows the impedance characteristics of the cast samples upon initial (24 h) and prolonged (120 h) exposure to chloride-containing corrosive medium as impedance complex plane plots.

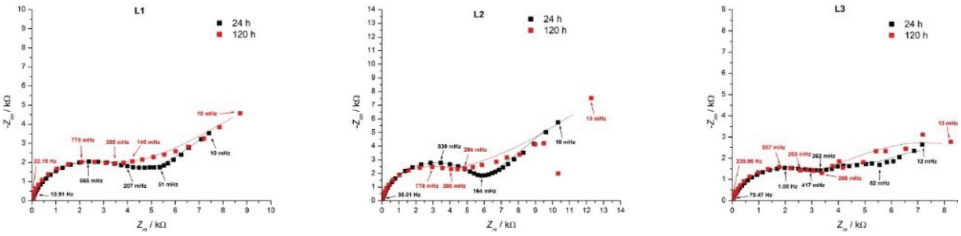

Fig. 3. Impedance complex plane plots of as-cast Al–Mg alloy samples upon initial (24 h) and prolonged (120 h) exposure to 0.51 M NaCl solution. Symbols: registered data; lines: the data of equivalent electrical circuit.

Complex plane spectra of all samples feature high-frequency loop, which is, in the cases of lower Mg content (L1 and L2), followed by well-defined semi-infinite diffusion impedance characteristics at low frequencies. Prolonged exposure causes the deviation of a near-45°-inclined straight line to more resistance-defined behavior as the corrosion proceeds. This indicates the transition from semi-infinite to more noticeable finite diffusion conditions due to the generation and growth of a passive layer on the sample surface. While electrolyte species participating in the corrosion processes diffuse initially from the electrolyte bulk, the corrosion-induced formation of defined porous structure of a layer makes dominant the finite diffusion through the pores upon prolonged exposure. The layer over L3 sample of highest Mg content seems to be formed much quickly, since finite diffusion characteristics are more resolved already in the initial stage of exposure. The photographs of corroded samples (Fig. 4) show that the surface layer of L3 appears the most compact with the least frequent pitting corrosion sites. However, the radii of corrosion products (white zones) around pits are largest, which indicates that pitting corrosion is dominant mechanism in the initial stage. According to Fig. 4, it appears that the increase in Mg content favors the pitting corrosion and induces the formation of more compact passive layer. The most compact layer apparently causes the most pronounced and well-resolved finite diffusion features in the impedance spectra of L3. The differences between the properties of a layer on L3 and that on L1 and L2 are indicated also by the measures of the high-frequency loop. Although the associated resistances are similar for all of the three samples, the imaginary impedance is lower for L3 due to larger capacitance of a thinner and more compact layer.

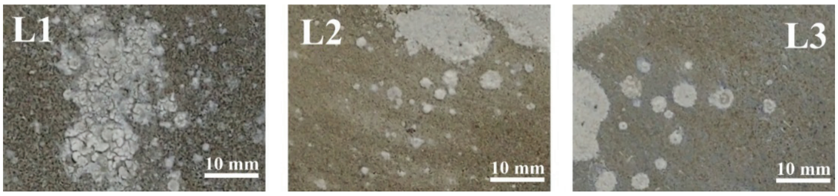

Fig. 4. Optical images of the tested samples after 120 h exposure to 0.51 M NaCl solution.

The considerations of the features of impedance spectra are proved further by the structure of the most suitable equivalent electrical circuit which describes best the physicochemical properties of the samples while they corrode (Fig. 5). The samples of lower Mg content and of less compact passive layers behaves equivalently to the circuit consisted of a parallel connection of capacitor and resistor, which is in series to Randles–Sevcik (R–S) conformation.

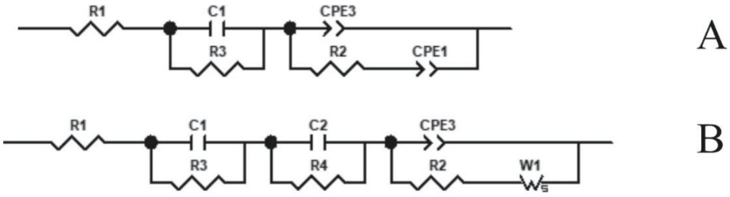

Fig. 5. Equivalent electrical circuits of as-cast Al–Mg alloy samples: a) for L1 and L2 and b) L3 upon initial (24 h) and prolonged (120 h) exposure to 0.51 M NaCl solution.

RC in parallel describes the properties of a layer, whereas R–S relates to diffusion-controlled corrosion processes. Owing to the most distinguishable pitting corrosion and an indication of more compact layer structure, the circuit for L3 required additional RC time constant in series, which indicates the difference between the properties of a bulky layer and that formed around the pits. The values of the circuit parameters are presented in Fig. 6.

The highest values of layer resistance is found for L2 of mid Mg content, associated to the lowest layer capacitance, which indicates the thickest layer is formed on this sample. In Fig. 4 it can be seen that massive layer is formed over the sample surface except the areas close to the sample surface, where pitting corrosion appears dominant. The formation of a massive layer is followed by considerable increase in charge transfer resistance (R2, which was the lowest initially) and double layer capacitance (CPE-T3). This indicates that corrosion processes take place much faster on L2 than on L1 and L3; however, fast corrosion produces the thickest layer, whose porous structure did not change significantly while the layer grows (initial layer resistance and diffusion admittance are similar to those found upon prolonged exposure (day 1–day 5). Consequently, the corrosion proceeds at the sample surface accessible through the pores of the layers, which area is considerably smaller with respect to L1 and L3. Hence the R2 and CPE-T3 for L2 are considerably larger.

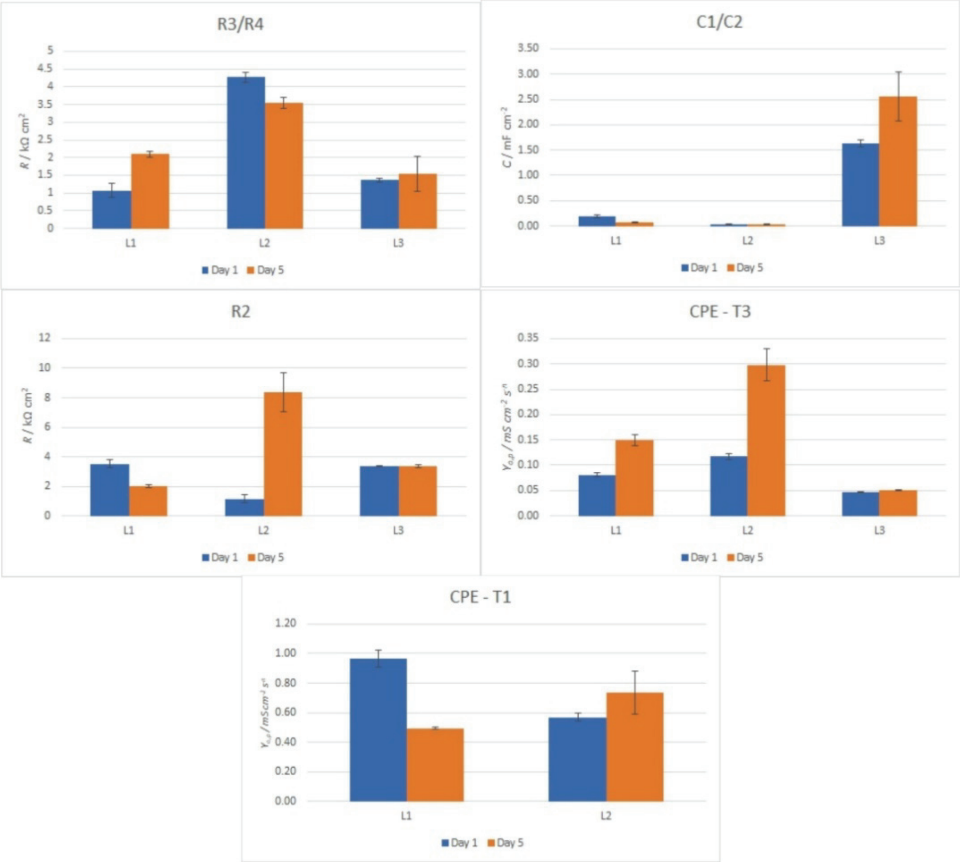

Fig. 6. The values of circuit parameters of the investigated samples; R3/R4 and C1/C2 – resistances and capacitances of the passive layer; R2 and CPE-T3 – charge transfer and double layer capacitance (the values of CPE exponent are above 0.75) associated to corrosion processes; CPE-T1 – diffusion admittance.

Layer resistance of L1 considerably increases during exposure, but it is still lower than the resistance found for L2. This increase is associated with the lowest charge transfer resistance and diffusion admittance among the samples upon prolonged exposure. This finding is the strong indication of the highly porous layer, unable to slow down the corrosion rate at the layer/sample surface interface. Huge pores homogeneously distributed over the layer surface are also seen in Fig. 4, and even appearance of a cracks around the pits in the middle of the sample is clearly visible. It can be concluded that the L1–L2 increase in Mg content improves the corrosion resistance and clearly separates bulky corrosion from localized pitting corrosion. However, it increases the thickness of more compact, poorly adhesive, layer.

Further increase in Mg content applied in L3 decreases additionally the layer thickness and makes it considerably more compact, which should be beneficial for the formation of a more adherent protective film. This is reflected in the highest layer capacitance and diffusion admittance that is for L3 straightforwardly defined by finite diffusion mechanism (finite Warburg element was only suitable in equivalent circuit for L3, whereas classical Warburg element met the requirement to describe the diffusion in the cases of L1 and L3). However, for the applied exposure the growth rate of a layer was apparently not adequate for the remarkable closing of the pits, since the increase in charge transfer resistance and double layer capacitance was not registered for L3 upon prolonged exposure. The weakness of L3 sample toward the pit activity could be connect to the presence of additional RC time constant, of quite different values of the parameters with respect to that for a layer. Namely, the resistance is much lower, few tens of Ω, and even deceases to *ca.* 8 Ω upon prolonged exposure. The associated capacitance is close to 0.1 mF, which is much lower than that of a layer – thus indicating its highly localized appearance on the surface. Despite this poor immunity of L3 sample toward pitting corrosion, the registered propagation of the properties of a protective layer during 5-day exposure should be expected to show protective features upon much longer exposures to corrosive medium.

CONCLUSION

The article describes the results of an experiment aimed at investigating the corrosion behavior of as-cast Al alloys in NaCl solution. The study employed different electrochemical techniques, including corrosion potential measurements, linear polarization and potentiodynamic polarization curves, as well as impedance measurements. The results show that the Al alloys form a protective oxide film on the surface, which prevents the passage of aggressive chloride ions from the solution, thus protecting the material from further corrosion.

The study found that the impedance characteristics of the cast samples change upon initial and prolonged exposure to the chloride-containing corrosive medium. The complex plane spectra of all samples feature a high-frequency loop followed by well-defined semi-infinite diffusion impedance characteristics at low frequencies. Prolonged exposure causes the deviation of a near-45°-inclined straight line to more resistance-defined behavior as the corrosion proceeds. The most compact layer apparently causes the most pronounced and well-resolved finite diffusion features in the impedance spectra of L3. The article concludes that the increase in Mg content favors the pitting corrosion and induces the formation of a more compact passive layer.

The study used the most suitable equivalent electrical circuit to describe the physicochemical properties of the samples while they corrode. The samples of lower Mg content and less compact passive layers behave equivalently to the circuit consisted of a parallel connection of a capacitor and resistor, which is in series to the Randles–Sevcik conformation. The circuit for L3 required an additional RC time constant in series, indicating the difference between the properties of a bulky layer and that formed around the pits. The highest values of the layer resistance are found for L2 of mid Mg content, associated with thicker and more compact layers. These results provide insights into the corrosion behavior of as-cast Al alloys and can be useful for the design of new alloys with better corrosion resistance.

In conclusion, the study investigated the corrosion behavior of as-cast Al alloys in NaCl solution, using various electrochemical techniques. The study found that the Al alloys form a protective oxide film on the surface, which prevents the passage of aggressive chloride ions from the solution, thus protecting the material from further corrosion. The study also found that the impedance characteristics of the cast samples change upon initial and prolonged exposure to the chloride-containing corrosive medium, and that the increase in Mg content favors the pitting corrosion and induces the formation of a more compact passive layer. These results provide insights into the corrosion behavior of as-cast Al alloys and can be useful for the design of new alloys with better corrosion resistance. The findings of this study can have significant implications for the development of new corrosion-resistant alloys for a variety of applications. The results demonstrate that the corrosion behavior of Al alloys can be controlled by the composition of the alloy and the formation of a protective oxide layer on the surface. Overall, the study highlights the importance of understanding the corrosion behavior of materials and provides a valuable contribution.

Acknowledgement. This work was supported by the Ministry of Science, Technological Development and Innovation of the Republic of Serbia, Grant No. 451-03-47/2023-01//200026.

ИЗВОД

ИМПЕДАНСНИ ОДЗИВ АЛУМИНИЈУМСКИХ ЛЕГУРА СА РАЗЛИЧИТИМ САДРЖАЈЕМ МАГНЕЗИЈУМА ТОКОМ ИЗЛОЖЕНОСТИ ХЛОРИДНОЈ КОРОЗИОНОЈ СРЕДИНИ

ЈЕЛЕНА ШЋЕПАНОВИЋ[1], МАРИЈАНА Р. ПАНТОВИЋ ПАВЛОВИЋ[2,3], ДАРКО ВУКСАНОВИЋ[1],
ГАВРИЛО М. ШЕКУЛАРАЦ[2] и МИРОСЛАВ М. ПАВЛОВИЋ[2,3]

[1]*Металуршко-технолошки факултет, Универзитет у Црној Гори, Подгорица, Црна Гора,* [2]*Институт за хемију, технологију и металургију, Институт од националног значаја за Републику Србију, Центар за електрохемију, Универзитет у Београду, Београд и* [3]*Центар изузетних вредности за хемију и инжењеринг животне средине, Институт за хемију, технологију и металургију, Београд*

Ово истраживање се бави понашањем корозије Al легура са различитим садржајем Mg уз примену потенциостатске електрохемијске импедансне спектроскопије (PEIS). Спектри у комплексној равни свих узорака се карактеришу петљом високе фреквенције праћеном карактеристикама полу-бесконачне дифузије на ниским фреквенцијама, са формирањем дефинисане порозне структуре слоја услед корозије, што доводи до доминације коначне дифузије кроз поре при продуженој изложености. Најкомпактнији слој узрокује најизраженије и најјасније карактеристике коначне дифузије у импедансним спектрима узорка са највећим садржајем Mg, док узорак са најмањим садржајем Mg има високо порозан слој који не може успорити брзину корозије на граници фаза слој/узорак. Највећу капацитивност и адмитанцију дифузионог слоја има узорак са највећим садржајем Mg, са очекиваном појавом адекватног заштитног филма. Међутим, брзина раста слоја није била довољна за значајно затварање питова, што указује на слабост овог узорка према питинг корозији. Резултати показују да повећање садржаја Mg побољшава отпорност на корозију и јасно раздваја корозију у маси материјала од локализоване питинг корозије, али истовремено повећава дебљину слоја који је слабије адхезије и компактнији.

(Примљено 5. маја, ревидирано 23. јуна, прихваћено 1. јула 2023)

REFERENCES

1. X. Zhang, M. Zhang, R. Li, X. Feng, X. Pang, J. Rao, D. Cong, C. Yin, Y. Zhang, *Coatings* **11** (2021) (https://doi.org/10.3390/coatings11111316)
2. K. A. Yasakau, M. L. Zheludkevich, S. V Lamaka, M. G. S. Ferreira, *Electrochim. Acta* **52** (2007) 7651 (https://doi.org/10.1016/j.electacta.2006.12.072)
3. L. Garrigues, N. Pebere, F. Dabosi, *Electrochim. Acta* **41** (1996) 1209 (https://doi.org/10.1016/0013-4686(95)00472-6)
4. S. O. Adeosun, O. I. Sekunowo, S. A. Balogun, V. D. Obiekea, *Int. J. Corros.* **2012** (2012) 927380 (https://doi.org/10.1155/2012/927380)
5. S. P. B., T. U. Dhanaji, S. Dassani, M. Somasundaram, A. Muthuchamy, A. Raja Annamalai, *Crystals* **13** (2023) (https://doi.org/10.3390/cryst13020344)
6. B. Li, Z. Zhang, T. Liu, Z. Qiu, Y. Su, J. Zhang, C. Lin, L. Wang, *Materials (Basel, Switzerland)* **15** (2022) (https://doi.org/10.3390/ma15113912)
7. S. Ren, X. He, X. Qu, I. S. Humail, Y. Li, *Mater. Sci. Eng., B* **138** (2007) 263 (https://doi.org/10.1016/j.mseb.2007.01.023)
8. F. Andreatta, H. Terryn, J. H. W. de Wit, *Corros. Sci.* **45** (2003) 1733 (https://doi.org/10.1016/S0010-938X(03)00004-0)
9. M. Popović, E. Romhanji, *Mater. Sci. Eng., A* **492** (2008) 460 (https://doi.org/10.1016/j.msea.2008.04.001)

10. L. Ren, H. Gu, W. Wang, S. Wang, C. Li, Z. Wang, Y. Zhai, P. Ma, *Materials (Basel, Switzerland)* **12** (2019) (https://doi.org/10.3390/ma12244160)
11. H. P. Godard, *The corrosion of light metals*, Wiley, New York, 1967, ISBN: 978-0471308614
12. A. D. Cristian, M. M. Georgiana, S. A. Victor, M. M. A. B. Abdullah, *AIP Conf. Proc.* **1835** (2017) 20051 (https://doi.org/10.1063/1.4983791)
13. N. Loukil, in *Magnesium Alloys Structure and Properties*, T. Tański, P. Jarka, Eds., IntechOpen, Rijeka, 2021, p. 833 (https://doi.org/10.5772/intechopen.96232)
14. S. K. Kairy, P. A. Rometsch, K. Diao, J. F. Nie, C. H. J. Davies, N. Birbilis, *Electrochim. Acta* **190** (2016) 92 (https://doi.org/10.1016/j.electacta.2015.12.098)
15. F. Song, X. Zhang, S. Liu, Q. Tan, D. Li, *Corros. Sci.* **78** (2014) 276 (https://doi.org/10.1016/j.corsci.2013.10.010)
16. C. Brito, T. Vida, E. Freitas, N. Cheung, J. E. Spinelli, A. Garcia, *J. Alloys Compd.* **673** (2016) 220 (https://doi.org/10.1016/j.jallcom.2016.02.161)
17. M. M. Tawfik, M. M. Nemat-Alla, M. M. Dewidar, *J. Mater. Res. Technol.* **13** (2021) 754 (https://doi.org/https://doi.org/10.1016/j.jmrt.2021.04.076)
18. J. Liu, M.-J. Tan, A.-E.-W. Jarfors, Y. Aue-u-lan, S. Castagne, *Mater. Des.* **31** (2010) S66 (https://doi.org/10.1016/j.matdes.2009.10.052)
19. J. H. W. de Wit, *Electrochim. Acta* **49** (2004) 2841 (https://doi.org/10.1016/j.electacta.2004.01.045)
20. N. Birbilis, R. G. Buchheit, *J. Electrochem. Soc.* **152** (2005) B140 (https://doi.org/10.1149/1.1869984)
21. J. Wloka, G. Bürklin, S. Virtanen, *Electrochim. Acta* **53** (2007) 2055 (https://doi.org/10.1016/j.electacta.2007.09.004)
22. A. Pardo, M. C. Merino, R. Arrabal, S. Merino, F. Viejo, A. E. Coy, *Appl. Surf. Sci.* **252** (2006) 2794 (https://doi.org/10.1016/j.apsusc.2005.04.023).

Journal of the Serbian Chemical Society
JSCS-info@shd.org.rs • www.shd.org.rs/JSCS
J. Serb. Chem. Soc. *88* (10) 1039–1053 (2023)
JSCS–5679
Original scientific paper
Published 24 October 2023

Recovery of copper from printed circuit boards (PCBs) using shaking table

ÖZGE GÖK* and GÜL AKAR ŞEN

Dokuz Eylul University, Faculty of Engineering, Mining Engineering Department, İzmir, Turkiye

(Received 16 March, revised 8 April, accepted 12 April 2023)

Abstract: In recent years, there has been a growing focus on the reuse of metallic components from waste electrical and electronic equipment (WEEE) which refers to electrical and electronic equipment that has become obsolete, stopped working, or developed defects during production. In this research, shaking table was selected as a gravity concentration tool for the recovery of copper from the light components. The flowsheet included comminution, gravimetric concentration and physical/chemical characterization of feed material and products. The process parameters were deck angle (degrees), motion frequency (Hz), wash water rate (L/m) and particle size diameter. The Box Behnken Design (BBD) was used to optimize the performance of the wet shaking table and to identify the ideal combination of its operating parameters. By analysing the experimental design, it was found that the optimal settings for deck angle, motion frequency, wash water rate and particle size diameter were 2°, 50 Hz, 12 L/m, and –500+300 mm, respectively. These optimal settings were located near the central points of the experimental design, suggesting that the actual optimal point could be within the designed space.

Keywords: printed circuit boards; recycling; shaking table; copper; ANOVA.

INTRODUCTION

Several electrical and electronic equipment such as cell phones, computers, televisions, and printers that are obsolete, no longer work or had defects during their production are classified as waste electrical and electronic equipment. The re-utilization of WEEE components (printed circuit boards (PCBs), batteries, LCD, *etc.*) has received special attention in recent years because some of the metals (Cd, Pb, Hg, Br, Be and organics) have toxic effects on health and the environment. One of the most researched electronic parts, PCBs, are made of copper sheets laminated onto a non-conductive substrate used to support elec-

---

* Corresponding author. E-mail: ozge.solak@deu.edu.tr

https://doi.org/10.2298/JSC230316056G

tronic components mechanically and maintain the electrical connectivity of the circuits. Thin boards are composed of 28–32 % metallic components and 68 % non-metallic components that mainly include plastics, epoxy resin reinforced glass fibers and ceramics.[1,2] Metallic fraction includes Fe, Cu, Al, Pb, Sn, Pd, PGM, Zn and precious metals that are more than 10 times that of rich-content minerals. Typical metal contents are 10–27 % Cu, 2–8 % Al, 1–4 % Pb 1–8 % Fe, 1–6 % Sn and <0.1 % precious metals (Au; 10–1600 ppm, Ag: 20–200×10^3 ppm, Pd: 5–970 ppm).[3] There are: *i*) mechanical/physical,[4–7] *ii*) thermal[8,9] and *iii*) chemical,[10–14] *iv*) physicochemical techniques[15] and their combinations[16–18] applied to recover the targeted metallic fraction from PCBs. Physical methods include dismantling; screening; shape separation; flotation; jigging; air, electrostatic, magnetic, eddy current and density-based separation. These methods are generally used as pre-treatment methods to simplify the following metal recovery methods. Thermal recovery techniques having high operating costs with low-efficiency consist mainly of pyrolysis and combustion generating air pollution through the release of furans and dioxins. Chemical methods, hydro- and electrometallurgical techniques, provide high metal recoveries, while producing large quantities of waste acidic electrolytes which must be carefully handled.[5,19]

Among numerous recycling applications, more preferred process worldwide might be the mechanical/physical recycling techniques owing to a fact that valuable metals in PCBs are elementary substance.[20] Typical flow sheet starts with dismantling step to recover large iron, lead and aluminium parts and precious metal-concentrated parts separately. The target metal on the dismantled board is copper that is widely used in electrical circuits, machine, construction, defence industry and other fields.[21] However, the complex nature of the copper/other metals–epoxy resin–ceramic–glass fibre embedded board complicates the recycling process. Non-metallic fraction (1.1–2.5 g/cm^3) has lower densities compared to metallic fraction while metals have higher densities in the range of 7–21.4 g/cm^3. Thus, most of the time multiple steps are needed to recover pure metals.

Gravity concentration methods as an environmentally benign method to recover valuable metals from PCBs are the popular options for the pre-treatment steps. After sufficient liberation, metals and plastic fractions can be easily separated which can be supported by the concentration criteria ($CC = (\rho_{\text{heavy}}/\rho_{\text{fluid}})/(\rho_{\text{light}}/\rho_{\text{fluid}})$). The studies in the literature attempted to recover metallic contents by gravity methods are jigging, sorting on aero-tables, sink-float separation.[6,7,22–24] Bilesan *et al.*[7] used hydrocyclone to recover PMs and Cu and reported 72 % total separation efficiency of copper. In the other study[23] on pneumatic separation method followed by electrostatic/magnetic separation, copper recovery was 57 % for 0.3–0.6 mm size fraction. Das *et al.*[22] applied a multi-step process in which the table was used for two purposes: classification and pre-concentration. Copper grade in concentrate was 38 %. Total metal grade and recovery was 92 and 97 %, respectively, in the study of Duan *et al.*[6] in which Falcon concentrator was used. Similarly, Ma *et al.*[25] investigated heat-treated product grade after concentrating with Falcon and found product grades approximately 90 %. Burat and Özer[26] analysed the recovery of metals with shaking table-electrostatic/magnetic separators and obtained a heavy fraction with 41 % copper grade and 95 % copper recovery from the first process. The research on metal separation from PCBs by wet jigging and flotation processes gave as a result the metal product with 92.5 % grade at the size fraction of 0.59–1.68 mm.[1] In the Ventura *et al.* work,[27] physical processing alone as well as combined with thermal treatment (200–500 °C) has been performed to recover gold and copper. Physical treatment alone showed recoveries of 67 and 87 wt. % for gold and copper, respectively.

In this article, a shaking table was selected as a gravity concentration tool for the separation of the light material (plastic) from the heavier material (metal). The success of separation with concentrators depends on the selection of suitable design of variables and conditions. The effect of different operating and process parameters are crucial to understand and control the process.[25,28] However, it is very time consuming to test the influence of all factors on the process efficiency. Thus; a well-designed experimental test program should be followed to determine the response of the process to each parameter.[29–31] The objective of the present study was to determine the effect of the important operating variables of the shaking table using response surface methodology (RSM) in conjunction with Box Behnken method (BBM). The selective separation of heavy metals (copper, zinc, brass, gold, *etc.*) was not considered. It was intended to minimize the environmental drawbacks of electronic wastes and the effective recovery of metallic resources. The data collected from the experiments were analysed and the analysis of variance (ANOVA) of the model was performed using Design expert software version 9.0.2.0 from Stat Ease Inc., USA.

EXPERIMENTAL

In the present study, tests were implemented with the main PCBs from the same model/ /brand LED TVs after removal of electronic components (resistor, capacitor, diode, transistor, *etc.*) on the board (Fig. 1). The operations included comminution, gravimetric concentration and physical/chemical characterization of feed material and products.

In order to reduce the size effect in the concentration process, the components of PCB (epoxy resin, glass fibre cloth and copper) were liberated by two step-comminution. Dismantled PCBs were crushed in a shredder knife crusher with a 10 mm grid. In this type of crusher, hammers, which swing freely, are attached to rotating arms. The swinging hammer contacts the feed material at a high speed and imparts kinetic energy to fracture the feed. Pulse-jet bag filters are used to collect and recycle the dust throughout the comminution. In the second step, the particle size was reduced in closed circuit by a laboratory type ring mill up to –300 μm. Particle size measurement was applied using a vibratory laboratory sieve shaker. The microscope analyses were conducted to determine the copper liberation. Shaking table method was chosen to separate Cu from the PCBs.

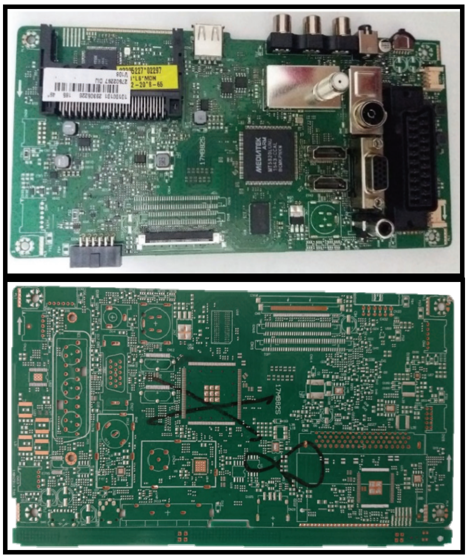

Fig. 1. PCB of LED TV original (top), dissembled board used for the experiments (bottom).

Experimental set-up

A Wilfley shaking table was used to recover the copper particles. It is an efficient technique to prevent the dust problem. It separates materials by particle density on inclined planes having smoothed/grooved shapes by the vibration of pulp material back and forth while wash water is flowing. Fig. 2 presents its schematic representation and the separation for WPCBs. The principle is based on the separation of rapid-moving coarse light particles from slower-moving small dense particles in the flowing water film with longitudinal vibration. Separation process starts: *i*) after feeding a 20–25 mass % pulp from the feed box which moves along the table with wash water; *ii*) continues with the diagonal movement of particles depends on their size and density by the vibration mechanism, using a slow forward stroke and rapid return; *iii*) ends by the collection of small-dense particles at the left end of table and large-lighter particles from opposite the feed box. The separation of metal and plastic materials can be conducted using a Wilfley model to the particle size from 100 μm to 1 mm.[32]

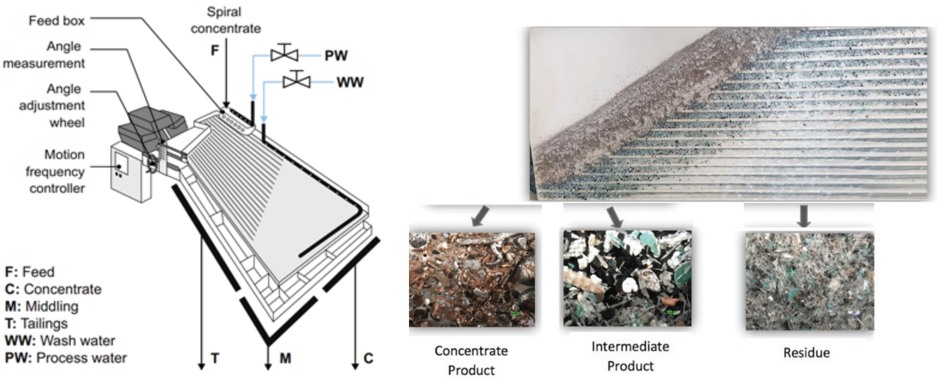

Fig. 2. Left: shaking tabletop view; right: WPCB separation.[33,34]

Response surface methodology (RSM) in conjunction with Box Behnken design (BBD)

BBD was developed by George E. P. Box and Donald Behnken in 1960.[35] The BBD of experiments offer modelling of the response surface methodology. The BBD make it possible to study sequentially the effect of the various factors of the design if, during the study of the first factors, the other factors are maintained at a constant level.[36] RSM and BBD are experimental design statistical tools used to evaluate complex multivariable systems, analyse the cause-and-effect relationship between true mean responses and input control variables, and optimize the response of multiple variable processes. The designs are not based on full or fractional factorial models.[37,38] It is specifically designed to fit a second-order model that is the primary interest in most RSM studies. To fit a second-order regression model (quadratic model), the BBD only needs three levels for each factor.[29,39] The BBD fixed a mid-level between the original low and high level of the factors, avoiding the extreme axial points and using face points. The addition of the mid-level point allows the efficient estimation of the coefficients of a second-order model.[40]

In the present study, the experiments are conducted using a BBD combined with RSM and the empirical relations are established for correlating the interactive and higher-order influences of various machining parameters on the laboratory type shaking table. Four different factors, particle size (mm); wash water flow rate (L/m); deck angle (°); motion frequency (Hz) and their influence on the copper grade and recovery of the concentrate were evaluated. 24 set of trials and four control experiments were conducted during the studies. The main advantage of the RSM–BBD methodology is the ability to perform analysis of several parameters with fewer experimental trials matched to other methods. 4 factors on 3 levels (low, medium and high) were assessed which were represented by a (−1), a (0) and a (+1) sign, respectively. The test variables chosen for the study are designated as particle size (A), wash water flow rate (B), deck angle (C) and motion frequency (D). These independent variables to predict responses, namely Cu grade and recovery of the shaking table separator, are named as $Y1$ and $Y2$, respectively. Variables (A, B, C and D) and their coded/actual levels used in this study are indicated in Table I.

TABLE I. Box Behnken design parameters and experimental conditions; –1: factor at low level; 0: factor at medium level; +1: factor at high level

Variable	Symbol	Coded variable levels		
		–1	0	+1
Particle size, mm	A	–300	500–300	+500
Wash water flow rate, L/m	B	6	12	18
Deck angle, °	C	1	2	3
Motion frequency, Hz	D	40	50	60

The mathematical model of second-order polynomial equations was used to predict the relationship between the four factors and the response. The Eq. (1) is shown by the second order polynomial:

$$Y_{1,2} = b_0+b_1A+b_2B+b_3C+b_4D+b_{12}AB+b_{13}AC+b_{14}AD+ \\ b_{23}BC+b_{24}BD+b_{34}CD+b_{11}A^2+b_{22}B^2+b_{33}C^2+b_{44}D^2 \quad (1)$$

where Y is the predicted response, b_0 model constant; A, B, C, D independent variables; b_1, b_2 and b_3, b_4 are linear coefficients; b_{12}, b_{13}, b_{14}, b_{23}, b_{24} and b_{34} are cross product coefficients and b_{11}, b_{22}, b_{33} and b_{44} are the quadratic coefficients. Table I shows the experimental matrix design and the results of response variables considered. ANOVA for response surface quadratic model was applied on the results of beneficiation for the goodness of fit of the model and significance of each regression. 3D surface plots were generated using Design Expert 9.0.2 software.

RESULTS AND DISCUSSION

Physical and chemical characterization of PCBs

Particle size measurement of the ground PCBs was applied using a vibratory laboratory sieve shaker for 20 min. After agitation of sieve shaker PCBs collected on each sieve were weighted to calculate the particle size distribution. Wet chemical analysis was done to determine the Cu content of each different size fractions. Results are shown in Table II.

TABLE II. Size wise chemical analysis results of Cu from PCBs

Particle size, µm	Content, wt. %	Grade (Cu)
+500	41.3	12.50
–500+300	35.1	21.38
–300	23.6	11.29
Total	100	15.33

Wet chemical analyses in aqua region were performed to determine the metal content. The spectroscopic analyses of electrolyte solutions were carried out on Analytik Jena NovaA 300 AAS. The chemical composition of PCB is shown in Table III. A major component was copper. Thus, the remaining metallic elements (Fe, Sn, Al, Ca, *etc.*) were not traced for this study.

TABLE III. Chemical analysis of PCB of LED TV

Component	Cu	Sn	Al	Ni	Pb	Zn	Fe	Ca	Non-metals
Grade, %	15.37	3.72	3.22	2.10	1.45	1.04	0.09	6.42	66.31

Microscopic and mineralogical characterization of PCBs

The microscope analysis with the Nikon SMZ 1500 binocular microscope revealed that the copper liberation occurred under the particle sizes of 1 mm. The microscope pictures of all size fractions are given in Fig. 3. Three size fractions were selected to conduct the shaking table experiments: –1+0.50, –0.5+0.3 and –0.30 mm. X-Ray diffraction analyses of PCBs were performed using a Rigaku Miniflex II diffractometer with CuKα radiation. Qualitative XRD analysis of the head sample indicated the presence of polymer, ceramic and copper as major components and small amounts of tin and aluminium in the PCB.

Shaking table experiments

24 sets of trials and four control experiments were conducted to assess the effects of the four variables. The actual data achieved from the tests were also used

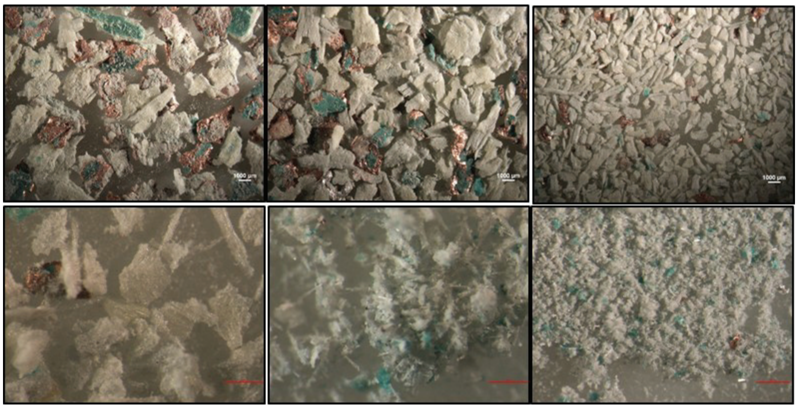

Fig. 3. Microscope analyses of ground sample (top left: –2+1, –1+0.5, –0.5+0.3 mm; bottom left: –0.3+0.2, –0.2+0.1, –0,1 mm).

to make the mathematical equation presenting copper grade and copper yield as a function of the independent variables. The experimental results of the design matrix along with their condition are presented in Table IV. The experimental programme provided a broad range of grade and recovery values which foresaw that the concentrate fraction had been enriched up to with an amount of 53.29 % Cu grade and 83.72 % Cu recovery whereas a maximum amount of 89.99 % Cu recovery (with content of 37.33 % Cu grade).

The experiments were carried out using the laboratory type-shaking table (gravity concentrator) to concentrate the copper particles. The regression coefficient values for the copper grade and copper yield are listed in Table V. The significance of each coefficient was determined by the Student's *t*-test. As it is shown, both independent variables and their interactions can affect the copper grade and yield of the PBCs. From Table V, the model *F*-value of implies that the model is significant for the Cu grade and yield, 98.60 and 19.51, respectively. There is only a 0.01 % chance that a "model *F*-value" this large could occur due to noise. Values of "$Prob > F$" less than 0.05 indicate model terms are significant. In this case A, B, A^2, B^2 are more significant model terms for grade. Values greater than 0.1000 indicate the model terms are not significant. The significance level of the coefficients is evaluated with the *F*-value. In other words, for the coefficient to be more significant, the *F*-value is expected to be large.

The response of yield (%) and grade (%) fitted to the second-order polynomial equations. The uncoded model equation for grade (Y_1) and recovery (Y_2) of the concentrate fraction of the shaking table is in Eqs. (2) and (3), respectively. A positive value of the parameter coefficients shows a direct effect on yield and copper content, while a negative sign indicates an adverse effect.

$$Y_1 = +53.27–6.30A+1.65B–0.59C–0.075D+0.13AB+1.48AC–$$
$$–0.43AD–0.17BC+0.27BD+0.27CD–20.38A^2–5.37B^2–3.92C^2–3.47D^2 \quad (2)$$
$$Y_2 = +83.56–10.49A–1.75B–3.30C–1.91D+2.05AB+4.45AC+$$
$$1.56AD–2.16B+0.014BD–2.57CD–4.66A^2–9.067B^2–7.15C^2–3.94D^2 \quad (3)$$

TABLE IV. RSM–BBD designed experimental results

Run number	Actual independent variables				Grade, Cu %		Yield, Cu %	
	A	*B*	*C*	*D*	Actual	Predicted	Actual	Predicted
1	300–500	12	2	50	52.63	53.27	84.95	83.56
2	300–500	12	1	60	47.22	46.12	77.95	76.43
3	300–500	18	2	60	45.44	46.28	64.04	66.92
4	500	18	2	50	23.68	23.00	60.44	59.66
5	300–500	18	2	40	47.35	45.88	72.76	70.71
6	300	12	1	50	38.26	37.33	91.92	89.99
7	300–500	12	2	50	53.02	53.28	82.19	83.56
8	300–500	12	2	50	53.96	53.27	83.40	83.56
9	500	6	2	50	20.42	19.44	59.93	59.06
10	500	12	1	50	22.69	21.77	62.60	60.11
11	300–500	18	3	50	46.22	44.87	62.90	60.15
12	300–500	12	3	50	32.65	33.18	71.38	74.50
13	300–500	12	1	40	46.91	46.81	71.82	75.10
14	300–500	6	2	40	44.35	43.13	76.45	74.23
15	300	6	2	50	31.42	32.29	82.74	84.14
16	500	12	3	50	23.02	23.56	59.82	62.41
17	300	18	2	50	34.16	35.33	75.06	76.55
18	500	12	2	60	22.24	22.61	63.43	64.12
19	300–500	12	3	60	45.2	45.48	67.35	64.69
20	300–500	6	2	60	41.35	42.43	67.68	70.39
21	300–500	6	1	50	41.19	42.74	68.80	70.24
22	300–500	12	3	40	43.8	45.09	71.52	73.65
23	300–500	6	3	50	43.21	41.91	70.43	67.97
24	300–500	12	2	50	53.45	53.29	83.72	83.56
25	300	12	2	60	37.53	36.06	84.10	81.99
26	500	12	2	40	21.94	23.61	63.99	64.82
27	300	12	2	40	35.53	35.36	90.90	88.92
28	300–500	18	1	50	44.89	46.39	69.88	71.07

Fig. 4 shows the solid linear relationship between the experimental and predicted values of the responses. The determination coefficients R^2 of 0.9907 and 0.9546 of grade and yield cupper content of PCBs, respectively, shows that the fit is reasonably good. The predicted R^2 values of grade and yield copper content of PCB 0.9475 and 0.9346, respectively, are reasonably consistent with the adjusted R^2 values 0.9806 and 0.9256, and the difference between these two values is less than 0.2 for both models, implying that the overall mean may be a better predictor of the response. The actual and predicted values of both the concentrate grade and yield obtained using model Eqs (2) and (3) are presented in Fig. 4a and b, respectively. The predicted values are in well agreement with the experimental values.

TABLE V. Regression coefficient values for the parameter and parameter interaction effects

Factor	Cu (%) grade			Cu (%) yield		
	Coefficient estimate	*F*-value	*Prob>F*	Coefficient estimate	*F*-value	*Prob>F*
Intercept	53.27	98.60	<0.0001	83.56	19.51	< 0.0001
A-particle size, mm	–6.30	215.92	<0.0001	–10.49	154.05	< 0.0001
B-wash water flow rate, L/m	1.65	14.83	0.0020	–1.75	4.28	0.0592
C-deck angle, °	–0.59	1.89	0.1930	–3.30	15.21	0.0018
D-motion frequency, Hz	–0.075	0.031	0.8638	–1.91	5.09	0.0419
AB	0.13	0.031	0.8637	2.05	1.95	0.1859
AC	1.48	4.00	0.0667	4.45	9.23	0.0095
AD	–0.43	0.33	0.5767	1.56	1.13	0.3069
BC	–0.17	0.054	0.8198	–2.16	2.18	0.1634
BD	0.27	0.13	0.7194	0.014	$8.675*10^{-5}$	0.9927
CD	0.27	0.13	0.7194	–2.57	3.09	0.1022
A^2	–20.38	1131.48	<0.0001	–4.66	15.17	0.0018
B^2	–5.37	78.44	<0.0001	–9.06	57.38	<0.0001
C^2	–3.92	41.83	<0.0001	–7.15	35.79	<0.0001
D^2	–3.47	32.78	<0.0001	–3.94	10.87	0.0058
Lack of fit		8.46	0.0526		8.36	0.0535

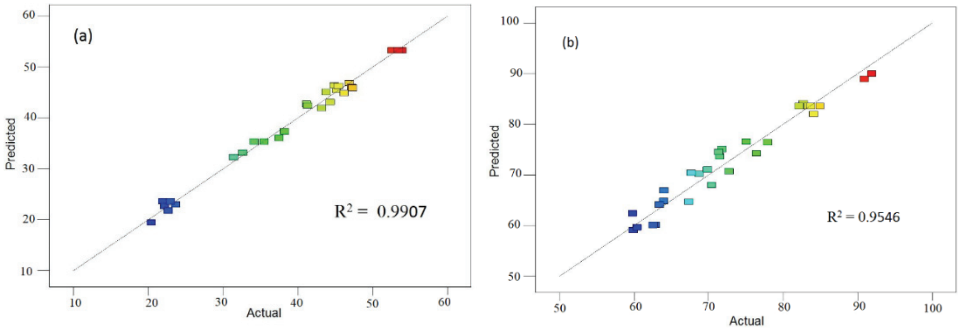

Fig. 4. Relationship between observed and predicted values (a: grade, b: recovery).

Table VI shows the analysis of variance of the developed models for the concentrate fraction of Cu grade and yield. Fisher's test with corresponding *P* values was used to study the effect of different parameters on two responses (grade and recovery) in the result analysis by ANOVA analysis model. The models are significant as the *F*-value is high, the *Prob*>*F* value is less than 0.05 and the standard deviation is very small 1.48 for the grade and 2.93 for the recovery.

TABLE VI. ANOVA for the parameters of RSM-BBD for the grade and yield models

Statistics	Source	
	Cu (%) grade model	Cu (%) yield model
Sum of square	3041.68	2342.52
Degree of freedom	14	14
Mean square	217.26	167.32
F-Value	98.60	19.51
Prob>*F*	<0.0001	<0.0001
Standard deviation	1.48	2.93
R^2	0.9907	0.9546

According to the results of the shaking table tests, which were divided into narrow sizes to obtain maximum grade and yield; the lowest grade value 20.42 %, the highest grade value 53.96 %, the lowest yield 59.82 % and the highest yield 91.92 % were found (Table VII).

TABLE VII. Statistical analysis for responses (grade and yield)

Variable	Unit	Type	Value		
			Std. Dev.	Low	High
Particle size	mm	Factor	0	–300	+500
Wash water flow rate	L/m	Factor	0	6	18
Deck angle	°	Factor	0	1	3
Motion frequency	Hz	Factor	0	40	60
Rrecovery of concentrate	%	Response	1.48	59.82	91.92
Grade (Cu)	%	Response	2.93	20.42	53.96

Effect of shaking table variables on concentrate grade

Due to the significant difference between the specific gravity of plastics and metals, PCB powder can be separated through low-cost gravity operations such as tabling. To provide the better understanding of the results, the predicted models are described in terms of three dimensional (3D) response surface plots which show the effect of process variables on grade and yield of Cu in concentrate fraction of shaking table. Fig. 5 explains the effect of the process parameters of Wilfley table on the grade of concentrate fraction and it shows the effects of particle size (*A*), wash water flow rate (*B*), deck angle (*C*) and frequency (*D*) on the grade of the concentrate fraction. It is observed that higher grade is obtained at lower level of wash water, flow rate and higher level of deck tilt angle, which is caused due to a decrease in the residence time of the gangue minerals and that results in the wash away of the low-density minerals to the tailing fraction. Also, it is observed that higher grade is obtained at 300–500 particle size range at level of wash water flow rate. When evaluating the effect of changes made among the *B*, *C* and *D* parameters on the grade, it was observed that the results showed relatively moderate values and there was not a significant difference. From the graphs and the equation obtained through ANOVA analysis, it is understood that the particle size has the greatest impact on the Cu % grade. The results depicted in Fig. 5 indicate that the highest copper grade, 53.96 %, is obtained at the centre level of the inclination and the wash water flow rate recovery is necessary. Therefore, the tabling stage serves a dual purpose as a classification and a pre-concentration operation. The process targets a high yield clean product with a middling stream having relatively lower purity, and a low-grade rejectable tailings stream.

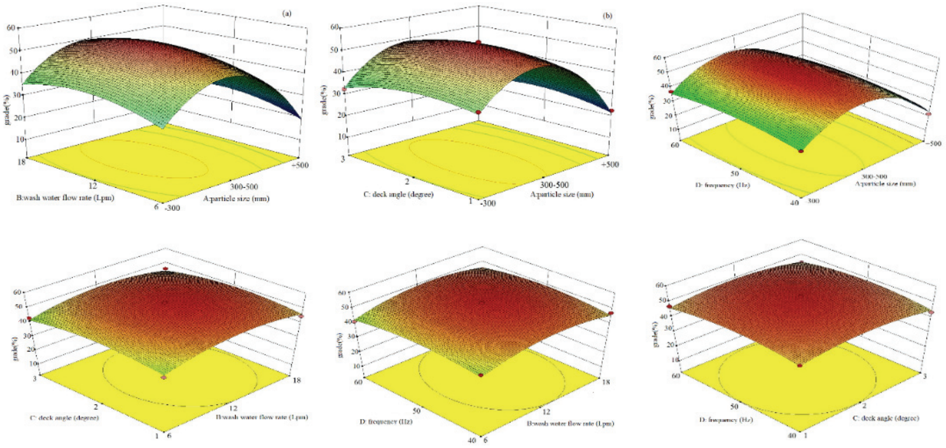

Fig. 5. Results of effecting variables on concentrate for Cu % grade.

Effect of of shaking table variables on concentrate yield

Based on the information provided, Fig. 6 shows the variables that affect the concentration of Cu % yield in a separation process. The relationship between these variables is complex, and the values of some parameters are dependent on the level of other parameters. Specifically, it has been observed that the effect of deck angle on the Cu % yield is dependent on the washing water flow rate. Increasing the deck angle level reduces the washing water flow rate, especially when the washing water flow rate is at its lowest level. Therefore, a moderate level of deck angle should be selected to increase the Cu % yield. Additionally, the results show that the Cu % yield increases when the deck angle and particle size are at their lowest, and the main effects of particle size, deck angle, square of wash water flow rate, and frequency have a significant impact on the separation process.

Among the interactional effects, the interactions between particle size, deck angle, and wash water flow rate have a considerable effect on the recovery of the concentrate fraction. However, the frequency and interaction between frequency and deck angle, as well as the interaction between wash water flow rate and frequency, are less significant. Empirical models were used to describe the effect of each variable at different combination variables on concentrate recovery in Fig. 6. Overall, understanding the relationships and interactions between these variables is critical to optimizing the separation process and achieving the desired Cu % yield.

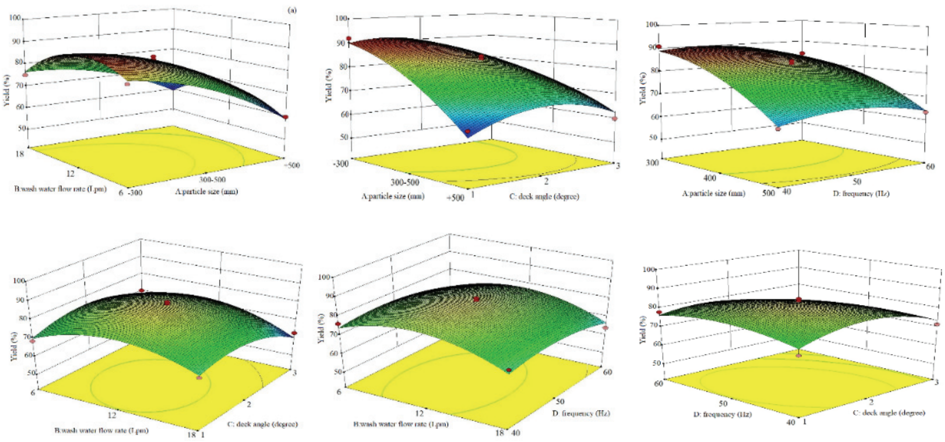

Fig. 6. Results of effecting variables on concentrate for Cu % yield.

Validation of the model

Grade and recovery are significant terms for evaluating the performance of any unit operation in mineral processing. In addition, the grade and recovery of any process are inversely related to each other. To validate the obtained model for predicting the grade and recovery of copper content in concentrate, several tests were conducted based on the empirical model. The observed and predicted results for both responses are illustrated in Fig. 7. Fig. 7 shows that the predicted values are in good agreement with the observed values, with R^2 values of 0.9525 and 0.9413 for grade and recovery of copper concentrates, respectively. Overall, this study provides valuable insights into the performance of the described unit operation for copper processing.

It was also found that the predicted values of the experimental values are in reasonably good agreement, with R^2 value for grade and recovery of the concentrate fraction of the laboratory shaking table is 0.9907 and 0.9806, respectively. According to the results of the ANOVA analysis, the particle size was found to be the most effective parameter in terms of both grade and metal recovery. The optimized values for the greatest grade and the recovery were 53.96 and 83.40 %, respectively.

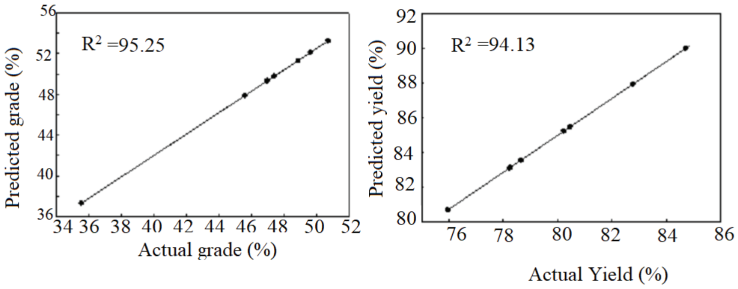

Fig. 7. Relationship between observed and predicted values for the grade and yield (% Cu).

CONCLUSION

In this study, the Box Behnken design was used to optimize the performance of the wet shaking table and to identify the ideal combination of its operating parameters. The four process parameters were investigated: deck angle, motion frequency, wash water rate, and particle size diameter. The mathematical models were developed for both grade and recovery of Cu in the concentrate fraction by using a set of experimental data and the mathematical software package Design Expert 9.0.2 software. The optimal settings were determined to be a deck angle of 2°, motion frequency of 50 Hz, wash water rate of 12 L/m, and particle size diameter of –500+300 mm. Optimal settings were determined to be near the central points of the experimental design, indicating that the true optimal point may lie within the designed space.

Acknowledgments. The authors would like to thank Barış Kızıltepe for his help during the comminution steps, Assoc. Prof. Dr. Hatice Yılmaz for mineralogical characterization and Lecturer Fatih Turan for chemical characterization.

ИЗВОД

ИЗВЛАЧЕЊЕ БАКРА СА ШТАМПАНИХ КОЛА (PCB) ПОМОЋУ ВИБРАЦИОНОГ СТОЛА

ÖZGE GÖK и GÜL AKAR ŞEN

Dokuz Eylul University, Faculty of Engineering, Mining Engineering Department, İzmir, Turkiye

У последњих неколико година расте заинтересованост за поновну употребу металних компоненти из електричне и електронске опреме отпадног порекла (WEEE), што се односи на електричне и електронске уређаје који су постали застарели, престали да раде или показали дефекте током производње. У овом истраживању као алат за гравитациону концентрацију за рециклажу бакра из лаких компонената изабран је вибрациони сто. Технолошки поступак је укључивао уситњавање, гравиметријску концентрацију и физичко–хемијску карактеризацију улазног материјала и продуката. Параметри процеса су били угао стола (у степенима), фреквенција покрета (Hz), брзина воде за испирање (L/m) и пречник честица. Бох Бехнкен (Box Behnken) дизајн (BBD) је употребљен за оптимизацију перформанси мокрог вибрационог стола и идентификацију идеалне комбинације његових радних параметара. Анализом експерименталног дизајна утврђено је да су оптималне вредности за угао стола, фреквенцију покрета, брзину воде за испирање и пречник честица износили 2°, 50 Hz, 12 L/m и –500+300 mm, редом. Ове оптималне поставке биле су лоциране близу централних тачака експерименталног дизајна, што сугерише да се стварна оптимална тачка може налазити унутар одређеног простора.

(Примљено 16. марта, ревидирано 8. априла, прихваћено 12. априла 2023)

REFERENCES

1. M. Sarvar, M. M. Salarirad, M. A. Shabani, *Waste Manage.* **45** (2015) 246 (https://doi.org/10.1016/j.wasman.2015.06.020)
2. W. Zhang, J. Ren, S. Liu, Z. Yuan, *Proc. Environ. Sci.* **31** (2016) 171 (https://doi.org/10.1016/j.proenv.2016.02.023)
3. P. M. S. Sousa, L. M. Martelo, A. T. Marques, M. M. S. M Bastos, H. M. V. M. Soares, *Chem. Eng. J.* **434** (2022)134 (https://doi.org/10.1016/j.cej.2022.134604)
4. Y. Zhao, X. Wen, B. Li, D. Tao, *Min. Metall.Proc*. **21** (2004) 99 (https://doi.org/10.1007/bf03403310)
5. J. Li, Z. Xu, Y. Zhou, *J. Electrostatics* **65** (2007) 233 (https://doi.org/10.1016/j.elstat.2006.08.004)
6. C. Duan, X. Wen, C. Shi, Y. Zhao, B. Wen, Y. He, *J. Hazard. Mater.* **166** (2009) 4780 (https://doi.org/10.1016/j.jhazmat.2008.11.060)
7. M. R. Bilesan, I. Makarava, B. Wickman, E. Repo, *J.Cleaner Prod.* **286** (2021) 125505 (https://doi.org/10.1016/j.jclepro.2020.125505)
8. T. Fujita, H. Ono, G. Dodbiba, K Yamaguchi, *Waste Manage.* **34** (2014) 1264 (https://doi.org/10.1016/j.wasman.2014.03.002)
9. W. Chen, Y. Chen, Y. Shu, Y. He, J. Wei, *J. Cleaner Prod.* **313 (**2021) 127881 (https://doi.org/10.1016/j.jclepro.2021.127881)
10. E. Y. Yazici, H. Deveci, *Int. J. Min. Proc.* **134 (**2015) 89 (https://doi.org/10.1016/j.minpro.2014.10.012)
11. I. Birloaga, F. Vegliò, *J. Environ. Chem. Eng.* **4** (2016) 20 (https://doi.org/10.1016/j.jece.2015.11.021)
12. C. Cocchiara, S. Dorneanu, R Inguanta, C. Sunseri, P. Ilea, *J. Cleaner Prod.* **230** (2019) 170 (https://doi.org/10.1016/j.jclepro.2019.05.112)
13. D. Bourgeois, V. Lacanau, R. Mastretta, C. Contino-Pépin, D. Meyer, *Hydrometallurgy* **191** (2020) 105241 (https://doi.org/10.1016/j.hydromet.2019.105241)
14. S. Choubey, P. Goswami, S. Gautam, *Mater. Today Proc.* **42** (2021) 2656 (https://doi.org/10.1016/j.matpr.2020.12.596)
15. D. Franke, T. Suponik, P.M. Nuckowski, K. Golombek, K. Hyra, *Manage. Syst. Prod. Eng*. **28** (2020) 213 (https://doi.org/10.2478/mspe-2020-0031)
16. A. Akcil, C. Erust, C. S. Gahan, M Ozgun, .M. Sahin, A. Tuncuk, *Waste Manage.* **45** (2015) 258 (https://doi.org/10.1016/j.wasman.2015.01.017)
17. P. Hadi, M. Xu, C. S. K Lin, C. Hui, G. McKay*, J. Hazard. Mater.* **28** (2015) 234 (https://doi.org/10.1016/j.jhazmat.2014.09.032)
18. H. M. Veit, A. M. Bernardes, J. Z. Ferreira, J. A. S Tenório,. C. de Fraga Malfatti, *J. Hazard. Mater.* **137** (2006) 1704 (https://doi.org/10.1016/j.jhazmat.2006.05.010)
19. M. Kaya, *Electronic waste and printed circuit board recycling technologies,* Springer International Publishing, Berlin, 2019 (ISBN: 9783030265939)

20. X. Zeng, L. Zheng, H. Xie, B. Lu, K. Xia, K. Chao, W. Li, J. Yang, S. Lin, and J. Li, *Proc. Environ. Sci.* **16 (**2012) 590 (https://doi.org/10.1016/j.proenv.2012.10.081)
21. M. Somasundaram, R. Saravanathamizhan, C. Ahmed Basha, V. Nandakumar, S. Nathira Begum, and T. Kannadasan. *Powder Technol.* **266** (2014) 1 (https://doi.org/10.1016/j.powtec.2014.06.006)
22. A. Das, A. Vidyadhar, S.P. Mehrotra, *Conserv. Recycl.* **53** (2009) 464 (https://doi.org/10.1016/j.resconrec.2009.03.008)
23. G. Chao, W. Hui, L. Wei, F. Jiangang, Y. Xin, *Waste Manage.* **31** (2011) 2161 (https://doi.org/10.1016/j.wasman.2011.05.011)
24. J. Hanafi, E. Jobiliong, A. Christiani, D.C. Soenarta, Kurniawan, J., Irawan, *J. Soc. Behav. Sci.* **57** (2012) 331 (https://doi.org/10.1016/j.sbspro.2012.09.1194)
25. F. Ma, Y. Tao, Xian, Y, *Metall. Exploration* **38** (2021) 117 (https://doi.org/10.1007/s42461-020-00234-5)
26. F. Burat, M. Özer, *Physicochem. Prob. Min. Proc.* **54** (2018) 554 (https://doi.org/10.5277/ppmp1858)
27. E. Ventura, A. Futuro, S. C. Pinho, M. F Almeida. J. M. Dias, *J. Environ. Manage.* **223** (2018) 297 (https://doi.org/10.1016/j.jenvman.2018.06.019)
28. M. M. H. Al-Tigani, A. Awdekarim, A. A.Abdueldaem, A. A. S. Seifelnasr,. *Int. J. Acad. Multidiscip. Res. (IJAMR)* **4** (2020) 63 (https://www.researchgate.net/publication/342052572_Application_of_Response_Surface_Methodology_on_Beneficiation_of_Sudanese_Chromite_Ore_via_Pilot_Plant_Shaking_Table_Separator/link/5ee06f26299bf1d20bdebebf/download)
29. S. K. Tripathy, Y. R. Murthy, *Powder Technol.* **221** (2012) 387 (https://doi.org/10.1016/j.powtec.2012.01.035)
30. N. Aslan, *Powder Technol.* **174** (2007) 127 (https://doi.org/10.1016/j.powtec.2007.01.007)
31. G. Akar, *Minerals* **6** (2016) 5 (https://doi.org/10.3390/min6010005)
32. B. A. Wills, J. A. Finch, *Wills' Mineral Processing Technology*, 8th ed., Butterworth-Heinemann, Oxford, 2016 (ISBN: 9780080970547)
33. Q. Dehaine, L. O. Filippov, R. Joussemet, *Min. Eng.* **100** (2017) 200 (https://doi.org/10.1016/j.mineng.2016.10.018)
34. *Recyclinginside*, https://recyclinginside.com/recycling-technology/separation-and-sorting-technology/what-is-the-shaking-table (visited 24 September 2022)
35. http://en.wikipedia.org/wiki/Box%E2%80%93Behnken_design (visited 24 October 2022)
36. B. Ait-Amir, P. Pougnet, A. El-Hami, *Embedded Mechatronic Systems 2,* 2nd ed., ScienceDirect, Elsevier, Amsterdam, 2020 (ISBN: 9781785481901)
37. S. L. C. Ferreira, R. E. Bruns, H. S. Ferreira, G. D. Matos, J. M. David, G. C. Brandao, E. G. P. Silvaa, L. A. Portugal, P. S. dos Reis, A. S. Souzaa, W. N. L. dos Santos, *Anal. Chim. Acta* **597** (2007) 179 (https://doi.org/10.1016/j.aca.2007.07.011)
38. T. J. Robinson, *Box-Behnken Designs,* John Wiley & Sons, Ltd., Chichester, 2014 (https://doi.org./10.1002/9781118445112.stat04101)
39. M. Alhajabdalla, H. Mahmoud, M. S. Nasser, I. A. Hussein, R. Ahmed, H. Karami,. *ACS Omega* **6** (2021) 2513 (https://doi.org/10.1021/acsomega.0c04272)
40. S. Ahmed, *The Open Educator*, https://www.theopeneducator.com/doe/Response-Surface-Methodology/Box-Behnken-Response-Surface-Methodology (visited 10 January 2023).

Journal of the Serbian Chemical Society
JSCS@tmf.bg.ac.rs • www.shd.org.rs/JSCS

J. Serb. Chem. Soc. 88 (10) 1055–1064 (2023)
JSCS–5680

Original scientific paper
Published 24 October 2023

Potentially toxic element accumulation in two *Equisetum* species spontaneously grown in the flotation tailings

GORDANA ANDREJIĆ[1]*, MILIJANA KOVAČEVIĆ[2], ŽELJKO DŽELETOVIĆ[1],
UROŠ ALEKSIĆ[1], ISIDOR GRDOVIĆ[2] and TAMARA RAKIĆ[2]

[1]*University of Belgrade, Institute for the Application of Nuclear Energy, Banatska 31b, 11080 Belgrade, Serbia and* [2]*University of Belgrade, Faculty of Biology, Studentski trg 16, 11000 Belgrade, Serbia*

(Received 13 January, revised 21 June, accepted 1 July 2023)

Abstract: Decades of mining activity have resulted in the accumulation of significant amounts of tailings that are deposited over the natural vegetation, forming deposits tens of meters thick. The tailings are poor in organic matter and macronutrients and contain a high concentration of potentially toxic elements (PTE). Their surface remains unvegetated for long periods of time and is susceptible to fluvial and wind erosion. *Equisetum arvense* and *E. telmateia* appear to be the first colonizers in the tailings of the Pb–Cu–Zn mine in Serbia. Each plant was sampled along with its associated substrate. Pseudototal and available metals in the substrate, as well as total As, Cd, Cu, Fe, Mn, Ni, Pb and Zn concentrations in the plant parts were determined by atomic absorption spectrophotometry. The findings show that both species have high bioaccumulation capacity and tolerance to otherwise toxic concentrations due to efficient accumulation, immobilization and detoxification of these elements in their underground parts. It is expected that the long-term presence of metal-tolerant horsetail species would increase the organic matter content of flotation residues, thus gradually improving their physical, chemical and biological properties. This, in turn, would promote the natural succession of other metal-tolerant plant species and soil microorganisms.

Keywords: potentially toxic element; pollution; phytoremediation.

INTRODUCTION

As a result of the substantial global demand for mineral raw materials and their extensive use in various industries, mining and ore processing remain prominent sectors within the primary industry of certain countries, yielding significant financial profits. Despite advancements in mining technology and waste reduction strategies, mining activities continue to pose a significant threat to the

---

* Corresponding author. E-mail: gordanaa@inep.ac.rs

https://doi.org/10.2298/JSC230113028A

environment due to the generation of spoils and effluents containing exceedingly high concentrations of potentially toxic elements (PTEs). It is worth noting that only a small fraction of the total processed material is extracted as a concentrated metal product, while a substantial proportion, up to even 97–99% of the mined ore, becomes flotation tailings. Flotation tailings share a similar composition to the original ore, and containing significant amounts of unrecovered minerals, contribute to the environmental pollution.[1–3] Flotation tailings consists of fine particles ($d_p \leq 75$ μm) that remain after the technological processing and extraction of desired elements from the polymetallic ore, and are discarded with water into the tailing pond. Further release of PTEs from these particles occurs through various processes of chemical and physical particle disintegration. Eventually, PTE enter the food web, often leading to adverse effects on the health and biodiversity of surrounding ecosystems, as well as posing risks to human health.[4] This issue is particularly prominent in countries where regulatory framework to mitigate environmental pollution risks is not effectively enforced. Furthermore, the flotation tailings are also abundant in process chemicals, including organic solvents like xanthate, which are utilized for the effective separation of metals during mineral flotation processes. It is noteworthy that a significant portion, nearly half, of the xanthates employed in the mineral flotation process is ultimately discharged into the flotation tailings.[5] The presence of these process chemicals within the tailings, further emphasizes the complex composition and potential environmental impact of these waste materials. Additionally, flotation tailings surface layers are prone to fluvial erosion and the dispersion of fine particles through wind, further exacerbating their environmental impact.[4,6,7] Therefore, PTE contamination can extend several km beyond the mining site, significantly affecting local and regional land use and posing health risks to nearby human communities.

Restoring large areas covered by flotation tailings presents significant challenges due to unfavourable physical and chemical properties of these technosols, which strongly hinder plant growth and result in consequent long-term lack of vegetation cover.[8–10] Vascular plants that establish themselves as the initial colonizers of flotation tailings are uncommon and exhibit remarkable adaptability to the challenging environmental conditions found in such areas. Among these rare plant species that pioneer the colonization of polymetallic flotation tailings, several belong to the genus *Equisetum*. *Equisetum* is an ancient genus of vascular plants with a long evolutionary history dating back to the Upper Devonian period.[11] All species within the *Equisetum* genus are perennial plants, possessing erect herbaceous stems that emerge from an extensive rhizome system bearing adventitious roots.[11,12] Horsetails have demonstrated a remarkable ability to tolerate unfavourable physical and chemical properties of substrates, even allowing for the accumulation of metals at higher concentrations.[13,14] This resilience in the face of challenging soil conditions is thought to be linked to their archaic adaptation to geothermal environments characterized by high levels of potentially toxic metals and metalloids harmful to most plant species, such as arsenic or mercury.[15] In the specific context of this study, the two horsetail species, *Equisetum arvense* and *E. telmateia*, were observed as the initial colonizers in the flotation tailings of a lead–copper–zinc mine in Serbia. The objectives of this research were twofold: *i*) to analyse the concentrations of potentially toxic elements (PTEs) in the flotation tailings as well as in the underground and aerial parts of the two *Equisetum* species and *ii*) to evaluate their capacity for bioaccumulation and their potential for utilization in the initial stages of bioremediation efforts.

EXPERIMENTAL

Details related to site description and plant and substrate sampling are given in Supplementary material to this paper.

Substrate analysis

The substrate samples were cleaned from stones and biotic material. After air drying, the samples were ground and sieved (pore diameter 200 μm). Ten grams of a homogenized substrate was mixed with 25 ml of distilled water or with 25 ml of 1 M KCl to determine active (pH_{H2O}) and exchangeable (pH_{KCl}) substrate acidity, respectively.[16] The samples were stirred for 30 min and the pH was measured directly in the suspension (Iskra MA 5730).

For determination of the pseudo-total PTE concentration (As, Cd, Cu, Fe, Mn, Ni, Pb, Zn) in the substrate, samples were dried to constant weight at 100 °C, and digested in 65 % HNO_3 at 150 °C in Kjeldaltherm® digestion block (Gerhardt, Germany), according to the US EPA method 3051.[17] Solutions for determining available PTE concentrations were made by extraction for 2 h in 1 M ammonium acetate and 0.01 M EDTA mixture (pH 7).[18] The concentrations of PTE were determined by atomic absorption spectrophotometer (Shimadzu AA-7000, Japan) comparing sample absorption values with those of known standards. The precision of the procedure for PTE was evaluated by analyzing the certified soil material (Soil 90-0115-0106, BIPEA-Bureau Interprofessionnel d'Etudes Analytiques).

Plant analysis

To avoid contamination by residual substrate particles, the collected plant samples were carefully washed in tap water and then thoroughly rinsed with deionized water. The plant material was divided into (vegetative) shoots and underground parts, air-dried, powdered, oven-dried at 100 °C for 24 h, and completely digested in 65 % HNO_3 at 150 °C in Kjeldaltherm® digestion block, according to the US EPA method 3051.[17] Concentrations of PTE (As, Cd, Cu, Fe, Mn, Ni, Pb, Zn) in plant samples were determined by atomic absorption spectrophotometer (Shimadzu AA-7000, Japan), comparing the sample absorption values with those of known standards. Analytical procedure accuracy was assessed by analysis of the standard reference plant material NIST 1515 (apple leaves).

Phytoremediation potential

The phytoremediation potential of two horsetail species was determined on the basis of bioconcentration factor (BCF) and translocation factor (TF).[19] BCF provides information on the accumulation of PTE in the underground plant parts and their efficiency of PTE removal from the substrate. Translocation factor (TF) is the ratio of the PTE concentration in the aboveground part of the plant and its concentration in the undergound parts, and provides information on the plant's efficiency in translocating a certain PTE from underground to its aboveground parts. BCF and TF values were calculated using the following formulas:

$$BCF = c_{\text{underground plant parts}} / c_{\text{substrate}} \tag{1}$$

$$TF = c_{\text{shoot}} / c_{\text{underground plant parts}} \tag{2}$$

where $c_{\text{underground plant parts}}$ and c_{shoot} represent PTE concentrations in plant underground parts and shoots, respectively, whereas $c_{\text{substrate}}$ is the available PTE concentration in the belonging substrate.

Statistical analysis

Data are expressed by the mean ± standard deviation of eight replicates. All data were initially tested by the Shapiro-Wilk test for normality. Statistically significant differences between two independent groups were calculated using the non-parametric Mann-Whitney U test because of the non-normality of the data. Statistical analyses were performed in R (ver. 3.5.1; R Core Team 2018).

RESULTS AND DISCUSSION

Flotation tailings chemical properties

As indicated in Table I, both the active (pH_{H2O}) and exchangeable soil acidity (pH_{KCl}) were within the neutral range. The pH_{H2O} was statistically significantly lower in *E. arvense* substrate compared to that of *E. telmateia*, whereas pH_{KCl} was lower again in the *E. arvense* substrate, but without statistical significance (Table I). At a soil pH around neutral, it is assumed that all the studied elements are well dissolved in the soil water solution, although their availability would increase with decreasing pH, except for As.

Both substrates exhibited elevated pseudo-total concentrations of several elements (As, Cd, Cu, Pb, Zn) that surpassed the maximum allowable concentrations (*MAC*) specified in international soil guidelines (Table I). These concentrations were several-fold higher (Ni, Pb, Zn, Cd, Cu) and approximately 25-fold higher (As) than the *MAC* values. Since the substrates studied were solid waste materials from extractive metallurgical processes, it was expected that such high concentrations of potentially toxic elements (PTEs) would be observed. Although detected pseudo-total PTE concentrations were very similar between the substrate samples, there were statistically significant differences regarding all elements, with exception of As. This heterogeneity is a common characteristic of the flotation tailings resulting from the deposition of waste material originating from different mined ores, which can vary in their metal content.[20]

The portion of EDTA-available elements in the pseudo-total content in F_{ET} and F_{EA} substrate is listed in descending order, respectively, and was as follows: Pb (45 %, 44 %) > Cd (36 %, 37 %) > Mn (16 %, 20 %) > Ni (13 %, 8 %) > Zn (8 %, 10 %) > Cu (7 %, 10 %) > Fe (0.2 %). The presence of elevated metal availability in flotation tailings has been previously established in the literature for various metals. For instance, Kasowska *et al.*[21] highlighted the considerable presence of readily available copper (Cu) in copper ore flotation tailings, which constituted approximately 41 % of its pseudo-total concentration. Additionally, Karczewska and Milko[22] reported that EDTA exhibited the highest effectiveness as a chelating agent, enabling the release of up to 16 % of EDTA-available lead from the pseudo-total metal content. The prominent metal availability in the investigated flotation tailings may be attributed to the presence of residual metal xanthates and their degradation products in the tailings. The highest Pb and Cd EDTA-availability can be attributed to very high EDTA efficiency for desorption of listed metals from xanthates.[23,24] While it is commonly known that metal availability is moderate at neutral and tends to be higher under acidic conditions, it is important to consider that in substrates already colonized by plants the metal bioavailability can be further increased in plant rhizosphere. This enhanced bioavailability of metals can be attributed to some microbiome and plant roots exudates, such as organic acids and hydrogen ions, that acidify the root micro-environment and desorb metals at the negatively charged reactive sites of soil particles making them more available for uptake by roots.[25]

TABLE I. pH values and PTE concentrations (mg kg^{-1}) in the flotation tailings; *MAC* – maximum allowable concentration.[26] Values with no letter in common are significantly different (Mann-Whitney U, $p < 0.05$)

Parameter	Substrate		*MAC* / mg kg^{-1}
	F_{ET}	F_{EA}	
pH_{H_2O}	7.6 ± 0.05^b	7.5 ± 0.03^a	–
pH_{KCl}	7.4 ± 0.1^a	7.0 ± 1.3^a	–
Pseudo-total			
As	484 ± 243^a	533 ± 36^a	15–20
Cd	9.6 ± 0.2^b	8 ± 0.1^a	1–5
Cu	349 ± 12^b	300 ± 4^a	60–150
Fe	25848 ± 95^b	25399 ± 145^a	–
Mn	2003 ± 25^b	1759 ± 61^a	1500–3000
Ni	68 ± 1.3^a	75 ± 1^b	20–60
Pb	448 ± 43^a	558 ± 6^b	20–300
Zn	1823 ± 24^b	1445 ± 30^a	100–300
EDTA available			
Cd	3.5 ± 1.6^a	3.0 ± 0.2^a	–
Cu	25 ± 18^a	33 ± 0.8^a	–
Fe	49 ± 4.6^a	62 ± 7^b	–
Mn	328 ± 24^a	348 ± 11^a	–
Ni	8.5 ± 7^a	6 ± 4^a	–
Pb	200 ± 7^a	247 ± 21^a	–
Zn	153 ± 37^a	149 ± 40^a	–

Potentially toxic element accumulation by horsetails

The analysis of concentrations of potentially toxic elements in the investigated species, *E. arvense* and *E. telmateia*, reveals a significant accumulation of PTE in their underground parts. Notably, the concentrations of the investigated elements, except for As and Mn, were considerably higher in the underground plant parts (Table II) compared to the corresponding EDTA-available element concentrations in the substrates (Table I). Consequently, this disparity led to their BCFs > 1 (Table III). Both *E. arvense* and *E. telmateia* exhibited the highest bioconcentration factors for Fe and Ni, followed by Zn and Cu. Generally, *E. arve*nse demonstrated higher BCFs compared to *E. telmateia*, with Cu and Ni showing a 1.7-fold and 4.5-fold higher BCFs in *E. arvense*. Both *Equisetum* species efficiently retained and immobilized accumulated PTE in their underground parts, manifesting low transfer rates to shoots. This was detected through significantly lower concentrations of the elements in the shoots, accompanied by $TF < 1$ (Table III). However, an exception was noted only for Mn ($TF = 1.24$) in *E. telmateia*. The overall results indicate that both species possess a substantial bioaccumulation capacity and tolerance to elevated concentrations of PTE in their underground parts. Their metal tolerance is attributed to complex and efficient PTE detoxification systems in rhizomes that could be also associated with typically high silicon content in *Equisetum* that is not simply beneficial, but essential mineral element.[27,28] It is well documented that Si alleviates heavy metal stress in horsetails and some other plants by being involved in external and internal mechanisms of Si-mediated alleviation of metal toxicity, as a part of their biochemistry.[14,29,33] Previous studies have shown that horsetails are often behaving as extremophiles regarding their substrate properties. Thus, *E. arvense* was found to tolerate nitrogen deficiency and specific elemental composition in volcanic tephra and flotation tailings, therefore being the most or among the most successful and dominant herbaceous species in such specific disturbed habitats.[34–36] Also, *E. palustre*, *E. ramosissimum* and *E. ramosisti* were among the first plant colonizers in natural succession of the mine and flotation tailings.[37–40] Furthermore, owing to its metal tolerance *E. hyemale* was efficiently used in the removal of Pb and Cr from the leachate in the wastewater treatment biotechnology.[41]

Even though *Equisetum* species typically form extensive colonies on wetlands, they have some properties that can be helpful in substrates that appear dry on the surface. One such trait is the presence of an extensive underground rhizome system that can penetrate up to a depth of one meter, allowing them to access water from deeper soil layers.[12] This morphological adaptation proves particularly valuable in colonising substrates with unfavourable granulometric structure and water conditions, such as flotation tailings.

TABLE II. PTE concentrations in underground parts and shoots of *E. telmateia* and *E. arvense* grown in the flotation tailings (mg kg^{-1})

Sample	Element	*E. telmateia*	*E. arvense*	Upper concentration limits[20]
Underground parts	As	18±1^{a}	23±0.7^{b}	–
	Cd	5.0±0.1^{a}	9.3±0.3^{b}	–
	Cu	51.6±3.3^{a}	117±8^{b}	–
	Fe	711±6^{a}	842±15^{b}	–
	Mn	93.9±3.3^{a}	318±15^{b}	–
	Ni	13.8±0.5^{a}	44.2±2.8^{b}	–
	Pb	65.4±2.4^{a}	232±24^{b}	–
	Zn	389±14^{a}	633±33^{b}	–
Shoots	As	35.5±2.6^{b}	10±0.4^{a}	5–20
	Cd	1.3±0.1^{a}	3.1±0.1^{b}	5–30
	Cu	10.5±0.7^{b}	8.0±0.3	20–100
	Fe	618±4^{b}	380±4^{a}	–
	Mn	116±3.6^{a}	270±6^{b}	400–1000
	Ni	6.5±0.3^{b}	5.9±0.4	10–100
	Pb	26.2±0.8^{b}	24.3±0.6	30–300
	Zn	317±14^{b}	235±4	100–400

TABLE III. Bioconcentration (*BCF*) and translocation factor (*TF*) for two horsetail species grown in flotation tailings

Element	*BCF*		*TF*	
	Species			
	E.telmateia	*E. arvense*	*E.telmateia*	*E. arvense*
Cd	1.43	2.66	0.26	0.33
Cu	2.06	4.68	0.20	0.07
Fe	14.51	17.18	0.87	0.45
Mn	0.29	0.91	1.24	0.85
Ni	1.62	5.20	0.47	0.13
Pb	0.33	1.16	0.40	0.10
Zn	2.54	4.14	0.81	0.37

CONCLUSION

The current study demonstrates the ability of wetland species *Equisetum arvense* and *E. telmateia* to successfully establish themselves in heavily metal-polluted flotation tailings. Despite absorbing substantial concentrations of various potentially toxic elements (As, Cd, Cu, Pb and Zn) in their underground parts, these plants exhibit no adverse effects from the elevated levels of these elements. Remarkably, the concentrations of PTE in the shoots remain consistently low, indicating that the PTE tolerance of the two investigated horsetail species relies primarily on their capacity to exclude these elements. The findings provide further evidence that the PTE tolerance observed in both species is supported by efficient adaptive mechanisms, enabling the accumulation, effective immobilization, and detoxification of PTE within the underground plant parts.

Furthermore, the significant availability of potentially toxic elements (PTE) within the flotation tailings, containing multiple metals, highlights the potential for secondary extraction of residual metals from this type of waste material. Reprocessing the tailings would not only reduce metal leaching that are precious for industry, but also mitigate their detrimental environmental impact. Although PTE-tolerant horsetail plants could be suitable candidates for metal extraction from the rhizosphere, the collection of their underground parts from flotation tailings presents technical challenges. However, their vital ecological role in such technosols primarily lies in increasing organic matter content through the decomposition of old underground and aerial parts. This, in turn, enhances the substrate's capacity to retain PTE. Over the long term, this process facilitates gradual improvements in the physical, chemical, and biological properties of the substrate and promotes natural ecological succession by other metal-tolerant plant species and soil microorganisms.

SUPPLEMENTARY MATERIAL

Additional data and information are available electronically at the pages of journal website: https://www.shd-pub.org.rs/index.php/JSCS/article/view/12228, or from the corresponding author on request.

Acknowledgement. This work was supported by the Serbian Ministry of Education, Science and Technological Development (Grant No. 451-03-68/2022-14/ 200178 and 451-03-68/2022-14/ 200019).

ИЗВОД

АКУМУЛАЦИЈА ПОТЕНЦИЈАЛНО ТОКСИЧНИХ ЕЛЕМЕНАТА КОД ДВЕ САМОНИКЛЕ ВРСТЕ РОДА *Equisetum* НА ОДЛАГАЛИШТУ ФЛОТАЦИОНЕ ЈАЛОВИНЕ

ГОРДАНА АНДРЕЈИЋ[1], МИЛИЈАНА КОВАЧЕВИЋ[2], ЖЕЉКО ЦЕЛЕТОВИЋ[1], УРОШ АЛЕКСИЋ[1],
ИСИДОР ГРДОВИЋ[2] и ТАМАРА РАКИЋ[2]

[1]*Универзитет у Београду, Инстиут за примену нуклеарне енергије, Банатска 31б, 11080 Београд* и
[2]*Универзитет у Београду, Биолошки факултет, Студентски трг 16, 11000 Београд*

Резултат вишедеценијских рударских активности су знатне количине флотационе јаловине која се одлаже на велике површине стварајући наносе дебљине неколико десетина метара. Јаловина се карактерише дефицитом органске материје и макронутријената, садржи хемикалије пореклом из технолошког процеса и високу концентрацију потенцијално токсичних елемената (PTE). Последично, површина јаловишта изузетно дуго остаје без вегетације и подложна је флувијалној и еолској ерозији. *Equisetum arvense* и *E. telmateia* се појављују као пионирске врсте на одлагалишту флотационе јаловине рудника Pb–Cu–Zn у Србији који је истраживан у овој студији. Свака биљка је узоркована заједно са супстратом из зоне ризосфере. Псеудоукупне и приступачне концентрације As, Cd, Cu, Fe, Mn, Ni, Pb, Zn у супстрату и концентрације у биљним ткивима одређене су атомском апсорпционом спектрофотометријом. Резултати показују да су механизми толеранције засновани на ефикасној акумулацији, имобилизацији и детоксификацији PTE у подземним биљним деловима. Ове две врсте раставића имају неизоставну улогу у повећању садржаја органске материје што постепено побољшава физичка,

хемијска и биолошка својстава супстрата, а тиме и подржава природне еколошке сукцесије другим биљним врстама и земљишним микроорганизмима отпорним на метале.

(Примљено 13. јануара, ревидирано 21. јуна, прихваћено 1. јула 2023)

REFERENCES

1. J. S. Adiansyah, M. Rosano, S. Vink, G, Keir, *J. Cleaner Prod.* **108** (2015) 1050 (https://doi.org/10.1016/j.jclepro.2015.07.139)
2. Y. Liu, F Du, L. Yuan, H. Zeng, S. Kong, *J. Hazard. Mater.* **178** (2010) 999 (https://doi.org/10.1016/j.jhazmat.2010.02.038)
3. C. Bayliss, M. Bertram, K. Buxmann, B. de Gelas, S. Jones, L. Wu, Global primary aluminium industry 2010 life cycle inventor, in Energy Technology 2012: Carbon dioxide management and other technologies, M.D.Salazar-Villalpando, N.R. Neelameggham, D. P. Guillen, S. Pati, G. K. Krumdick, Eds., Wiley-TMS, Toronto, pp. 85–92
4. J. Escarré, C. Lefèbvre, S. Raboyeau, A. Dossantos, W. Gruber, J. C. Cleyet Marel, H. Frérot, N. Noret, S. Mahieu, C. Collin C, F. van Oort F, *Water Air Soil Pollut.* **216** (2011) 485 (https://doi.org/10.1007/s11270-010-0547-1)
5. R. Rezaei, M. Massinaei, A. Z. Moghaddam, *Miner. Eng.* **119** (2018) (https://doi.org/10.1016/j.mineng.2018.01.012)
6. J. V. Kalinović, S. M. Šerbula, A. A. Radojević, J. S. Milosavljević, T. S. Kalinović, M. M. Steharnik, *Environ. Monit. Assess.* **191** (2019) 15 (https://doi.org/10.1007/s10661-018-7134-0)
7. G. Andrejić, J. Šinžar-Sekulić, M. Prica, Ž. Dželetović, T, Rakić, *Environ. Sci. Pollut. Res.* **26** (2019) 34658 (https://doi.org/10.1007/s11356-019-06543-7)
8. R. A. Crane, D. E. Sinnett, P.J. Cleall, D. J. Sapsford, *Resour. Conserv. Recycl.* **123** (2017) 117 (https://doi.org/10.1016/j.resconrec.2016.08.009)
9. R. Ginocchio R, P. León-Lobos, E. C. Arellano, V. Anic, J. F. Ovalle, A. J. M. Baker, *Environ. Sci. Pollut. Res.* **24** (2017) 13484 (https://doi.org/10.1007/s11356-017-8894-8)
10. M. T. González, V. Á. López, Á. P. Fernández, B. R. Garrido, C. T. Cepeda, M. Mench, M. Puschenreiter, C. Q. Sabarís, F. M. García, P. S. Kidd, *J. Environ. Manage.* **168** (2017) 301 (https://doi.org/10.1016/j.jenvman.2016.09.019)
11. C. Husby, *Bot. Rev.* **79** (2013) 147 (https://doi.org/10.1007/s12229-012-9113-4)
12. R. L. Hauke, *A taxonomic monograph of the genus Equisetum, subgenus Hippochaete* Nova Hedwigia 8. Stuttgart, 1963, pp. 1–123 (https://western.marmot.org/Record/.b2346849x)
13. H. L. Cannon, H. T. Shacklette, H. Bastron, *Geological Survey Bulletin 1278-A*, United States government printing office, Washington, DC, 1968
14. D. Pant, V. Sharma, P. Singh, *Toxicol. Rep.* **2** (2015) 716 (https://doi.org/10.1016/j.toxrep.2015.04.006)
15. A. Channing, A. Zamuner, D. Edwards, D. Guido, *Am. J. Bot.* **98** (2011) 680 (https://doi.org/10.3732/ajb.1000211)
16. L. P. van Reeuwijk, *Procedures for soil analysis*, FAO/ISRIC, Wageningen, 2002, pp. 1–120 (https://www.isric.org/sites/default/files/ISRIC_TechPap09.pdf)
17. *U.S. EPA 3051: Microwave assisted acid digestion of sediments, sludges and oils*, 1998
18. M. Pansu, J. Gautheyroy, *Handbook of soil analysis. Mineralogical, organic and inorganic methods,* Springer, Berlin, 2006, pp.1–993 (https://doi.org/10.1007/978-3-540-31211-6)
19. A. J. Baker, *J. Plant Nutr.* **3** (1981) 643 (https://doi.org/10.1080/01904168109362867).

20. V. Stanković, V. Milošević, D. Milićević, M. Gorgievski, G. Bogdanović, *Chem. Ind. Chem. Eng. Q.* **24** (2018) 333 (https://doi.org/10.2298/CICEQ170817005S)
21. D. Kasowska, K Gediga, Z. Spiak, *Environ. Sci. Pollut. Res.* **25** (2018) 824 (https://doi.org/10.1007/s11356-017-0451-y)
22. A. Karczewska, K. Milko, *Ecol. Chem. Eng., A* **17** (2010) 395
23. W. Khalir, M. Hanafiah, S. So'ad, W Ngah, *Pol. J. Chem. Technol.* **13** (2012) 84 (https://doi.org/10.2478/v10026-011-0054-1)
24. L. Zheng, P. Meng, *J. Taiwan Inst. Chem. Eng.* **58** (2016) 391 (http://dx.doi.org/10.1016/j.jtice.2015.06.017)
25. N. Osmolovskaya, V. V. Dung, L. Kuchaeva, *Bio. Comm.* **63** (2018) 9 (https://doi.org/10.21638/spbu03.2018.103)
26. A. Kabata-Pendias, *Trace elements in soils and plants*, CRC Press, London, 2011
27. E. Epstein, *Annu. Rev. Plant Physiol*. **50** (1999) 641 (https://doi.org/10.1146/annurev.arplant.50.1.641)
28. V. García-Gaytán, E. Bojórquez-Quintal, F. Hernández-Mendoza, D. K. Tiwari, N. Corona-Morales, Z. Moradi-Shakoorian, *J. Chil. Chem. Soc.* **64** (2019) 4298 (http://dx.doi.org/10.4067/s0717-97072019000104298)
29. K. M. Cocker, D. E. Evans, M. J. Hodson, *Physiol. Plant.* **104** (2002) 608 (https://doi.org/10.1034/j.1399-3054.1998.1040413.x)
30. C. Zhang, L. Wang, Q. Nie, W. Zhang, F Zhang, *Environ. Exp. Bot.* **62** (2008) 300 (https://doi.org/10.1016/j.envexpbot.2007.10.024)
31. M. Sahebi, M. M. Hanafi, A. Siti Nor Akmar, M. Y. Rafii, P. Azizi, F. Tengoua, J. Nurul Mayzaitul Azwa, M. Shabanimofrad, *Biomed Res. Int.* **2015** (2015) 396010 (https://doi.org/10.1155/2015/396010)
32. J. A. Bhat, S. M. Shivaraj, P. Singh P, D. B. Navadagi, D. K. Tripathi, P. K. Dash, A. U. Solanke, H. Sonah, R. Deshmukh, *Plants* **8** (2019) 71 (https://doi.org/10.3390/plants8030071)
33. S. M. Zargar, R. Mahajan, J. A. Bhat, M. Nazir, R. Deshmukh, *3 Biotech* **9** (2019) 73 (https://doi.org/10.1007/s13205-019-1613-z)
34. T. Morishita, J. K. Boratynski, *J. Soil Sci. Plant Nutr.* **38** (1992) 781 (https://doi.org/10.1080/00380768.1992.10416712)
35. A. A. Meharg, J. Hartley-Whitaker, *New Phytol.* **154** (2002) 29 (https://doi.org/10.1046/j.1469-8137.2002.00363.x)
36. A. Clark, T. Hutchinson, *Enhancing natural succession on Yukon mine tailings sites: a low-input management approach, in: Mining Environment Research Group Report 2005-3*, Geoscience Information and Sales, Indian and Northern Affairs, Whitehhorse, 2005
37. H. Deng, Z. H. Ye, M. H. Wong, *Environ. Pollut.* **132** (2004) 29 https://doi.org/10.1016/j.envpol.2004.03.030
38. I. W. R. Young, C. Naguit, S. J. Halwas, S. Renault, J. H. Markham, *Restor. Ecol.* **21** (2013) 498 (https://doi.org/10.1111/j.1526-100X.2012.00913.x)
39. J. May, Q. Yang, Y. Zhang, X. Zeng, Y. Zhong, D. Liu, *MATEC Web of Conferences* **100** (2017) 04030, https://doi.org/10.1051/matecconf/201710004030
40. D. Ranđelović, N. Mihailović, S. Jovanović, *Int. J. Phytorem.* **21** (2019) 707 (https://doi.org/10.1080/15226514.2018.1556590)
41. E. Kurniati, T. Imai, T. Higuchi, M. Sekine, *J. Deg. Mining Lands Manage.* **1** (2014) 93 (ISSN: 2339-076X).

Journal of the Serbian Chemical Society
JSCS@tmf.bg.ac.rs • www.shd.org.rs/JSCS
J. Serb. Chem. Soc. 88 (10) S316–S317 (2023)
Supplementary material

SUPPLEMENTARY MATERIAL TO

Potentially toxic element accumulation in two *Equisetum* species spontaneously grown in the flotation tailings

GORDANA ANDREJIĆ[1]*, MILIJANA KOVAČEVIĆ[2], ŽELJKO DŽELETOVIĆ[1],
UROŠ ALEKSIĆ[1], ISIDOR GRDOVIĆ[2] and TAMARA RAKIĆ[2]

[1]University of Belgrade, Institute for the Application of Nuclear Energy, Banatska 31b, 11080 Belgrade, Serbia and [2]University of Belgrade, Faculty of Biology, Studentski trg 16, 11000 Belgrade, Serbia

J. Serb. Chem. Soc. 88 (10) (2023) 1055–1064

Site description

Plants and their belonging substrates were collected from two different parcels of the flotation tailings of the active Pb-Cu-Zn mine on Mt. Rudnik (44,11 N; 20,495 E; 500 m asl), located in central Serbia (Fig. S-1A). *Equisetum arvense* and *E. telmateia* populations are distributed across two distinct sections within the peripheral area of the flotation tailings, adjacent to the surrounding natural vegetation. These sections benefit from a sufficient water supply as a result of the presence of a nearby stream (Fig. S-1B). It is worth noting that no deposition of waste material has occurred in either of these tailing parcels for the past four years preceding the sampling. The climate in this region and at this altitude is temperate.

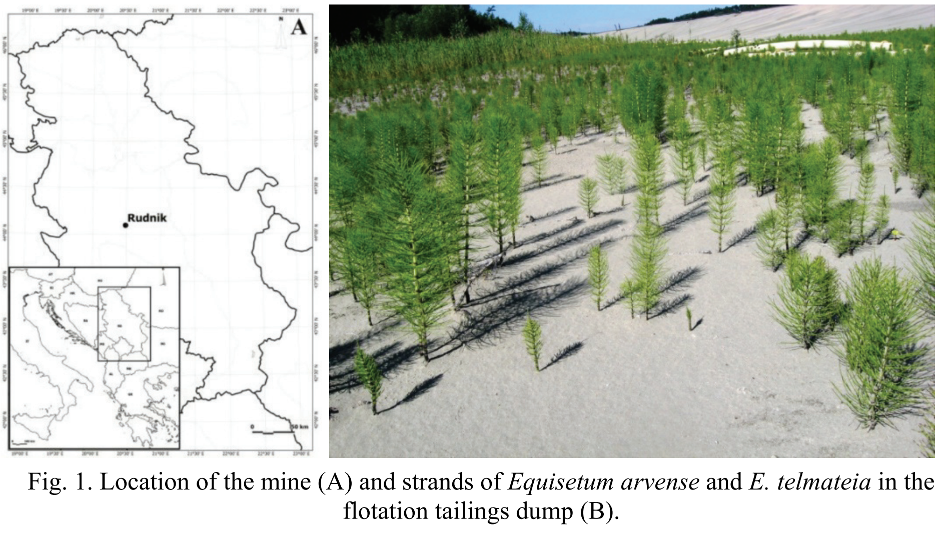

Fig. 1. Location of the mine (A) and strands of *Equisetum arvense* and *E. telmateia* in the flotation tailings dump (B).

---

* Corresponding author. E-mail: gordanaa@inep.ac.rs

Substrate and plant sampling

Each plant was sampled together with the substrate surrounding the rhizome and its adventitious roots, from the depth 0-20 cm, in August 2017. Each composite substrate sample (F_{EA}, *E. arvense* flotation tailings substrate; F_{ET}, *E. telmateia* flotation tailings substrate) was composed of well mixed substrate samples collected from the rhizosphere of 15 individuals.